INVESTIGATING THE USE OF FAST REPETITION RATE FLUOROMETRY IN UNDERSTANDING ALGAL PHYSIOLOGY IN OPTICALLY COMPLEX OCEANS

DEREK CONNOR

DEPARTMENT OF PHYSICS

UNIVERSITY OF STRATHCLYDE

A thesis submitted to the University of Strathclyde in accordance with the requirements for the degree of Doctor of Philosophy.

COPYRIGHT

Signed:

Date:

ACKNOWLEDGEMENTS

First and foremost, I would like to thank my long-suffering supervisor, Dr. David McKee, for his help, support, and insight that allowed this thesis to be here just now. If only I had listened, we could have saved each other plenty of pain, however, it has been a pleasure working with you.

There are a number of people without whom, this project would never have been completed- from those who helped me learn new techniques to others who were simply faces in the corridor with a friendly hello. Their enthusiasm, time, and support have been invaluable and greatly appreciated. Furthermore, my parents deserve a great deal more thanks than I can show on this page. They've supported me all the way from primary school to now coming out as a doctoral physicist and truly, without them, this wouldn't have been possible.

Finally, I would like to thank Hazel- for everything. This has been a long, winding, and difficult road, which you have walked with me without hesitation or question. I don't have the words to describe how much that has meant to me. Thank you (BEE!).

p.s. to all those whom insisted on asking whether it was done yet… it's done.

ABSTRACT

Increased mechanisation and burning of fossil fuels has resulted in year-on-year increases in the concentration of atmospheric carbon dioxide, a key greenhouse gas. Phytoplankton are photosynthesising organisms that are ubiquitous with water and responsible for approximately 50 % of global primary productivity. These organisms have adapted, evolved, and survived over many millions of years, however, the current rate of change being introduced into the biosphere by anthropogenic climate change raises significant questions about how these organisms will adapt to rapidly changing ocean temperatures and acidity.

It is possible to determine the physiological state of phytoplankton using changes in the variable fluorescence output from the photosynthetic pathways present in all phytoplankton. Here this was achieved using a Fast Repetition Rate fluorometer (FRRf). Algal dynamics respond rapidly to changes in environmental conditions making it essential that measurements are made as quickly and accurately as possible. A core aim of this thesis was to conduct a series of characterisation experiments to optimise the use and define the limits of performance of the FRRf with particular focus on the impact of conducting measurements in optically complex Case II waters. In April, 2015, the Marine Optics and Remote Sensing Group here at the University of Strathclyde together with colleagues from the Helmholtz Zentrum Geesthacht (HZG) in Germany, and Wet Labs Inc. (USA) undertook a research cruise around UK coastal waters. During this cruise, FRRf was used to determine the physiological status of phytoplankton in a variety of optically complex waters with support from data produced by a host of *in situ* and lab-based instruments. Data was analysed to establish if any simple patterns could be observed between the physical, optical, and biogeochemical parameters measured in combination with the FRRf measurements with it being found that temporal variability had the most impact on algal physiology. Subsequently, temporal variability over the course of a single day was investigated using a full day of measurements at a single location in Loch Fyne. A series of six measurements were made over the course of the day providing an opportunity to analyse the impact of overhead conditions on the *in situ* algal dynamics. Using the inherent optical properties (IOP) data collected at Loch Fyne, it was possible to model the underwater light fields using Hydrolight radiative transfer modelling, which was combined with the FRRf data measured over the day to produce estimates of the daily, column-integrated gross primary productivity (DCIGPP). This DCIGPP model was compared to three existing models for net primary productivity (NPP) from the literature so as to determine how useful an estimate of

GPP the DCIGPP model provided. Using a value for the respiration rate of 97 % from the literature, good agreement was found between the DCIGPP-NPP estimates and the estimates of NPP from the VGPM and CbPM models. This suggests that the model of DCIGPP based on FRRf data is potentially useful in estimating the daily gross primary productivity.

Contents

List of Figures

List of Tables

LIST OF SYMBOLS

Symbol	Description	Unit
A	Filter pad clearance area	m^2
a	Absorption coefficient	m^{-1}
a_{CDOM}	Absorption due to CDOM	m^{-1}
a_g	Absorption coefficient of gelbstoff	m^{-1}
a_{gp}	Absorption coefficient of gelbstoff and particles	m^{-1}
a_n	Non-water absorption coefficient	m^{-1}
a_p	Absorption coefficient of particles	m^{-1}
a_{ph}	Absorption due to phytoplankton	m^{-1}
$a_{ph}^*{}_{Chl}(\lambda)$	Chlorophyll-specific algal absorption	$m^2\ mg^{-1}$
a_{NAP}	Non-algal absorption coefficient	m^{-1}
b	Scattering coefficient	m^{-1}
b_{bp}	Particulate backscattering coefficient	m^{-1}
β	(1) Saturation phase weighting of FLC to improve fit (2) Pathlength amplification factor	Dimensionless
c	attenuation coefficient	m^{-1}
c_n	fraction of closed reaction centres after n^{th} flashlet	
C,T,D	conductivity, temperature, and density measurements made off the side of a ship	
CbPM	Carbon biomass productivity model for estimating net primary productivity	$mg\ C\ m^{-2}\ d^{-1}$

CDOM	coloured dissolved organic matter	
Chlorophyll *a*	concentration of chlorophyll *a* in the water	mg m^{-3}
Chl_F	estimate of chlorophyll *a* concentration from FRRf parameters	mg m^{-3}
Chl_{OCRS}	sea-surface chlorophyll concentration determined by remote sensing	mg m^{-3}
DCIGPP	daily, column-integrated GPP derived from FRRf and Hydrolight measurements	gC m^{-2} d^{-1}
Daily Light Integral	Instantaneous surface PAR multiplied by 86,400 s for a full day and divided by $1x10^6$ to convert from micromoles to moles	mol photons m^{-2} d^{-1}
DOC	Dissolved organic carbon content	mg m^{-3}
E	irradiance	mW m^{-2} nm^{-1}
E_u	Upwelling irradiance	mW m^{-2} nm^{-1}
E_d	incident downward irradiance	mW m^{-2} nm^{-1}
E_k	light saturation parameter	µmol photons m^{-2} s^{-1}
$E_{k\beta}$	beta phase light saturation parameter	µmol photons m^{-2} s^{-1}
E_{LED}	photon irradiance of FRRf excitation LEDs	$x10^{22}$ photons m^{-2} s^{-1}
ETR	Electron transport rate	µmol electrons m^{-2} s^{-1}
F’	Fluorescence at zeroth flashlet of a single turnover measurement	dimensionless

$F_o(')$	Fluorescence at zeroth flashlet of a single turnover measurement when C=0 (under ambient light)	dimensionless
$F_m(')$	Fluorescence when C=1 (under ambient light)	dimensionless
F_q'	$F_m' - F'$	dimensionless
$F_v(')$	$F_m(') - F_m(')$	dimensionless
$F_v(')/F_m(')$	Fluorescence parameter providing an estimate of photosystem II photochemical efficiency when C=0	dimensionless
F_q'/F_m'	Fluorescence parameter providing an estimate of photosystem II photochemical efficiency under ambient light	dimensionless
F_{Chl}	Proxy of chlorophyll concentration made using BBFL2	mg m^{-3}
F_{RAW}	Standardised raw fluorescence signal	dimensionless
F81	Falkowski (1981) model of net primary productivity	mg C m^{-2} d^{-1}
GPP	Gross primary productivity	mg C m^{-2} d^{-1}
HPLC	High Performance Liquid Chromatography	
I_o	Daily light integral of the surface PAR	mol photons m^{-2} d^{-1}
JV_{PSII}	PSII flux per unit volume	electrons (PSII m^{-3}) s^{-1}
k_g	air-sea gas exchange coefficient	length $time^{-1}$
L	radiance	W m^{-2} sr^{-1}
L_u	Upwelling radiance	W m^{-2} sr^{-1}
μ_g	Phytoplankton growth rate	d^{-1}
NPP	Net primary productivity (GPP – respiration)	mg C m^{-2} d^{-1}

NSV	Normalised Stern-Volmer Coefficient	dimensionless
OD	Optical density	dimensionless
p	Connectivity between reaction centres within photosystem II	dimensionless
ΔpCO_2	difference in equilibrium partial pressure of CO_2	ppm
P^B_{opt}	Chlorophyll-specific maximum daily rate of carbon fixation	mg C mg Chl^{-1} d^{-1}
PAR	Photosynthetically active radiation	µmol photons m^{-2} s^{-1}
POC	Particulate organic matter content	mg m^{-3}
$\varphi_{e,C}$	electron to carbon exchange factor	mol electrons (mol carbon)$^{-1}$
ψ	water column light utilisation index	mg C m^3 µmol photons^{-1} mg Chl^{-1}
R_{rs}	Remotely sensed reflectance signal	sr^{-1}
[RCII]	Concentration of photosystem II reaction centres	RCII m^{-3}
$R\sigma_{PII}$	Probability that a reaction centre closes after the first flashlet	dimensionless
σ_{PII}	functional absorption cross-section of photosystem II	m^2 $PSII^{-1}$
σ_T	Density anomaly	kg m^{-3}
TSS	Total suspended solid content	mg m^{-3}
VGPM	Vertically generalised productivity model for net primary productivity	mg C m^2 d^{-1}
Z_{eu}	Euphotic depth	m

1. Introduction

1.1. Anthropogenic Climate Change

Since the dawn of the Industrial revolution at the beginning of the 19th century, increasing quantities of pollutants especially greenhouse gases have been injected into the atmosphere. Through increasing mechanisation and burning of fossil fuels, there have been year-on-year increases in atmospheric CO_2 concentrations that are discordant with predicted trends in atmospheric carbon levels from historical ice cores (Oreskes, 2004; Karl and Trenberth, 2003). The measure of historical atmospheric CO_2 is made possible through measurements on ice cores and in more recent times by direct measurement at observatories such as Mauna Loa in Hawaii, which since the late 1950s has been keeping daily readings of atmospheric CO_2 (Figure 1.1).

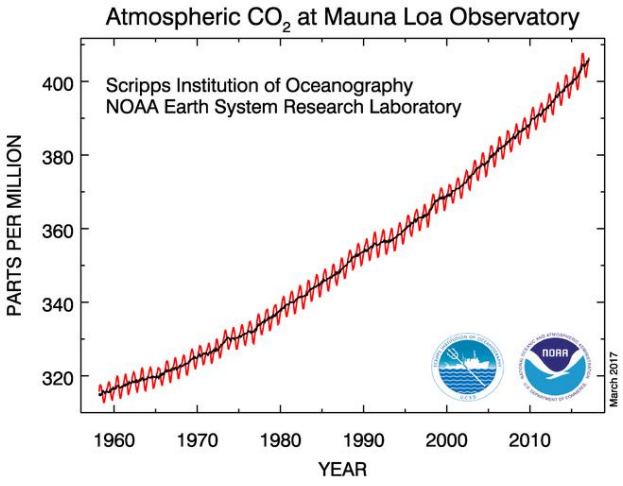

Figure 1.1: Monthly mean atmospheric CO_2 readings from the Mauna Loa observatory (Dr. Pieter Tans, NOAA/ESRL (www.esrl.noaa.gov/gmd/ccgg/trends/) and Dr. Ralph Keeling, Scripps Institution of Oceanography (scrippsco2.ucsd.edu/)).

There is an almost unanimous agreement amongst scientists that these year-on-year rises in greenhouse gas concentrations are a direct result of anthropogenic action and the global impact of our actions is becoming increasingly obvious. For example, in July 2017, iceberg A-68, an iceberg measuring 5.8×10^3 km^2 and weighing 1×10^{15} kg, calved from the Larsen C ice shelf in Antarctica, an event that, although not definitively attributable to warming

temperatures is generally considered to be associated with the effects of global climate change.

The warming temperatures associated with the greenhouse effect are causing significant changes to physical and biological systems around the world, on most continents and in most oceans. Some of these effects include shrinking glaciers and ice sheets, seawater temperatures increasing, increased average global precipitation, and floral and faunal shifts in response to changing regional climates (Rosenzweig *et al*., 2008).

Mass deforestation also plays a contributing role in increasing greenhouse gas concentrations in the atmosphere. The impact of deforestation is twofold, in that the trees that are felled are no longer able to photosynthesise so carbon fixation ceases and secondly, the carbon that was stored in the trees may be released to the environment through burning or rotting. It is estimated that deforestation contributes up to 15 % of the carbon dioxide in the atmosphere, which is more than the sum impact of all cars and trucks on the world's roads today (14 % of emissions) (Moeini-Meybodi *et al*., 2009). Deforestation and burning of fossil fuels not only cause global temperatures to rise but the increasing CO_2 concentrations in the atmosphere mean more CO_2 is being dissolved in the world's oceans leading to ocean acidification.

Seawater is slightly basic but increasing dissolution of carbon dioxide in the oceans results in a greater concentration of hydrogen ions reducing the pH, with it being estimated that since the Industrial revolution there has been a 29 % increase in hydrogen ion concentration in the world's oceans (Mora *et al*., 2013).

Increased ocean temperatures and acidification culminate in a situation where there are so many complex variables in play, it is difficult to identify exactly what the results are going to be. What is clear though is that these anthropogenically-driven environmental changes are occurring much more quickly than biological organisms have experienced previously. One organism that is of particular concern are phytoplankton.

Phytoplankton and the Environment

Phytoplankton form the base of the global marine food web occupying the first trophic level (Tilman *et al*., 1982) with their name deriving from the Greek 'phyto' meaning 'plant' and 'plankton' meaning 'wanderer'.

All phytoplankton are autotrophic meaning they are able to produce energy from inorganic compounds. This is done through the process of photosynthesis. There are very many different types of phytoplankton with the most commonly found being cyanobacteria, diatoms, coccolithophores, and dinoflagellates. Phytoplankton need to remain within the euphotic zone, defined as the depth of the water column that receives enough sunlight to allow photosynthesis to occur. There are many thousands of different species of phytoplankton (Sournia *et al.*,1991) that have developed various techniques to fulfil their ecological niche including methods to ensure they stay within the euphotic zone and also to allow them to move up and down the water column to access the nutrients they require. Some techniques include chain-forming phytoplankton as is the case with *Arthrospira maxima*, helping them float and to ward off predators. Phytoflagellates are those phytoplankton that, at some point in their life cycle, possess flagella which allow them to propel through the water column. An example of a phytoflagellate are the *Dunaliella* species, a chlorophyceae of the order chlamydomonadales.

Phytoplankton are microscopic marine organisms that range in size from 0.2 µm such as some picoplankton like *Microcystis aeruginosa*, a cyanobacteria from the order Chroococcales; up to 2 mm, such as the largest known diatom *Ethmodiscus rex. (*Li *et al.*, 1983; Schmidt *et al.*, 1991; de Deckker *et al.*, 2002*).*

Phytoplankton are ubiquitous with water. As they are photosynthesising organisms, they will tend to be found in the upper layer of the water column. Behrenfeld *et al*. (2008) defined the three conditions that phytoplankton require for growth and productivity as light, i.e. ability to remain within the euphotic zone, nutrients for growth, and the water temperature as enzyme efficiency operates as a function of temperature (Behrenfeld *et al*., 2008). Although all three conditions are integral to the phytoplankton physiological status, it is not uncommon for a single condition to be vastly more important under the right setting, for example, iron deficiency in oligotrophic waters where there are a low accumulation of dissolved nutrients and high oxygen content.

Phytoplankton distributions tend to be greatest around the shelf edges of landmasses, coastal areas, along the equator in the Atlantic and Pacific oceans as well as in higher latitudes, such as in the Polar Regions, as can be seen in Figure 1.2. Deep water containing large concentrations of nutrients are drawn to the sea surface around these regions, which are crucial to phytoplankton survival and growth. Nutrient levels are further bolstered by input

from terrestrial sources. Figure 1.2 also shows low chlorophyll concentration areas in the middle of the Atlantic, Indian, and Pacific oceans that are around ocean gyres where nutrient levels are significantly lower due to permanent stratification of the water column. (Lindsey and Scott, 2010; McManus *et al.*, 2012)

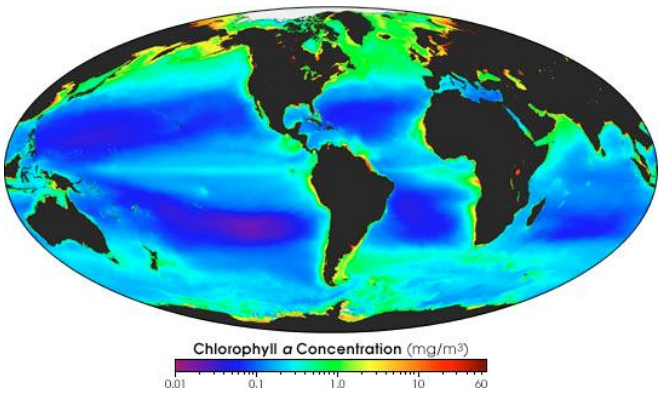

Figure 1.2: Chlorophyll distributions tend to be highest around Polar Regions and shelf edges however, they are predominantly dictated by nutrient availability (Image courtesy of SeaWiFS Project, NASA Earth Observatory, NASA Goddard Space Flight Centre).

Whilst accounting for only 1 % of the World's biomass, phytoplankton are estimated to be responsible for approximately 40-50 Pg C yr^{-1} (Longhurst *et al.*, 1995) of carbon fixation, which is roughly 50% of global primary production. This means that, on average, every second breath of oxygen was originally produced by phytoplankton photosynthesis. The short lifespan of individual algal cells and the general lack of commercial exploitation of phytoplankton mean that these organisms are sensitive indicators of environmental change. Some long-term plankton studies are now beginning to show changes in the community structure and abundance of key species that are relevant to the subsistence of many marine mammals (Atkinson *et al*., 2004; McGowan *et al.*, 1996). Boyce *et al*. (2010) used a combination of ocean transparency measurements and *in situ* chlorophyll observations from as early as 1899 to estimate the time dependence of phytoplankton biomass at different geographical scales showing a decline in the global median phytoplankton concentration of approximately 1 % per year.

The impact of increasing anthropogenic climate change on phytoplankton communities is not clear and continued monitoring and research into these organisms is necessary to understand the mechanisms they use to respond to changes in their physical environment and whether they are capable of responding quickly enough, genetically and phenotypically, to the new

environment that climate change is producing (Hallegraeff, 2010). Monitoring of algal physiology with variable fluorescence instruments such as the fast repetition rate fluorometer employed in this thesis, provide an opportunity to study variations in the algal response and model their capacity for carbon fixation with regard to varying chemical and physical environments.

1.2 Phytoplankton and the Global Carbon Cycle

Carbon and the Atmosphere

There are three reservoirs for carbon on Earth: the atmosphere, the terrestrial environment, and the oceans. The oceans are the largest reservoir for carbon whilst the atmosphere is the smallest of the three. The oceans play a key role in exchange between the other two reservoirs (Post *et al*., 1990).

Ocean carbon is stored in one of three ways; through dissolved inorganic carbon, for example dissolved CO_2, as HCO^-_3 or as CO_3^{2-}; as dissolved organic carbon or particulate organic carbon. The net exchange of carbon dioxide (CO_2) between the atmosphere and the world's oceans is responsible for approximately 2.2 Tg C yr^{-1} (Denman *et al*., 2007). The oceans are described as a net sink of CO_2 with the primary driver of ocean uptake of CO_2 being the partial pressure differential of the gas. Partial pressure is defined as the pressure exerted by a single gas in a mixture, for example CO_2 in air. Dalton's law of partial pressures defines the sum of all partial pressures as the total pressure assuming the gases are ideal gases. The partial pressure of CO_2 (pCO_2) is the gas phase pressure of CO_2 which would be in equilibrium with the dissolved CO_2 in the water as defined by Henry's Law at a constant temperature. The net air-sea flux can be defined by equation 1.1.

$$F \approx k_g\left(pCO_{2_a} - pCO_{2_s}\right) = k_g \Delta pCO_2 \quad (1.1)$$

where k_g is the air-sea gas exchange coefficient, pCO_{2_a} is the partial pressure of CO_2 in the air, and pCO_{2_s} is the equilibrium partial pressure of CO_2 in surface seawater (Siegenthaler and Sarmiento, 1993). The solubility of CO_2, the rate of biological activity, and ocean temperature are the key drivers of the partial pressure differential of carbon dioxide.

There is a complex and fragile relationship between the processes that regulate exchange of CO_2 between the atmosphere and the oceans. The oceans, being the largest reservoir of carbon on Earth, utilises many processes in storing and cycling carbon, for example through physical processes such as water column mixing, chemical processes such as buffering, and biological processes such as phytoplankton productivity and growth (Falkowski *et al*., 2000).

Phytoplankton are particularly important in the global carbon cycle as they have a pivotal role in sequestering atmospheric CO_2 and transporting it to the deep ocean (Street *et al*., 2005). It has been estimated that, each day, in excess of 100 million tonnes of carbon is fixed by phytoplankton in the global oceans (Behrenfeld *et al*., 2006). Antoine *et al*. (1996) estimate annual carbon fixation rates of between 40-50 Pg C yr^{-1}, with Bishop (2009) suggesting that 10 Pg C yr^{-1} is sequestered to the deep ocean by the biological carbon pump (BCP). This mechanism occurs as a result of the senescence of marine phytoplankton biomass and its subsequent sinking to the deep ocean. Some estimates claim that the entire marine phytoplankton biomass turns over on average within 6 days (Field *et al*., 1998). The BCP is crucial to the vertical carbon distribution through the water column and as such is important to the value of the partial pressure of CO_2 governing the sea-air CO_2 exchange rate (Bishop 2009; Antoine *et al*., 1996).

The biological carbon pump ensures that the Redfield ratio of carbon, nitrogen and phosphorus are cycled through the water column every time a single phytoplankter dies with on average 100 atoms of carbon then sinking down to the seabed (Chisholm , 1995). First discovered by American oceanographer, Alfred Redfield, the Redfield ratio describes the stoichiometric relationship between carbon, nitrogen, and phosphorus in the water column, with a consistent stoichiometry of 106:16:1 (Redfield, 1934). The Redfield ratio provides a useful marker for identifying nutrient limitation in specific regions and has been extended further in recent times to describe specific marine conditions and environments (Twining and Baines, 2004; Martiny, 2013; Klausemeier *et al*., 2008).

Bacteria and decomposition mechanisms break down the dead and sinking phytoplankton with a small proportion eventually settling on the seafloor. Carbon that settles on the seafloor is isolated from the global carbon cycle for decades to millennia depending on the depth of the water column (Denman *et al*., 2007).

The global consequences of anthropogenic climate change are rapidly becoming apparent and with many aspects of the biological carbon cycle still not well understood, it is imperative

that research into phytoplankton and their photophysiological processes are pursued to understand the role that these tiny organisms are playing and will continue to play with increasing ocean temperatures and acidification.

Phytoplankton Photosynthesis

Phytoplankton produce energy through the physicochemical process known as photosynthesis, using light, carbon dioxide, and water to produce the energy required for metabolic processes. However, an adequate supply of nutrients is necessary for the organisms to grow. They require a large variety of different nutrients but some of the most important to phytoplankton survival are the elements nitrogen, phosphorus, and iron. Phytoplankton require nitrogen and phosphorus in large concentrations. However, these two elements tend to be limiting factors for phytoplankton growth in the marine environment due to their low concentrations. Smith (1984) wrote that phytoplankton often tend to be operating near their required critical minimum of nutrients necessary for survival, that is to say, there are no surplus nutrients present. Nitrogen and phosphorus over-enrichment in coastal waters via agricultural activities is referred to as eutrophication. Eutrophication is damaging to the environment as it can result in harmful algal blooms and hypoxia creating dead zones across large coastal areas.

Geider and La Roche (1994) discuss bioassays that show in the presence of iron limitation, the algal response is to increase the concentration of iron transport molecules on cell surfaces with a concurrent reduction in the number of iron-containing molecules in the photosynthetic pathways. The reduction in iron-containing molecules impacts the ability of the cell to efficiently carry out photosynthesis. Furthermore, Behrenfeld and Kolber (1999) showed that diel fluorescence patterns found for phytoplankton in the South Pacific Ocean, a relatively iron-limited region rapidly disappeared following *in situ* iron enrichment of the waters highlighting the influence this element has on the physiological characteristics of phytoplankton.

The most prevalent form of photosynthesis used by organisms on Earth is oxygenic photosynthesis, where catalysed oxidation of water by light (*hν*) liberates molecules of oxygen as in equation 1.2.

$$CO_2 + H_2O \xrightarrow{h\nu} O_2 + \{CH_2O\} + energy\ loss\ as\ heat\ and\ fluorescence \qquad (1.2)$$

Photosynthesis is traditionally divided into two sets of reactions: the 'light' reactions and the 'dark' reactions. The 'light' reactions consist of the electron and proton transfer reactions

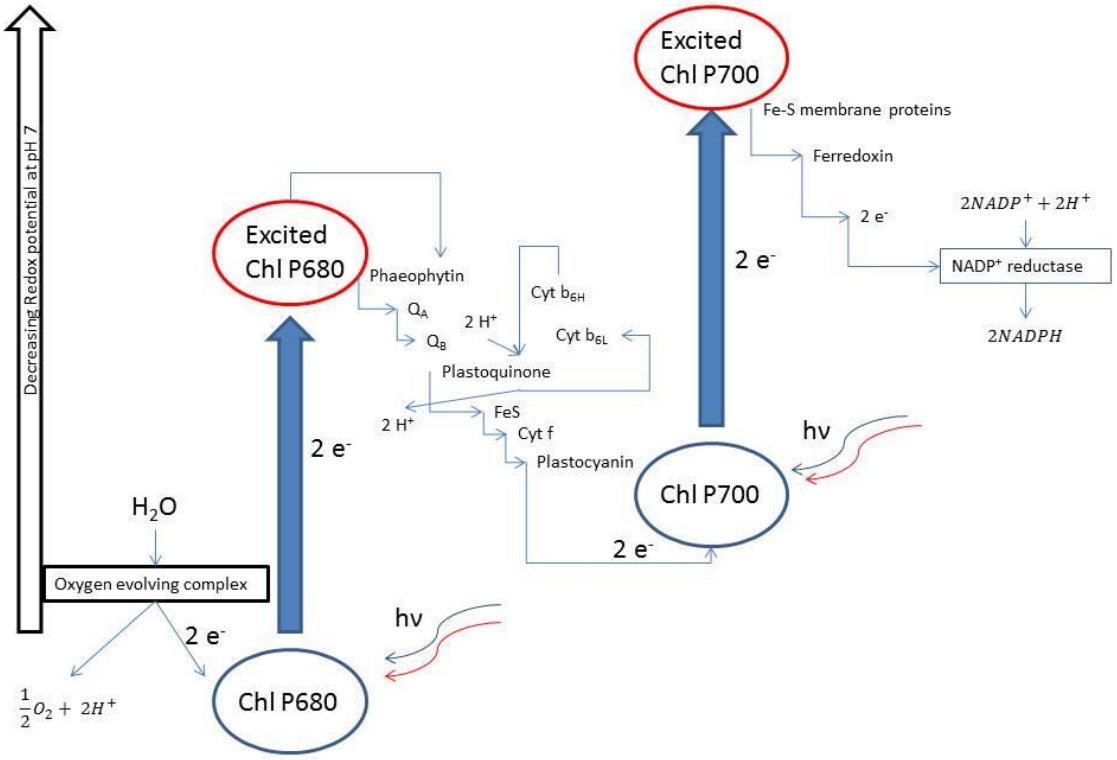

Figure 1.3: Simplified Z-scheme of photosynthetic electron transport (Adapted from Govindjee, 2000) Chl P680 is at photosystem II and Chl P700 is at photosystem I. Phaeophytin is the primary electron acceptor for photosystem II, Q_A and Q_B are chemically identical plastoquinone molecules that are tightly bound and loosely bound to the photosystem II complex at different binding sites, respectively. FeS is the Rieske iron-sulfur protein and cytochrome b_6 is composed of two states: a high energy and low energy state denoted by H and L.

through the photosynthetic pathways whereas the ‘dark’ reactions are further down the path at the Calvin cycle , as discussed later, and are responsible for biosynthesis of carbohydrate molecules from CO_2 (Whitmarsh and Govindjee, 1995).

Oxygenic photoautotrophs utilise two photochemical reaction centres, photosystem II and photosystem I, respectively, to coordinate electrons from the water-splitting reactions through the linear electron transport chain to NADPH (see *The Linear Electron Transport (LET) Chain*) (Behrenfeld *et al.*, 2013). Electrons travel through the linear electron transport chain by electron coupling and FRET interactions between a series of pigment-protein complexes (Behrenfeld *et al.*, 2013). This linear electron transport chain is most commonly visualised using a Z-scheme as is shown in Figure 1.3, which can be used to track the main stages of the photosynthetic process.

Oxidation of Water

Electrons are stripped from water molecules through oxidation catalysed by a manganese complex. Two molecules of water are required to produce 4 protons, 4 electrons and a molecule of diatomic oxygen. Electrons are then shuttled from the manganese complex to P680 by tyrosine. The excited P680 reaction centre then transfers the electron through phaeophytin to the first stable electron acceptor, a bound plastoquinone molecule (Q_A). Q_A is only capable of accepting a single electron at a time, which is then passed to a loosely bound plastoquinone molecule at a separate binding site (Q_B) along with two protons allowing the molecule to detach as plastoquinone. The plastoquinone (PQ) molecule is mobile through the hydrophobic interior of the thylakoid membrane. These reactions form the light-dependent reactions. Electrons are able to pass between these molecules due to the difference in their respective redox potentials. Molecules at the top of the Z-scheme have a lower redox potential and hence more readily give up electrons to those with a higher redox potential (lower down the scheme).

The Linear Electron Transport (LET) Chain

Photosystem II and photosystem I act in series and in that order, despite the nomenclature (Cournac *et al.*, 2000). The ultimate aim of the LET chain is to shuttle electrons from water to

$NADP^+$ (nicotinamide adenine dinucleotide phosphate), a molecule produced at ferredoxin beyond photosystem I. The addition of two electrons and a proton transforms $NADP^+$ into NADPH, an important molecule required for carbon fixation in the Calvin cycle and downstream synthesis of glucose (Singh, 2013).

The second molecule synthesised during the "light" reactions is adenosine triphosphate (ATP). During water oxidation, protons are pumped from the stroma into the thylakoid membrane, creating a concentration gradient between these two regions of the chloroplast. When the concentration of protons is greater in the thylakoid membrane than in the stroma, protons begin to flow back into the stroma via ATP synthase making the reaction between adenosine diphosphate (ADP) and inorganic phosphate energetically favourable allowing formation of ATP (Steinberg-Yfrach *et al*., 1998) in a process known as photophosphorylation.

Formation of NADPH and ATP is the ultimate biochemical aim of the photosynthesis process thereby allowing the fixation of carbon dioxide and its chemical transformation into sugars which can be used as fuel by the system.

Plastoquinone as an Electron Carrier

ATP synthesis is closely bound to the redox reactions of plastoquinone. The plastoquinone (PQ) pool is affected by the flux rate of electrons passing in and out of it, changing its redox potential (Schuurmans *et al*., 2014). The PQ pool acts as a buffer with photosystem I, preventing too many electrons from entering PS I as the photosynthetic machinery at PS I oxidise more rapidly than the PQ pool. As such, the PQ pool is often thought of as a rate determining step of the photosynthetic process (Falkowski and Raven, 1997).

The primary accepting quinone (Q_A) rapidly transfers an electron to Q_B, the secondary accepting quinone forming an intermediate complex known as semiquinone before being reduced to plastoquinol. Plastoquinol reaches an equilibrium with the PQ pool, a structure which is approximately twice in number of that of the PSII reaction centres (Melis and Brown, 1980). The extent to which the plastoquinone pool has been filled generally depends on the ambient irradiance. The higher the irradiance, the greater proportion of the PQ pool that is filled, assuming that equilibrium has been attained between irradiance and the photosynthetic apparatus.

Chlorophyll and the Photosynthetic Pigments

The chlorophylls are all cyclic tetrapyrrole compounds with a magnesium atom chelated at the centre of the ring system. Chlorophylls *a* & *b* are structurally similar except for the position of a long chain hydrocarbon on the ring. Chlorophylls *c* & *d* are further distinct from chlorophyll *a* but still focus around the same basic structure. All photosynthetic plants contain chlorophyll *a* with the other chlorophyll structures being present in varying concentrations. All chlorophylls have a strong absorption band (Q-band) which appears in the red region of the visible spectrum (Stockett *et al*., 2015). They also have another band, which is stronger and present in the blue region, this is referred to as the Soret band and occurs at approximately 435 nm for chlorophyll *a in vivo* (Rabinowitch and Govindjee, 1969). Chlorophyll exciton transfer and quantum coherence is controlled by the Q-band (Reimers *et al*., 2013). The Gouterman model of porphyrins states that chlorophyll has two electronic transitions in this region, Q_x (S_2) and Q_y (S_1) (Weavers, 2005; Reimers *et al*., 2013). Carotenoids are the second photosynthetic pigment. They are chemically very different from the chlorophylls as they are composed of C40 isoprenoid compounds (Baranska and Kaczor, 2016).

Chlorophyll and the carotenoids occur complexed to protein structures. Photosynthetic pigments essentially only function in their photosynthetic roles as long as they are in one of these supramolecular complexes (Paulsen *et al*., 1993). These proteins occur bound to several chlorophylls as well as perhaps one or even several carotenoids. The bulk of these pigment-protein interactions are necessary for collecting light from the ambient environment before transferring the energy that has been absorbed to the photosystem II reaction centres. The pigment molecules are actually encapsulated within the protein (Frausto da Silva, 2001) rather than being attached covalently to the surface with the protein-pigment complex held together through highly specific non-covalent interactions.

These pigment-protein complexes may be grouped into two classes: reaction centre complexes & light-harvesting complexes (Brennan, 2008). Light harvesting complex concentration is highly dependent upon light intensity and light quality. Ordinarily, an excited electron would relax by release of energy non-radiatively however if there is a suitable electron acceptor close by then the excited electron can transfer from the initial molecule to the acceptor. This positively ionises the initial molecule and negatively ionises the acceptor, a process known as photo-induced charge separation and takes place at the reaction centre. The

electron that was removed from the initial molecule can be used to reduce other organic compounds thereby creating a method for the plant to store the energy absorbed from the photon in chemical form.

Light Harvesting Complexes and Reaction Centres

The light harvesting complexes of photosystem II and the P680 reaction centres are inextricably connected (Pascal *et al*., 2005). The light harvesting complexes (LHCs) form large antennae arrays composed of chlorophyll, carotenoids, and other pigments that act to absorb as much of the visible light incident on the organism as possible. This light is then funnelled down into the reaction centre at P680 exciting a chlorophyll molecule, starting the linear electron transport chain as in Figure 1.5. The transport of electrons through the photosystems is referred to as photochemical quenching (Schreiber *et al.,* 1986); with each reaction centre only capable of processing a single charge separation event at a time. When charge separation occurs at a photosystem II reaction centre, it is referred to as being closed, that is, it cannot accept any further electrons at that time.

The rate at which reaction centres close is determined by the conditions experienced by the algal cells at that time. Irradiance levels, excitation energy transfer efficiency, and the number of functional PSII reaction centres are determining factors in this (Fleming *et al.*, 1988; Allen *et al*., 2000). Photosynthetic organisms increase their productivity rates with increasing irradiance, to a point, where the photosynthetic machinery would be defined as light saturated. If irradiance continues to increase beyond this point, there is a risk that the proteins in the reaction centres may be damaged by the excess energy (Durrant *et al*., 1990; Telfer *et al*., 1991; Ohnishi *et al*., 2005). For this reason, photosynthetic organisms developed non-photochemical quenching (NPQ) mechanisms. NPQ can occur radiatively or non-radiatively (as thermal dissipation) (Lavaud *et al*., 2004; Herold, 1980).

Energy Quenching and Photosynthesis

Fluorescence as a competitive mechanism0 is key to our ability to probe the physiological state of phytoplankton. Fluorescence is a competitive mechanism and under natural conditions is always in competition with various quenching mechanisms (Genty *et al*., 1990).

Specifically, these are the photochemical quenching mechanism (q_p) and non-photochemical quenching mechanism (q_n). The non-photochemical quenching mechanism may be further sub-divided into three mechanisms- these are the high-energy state (q_E), state transitional quenching (q_T) & photoinhibitory quenching (q_I) (Mueller *et al*., 2001). The kinetics of these mechanisms vary greatly with the high-energy state being quenched in a matter of a few minutes whereas the photoinhibitory quenching mechanism may take up to hours and days to return to normal (Berteotti *et al*., 2016). Fluorescence is one of two mechanisms for the emission of light from an electronically excited substance, termed luminescence, the other being phosphorescence.

Chlorophyll and Fluorescence

Fluorescence occurs as a singlet to singlet mechanism where two electrons of opposite spin, with one in the excited singlet state and the opposite electron in the ground excited state, pair together. This is described as a spin-allowed process and occurs very rapidly with the fluorescence lifetime (Wong, 2017), i.e. the time between excitation and return to ground state, with this being a physiology-dependent variable. Our own data suggests that some components of the fluorescence lifetime may be less than 1 ns or as long as 5 ns.

The best way to visualise the absorption and emission processes that characterise fluorescence, and phosphorescence, is by a Jablonski diagram as in Figure 1.4. A Jablonski diagram is composed of energy levels incorporating electronic, vibrational and rotational energy levels with the total energy of the system being described by the sum of the three energy levels. Typically, the difference between electronic energy levels is on the nanometre scale, vibrational energy levels are separated on the micrometre scale and rotational energy levels are typically on the centimetres scale. Fluorescence occurs in three distinct steps: absorption of an incident photon by the fluorophore in the ground state, S0 creating an electronically excited singlet state, S1.

Certain processes as shown in Figure 1.4 may then come into play to return the excited fluorophore to the ground state; these include internal conversion and vibrational relaxation whereby the excited singlet state of the molecule relaxes to its lowest possible vibrational state, S1-0. The third step is the emission process itself, fluorescence. This occurs on a very different timescale with absorption and internal conversion occurring on the femto to

picosecond scale respectively whereas fluorescence occurs on the nanosecond scale (Kuhn *et al*., 2009). Quenching and non-radiative relaxation are two separate mechanisms for energy dissipation in a fluorophore. These operate concurrently to fluorescence, and compete, having an impact on the fluorescence lifetime and intensity of the fluorophore. As would be expected, the process of internal conversion as well as vibrational relaxation causes there to be a reduction in the energy, i.e. the incident photon has a shorter wavelength than the fluorescent photon. This is characteristic of fluorescence and is known as the Stokes shift.

The Stokes shift allows fluorescence to be usable as a spectroscopic technique as the energy of the emitted light is sufficiently red-shifted so as to be easily distinguishable from the absorbed light. Internal conversions occur on a picosecond time scale; this is fast enough that the atomic nucleus will not be significantly displaced during an internal conversion. This is known as the Franck-Condon principle and is why transitions are taken to be shown as vertical lines on the Jablonski diagram.

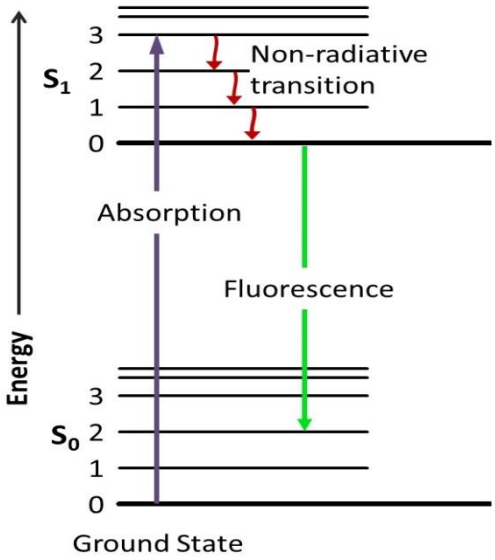

Figure 1.4: Jablonski diagram for fluorescence showing an S0 to S1 transition with non-radiative internal conversions, which are made up of rotational and vibrational energy losses. This Stokes' shift explains why the energy of a fluoresced photon is less than the absorbed photon.

1.3. Beyond Photosystem II

The Calvin Cycle and Carbon Fixation

Following the formation of ATP and NADPH during the "light" reactions, the second phase of photosynthesis begins, known as the "dark" reactions. This second phase involves the enzymatically-driven fixation of inorganic carbon dioxide and transformation into carbohydrate molecules. The basic equation representing this mechanism is shown in equation 1.3.

$$9ATP + 6NADPH + 3CO_2 \rightarrow Gal3P + 6NADP^+ + 9ADP + 8P_i \qquad (1.3)$$

Carbon dioxide enters the algal cell by two mechanisms: passive diffusion or via a carbon concentrating mechanism (CCM) (Raven and Beardall, 2003). Once in the algal cell, the enzyme ribulose bisphosphate carboxylase oxygenase (RuBisCO) binds the inorganic carbon molecule bringing it into the Calvin cycle. The evolution of the carbon concentrating mechanism is a response to the poor electron affinity of RuBisCO for carbon dioxide. Hundreds of millions of years ago, as the atmospheric concentration of carbon dioxide decreased, there was a concomitant increase in the atmospheric concentration of oxygen creating an issue as RuBisCO has dual competitive functions as both a carboxylase and oxygenase. Carbon concentrating mechanisms are diverse across different groups and families of phytoplankton to combat the inefficiencies of passive carbon dioxide uptake (Giordano *et al*., 2007).

The Calvin cycle can be thought to occur in three stages, as in Figure 1.5. The first step, carbon fixation, sees a molecule of carbon dioxide being catalytically incorporated into a molecule of 3-phosphoglyceric acid (PGA) by the enzyme RuBisCO. Two molecules of PGA are required for the conversion to glyceraldehyde 3-phosphate (PGAL). PGAL is the product of the Calvin cycle and can be converted into many other organic molecules including glucose phosphate. For the cycle to be maintained, 5 molecules of PGAL are re-circulated for the regeneration of RuBP.

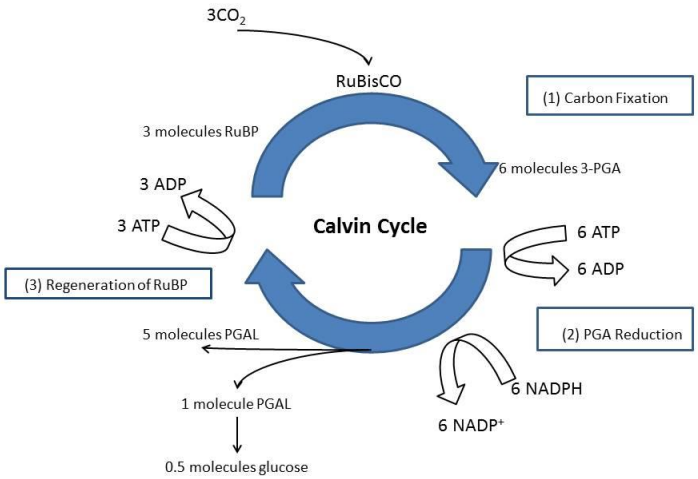

Figure 1.5: Simplified diagram of the Calvin cycle showing the process from the fixation of inorganic carbon and carbohydrate formation (adapted from Khan Academy- Calvin Cycle and Capra (1997) The Web of Life).

1.4. Active Fluorometry and Phytoplankton

The Beginnings of Active Fluorometry

G.G. Stokes was the first to recognise fluorescence as the emission of photons and so-named the process (Govdinjee, 1995). Prior to Stokes' work and certainly afterwards, many scientists worked with chlorophyll and recognised the apparent red colour when exposed to light. It was not until Hans Kautsky's 1931 paper that a correlation was made between chlorophyll exposure to light and CO_2 assimilation rates (Kautsky, 1931). The Kautsky phenomenon is recognised as a peak in chlorophyll fluorescence output followed by a decline in the emission. This rise to a maximum is acknowledged as the progressive closing of photosystem II reaction centres with the decline in fluorescence attributed to the switching on of non-photochemical quenching mechanisms (Krause *et al.*, 1991, Govindjee, 1995).

The Fluorescence Transient

Direct fluorescence is the measure of a sample that is intrinsically fluorescent. This is done using a spectrofluorometer operating at the required absorption and emission wavelengths to

induce fluorescence (Valeur, 2001). Fluorescence transients produced by photosynthetic organisms can be analysed to provide information on structure, conformation and function of the photosynthetic apparatus, primarily photosystem II. It can also identify various pigments and complexes and the electron excitation transfer occurring between them (Govindjee, 1995). Active chlorophyll fluorescence techniques are preferred for photophysiology studies over passive techniques (for example, *in situ* natural chlorophyll fluorescence measurements (Kiefer *et al.*, 1989)) as passive techniques tend to work under the flawed assumption that there is a constant ratio between photosynthetic and fluorescence yield. This is, in fact, a highly variable ratio (up to 10:1) meaning that measurements made via passive techniques can be unreliable and fail to capture the nuance of algal dynamics (Falkowski and Kolber, 1993). Active techniques, on the other hand, allow for the study of photosynthetic processes i.e. light absorption, primary photochemistry and electron transport from PSII to PSI. These measurements are not possible using passive techniques.

The fluorescence transient (also known as the Kautsky effect or OJIP curve as in Figure 1.6) is the phenomenon of characteristic changes in the chlorophyll *a* fluorescence intensity when exposed to continuous light. The Kautsky effect can be classified as being either fast (up to 1 second) or slow (several minutes). It must be noted that only 3-5% of energy is dissipated from excited chlorophyll in the form of fluorescence. The physiological state of phytoplankton varies with the chemical and physical environment, and the fluorescence signal produced is a complex of these factors and its light history. (Strasser *et al.*, 2000).

The quantum yield, Φ_f, of chlorophyll *a* is related to the rate constants of the various de-excitation pathways, *k*, available as shown in equation 1.4.

$$\Phi_f = \frac{k_f}{k_f + k_h + k_t + k_q + k_p} \tag{1.4}$$

where *f* is fluorescence, *h* is thermal dissipation, *t* is excitation energy transfer, *q* is for quenching by quenchers and *p* is for photochemical effects. As can be seen from equation 1.4, the fluorescence signal is affected by many different de-excitation pathways other than fluorescence.

The absolute quantum yield is the ratio of photons emitted to photons absorbed. This absolute quantum yield value will not agree with the Φ_f value if there is a change in the

environmental conditions or in the microenvironment. For example, changes in the absorption cross-section in the fluorescence pigment bed caused by static quenching.

Figure 1.6 is a typical fluorescence transient. O is the origin, I is the intermediary peak, D stands for dip, P is the peak- the peak is ordinarily reached within 50-100 ms, S is the quasi-steady state, M is the maximum, which is achieved by the system within 500-600 ms and T is the terminal steady state. The terminal steady state may take greater than 1 second to occur. OIDP is the fast transient & PSMT is the slow transient. It may also be that some aspects of the curve are not always observed, for example the maximum, M, is not always present and sometimes several steady-states appear (Govindjee, 1986).

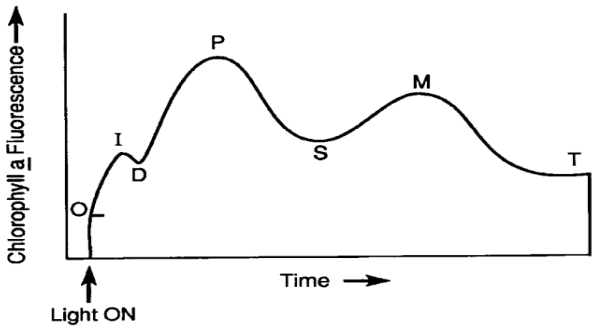

Figure 1.6: Typical Kautsky curve showing the fast and slow transients associated with closing and opening of reaction centres, where the time is shown on a log scale (Govindjee, 1995).

As discussed, there are several competitive de-excitation pathways and it is found that fluorescence is complementary to these other mechanisms, specifically photochemical de-activation and thermal dissipation. That is to say, fluorescence is brightest when these two mechanisms are less efficient and vice versa. The reduction in fluorescence after reaching its maximum is taken to be due to non-photochemical quenching. This has been attributed to a protection system used by plants to avoid over-exposure to light and subsequent damage to photosystem II.

Biochemically, the rise in fluorescence is assumed to be a reduction in the number of electron acceptors present in the photosynthetic pathway. Each quinone molecule is only able to accept and "process" one electron at a time (see *Plastoquinone as an Electron Carrier*), until this electron has been processed, the reaction centre is closed. This leads to a proportion of reaction centres, at any one time, being closed. As such, there is an increase in fluorescence

intensity. The quenching effect that occurs over the course of a few minutes, following the fluorescence peak is explained by an increase in the rate of electron transfer away from PSII. This increase in electron transfer is due to light-mediated activation of enzymes that are pivotal to carbon metabolism.

1.5. Fast Repetition Rate Fluorometry

Introduction to Fast Repetition Rate fluorometry

Fast Repetition rate fluorometry (FRRf) was first mentioned in the literature in 1992 by Zbigniew Kolber and Paul Falkowski in their description of the development of an *in vivo* instrument for measuring the photosynthetic rates of phytoplankton via fluorescence (Kolber and Falkowski, 1992). FRRf is described as being a minimally invasive and non-destructive means of probing photosystem II of algal cells (Kolber and Falkowski, 1998). The FRRf method takes advantage of the photochemical setup described previously where photolytic separation of water produces electrons, protons and molecular oxygen.

Theory behind Fast Repetition Rate fluorometry

The FastOcean Fast Repetition Rate fluorometer is the third version of Chelsea Technology Group's FRRf system. This instrument includes two additional excitation LED wavebands for probing of non-chlorophyll-based algal photophysiology. All details relating to the FRRf are specific to the FastOcean system in this thesis.

Illumination of an optically thin sample of phytoplankton with rapid pulses using an excitation LED produces a fluorescence signal during a single closing and re-opening sequence of the photosystem II reaction centres, known as a single turnover. An example of a single turnover fluorescence transient can be seen in Figure 1.7.

Fluorescence emits uniformly in all directions meaning a small fraction of this fluorescence reaches a photomultiplier tube, passing through two 3 mm RG665 Schott glass filters and a 682 nm bandpass filter. The photons incident on the PMT generates an electrical current, which is then digitised by an ADC. The digital signal is then standardised by adjusting for the

incident E_{LED} and PMT gain voltage. This adjusted signal is referred to as F_{RAW} and is proportional to the concentration of reaction centres in photosystem II (equation 1.5).

$$F_{RAW} \propto \sigma_{PII} \cdot [RCII] \tag{1.5}$$

where σ_{PII} is the functional absorption cross-section of PSII ($x10^{-18}$ m^2 (nm^2)), a measure of the maximal efficiency of light utilisation for photochemistry in PSII, and [RCII] is the concentration of photosystem II reaction centres.

Using equations from Kolber *et al.,* (1998), the fluorescence signal observed during a single turnover can be related to values for F_o, F_m, σ_{PII} and p.

$$C_n = C_{n-1} + R\sigma_{PII} \cdot \frac{1- C_{n-1}}{1- C_n \cdot p} \tag{1.6}$$

$$F_n = F_o + (F_m - F_o) \cdot C_n \cdot \frac{1- C_{n-1}}{1- C_n \cdot p} \tag{1.7}$$

Equation 1.6 defines the fraction of closed reaction centres after the n^{th} flashlet (C_n) of the LED excitation sequence, where p is a measure of the connectivity of the PSII reaction centres for energy dissipation. $R\sigma_{PII}$ is the probability that a reaction centre will close during the first flashlet (2 µs in length) of a single turnover saturation phase. The value of the fraction of closed reaction centres feeds into equation 1.7, where an estimate of the fluorescence during the n^{th} flashlet (F_n) is determined. Further to the closed fraction and connectivity, the initial and maximum fluorescence are also required. Equations 1.6 and 1.7 show the relationship between the reaction centres closing and incident photons with there being increasing fluorescence emission with closing reaction centres.

The fluorescence transient in Figure 1.7 was produced by means of a series of sub-saturating flashes leading to a single turnover, where these flashes closes all the photosystem II reaction centres once. The closing of all photosystem II reaction centres produces a maximum fluorescence, F_m.

The initial fluorescence, F_o, is defined as the low level of fluorescence being emitted from the pigment bed in the absence of solar irradiance or any light source sufficient to drive photosynthesis (Kromkamp and Forster., 2003). Under dark regulated conditions, Q_A is very effective at quenching fluorescence as a means of energy dissipation. With increasing illumination, the fluorescence will increase. F_o is calculated from linear regression of the

initial eight points of a fluorescence transient, whilst F_m is calculated by linear regression through the final 24 points of the transient

During the saturation phase, the fast repetition rate fluorometer allows wide-ranging control over the excitation LED inputs. The number of flashlets in the saturation phase can be varied between 0 and 12,000 flashlets on a pitch between 2 to 200 µs. In Figure 1.7, the vertical dotted line represents the beginning of the relaxation phase of the pulse sequence. Evaluation of relaxation phase Q_A^- reoxidation kinetics can be monitored during the relaxation phase by varying the number of flashlets between 0 and 2000 on a pitch of between 8 µs to 20 ms, which is up to 100 times slower than the saturation phase (Kolber *et al.*, 1998). The number of sequence repetitions can be set to between 1 and 160 repetitions with variable intervals of 40 to 120,000 µs.

In a single turnover saturation phase, equations 1.6 and 1.7 are utilised. The initial phase of the fitting process calculates for the initial and maximum fluorescence, F_o and F_m respectively, if these numbers are biophysically reasonable, for example F_o is smaller than F_m, then the second stage of the fitting process proceeds to estimates of $R\sigma_{PII}$ and *p*. Once this fitting process is complete, an estimate of F_v/F_m is made. F_v/F_m is a measure of the dark-regulated maximum potential quantum efficiency of photosystem II in the algal cell. This is the ratio of the difference between F_m and F_o (F_v) divided by F_m.

If the assumption is made that a single charge separation event closes a single reaction centre, with each charge separation event being driven by a single photon then $R\sigma_{PII}$ can be equated to RJ_{PII}, the probability of electron flux through photosystem II allowing calculation of σ_{PII} as in equation 1.8:

$$\sigma_{PII} = \frac{RJ_{PII}}{E_{LED}} \tag{1.8}$$

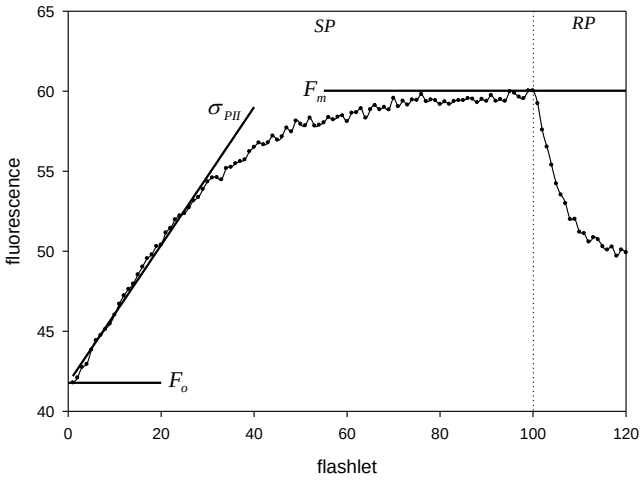

Figure 1.7: A fluorescence transient (A single 2 µs flashlet produced by FastPro8 of a sample of D.tertiolecta. The fluorescence rises from an initial value, F_o, to a maximum after a pre-set number of pulses at F_m. The relaxation phase monitors the relaxation kinetics. The functional absorption cross-section (σ_{PII}) is calculated as the iterative curve fit of the saturation phase as shown as the slope of the transient. The saturation phase is the first stage as shown by SP and the relaxation phase follows as shown by RP.

Connectivity of Photosystem II Reaction Centres

Connectivity describes the degree to which reaction centres interact with one another. When an electron arrives at a reaction centre, the reaction centre will be open or closed. If it is open, charge separation will occur, closing the reaction centre. If the reaction centre is already closed, the degree of connectivity describes the likelihood that the electron will transfer to a different reaction centre to attempt charge separation. If the electron cannot undergo charge separation then its energy is dissipated via a non-photochemical pathway, for example fluorescence.

Accounting for connectivity, as can be seen in equations 1.6 and 1.7, helps to define the number of fluorescence quanta produced and the rate of photochemistry within the organism. Vredenberg and Duysens (1963) showed that closing of reaction centres results in an increase in the fluorescence yield. Further work by Joliot and Joliot (1964) found the same thing for *Chlorella*, a different species from Vredenberg and Duysens. Joliot and Joliot took this work further and derived expressions for the photochemical yield and fluorescence yield, based on

the fraction of open photosystem II reaction centres. Central to this was the connectivity parameter (p), which determined the likelihood that an electron would transfer to a neighbouring reaction centre from a closed reaction centre (Stirbet, 2013). Chelsea Technology Group, in their FastPro8 software provide four models of varying connectivity to describe the interconnectedness of photosystem II reaction centres.

One model of connectivity is the separate package model. This assumes there is zero connectivity between reaction centres, i.e. $p = 0$. The separate package model theoretically results in an exponential rise in the fluorescence yield, which is not the case, as was shown by Vredenberg and Duysens (1963).

At the opposite extreme from the separate package model is the lake model, where $p = 1$. The lake model assumes unrestricted electron diffusion through the pigment bed to find an open reaction centre, producing a single statistical entity (Stirbet, 2013). The lake model was rejected as being an incorrect description of pigment bed dynamics as experiments by Joliot and Joliot (1972) and Lavorel and Joliot (1972) found inconsistencies with this approach. The lake package model is still used occasionally for simplification when modelling pigment bed interactions.

The dimer model of reaction centre connectivity describes a situation where pairs of reaction centres are connected with no connectivity between those that are not in the dimer. A mixture of the lake model and the dimer model produce what is known as the heterogeneous model, which is the standard connectivity model for FastPro8. This assumes that all reaction centres are connected to some extent throughout photosystem II (Nedbal *et al.,* 1999; Strasser *et al.,* 2001). The applied complexity of connectivity when calculating the fluorescence induction curve affects the shape of the transient. All FRRf measurements conducted throughout this thesis have applied the heterogeneous model of reaction centre connectivity. Values of p in our measurements vary between 0.1 and 0.5 generally.

Fluorescence Light Curves

Fluorescence light curves (FLCs) effectively measure the photosynthetic capacity of algal cells at different actinic irradiances. Successive probing of a sample with stepwise increases in the light intensity progressively build the FLC (Herlory *et al*., 2007) with an example shown in Figure 1.8. FastPro8, the software that is shipped with the FastOcean unit, uses a

relative measure of photosynthesis (rP), which is a function of the light-adapted photochemical efficiency (F'_q/F'_m) and PAR as shown in equation 1.9.

$$rETR = {F'_q}/{F'_m} \cdot PAR \tag{1.9}$$

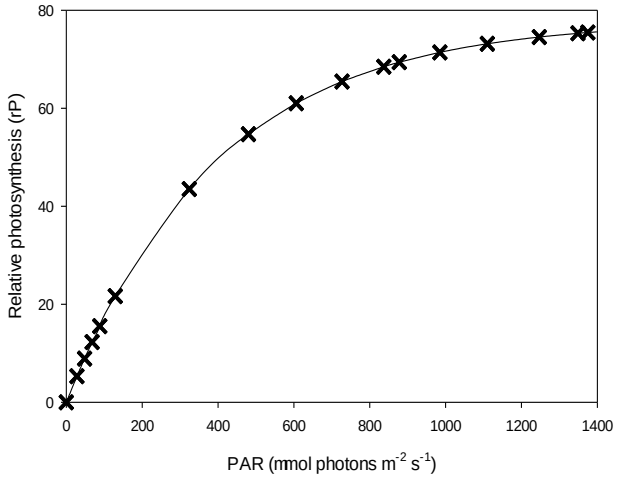

Figure 1.8: An idealised FLC showing the relationship between the actinic irradiance and the photosynthetic response under normal conditions. FLC parameters used were taken from station 25 data of the He442 UK coastal waters cruise.

FastPro8 employs a two stage fitting process comprised of the alpha phase and the beta phase with the fit being produced using a minimisation of the sum of squares of the difference between the actual and fit values. The equations used to produce the alpha and beta phase fits are adapted from Webb *et al.*(1974) and are shown in equations 1.10 and 1.11 respectively.

$${F'_q}/{F'_m} = \alpha \cdot E_k \cdot \left(1 - e^{-\frac{PAR}{E_k}}\right) \cdot PAR^{-1} \tag{1.10}$$

$${F'_q}/{F'_m} = \left(\alpha \cdot E_k \cdot \left[1 - e^{-\frac{PAR}{E_k}}\right] - \beta \cdot E_{k\beta} \cdot \left[1 - e^{-\frac{PAR - E_k}{E_{k\beta}}}\right]\right) \cdot PAR^{-1} \tag{1.11}$$

The alpha phase generates values for α, the fit value of the dark regulated photochemical efficiency, and E_k, the saturation parameter describing the point in the algal dynamics where the cells are moving from light-limited to light-saturated.

The beta phase introduces additional parameters that are designed to modify the shape of the light curve to improve the fit of the curve, and so take into account the effects of photoacclimation at irradiances greater than E_k.

Different phytoplankton under different conditions exhibit variations in light curve response. These differences may be indicative of changes in photophysiology and photosynthetic capacity of the cells, for example, a cell with damage to photosystem II proteins due to high actinic irradiance would produce a different FLC fit from that of a sample that is responding to the first light of the day after a night of dark acclimation and respiration.

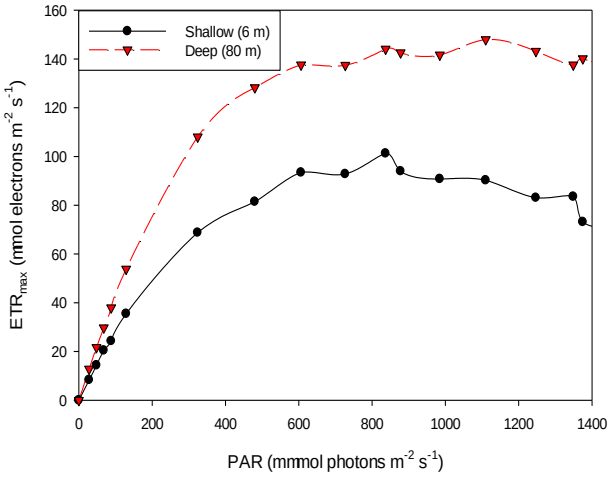

Figure 1.9: FLC data for two casts at station 61 in the North Sea during the UK Coastal Waters cruise. The first cast was taken at 6 m and is shown with the black line and circle symbols on the graph. The second cast was taken at 80 m and is represented by the dashed, red line and triangle symbols. The graph shows that the surface phytoplankton are showing decreasing ETR_{max} at high irradiance suggesting those cells are beginning to be damaged by sunlight. This is in comparison to the deep water algae, which show much greater response to higher irradiance levels and are generally more physiologically robust and healthy.

Figure 1.9 shows two fluorescence light curves for algae that were present in the same water column: shallow-dwelling phytoplankton, that were close to the surface (6 m) at the time of measurement and deep-dwelling phytoplankton that were measured at 80 m depth. The two curves show differing responses to increasing actinic irradiance with the deep water sample showing a more robust and productive response to high actinic irradiance. The shallow-water sample has lower ETR_{max} at each light level with a reduction in ETR_{max} at the highest light levels that is commonly associated with photoinhibition. These plots show the differing responses of phytoplankton to irradiance based on their recent light histories.

Understanding the Underlying Processes in FastPro8

The processes that occur to transform a fluorescence photon emitted from a sample through to being a measure of the photochemical efficiency of an algal cell are not always well signposted in the literature. This includes the necessary calibration steps performed by the manufacturer. Figure 1.9 is a flow diagram of the processes undertaken by the FastPro8 software when generating the parameters produced by a FastOcean fast repetition rate fluorometer.

The flow diagram is separated into two distinct sections. There are the measurements that flow from the top left starting with "excitation protocol" and the calibration settings, which are manufacturer-set and produce a series of constants that are employed for parameter calculation. From the diagram, there is a clear progression in the complexity of parameters calculated with the photochemical efficiency, F_v/F_m, being the simplest of these. From this parameter, it is possible to estimate the electron transport rate (ETR) or the PSII electron flux on a volume basis (JV_{PSII}).

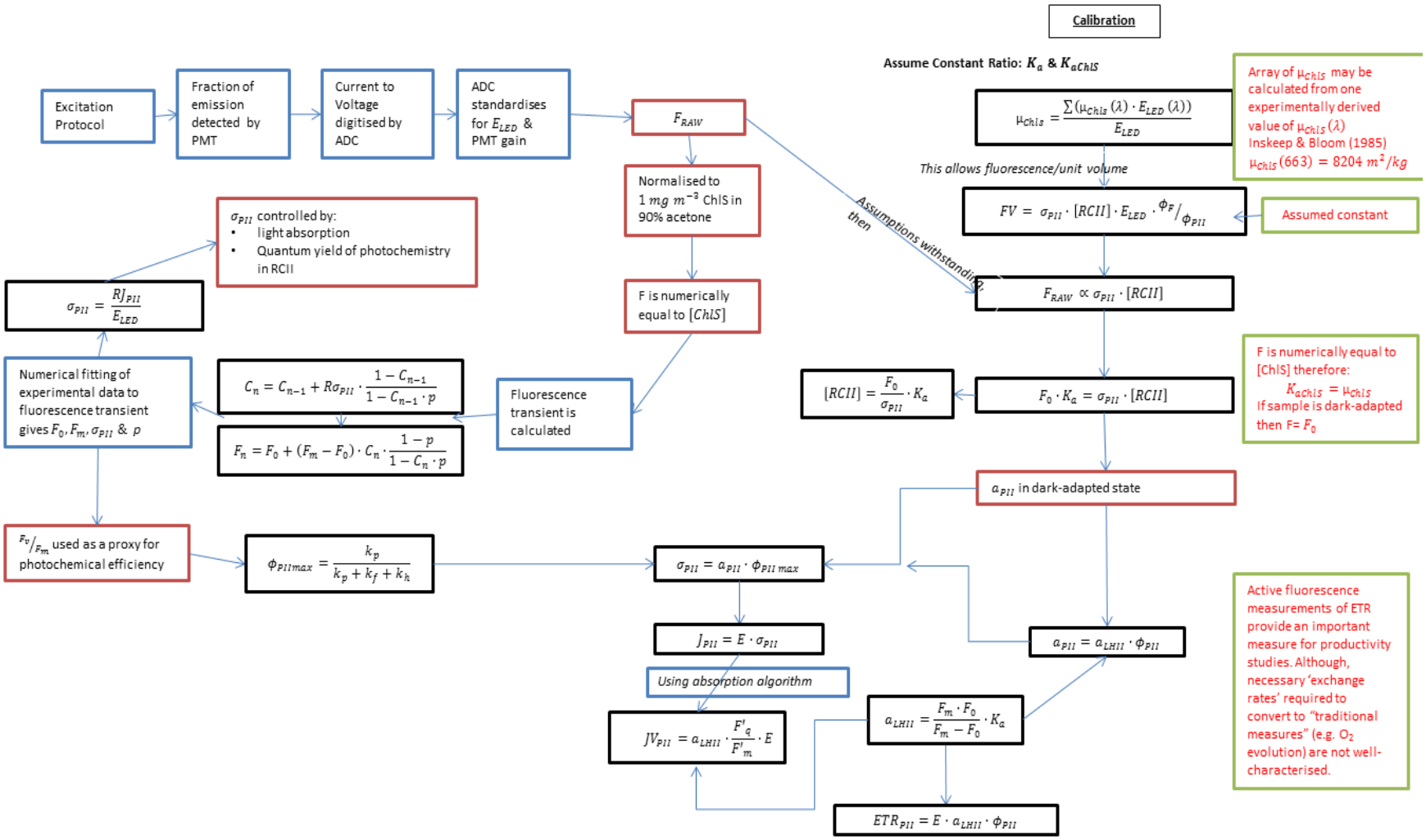

Figure 1.9: Flow diagram of the processes undertaken by FastPro8 to convert a fluorescence photon signal into a recognisable FRRf parameter.

Potential Limitations of FRRf in Coastal Waters

A review of the available literature shows that little to no work has been carried out into addressing the potential limitations of operating a fast repetition rate fluorometer in optically complex coastal waters. Personal communications with Kevin Oxborough, principal scientist at Chelsea Technology Group identified that it is theoretically possible for the emission signal to be affected by other optically active components in the water. It may be possible that there is no information in the literature as people are indirectly dealing with optical complexity by applying a filtered seawater blank. This issue is addressed in chapter 3, section 3.

1.6. Aim of Thesis

Phytoplankton are ubiquitous organisms, appearing anywhere with access to water and sunlight. Over the course of the last 1.5 billion years, phytoplankton have adapted to changing conditions on Earth allowing for these organisms to proliferate in the past 100 million years into multiple families consisting of hundreds of genus with thousands of species (Sournia *et al*., 1991; Falkowski *et al*., 1994; McClelland *et al*., 2016). Phytoplankton are intrinsic to the liberation of atmospheric oxygen and, anthropogenic climate change aside, maintaining equilibrium in the global carbon cycle. Fluorescence in phytoplankton is the radiative emission of excess energy to prevent damage to the photosynthetic apparatus. This process of emission can be tracked due to its variable nature using active fluorometry techniques that allow for the estimation of the phytoplankton physiological status. In the course of this investigation, the third generation fast repetition rate fluorometer, FastOcean, was employed. This thesis aims to improve the FastOcean measurement protocol to determine the optimal settings and procedures for rapid and accurate estimations of phytoplankton physiological state whilst operating in a time-limited cruise environment. Further to this, potential limitations of FastOcean in optically complex case II waters are assessed. Using data gathered during a research cruise around the coast of the United Kingdom, a multi-parametric survey of UK coastal waters is made and a time series gathered at Loch Fyne during this cruise is used to make estimates of daily, column-integrated gross primary productivity.

Specifically, the following problems were addressed:

- In order to make the most reliable and consistent results possible, it is important to understand the limits of performance of the FastOcean system and to determine optimal conditions and settings on the hardware and sample preparation. For example, is there an optimum time required for dark acclimation of an algal sample prior to measurement? Furthermore, optimisation of measurements was addressed looking at issues such as replicability of fluorescence light curves. The overarching goal of this is to establish a procedure that is as quick as possible without significantly compromising data quality.
- The performance of the FastOcean system in optically complex case II waters was investigated with the question of influence on measurements by the presence of high concentrations of CDOM and scattering particles, asking whether FastOcean is suitable for operation in optically complex waters such as the Bristol Channel.
- Using data collected during He442, a research cruise around UK coastal waters, a multi-parametric survey was performed and attempts made to understand the interrelationship of physiological, physical, optical, and biogeochemical parameters.
- Data from the time series station in Loch Fyne during He442 was used with Hydrolight model-led underwater light fields to make estimates of time and column-integrated gross primary productivity. An attempt was made to reconcile our estimates of *in situ* primary productivity with models used in ocean colour remote sensing to calculate net primary productivity. The time series analysis also allowed the question of an optimal sampling strategy for making a measurement of physiological state for estimates of GPP as well as addressing the issue of whether a single measurement is sufficient to extrapolate over the course of a day, as is often the norm.

2. Theory and Methodology of Ancillary Datasets

2.1. Introduction

The collection of a multiple instrument dataset during He442 allowed for biogeochemical characterisation and radiative transfer modelling of various UK coastal waters. Fast repetition rate fluorometry measurements were made in tandem with other biogeochemical and IOP measurements to produce a more comprehensive picture of the water column at each station. These ancillary measurements contextualise FRRf measurements and the physiological states measured for the algal cells in these locations and their associated light climate. Laboratory and field-based methods are discussed within the context of their relationship with algal photophysiological parameters, for example, the impact of temperature on photochemical efficiency or CDOM concentration on the measured fluorescence signal.

Water samples were prepared for on board analysis by lowering the CTD rosette to a specified depth and samples collected in Niskin bottles. Chapter 4, Table 4.1 provides an overview of the instruments deployed during He442 and the parameters measured by each. Several biogeochemical factors were measured optically or chemically in the lab, from the Niskin bottles; these include CDOM absorption measurements, HPLC chlorophyll concentration, total suspended solid and total carbon concentrations.

2.2. Theory of Methodologies

Optically Significant Water Constituents

Natural waters contain a continuous range of particle sizes ranging from the smallest viruses to blue whales. These particles are categorised into either dissolved or particulate matter, where dissolved matter is somewhat arbitrarily deemed to be that which is able to pass through a 0.2 µm pore size filter (Lock, 2012). Dissolved and organic matter both contribute to the optical properties of the water column.

Dissolved organic matter (DOM) is normally considered to originate from one of three sources- terrestrial runoff from soil; algal breakdown products; and from man-made sources such as fertilisers which run off the soil as well (Mostofa *et al*., 2013). In coastal areas, the most common sources of DOM are from humic and fulvic fractions that result from terrestrial

runoff (Therese Harvey *et al*., 2015) with the fraction of this DOM that interacts with light called coloured dissolved organic matter (CDOM).

CDOM absorbs light primarily in the ultraviolet and blue region of the electromagnetic spectrum (see section 3.3., Figure 3.19a). It is thought that high concentrations of CDOM in the water column have a negative impact on primary productivity due to competitive light absorption against phytoplankton, which require light from the blue end of the spectrum for efficient photosynthesis (Ask *et al*., 2009). This question is addressed in chapter 3, section 3.

Particulate matter (PM) is material that cannot pass through a 0.2 µm filter and is either of a biological or physical origin. In our measurements, we used GF/F filters which have a porosity of approximately 0.7 µm. This results in a 0.5 µm gap in the practical definitions of particular and dissolved matter. Anecdotal evidence from colleagues at HZG in Germany show that this produces a small but not negligible effect in measurements of particulate and dissolved matter. PM includes phytoplankton and some associated algal breakdown products, whereas PM produced via physical means tends to be a result of weathering and erosion. Phytoplankton are considered to be one of the most decisive factors in determining the optical properties of the water column in oceanic waters. The diversity of size, shape, and species-dependent composition means that the scattering properties of the water column are affected. Furthermore, the absorption and fluorescence emission associated with molecules such as chlorophyll, that are integral to the photochemical processes occurring within phytoplankton, contribute to the optical characteristics of the water.

Phytoplankton contain large concentrations of light harvesting molecules, with chlorophyll being the most common of these but many accessory pigments existing too, including the carotenoids. The pigment composition of phytoplankton and their physiological status impacts on the light harvesting efficiency of the cells and so affects the amount of light that is absorbed in the water column. The role of chlorophyll in phytoplankton is discussed in detail in section 1.2.

Practically, total suspended solids are anything greater than 0.7 µm in size as determined by retention characteristics of the GF filters in the water. These suspended solids may be organic or inorganic in nature but tend to be composed of sediment, silt, and sand as well as algae. The greater the concentration of suspended solids, the lower the water clarity; where water clarity is defined by the depth that solar irradiance is able to penetrate to in the water column. The greater the water clarity then the deeper the euphotic depth of the water column. The

total suspended solids can be considered as an indicator of water quality with clearer waters often being considered more healthy than more turbid waters (Capuzzo *et al*., 2015). Of course, the nature of the material contributing to TSS and the extent to which it has been influenced by anthropogenic factors is important in such studies.

Inherent Optical Properties

The inherent optical properties (IOPs) of natural waters are the absorption (*a*), scattering (*b*), and backscattering (b_b). Preisendorfer (1961) defined these IOPs as properties of the water that are unaffected by the geometrical structure of the incident light field. Measurements of the optical properties of the water column yields information on the biogeochemical composition and determine the structure of the underwater light field. The IOPs are controlled by the composition and concentration of optically significant constituents such as algae and sediment.

The two fundamental IOPs are the absorption coefficient ($a(\lambda)$) and the volume scattering function ($\beta(\lambda)$). Knowledge of the volume scattering function is sufficient to calculate other scattering coefficients (see equations 2.3 and 2.4) such as the backscattering coefficient. IOPs are additive and so the absorption coefficient is the sum of the absorption coefficients found within the water column:

$$a(\lambda) = a_w(\lambda) + a_{CDOM}(\lambda) + a_{ph}(\lambda) + a_{NAP}(\lambda) \quad (2.1)$$

where a_w is the absorption contribution of the water, a_{CDOM} is the contribution from CDOM, a_{ph} is the absorption related to the algal component of the water, and a_{NAP} refers to absorption by non-algal particles, each of which are wavelength dependent. IOPs are also inter-additive, for example, the absorption and scattering coefficients can be added to produce the beam attenuation coefficient (*c*) (Sosik, 2008).

$$c(\lambda) = a(\lambda) + b(\lambda) \quad (2.2)$$

where $b(\lambda)$ is the scattering coefficient and is defined as:

$$b(\lambda) = 2\pi \int_0^{\pi} \beta(\theta, \lambda) sin\theta \, d\theta \quad (2.3)$$

$b_b(\lambda)$ is the backscattering coefficient defined as:

$$b_b(\lambda) = 2\pi \int_{\pi/2}^{\pi} \beta(\theta, \lambda) sin\theta \, d\theta \quad (2.4)$$

where θ is the solid angle. The volume scattering function when integrated across all solid angles gives the total power of scattered light per unit incident irradiance per unit volume. Integration of only the backwards solid angles produces the spectral backscattering coefficient (equation 2.4).

Radiometry

Radiance

The radiance (L) is defined as the energy per unit time per unit solid angle ($d\Omega$) per unit area (dS) that occurs perpendicular to the direction of propagation.

$$L(\theta, \phi, \lambda) = \frac{d^2\Phi}{dS \, cos\theta \, d\Omega} \quad (2.5)$$

where θ and ϕ are the zenith and azimuth angles respectively. Radiance is measured in units of W m^{-2} sr^{-1} nm^{-1}.

Irradiance

The irradiance, E, is the radiant flux per unit area of a surface and can be described as upwards or downwards irradiance with each being the upper and lower faces of a horizontal surface, for example the water-air interface in a body of water.

Irradiance is related to radiance by the radiant flux incident on a surface, dS at solid angle $d\omega$. The total irradiance (E) is given by:

$$E = \int_{4\pi} L(\theta, \phi) dS cos\theta d\omega \quad (2.6)$$

and the downwards and upwards irradiance are defined as:

$$E_d = \int_{2\pi} L(\theta, \phi) dS cos\theta d\omega \quad (2.7)$$

$$E_u = -\int_{-2\pi} L(\theta, \phi) dS cos\theta d\omega \quad (2.8)$$

where E_d is calculated by integrating with respect to the whole of the upper hemisphere and E_u calculated by integration of the whole lower hemisphere. Equation 2.8 has a negative on the right hand side as cos θ is negative between 90-180°.

Planar irradiance is often used in the literature as the majority of sensors available use this configuration. However, algal cells collect light in an isotropic manner, i.e. without any preference for direction. For photosynthesis applications, the scalar irradiance is more appropriate. Scalar irradiance is therefore defined as equations 2.9 and 2.10.

$$E_{0d} = \int_{2\pi} L(\theta, \phi) d\omega \quad (2.9)$$

$$E_{0u} = \int_{-2\pi} L(\theta, \phi) d\omega \quad (2.10)$$

where scalar irradiance is measured in units of Wm^{-2} (Kirk, 1994).

2.3 Water Sample Analysis Methodologies

Biogeochemical parameters are used as proxies to characterise different water types and to provide understanding as to how light fields are influenced by dissolved and suspended materials. During the course of He442, several biogeochemical parameters were tested and their values recorded. This work was carried out by Rüdiger Röttgers, Kerstin Heymann, and Christian Utschig at the Helmholtz Zentrum Geesthacht (HZG) using protocols they have developed over multiple research cruises. PSICAM and LWCC measurements were carried out by Katharina Lefering from the Marine Optics and Remote Sensing Group at the University of Strathclyde.

Total Suspended Solids

Total suspended solid (TSS) was determined according to Röttgers *et al.* (2014). A few millilitres of purified water was used to saturate the edges of the pre-weighed filter pad before running an appropriate volume (between 100 ml to several litres of sample depending on concentration) through the filter under low vacuum (<0.2 bar). Röttgers *et al.* suggest using as large a volume of sample as possible to gain a maximum mass on the filter in an attempt to reduce systematic errors. Immediately following vacuum filtration of the sample,

the filter was washed three times with approximately 50 ml of ultrapure Milli-Q water. The filter pad was placed into a petri dish and allowed to air dry. The separation of TSS into its component organic and inorganic particulate matter (POM and PIM, respectively) is determined by loss on ignition (LoI) by volatising the organics at 500°C. The concentration of TSS and PIM is determined by the mass gained via sample filtration before and after combustion of the organic components being divided by the sample volume used. The influence of salt correction was performed according to Stavn *et al.*, (2009) and is discussed in Röttgers *et al.* (2014) in detail.

High Performance Liquid Chromatographic Determination of Chlorophyll Concentration

Chlorophyll concentration was determined according to Zapata *et al.* (2000). This method combines the use of a monomeric C_8 column developed by Göricke and Repeta (1993) with pyridine-containing mobile phases allowing for efficient separation of pigments in natural samples with 200 µL of sample being used as the injection volume. A full description of the HPLC setup can be found in Zapata *et al.* (2000). Chlorophylls were determined by fluorescence using excitation at 440 nm and emission at 650 nm with concentrations calculated by comparison to standards of known concentration for each pigment. Pigment standards were isolated from algal cultures of well-characterised pigment composition using semi-preparative HPLC and put into solvent as per Jeffrey *et al*. (1997).

Absorption by Coloured Dissolved Organic Matter (CDOM)

During He442, the presence of coloured dissolved organic matter (CDOM) was determined by absorption, as a proxy for concentration, using a point source integrating cavity absorption meter (PSICAM) and liquid waveguide capillary cell (LWCC). For the purposes of this thesis, only the PSICAM data is used.

The theory behind the point source integrating cavity absorption meter (PSICAM) has been extensively developed by Kirk (1997), Leathers *et al.*, (2000), and Lerebourg (2003), the details of which are beyond the scope of this thesis. To a first approximation, the PSICAM operates on the principle of scatter-free absorption measurements. Kirk (1995) described how by using an isotropically homogeneous light field, absorption determinations become

insensitive to scattering effects (Fry *et al.,* 1992; Hobbs *et al.,* 1999; Röttgers *et al.,* 2005; Röttgers *et al.*, 2007a; Röttgers *et al.*, 2007b). The cavity is constructed of OP.DI.MA (Gigahertz-Optic, Germany), a highly diffuse, reflective material, with Gigahertz-Optic giving the reflectivity of the material to be ~98 % across the visible spectrum. Light was provided by a stabilised 150 W halogen lamp, which was connected to a glass fibre bundle guiding light to a scattering sphere, creating a totally diffuse light field. The detection system was composed of a second glass fibre bundle positioned parallel to the light source (but outside the field of view of the light source).

Prior to measurement, the cavity was filled with ultrapure Milli-Q water for a minimum of 12 hours to hydrate the cavity material with the light source switched on for at least an hour prior to measurement to allow the output to stabilise. The calibration of the PSICAM had a strong influence on the quality of the data produced. Lerebourg *et al*. (2002) found that a 1 % error in the reflectivity resulted in a 10 % error in the measured absorption. Prior to calibration, the cavity was bleached using sodium hypochlorite (6-14 % NaOCl, Sigma Aldrich) for approximately 15 minutes. The cavity was then rinsed with running water and ultrapure Milli-Q water, twice each. A solution of nigrosine, a black dye, was prepared by dilution of a concentrated stock solution into 5 L of ultrapure Milli-Q water. The cavity was then filled with purified water to adjust the excitation lamp and integration time to produce a signal equivalent to 50,000 counts. The light intensity inside the cavity was measured for the Milli-Q water followed by a measurement of the light intensity when the cavity was filled with a subsample of the Nigrosine solution. After every use of the nigrosine solution, the process of bleaching and rinsing the cavity with sodium hypochlorite was strictly followed. After the nigrosine solution had been bleached and rinsed out, the intensity of the cavity for ultrapure Milli-Q water was again measured so as to ensure the stability of the system was maintained. For the reflectivity, ρ, to be determined, the absorption coefficient of the nigrosine solution was measured using the LWCC system according to suggestions in Leathers *et al*. (2000). The PSICAM was calibrated at least 3 times and up to 5 times a day on the UK coastal waters cruise.

All sample measurements were conducted in triplicate, alternating between purified water and the sample to be measured, finishing with a purified water reference. Total absorption measurements were recorded as quickly as possible following sampling to limit changes in phytoplankton cells that may have occurred as a result of being removed from their natural environment. The temperature and salinity of samples were recorded to correct for their

effects when processing the data. Following measurement of the total absorption, the sample was filtered through a 0.2 µm filter and the spectral absorption coefficient of CDOM was determined in triplicate as described above.

Particulate Spectral Light Absorption Using the Quantitative Filter Technique

The quantitative filter technique is a controllably sensitive means of determining the particulate absorption in a water sample, allowing measurement of the particulate absorption in even the most oligotrophic waters. This particulate absorption can then be further characterised into algal and non-algal particulate absorption by the oxidation of chlorophyll on the filter pad using oxidising agents such as sodium hypochlorite or hydrochloric acid.

The PSICAM is able to make a measure of the total particulate absorption of a sample by subtracting the absorption by dissolved matter (i.e. CDOM) from the total absorption coefficient. However, there is currently no method available to resolve the algal and non-algal components using the PSICAM. In contrast, it is possible to use bleaching or pigment extraction on material retained on filter pads to obtain the algal and detrital absorption coefficients (Stramski *et al*., 2015). The absorption by particulate matter is therefore still commonly determined using the quantitative filter pad technique.

The spectrophotometer was switched on at least an hour prior to use to allow the lamps and internal electronics to reach thermal stability. Reference filter pads were prepared by running 300 ml of 0.2 µm filtered seawater through Whatman 47 mm GF/F filter paper under a low vacuum (0.2 bar).The spectrophotometer was set to measure between 350-750 nm at 1 nm intervals. An initial baseline was run with no filters in the sample chamber. Following completion of the baseline, a reference sample was run using the two filtered seawater filter pads. Reference filters were stuck directly onto the beam windows using the moistness of the filter pad to adhere to the window.

To determine the absorption by particulate matter, one of the reference filters was removed and replaced by a sample filter. Sample filter pads were prepared by filtering a volume of seawater that was sufficient to colour the filter pad (from as little as 50 ml to many litres) under low pressure onto a Whatman 47 mm GF/F filter pad. The filter pad was kept covered at all times to prevent contamination (dust). The optical density (OD; equation 2.11) of the

samples was recorded using a single scan to account for possible heating effects that may result from prolonged periods within the sample chamber.

$$OD(\lambda) = -log_{10}\left(\frac{I_S}{I_R}\right) \quad (2.11)$$

where I_S and I_R are the radiant power of light transmitted through a reference and through a sample respectively.

The sample filter pad was then removed and a few drops of sodium hypochlorite (Canuti *et al.,* 2006) was added to the filter pad. The hypochlorite solution was allowed to work for three minutes before the filter pad was rinsed using filtered seawater again. Addition of an oxidising agent to chlorophyll causes the magnesium ion at the heart of the porphyrin ring to be stripped, whilst also protonating the four nitrogen atoms on the ring creating the molecule phaeophorbide. This change in structure has an associated change in absorption characteristics with a shift to shorter wavelengths. The filter was then rinsed before replacing on the beam window. This was to wash away any remaining pigment leaving only the detrital material. The sample filter pad was then replaced on the beam window and a measurement taken again to determine the OD of the detrital fraction. The absorption by phytoplankton can then be calculated as the difference between total particulate absorption and detrital absorption.

The filter pad absorption method is used in the determination of the particulate absorption, including phytoplankton and detrital absorption. However, the technique suffers in its overestimation of absorption coefficients due to measurement errors originating from scattering effects. In order to correct for the effects of scattering and to determine quantitative particulate absorption coefficients, filter pad measurements have to be corrected by applying a pathlength amplification factor, β, and a scattering offset. A variety of different correction strategies have been developed in the past (Mitchell and Kiefer, 1984; Mitchell and Kiefer, 1988; Bricaud and Stramski, 1990; Lohrenz, 2000; Tassan *et al*., 2000; Laurion *et al*., 2003 Stramski *et al.,* 2015). Pathlength amplification assumes that a photon travelling through the sample undergoes numerous scattering interactions within the filter pad. The correction factor, β, is the ratio of the optical to the geometrical pathlength. Knowledge of β is necessary for conversion of the optical density into particulate absorption coefficient information as shown in equation 2.12.

$$a_p(\lambda) = \frac{2.303\ OD_f(\lambda)A}{V\ \beta} \quad (2.12)$$

where a_p is the wavelength-dependent particulate absorption coefficient (m^{-1}), OD_f is the optical density of the sample on the filter, A is the filter clearance area (m^2), V is the volume of sample filtered (m^{-3}) and β is the pathlength amplification factor. Sample scattering affects all parts of the measured absorption spectrum. Algal absorption is negligible in the NIR, so the absorbed signal in this region is an unknown combination of detrital absorption and scattering offset. Many previous studies have applied a 750 nm null-point correction, but this is inappropriate for samples with significant inorganic content.

Numerous studies have shown that there is no universal pathlength amplification factor between different means of determining particulate absorption. The presumably most robust approach to correct particulate absorption data from filter pad measurements uses PSICAM data (unaffected by sample scattering) for cross-comparison. Lefering *et al*. (2016) showed that PSICAM data can be used to investigate the effect of different sources of error on filter pad measurements. The study showed that PSICAM data and filter pad data exhibit a consistent linear relationship which allowed the use of linear regression to derive coefficients for individual samples giving corrections for the pathlength amplification factor (the slope of the regression) and the scattering offset (intercept of the line). Filter pad data presented here was corrected using this new approach. A more detailed discussion of this method is available in Lefering *et al.* (2016b).

Particulate Organic Carbon (POC)

An updated version of the Strickland and Parson (1972) protocol was employed in determination of the particulate organic carbon concentration. This method involves the wet oxidation of carbon by acid dichromate.

A seawater sample was prepared by filtering through a Millipore AA filter that had been previously treated with a small quantity of magnesium carbonate to prevent adhesion to the membrane surface. The particulate matter that had concentrated on the surface of the membrane was washed off and used for analysis. The filtered sample was then filtered again through a sintered glass disc under vacuum. Small quantities of distilled water were applied to ensure all of the sample was filtered. The sintered glass containing the sample was then

removed from the filtration unit and replaced in the sample beaker. 1 ml of phosphoric acid and 1 ml of water were then mixed thoroughly before replacing the cover slip and heating the sample to 110°C for 30 minutes. After 30 minutes, the coverslip was removed and a sulfuric acid- dichromate oxidant added to the sintered disc with water, volumes appropriate to the anticipated quantity of carbon were required. The coverslip was replaced again and the sample heated for a further 60 minutes. Following this, the final extract was removed and made up to volume whereupon the optical density of the sample at 440 nm was measured from which the concentration of particulate carbon was determined.

Dissolved Organic Carbon (DOC)

The concentration of dissolved organic carbon was determined by an updated protocol from Strickland and Parsons (1972), which itself was based on Menzel and Vaccaro (1964).

A sample of 200 mg potassium persulfate was measured into an ampule. To this ampule, 5 ml of sample with unknown concentration of DOC was added. Finally, 0.25 ml of 0.3 % phosphoric acid was added. The glassware was setup to pass nitrogen gas through the sample for 5 minutes at 200 ml/ minute.

Using an oxyhydrogen flame, the glass ampule was sealed before being autoclaved for 40 minutes at 130 C and 24 psi. After autoclaving, the ampule was allowed to cool to room temperature before being placed in an IR spectrometer. Nitrogen gas was passed through the IR spectrometer at 10 psi and a flow rate of 200 ml/ minute. This was maintained until the micrometer metering valve read zero. The sample was then measured on the IR spectrometer. The dissolved organic carbon concentration was determined by reference to a calibration of known peak height.

2.4. Water Column Profiling Measurements

CTD Measurements

Profiles of salinity and temperature were collected using a Seabird SBE19*plus* CTD. Water samples were collected using the Niskin bottles of the water sampler mounted on the CTD frame at designated depths for analysis using shipboard instruments. The salinity and

temperature data collected were used to determine the densities at each sample depth. The CTD rosette was deployed and data processed following the SBE 19*plus* SeaCAT Profiler CTD user manual available from the manufacturer's website.

AC9 Measurements of in situ Absorption and Attenuation

A detailed description of data acquisition and post-processing for both *in situ* IOP measurements with AC-9/BB9 instruments and *in situ* radiometry, as well as an assessment of data quality can be found in Lefering *et al.* (2016a). A summary of the measurement procedure is outlined below.

A WETLabs AC-9 submersible absorption and attenuation meter was employed in the production of *in situ* profiles of $a(\lambda)$ and $c(\lambda)$. These parameters were determined for nine wavebands centred around 412, 440, 488, 510, 532, 555, 650, 676, and 715 nm using a 25 cm pathlength. The WETLabs AC-9 was calibrated prior to and during the He442 research cruise using ultrapure Milli-Q water. The data collected by the AC-9 was corrected for the temperature and salinity dependence of pure seawater (Pegau et al., 1997) as well as scattering error using the proportional correction (Zaneveld, 1994).

BB9 Measurements of Backscattering

A WETLabs ECO-BB-9 was used to determine spectral backscattering coefficients. The volume scattering function is measured using the BB-9 at nine wavebands, 412, 440, 488, 510, 532, 595, 650, 676, and 715 nm. Backscattering coefficients were determined based on the volume scattering function at an effective scattering angle of 117°. The BB-9 data was interpolated to the wavebands of the WETLabs AC-9. Backscattering data were corrected using the Zaneveld proportional correction for pathlength absorption effects. This was done using the proportionally-corrected AC-9 absorption data (McKee *et al*., 2008).

Radiometry Measurements

Radiometric data were collected using Trios RAMSES hyperspectral radiometers. These Trios sensors produce data for the upwards radiance $(L_u(\lambda, z))$, upwards irradiance

$(E_u(\lambda, z))$, and downwards irradiance $(E_d(\lambda, z))$ A deck reference sensor was also used to measure the incident solar radiation which is used for correction of sub-surface profiles.

The Trios sensors were lowered through the station water column stopping at particular depths for 120 second intervals. Data were corrected for changes in the incoming solar radiation (Sanjuan Calzado *et al.*, 2011) and final radiometric profiles of the water column were produced using the median data at each depth measured.

2.5. Algal Culturing

Four phytoplankton species were cultured for laboratory experiments: *Phaeodactylum tricornutum*, *Arthrospira maxima*, *Dunaliella maritima*, and *Dunaliella tertiolecta.* Phytoplankton were ordered from the Culture Collection of Algae and Protozoa (CCAP) at the Scottish Association for Marine Sciences (SAMS) in Dunstaffnage.

Media Preparation

Each species required the use of separate growth media that were best suited to the nutrient requirements of the organism. Growth media recipes for each species are available on the CCAP website (https://www.ccap.ac.uk/pdfrecipes.htm). The growth media employed for each of the four species are outlined in Table 2.1.

Table 2.1: Summary of phytoplankton used in laboratory-based studies during this PhD. Cultures were isolated and cultured by the team at CCAP based at SAMS in Oban.

Species	Genus	Class	Medium	CCAP Number
P. tricornutum	*Phaeodactylum*	Bacillariophyceae	f/2+ Si	CCAP 1055/1
A. maxima	*Arthrospira*	Cyanophyceae	ASW:BG	CCAP 1475/9
D. maritima	*Dunaliella*	Chlorophyceae	2ASW	CCAP 19/1
D. tertiolecta	*Dunaliella*	Chlorophyceae	f/2	CCAP 19/27

Media are stored in their component parts at 4°C and when required are mixed together and autoclaved prior to use. Growth media are prepared under axenic conditions in a laminar flow cabinet to prevent contamination from the air.

Algal Growth

The phytoplankton used in all experiments were maintained in a temperature-controlled incubator with fluorescent lighting. The cultures were maintained at 15°C on a 12:12 light:dark cycle to approximate their natural conditions.

The emission spectrum of the incubator lights is shown in Figure 2.1. Figure 2.1 shows that the wavelengths of the incubator lights are not specifically targeting the chlorophyll absorption peaks, which may inhibit growth of the cells. The PAR across the entire visible spectrum was calculated at approximately 23 µmol photons m^{-2} s^{-1}.

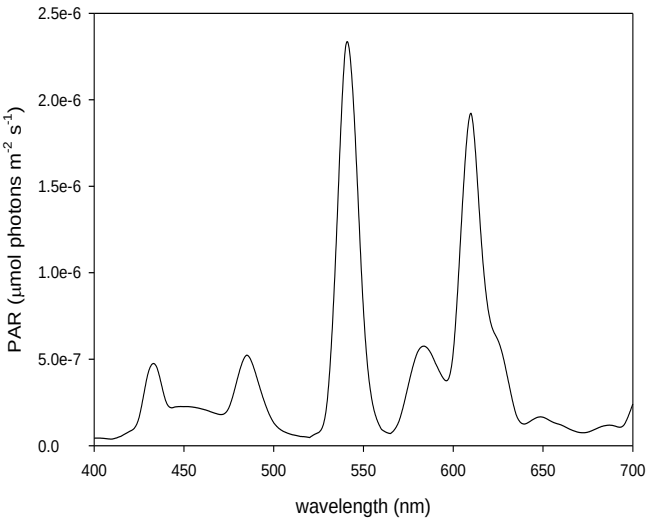

Figure 2.1: The emission spectrum of the algal incubator lights is shown with peaks around the green and red areas of the visible spectrum. These lights do not target the chlorophyll peak at around 450 nm which may inhibit the photosynthetic capacity of the cells.

Algal Sub-culturing

Approximately every two months, cultures were sub-cultured into fresh growth media. Sub-culturing was performed under axenic conditions to prevent contamination. Samples were stored in 50 ml tissue culture flasks. 20 ml of fresh growth media was transferred to the

culture flask; to this, 1 ml of dense algal culture was added. Flasks were placed face down in the incubator.

2.6. Radiative Transfer Modelling

Underwater light fields were modelled using Hydrolight 5.0, specifically to produce PAR with depth, although a suite of optical outputs are available from each run, e.g. Ed(λ), Eu(λ), and R(λ). Hydrolight calculates radiance distributions and their derived quantities for natural waters (Mobley, 1994). A one-dimensional time-independent radiative transfer equation is used for these calculations with the radiance distribution resolved spectrally and for depth. The Hydrolight model was populated using *in situ* IOP data collected from station profiles in Loch Fyne. The proportional correction (Zaneveld *et al.,* 1994) was applied to the absorption and attenuation data collected by the AC-9. Upper and lower boundaries on the modelled irradiance were set by varying the atmospheric cloud cover between 0 % and 100 % cloud cover. Pure water absorption values were taken from Pope and Fry (1997) and seawater scattering from Gordon (1973). Raman scattering of water molecules was accounted for in the models. However, due to insufficient data availability, such as the quantum yields, chlorophyll and CDOM fluorescence were not included in the calculations. Wind speed was kept constant at 0 ms^{-1}. Solar zenith angle was determined by the time, date, and spatial coordinates in Table 5.1. Hydrolight further assumes the upper boundary to be the air-water interface, the lower boundary to be either the physical limit of the water column or some determined plane below which the water remains homogeneous with depth, which in this case was 45 m. The model assumes that radiant flux is only incident upon the upper boundary and no radiant flux comes from below the lower boundary.

2.7. Summary

The collection of multiple datasets in combination with Fast Repetition Rate fluorometry data allows for a more complete understanding of the water column at each location during He442. This provides information about the chemical and physical environments that algal cells were exposed to, possibly giving a more nuanced and contextualised idea of the photophysiological conditions they were experiencing at the time.

Furthermore, the collection of IOP data and surface radiometry allows for the use of Hydrolight radiative transfer modelling for the calculation of underwater light fields. This allows for estimations of the daily, column-integrated gross primary productivity, something that is attempted in chapter 5 of this thesis.

3. FastOcean Characterisation

When operating at sea, it is often the case that multiple casts are made in a relatively short period of time. It is therefore imperative that the operational potential and performance limitations of the instruments used are understood to make best use of the limited time available for measurements. The FastOcean fast repetition rate fluorometer has a number of variable operating parameters that can be optimised for different sampling conditions.

The aim of this chapter is to characterise each of the FastOcean sub-systems and from this, develop an optimised measurement protocol for deployments in coastal waters. Several aspects of the instrument performance are analysed, covering the instrument hardware and measurement optimisation as well as dark acclimation and its impact on the quality of the data produced. These systems are probed with the aim of developing a protocol that provides photophysiological information for sample conditions as close as possible to the natural environment from which they were taken. The outcome of this effort is presented as a set of recommended standard settings (section 3.2).

3.1. Optimisation of FastOcean FRRf Measurement Protocol

Hardware

Instrument Warm-up Time

The properties of electronic components are temperature-sensitive. As the ambient and system temperature changes, the performance of these electrical components also varies. This can impact on LED excitation systems and detector systems, where system stability is essential. This is particularly important for fieldwork, as it is important to establish a system warm-up time and to decide if constant power-up is preferred. This was determined by using the temperatures of the three excitation LEDs, which were used as a proxy for the internal instrument temperature and monitoring changes in measured fluorescence signals from a pure water blank. The aim of this experiment was to find whether there was a minimum time required for the instrument temperature proxies to reach thermal equilibrium under typical lab operating conditions.

The FastOcean and FastAct system were setup following the normal protocol. A single 1 ml sample of purified Milli-Q water was placed in the test tube and inserted into the sample chamber. The LED irradiances used were 0.92, 0.32, and 0.70 µmol photons m^{-2} s^{-1} for 450, 530, and 624 nm respectively at a PMT gain of 300 V. Measurements were made over the course of 32 hours to identify whether there was a particular period required for thermal equilibrium to occur. The same sample of purified water was used throughout without being removed from the chamber for the entirety of the experiment.

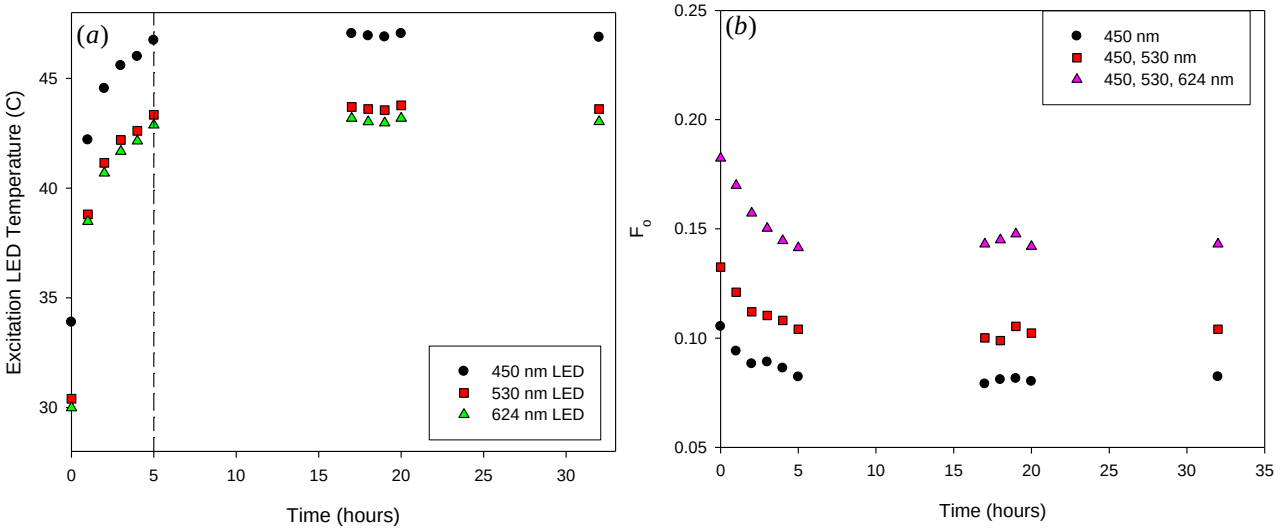

Figure 3.1: (a) Using the excitation LED temperature as a proxy for internal instrument temperature showed there was a measurable difference in LED temperature over the course of 32 hours. (b) The F_o signal produced by Milli-Q purified water across the same time period is recorded showing a reduction in F_o to a stabilised value.

Using the excitation LED temperature as a proxy for internal instrument temperature, Figure 3.1a suggests that the minimum period required for the instrument to reach thermal equilibrium is five hours. In the five hours prior to thermal equilibrium, Figure 3.1b shows that there is an effect on the value of F_o produced from the purified Milli-Q water sample. Over the course of five hours, there was a 22 % reduction in the size of the 450 nm fluorescence signal.

Multiplication of the 450 nm-calculated F_o by a variable factor gives a proxy for the chlorophyll concentration. The standard factor applied within FastPro8 is 8, however, during the UK Coastal Waters cruise discussed in chapter 4, we used a multiplication factor of 5.5. In Figure 3.1b, the 450 nm measured F_o value at t = 0 was 0.11 and after five hours, this had

reduced to approximately 0.08, a reduction of 22 % due to the small size of the numbers involved. However, multiplication of the difference between these values (0.03) by 5.5 gives a difference in chlorophyll concentration of 0.13 mg m^{-3}, a value that is significant if operating in oligotrophic waters but one that is unlikely to make any real difference when operating in eutrophic coastal waters.

In the interests of thermal stability and reproducibility of results, it is recommended that the FRRf is left switched on for the duration of a series of measurements, and potentially for the duration of a cruise.

Contribution of External Light Sources

The FastOcean system is designed to prevent ambient light from getting into the sample chamber or the detection system. The head unit is sealed from the bottom with the test tube creating a tight seal around the top of the head unit when making measurements, as can be seen in Figure 3.2a-b.

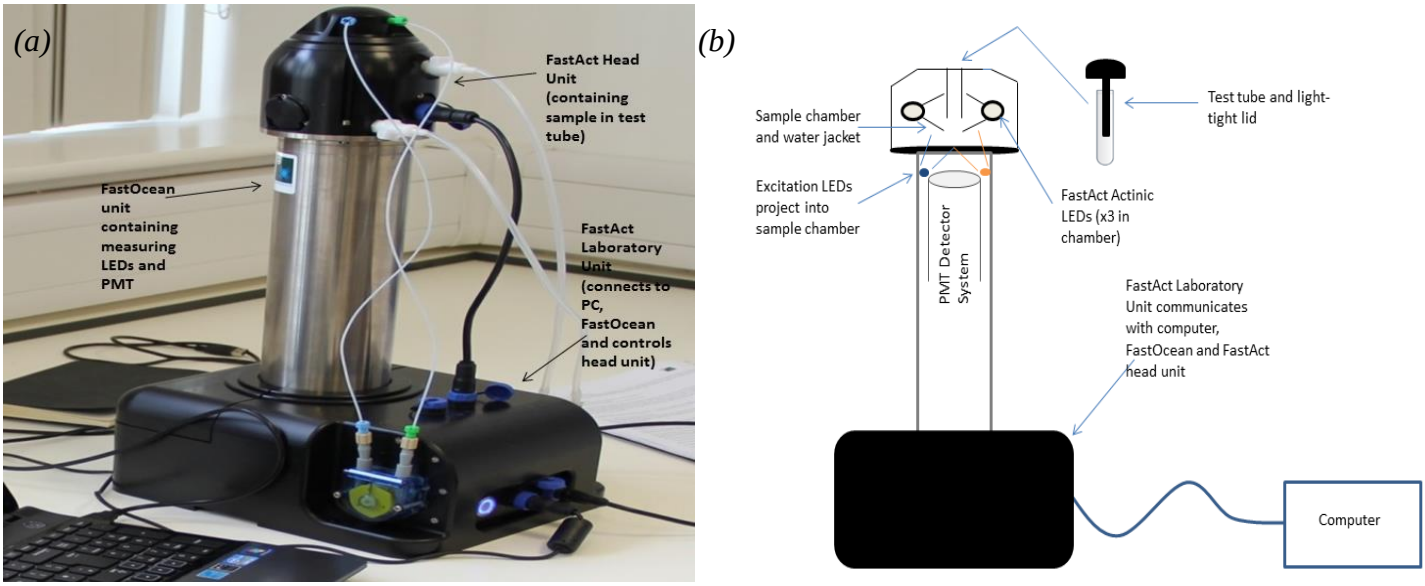

Figure 3.2: (a) Annotated diagram of the FastOcean unit shows the basic setup employed. (b) A diagrammatical cross-section of the FastOcean unit showing the layout of components for basic operation.

An experiment was devised to test whether there was any extraneous light being detected by the FRRf. A single sample of purified Milli-Q water placed into the sample chamber and was pulsed fifty times using the 450 nm excitation LED under two ambient lab conditions- pitch

darkness and all lights on. The F_o signal was averaged for both situations producing values of 0.134±0.007 and 0.136±0.009 respectively.

This experiment shows that the ambient lighting conditions do not have a detrimental effect on the measuring ability of the instrument. As such, there is no need for additional light shielding of the instrument for laboratory operations. However, further validation is required for using the instrument outdoors under the midday sun.

Useful Gain Range of the Photomultiplier Tube

The photomultiplier tube (PMT) is the detection instrument used within the Fast Repetition Rate fluorometer. The PMT used is a NIR-enhanced model with a 10-stage dynode chain. The PMT gain is an important parameter for setting up an FRRf measurement to ensure that sufficient signal is detected to reliably estimate the algal physiological conditions. Optimisation of the PMT gain is determined by the fraction of the ADC being used. Under normal operating conditions, the ADC fraction being used should be greater than approximately 80 %. Increasing or decreasing the PMT gain will increase or decrease the ADC fraction accordingly. Understanding the useful range of the FRRf is important for dealing with low and high concentration samples, e.g. operating in oligotrophic waters or in the middle of an algal bloom. Knowing this useful gain range allows the operator to be confident in the quality of the measurements being made.

To test this, a sample of purified Milli-Q water was put into the sample chamber. A fixed LED irradiance at 450 nm was set at $1x10^{22}$ µmol photons m^{-2} s^{-1}. Twelve measurements were made at each PMT gain setting and the averaged F_o used for comparison. Eleven gain settings ranging from 50 to 800 V were used, the results of which are shown in Figure 3.3.

Figure 3.3a shows that data produced from a PMT gain below 300 V results in unstable measurements, discounting the subsequent use of these voltages. Figure 3.3b shows the F_o values for measurements made above 300 V. This Figure shows there is a useful range of voltages, between 300 and 600 V, in which measurements should be made. Above 600 V, the F_o value drops off by approximately 66 % between 600 and 800 V.

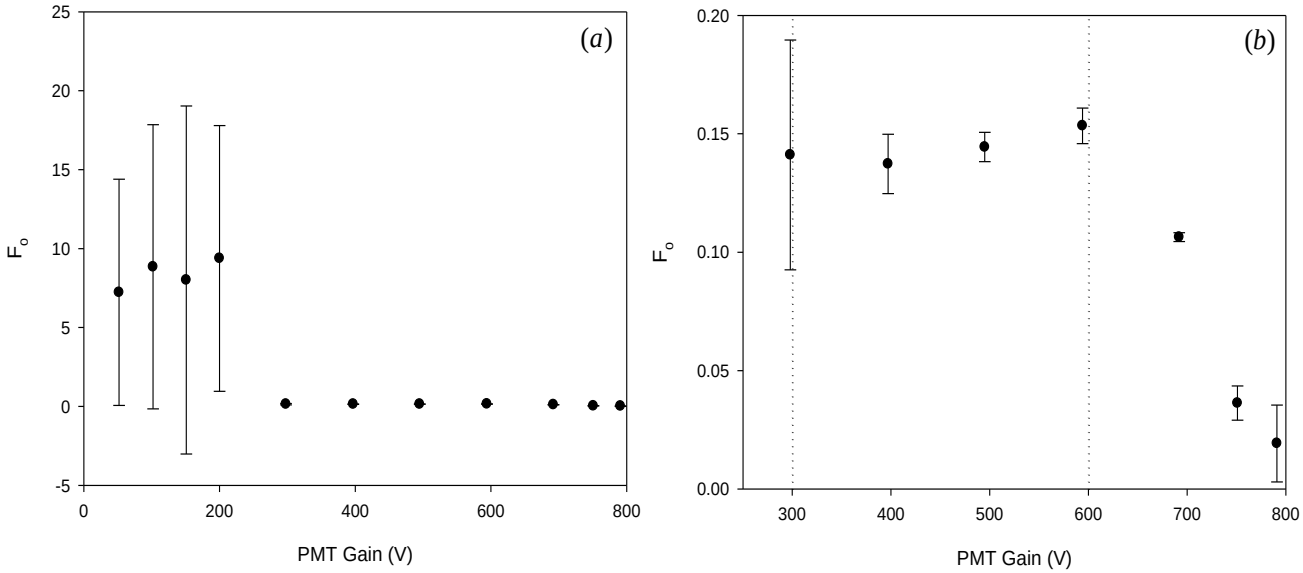

Figure 3.3: (a) The useful range of the PMT gain was tested across the entire range of voltages available using a purified Milli-Q water sample (b) The lack of stability in the signal below 300 V discounted their use. In Figure 3.3b, only PMT gain values greater than 300 V are included. The useful gain range of the PMT is identified by the two vertical dotted lines at 300 and 600 V. All uncertainties are to 2σ.

Figure 3.3b shows that despite the drop in F_o above 600 V, the uncertainty in these values is well constrained. In some particularly oligotrophic waters it may be necessary to employ gain voltages above 600 V, with a correction applied to the fluorescence values obtained to bring them in line with the F_o values obtained in the stable 300-600 V range.

Spectral Output of FastOcean Actinic LEDs

Actinic lighting is composed of wavelengths capable of driving photochemical reactions. Actinic LEDs are used during fluorescence light curves to approximate overhead (sunlight) ambient conditions. This allows estimations of the photosynthetic capacity and algal physiological state to be approximated for any time of the day producing the characteristic curve. Chelsea Technology Group (CTG) provided the spectral irradiance outputs for the actinic LEDs of the FastAct system. The spectral output of the actinic LEDs were calculated using an Ocean Optics irradiance sensor as shown in Figure 3.4.

There is a large broadband excitation band across the green and red regions of the spectrum with a sharper blue LED band at approximately 450 nm, which is presumably intended for specific excitation of chlorophyll pigments. The solar output incident on the Earth's surface

does not take the same shape as the spectral output of the actinic LEDs, however, the absorbing components of chlorophyll are well matched by the actinic LEDs. The spectral distribution of the actinic LEDs is integral to conversion of photosynthetically active radiation (PAR) to photosynthetically useable radiation (PUR).

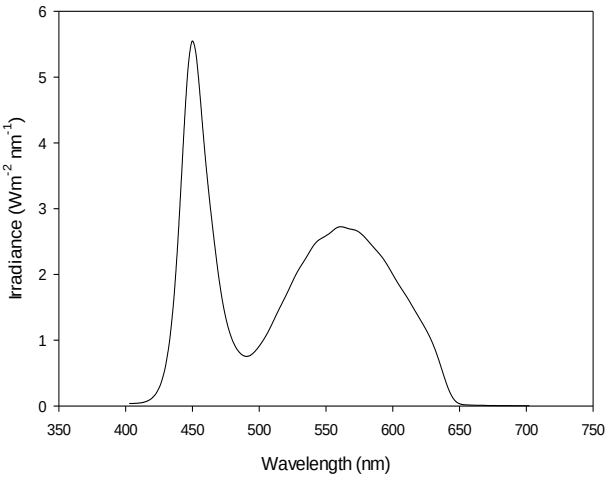

Figure 3.4: Trios Ramses irradiance sensor-measured spectral irradiance for the actinic "white" LEDs present in FastOcean FastAct FRRf system, data were normalised to 480 nm in this Figure.

Characterisation of the FastOcean Excitation LEDs

The FastOcean Fast Repetition Rate fluorometer system contains three excitation LED wavebands with central wavelengths at 450, 530, and 624 nm, each of which are calibrated to produce a maximum irradiance output of 1.77, 0.5, and 1.54×10^{22} photons m^{-2} s^{-1}, respectively as measured by CTG. The excitation LEDs are rapidly pulsed to produce a fluorescence transient. The rate at which the LEDs are normally pulsed at is 100 flashlets on a 2 µs pitch with a relaxation phase of 40 flashlets on a 50 µs pitch. This is discussed further in section 3.2.

The spectral output of the excitation LEDs was determined using an Andor iDUS spectrometer connected to the FastAct head unit by a fibre optic cable. Prior to measurement of the spectral output, the iDus camera was wavelength-calibrated using a Hg/Xe lamp.

The excitation LED spectra were normalised to the peak wavelength measured using the Andor iDUS camera in Figure 3.5a. These peak wavelengths were 436, 509 and 629 nm for the 450, 530, and 624 nm wavebands respectively. These spectral outputs show that the 530 nm LED produces a broad peak that is able to cover the middle of the visible spectrum between the primary areas of absorption of chlorophyll. The use of an LED in this region is important as it means that additional pigment packages that are not based on a chlorophyll *a/b* system can be accurately represented such as in the case of cyanobacteria (see Figure 3.5c). This is advantageous in natural waters where previously waters may have been labelled as unproductive, the use of additional wavebands means that a better picture of *in situ* productivity can be made. The normalised transmission of the RG665 longpass filter is also shown in Figure 3.5a, this is employed in front of the PMT detector to prevent any extraneous light not related to photosystem II fluorescence emission from contributing to the signal. The cut-on waveband coincides with the edge of the 624 nm excitation LED resulting in very little scattering breakthrough as discussed in section 3.3, whilst the chlorophyll fluorescence emission peak at 685 nm is well within the transmission range of the two 3 mm Schott RG665 filters. Scattering breakthrough is further blocked by a 682 nm peak, 30 nm half bandwidth interference filter.

Figure 3.5b shows the absorption spectrum of *D. maritima*, a green algae based on the chlorophyll *a/b* pigment system as can be seen from the largest peak occurring at approximately 440 nm, which overlaps very well with the 450 nm LED of FastOcean. The 530 nm LED proves useful in this algal species too, as there are additional pigments present in this phytoplankton that absorb up to approximately 550 nm. The additional LEDs therefore prove useful in this scenario producing a better estimate of the *D. maritima* physiological state. From this Figure, it is possible to see that chlorophyll absorption occurs primarily in the blue end of the visible spectrum with the two additional LED wavebands not having much influence on chlorophyll fluorescence. Figure 3.5c is the excitation LED wavebands overlaid with the absorption spectrum of the cyanobacteria, *Synechococcus*. *Synechococcus* is not solely composed of chlorophyll-based pigments, although as can be seen, it is present, with

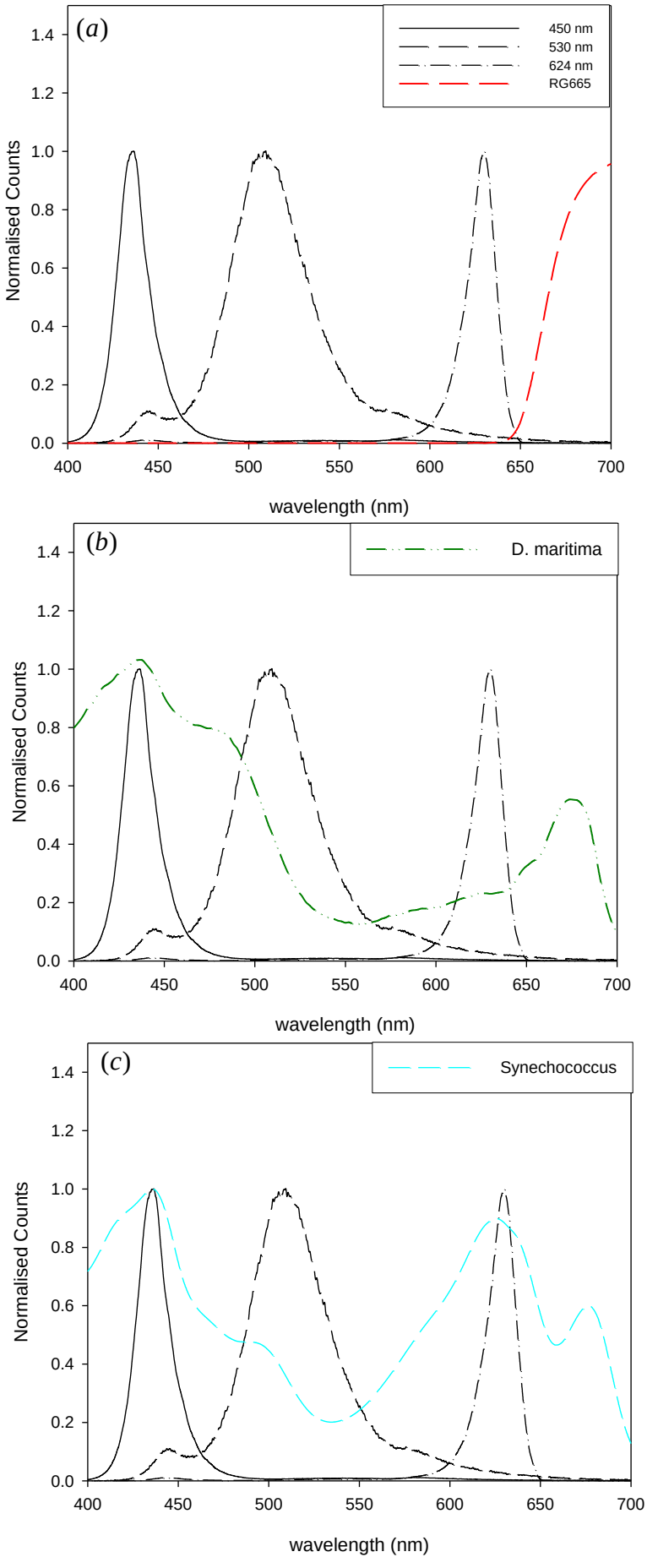

Figure 3.5: (a) Excitation LEDs were normalised to the peak irradiance measured on the Andor iDUS. The normalised excitation LED spectra are shown alongside the spectral transmittance for the RG665 longpass filter, which is present in front of the PMT (b) The D. maritima absorption spectrum is shown alongside the excitation LED spectral output. D. maritima is a green algae that is extensively used in the course of our laboratory studies. (c) The absorption spectrum of Synecochococcus (shown as the aqua blue dashed line), an algal species belonging to the cyanobacteria is shown. The large absorption from 575 nm is obvious, separating it from the chlorophyll a/b-based pigment systems.

the main accessory pigments being phycobiliproteins. The difference in the absorption spectra of Figures 3.5b and c are clear with *Synechococcus* producing a broad absorption from 575 nm beyond 650 nm. The use of the additional excitation LEDs means that a more accurate depiction of the physiological state of cells such as *Synechococcus* is possible.

Measurement Optimisation

Choice of Sample Blank

Sample blanking is classically defined as a measurement that is devoid of analyte, which is used to offset the effect of the solution containing the sample. Ideally, an appropriate blank will contain zero trace of the analyte as any contamination will itself create an offset that will affect the analyte concentration detected. The influence that accounting for the blank measurement will have is dependent upon the magnitude of the parameter being measured (Cullen and Davis, 2003). For example, the parameter may produce a very large signal and have a small associated blank value, in which case, the blank has little effect on the overall result. However, in oligotrophic waters, the chlorophyll signal will likely be very small and so blanking has a larger impact. The photochemical efficiency is given by:

$$\frac{F_v}{F_m} = \frac{F_m - F_o}{F_m} \tag{3.1}$$

However, if we assume that the measured value of F_m has a 'true' signal, F_m^T, and a component due to unresolved background fluorescence, f_B:

$$F_m = F_m^T + f_B \tag{3.2}$$

and the same is true for the measured value of F_o:

$$F_o = F_o^T + f_B \tag{3.3}$$

then equation 3.1 becomes:

$$\frac{F_v}{F_m} = \frac{F_m^T - F_o^T}{F_m^T + f_B} \tag{3.4}$$

Equation 3.4 shows that the impact of fluorescence not associated with the photosynthetic pathways is cancelled out in the numerator but is still present in the denominator.

Failure to account for the sample blank may result in an artificially high maximum photochemical efficiency (F_v/F_m). This has important downstream effects such as poor approximation of the photosynthetic capacity from a fluorescence light curve.

The choice of blank applied to an FRRf sample is very important. There are several variables to be considered when choosing an appropriate blank such as the timing between casts, the availability of purified Milli-Q water, whether measurements are being conducted in the field or in a laboratory, and the type of waters being measured in. The following experiments aimed to examine the relationship between the choice of blank and the effect these have on the maximum photochemical efficiency of PSII.

Three types of blank were utilised in this experiment- a sample of purified Milli-Q water (MQ), artificial seawater (ASW) composed of 34 g/L Ultramarine Synthetica salts, and an optically thick sample of *Phaeodactylum tricornutum* which was filtered through a 0.22 µm filter to produce a filtered seawater blank (FSW). Each blank sample was measured for the size of their initial fluorescence signal, separate from a measurement of phytoplankton physiology. Ten acquisitions were made using the 450 nm LED at 400 V and an averaged F_o signal taken.

Figure 3.6 shows the averaged F_o signal from each of the sample blanks. The Milli-Q water sample produced an F_o of 0.413 and the ASW sample produced a value of 0.520, approximately 25 % larger than the Milli-Q water. The filtered seawater blank produced a much larger signal. This may be for a number of reasons, such as the growth stage of the sample, for example, the cells may have been coming to the end of their growth cycle with limited nutrients available meaning the cells may have been breaking down releasing free chlorophyll into the water, which would not be inhibited by a 0.22 µm filter. Furthermore, the efficacy of the Spartan filter itself may be in question with the possibility of cells rupturing during filtration, a variable that is discussed later in this section.

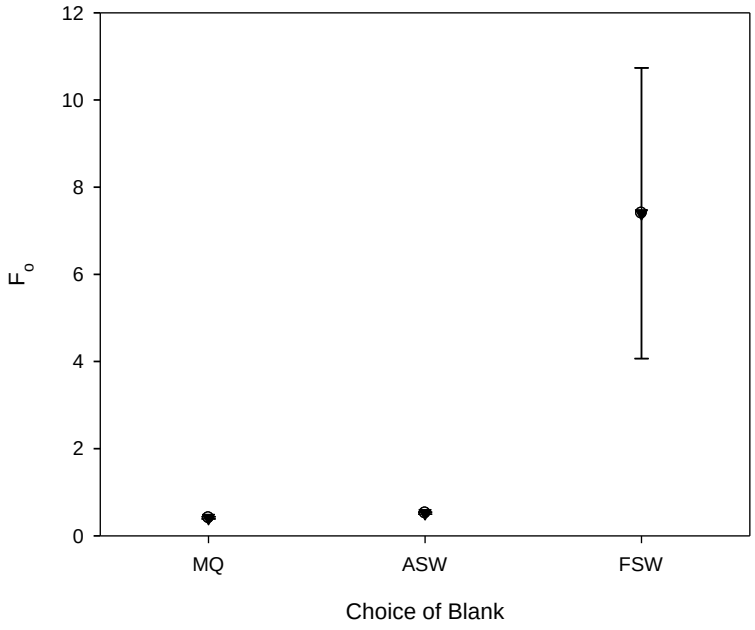

Figure 3.6: Three choices for the sample blank were tested. The purified Milli-Q (MQ) and artificial seawater (ASW) do not contain any traces of algal cells. The filtered seawater sample is produced using a natural seawater sample.

Efficacy of the Spartan Filter for Filtered Seawater Blanking

The Whatman Spartan 30 0.2 µm filter that is routinely used for the creation of filtered seawater blanks has a 0.2 µm pore size meaning each pore is about an order of magnitude smaller than the majority of phytoplankton species likely to be encountered. Anecdotal evidence suggests that high pressure vacuum filtration causes sample degradation on a filter pad. As such, this has the capacity to cause inaccuracies in

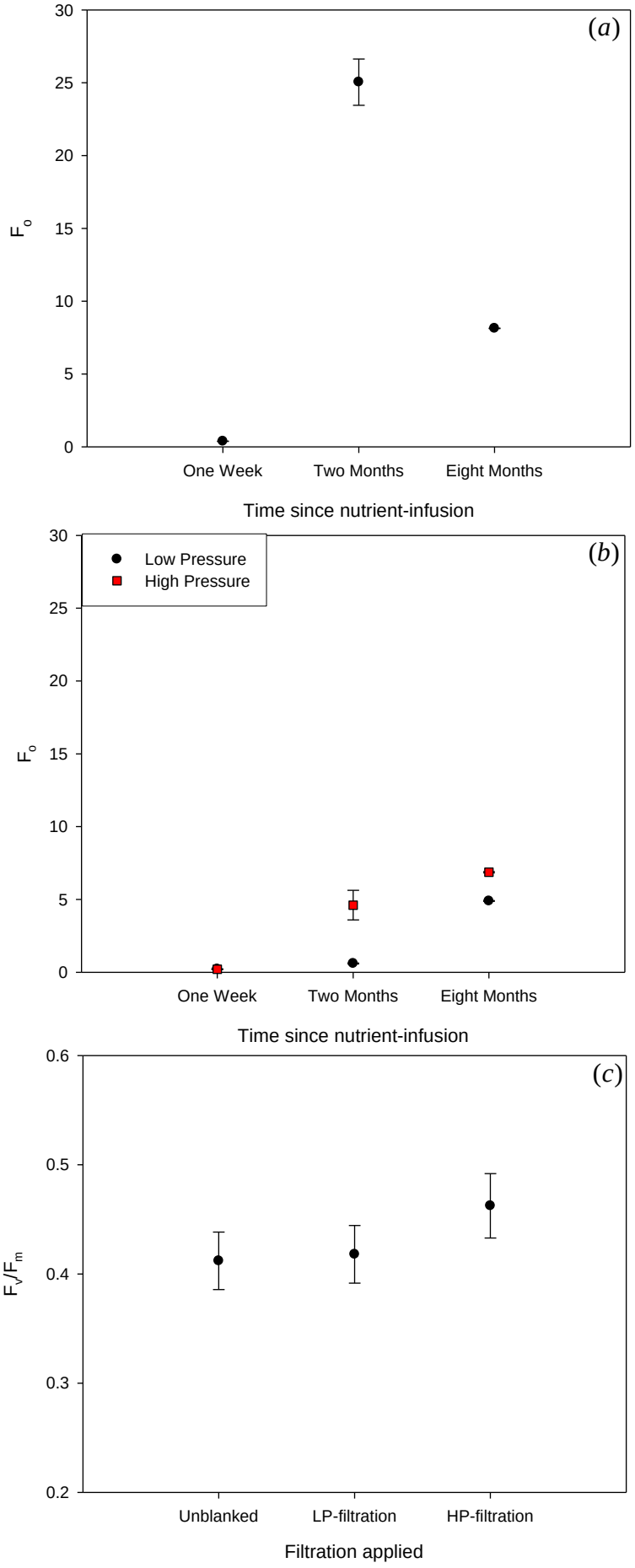

.

Figure 3.7: (a) The initial fluorescence (F_o) of each of the three cultures prior to Spartan filtering with associated error bars to 2σ (b) The F_o value is shown for the resulting Spartan filtering process for the three cultures employing either low or high pressure is shown (c) An unblanked sample of algal cells is shown followed by the F_v/F_m following blanking with both the low and high pressure blank values showing the difference each filtered seawater blank makes.

measured chlorophyll absorption, so filter pressure is kept low to counter this possibility.

This raises the possibility that the pressure applied in hand-filtered phytoplankton samples has a similar likelihood of damaging algal cells affecting the size of the measured filtered seawater blank. The aim of these experiments was to test the effect of the age of a phytoplankton culture on the measured filtered F_o signal by either gently or vigorously pushing the sample through the Spartan filter. Three cultures were used in these measurements: a fresh culture which had been infused a week prior to measurement with nutrients (culture 1); a two month old culture (culture 2), and a third culture that had not been infused with nutrients for eight months (culture 3) providing a broad range of physiological states.

Figure 3.7a shows the difference in the initial fluorescence in each sample. Culture 1, as expected, had the lowest F_o as there are fewer cells and so low overall chlorophyll present. Culture 2 contained higher concentrations of chlorophyll as it was thought to be in the stationary phase of the growth cycle and so had had a longer period to grow and feed from nutrients and irradiance. The oldest culture, culture 3, still contained large concentrations of chlorophyll but it must be assumed that this culture contains chlorophyll-degradation products given its age (Franklin *et al*, 2009). These three values serve as the starting point for measuring the efficacy of the Spartan filter at low and high pressure filtration. Figure 3.7b shows the effect of both gently and vigorously filtering a sample through the Spartan filter. Gently filtering a sample is taken to mean that minimal pressure is applied to the syringe plunger whereas vigorous filtration is taken to mean that as much force as possible is applied to the plunger without causing the filter itself to become detached from the syringe. The results shown in Figure 3.7b do certainly show that for culture 2 and culture 3 there was a difference in the measured fluorescence depending on the filtration pressure applied.

Culture 1 saw a 42 % drop in the fluorescence signal using low pressure filtration with culture 2 producing a 98 % drop in signal relative to the pre-filtration values of Figure 3.7a. These drops are likely related to the relative concentrations of each sample, as culture 1 was still relatively fresh, there would have been less ability for them to fluoresce. Culture 3 saw a 40 % reduction in signal. The relatively smaller reduction in signal is likely a result of the state of degradation of algal cells as they are no longer viable.

Culture 1 saw very little difference between either low or high pressure filtration, so was taken to be an insignificant change. Culture 2 saw an 82 % difference between the unblanked

value of 25.04 and the high pressure blank value of 4.61. Furthermore, a 16 % difference between the low and high pressure filtration F_o values was recorded. The difference between the low and high filtration measurements for culture 3 was approximately 25 % with a 16 % difference in F_o between the unfiltered and high pressure filtration measurements suggesting that large quantities of chlorophyll are passing through the filter. This may be due to the pressure breaking cells down or the cells were already in a state of advanced degradation.

The difference between low and high pressure filtration on a sample blank has direct implications for the value of the photochemical efficiency. Figure 3.7c shows the different blanks being applied to an unblanked sample of phytoplankton. Applying a filtered blank produced by high pressure filtration produces a statistically significant increase in the photochemical efficiency from 0.412 in the case of the unfiltered F_v/F_m to 0.462. Whilst it is important not to overstate the significance of this change in photochemical efficiency, a less physiologically robust sample may produce a greater overestimation of its physiological state than one that is healthy. These experiments do not call into question the efficacy of using a filtered seawater blank but rather raise important points about the way in which a filtered seawater blank is derived. It cannot be assumed that because a filtered seawater blank was used that it is better than a sample blanked using artificial seawater, for example. Operators should be mindful of their actions when preparing samples and making measurements.

Effect of the Choice of Blank on the Apparent Algal Physiological State

In the previous section, no attention was paid to the physiological state when choosing a particular sample blanking method. The aim of this section is to determine the effect of the blank used on the photochemical efficiency.. Sample blanks were prepared in the same way as before using purified Milli-Q water, artificial seawater, and a filtered seawater blank produced by low pressure filtration of *Dunaliella tertiolecta* through a Spartan 0.22 µm filter. A single sample of *Dunaliella tertiolecta* was dark-accilmated and measured three times to produce an average photochemical efficiency. An irradiance of $0.8x10^{22}$ photons m^{-2} s^{-1} was used for the 450 nm LED at 400 V gain.

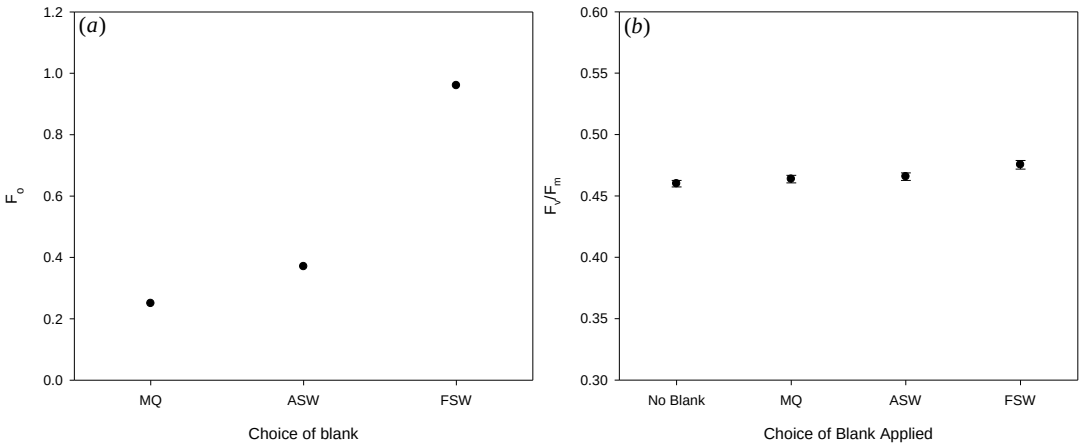

Figure 3.8: (a) F_o was recorded for three different sample blanking methods which were then compared for the difference in the resulting photochemical efficiency (b) The unblanked and blanked photochemical efficiencies using the three different sample blanking methods.

The trend in the magnitude of F_o for different sample blanks was maintained as shown in Figure 3.8a. The filtered blank of *D. tertiolecta* produced a signal much larger than from the purified Milli-Q water or artificial seawater. These values were applied to the unblanked *D.tertiolecta* data as shown in Figure 3.8b. There was very little difference in photochemical efficiency with a maximum increase of 0.015 when the filtered seawater blank was applied. Large changes in the value of the sample blank do not necessarily map to large changes in F_v/F_m.

Sample Blanking a Fluorescence Light Curve

Up to this point, sample blanking has only been mentioned in relation to a single measurement. However, fluorescence light curves may also be improved by sample blanking. The aim of this experiment was to determine the influence of sample blanking on the data produced by an FLC.

A twenty step FLC with incremental increases in irradiance from 0 to 1066 µmol photons m^{-2} s^{-1} was devised. A steady-state illumination period of 80 seconds was applied prior to measurement at each step. An optically thin sample of *D. tertiolecta* was used for this measurement.

Table 3.1: The effect of blanking on the FLC parameters is measured for each of the three sample blanking methods

450 nm FLC	α	F_v/F_m	E_k	P_M
Unblanked	0.458	0.458	214	86.6
Milli-Q Blank	0.464	0.464	217	88.8
Artificial Seawater Blank	0.467	0.467	219	89.9
Filtered Sample Blank	0.504	0.481	191	97.3

Changes in the initial slope (α), the saturation parameter (E_k) and the photosynthetic capacity were all noted with blanking. From the unblanked sample to a filtered seawater blanked sample, there was a 5 % increase in the photochemical efficiency. The initial slope of the curve increased by 10 % with a concomitant rise in E_k. The associated increase in these parameters was less for the purified Milli-Q water and artificial seawater. The variability between parameters for different blanks was not substantial with the biggest difference being the 12 % change in photosynthetic capacity (P_M) for the filtered seawater blank. Given the potential for cell damage, it may be safer to use an artificial seawater blank instead of the filtered seawater blank. The difference in size of the values in these experiments was small compared to the size of the maximum photosynthetic capacities. However, these differences would be amplified in extreme water envrionments, for example the open ocean or highly optically complex areas like the Bristol Channel.

FLC Measurement Optimisation

A fluorescence light curve can take anywhere from twenty minutes to over an hour to complete a single set of measurements. This places time constraints on the operator and, especially when on research cruises with pre-planned casts, can often mean there is only time to run a single FLC replicate. It is therefore highly desirable to optimise FLC setup parameters whilst minimising operation time.

FLC Replicability

Two separate approaches were taken in testing the replicability of an FLC. The first method (method 1) took a single sample of *D.tertiolecta* and measured it under the same experimental conditions three times before taking an average. The second method (method 2) took three aliquots of *D. maritima* and sub-sampled each three times for a total of nine FLCs before producing an average.

An eighteen step FLC was run with incremental increases in irradiance from 0 to 1358 µmol photons m^{-2} s^{-1} with a 450 nm excitation LED irradiance of $1.25x10^{22}$ photons m^{-2} s^{-1}. These conditions were maintained throughout the experiment for both method 1 and method 2.

The three replicates of method 1 in Figure 3.9a show little variation in their photosynthetic capacity particularly across the light-limited phase of the curve. As the samples reach light-saturation, there is some divergence found but at large photosynthetic capacities these variations are not statistically significant. Method 2 shown in Figure 3.9b is broadly similar to the results of method 1 with little variation in the light-limited phase and some divergence in the light-saturated phase. Figure 3.9c shows the grand means of method 1 and method 2, where the grand mean is defined as the mean of the means of sub-samples. The inter-comparison of methods 1 and 2 show that there is very little difference in the estimated photosynthetic capacities between both methods.

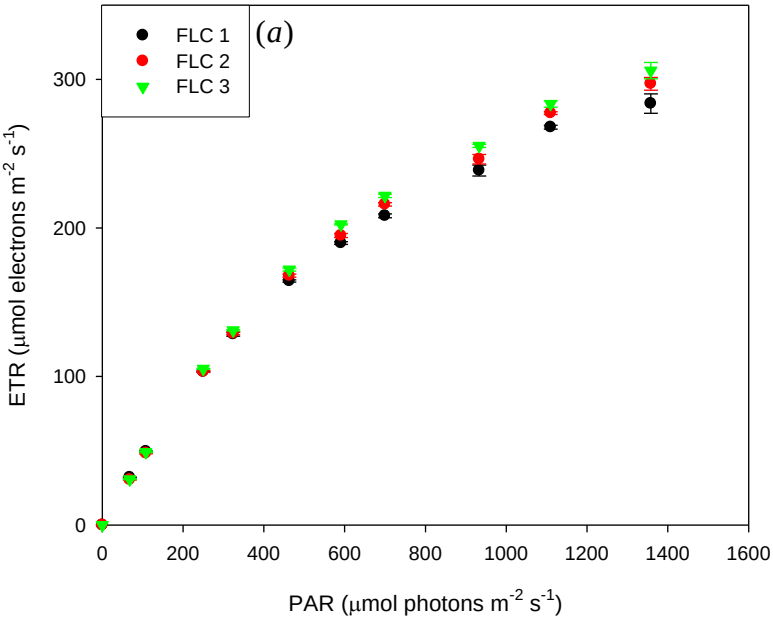

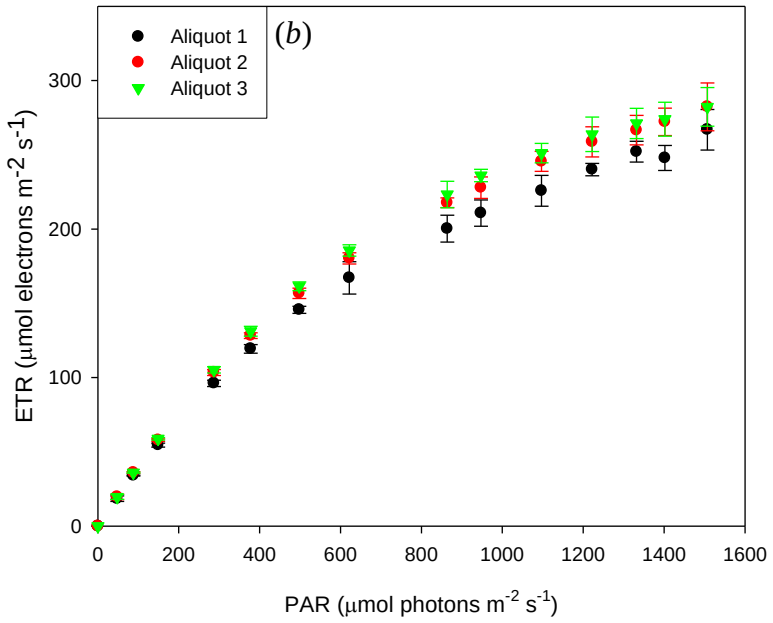

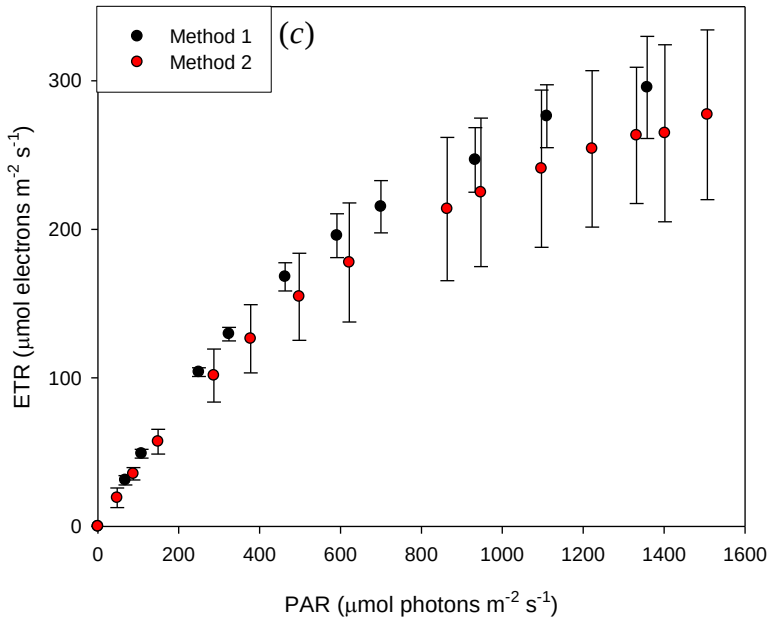

Figure 3.9:(a) The three replicates from method 1 are shown (b) The three sub-samples of each aliquot were averaged producing the data in Figure 3.9b (c) The grand mean and grand standard deviation were calculated for both methods and plotted with respect to one another where uncertainties are calculated to 2σ.

The major difference is that the estimated standard deviations in method 2 are larger than in method 1. This is intuitively correct as method 1 employed a single sample measured three times so there would be little expected deviation in the algal photophysiology between measurements. Method 2 employed several sub-samples of three aliquots producing a greater inherent variability as a broader cross-section of the phytoplankton population are being scrutinised. Furthermore, there was a period of three days between the method 1 measurements and method 2 measurements being made which may have been a reason for some of the deviation, such as the larger error bars found for the method 2 measurements.

Table 3.2: Inter-comparison of the FLC parameters produced for the 450 nm FLC measured using both methods 1 and 2 showing fluctuations in ETR_{max} and E_K as also described in Serôdio et al. (2013).

450 nm FLC	α	E_K	ETR_{max}
Method 1	0.486 ± 0.004	717 ± 95	302 ± 160
Method 2	0.422 ± 0.023	733 ± 135	327 ± 8

Table 3.2 shows the inter-comparison of the FLC parameters for methods 1 and 2 where the uncertainties are given to two standard deviations. The ETR data in Table 3.2 differ slightly from those in Figure 3.9 as Figures 3.9a-c represent the values measured at each individual step, whereas the ETR_{max} data in Table 3.2 is the maximum electron transport rate calculated by the fit of the curve to the data in Figure 3.9.

The initial slope of the curves show very little variation and so can probably be considered as a good estimate of the dark regulated, maximum photosynthetic efficiency of each sample. The most striking difference between methods 1 and 2 in Table 3.2 is the difference in the standard deviation associated with ETR_{max}. This may be a fortuitous alignment of numbers or may represent an actual difference in the way that the protocols are executed.

The data produced in this FLC replicability study does not suggest that there is any significant difference between the methods used. These experiments suggest that the use of a single sub-sample is potentially sufficient to estimate the FLC parameters and that a single FLC, run according to a standard FRRf protocol, would be sufficiently reliable to make further downstream estimates of gross primary productivity. Whilst replicates would be

comforting and would aid estimation of uncertainties, practical time constraints are often the limiting factor.

FLC Replicability of a Non-Chlorophyll-based Algal Culture

D.maritima is composed of a chlorophyll-based algal system and so, it is simple enough to make measurements using only the 450 nm excitation LED. This raises the question of the effectiveness of the FastOcean and FastAct system in producing reliable data for algae that are not centred around a chlorophyll-based light harvesting complex, such as cyanobacteria. The phytoplankton species specifically used in these experiments was *Arthrospira maxima*, a chain-forming cyanobacterium. The presence of phycobiliproteins in the light harvesting complex of *A.maxima* means that the additional 530 nm and 624 nm excitation LEDs have a greater influence on the fluorescence signal.

The same FLC protocol was applied from the previous section, however, samples were steady-state acclimated for 90 seconds prior to each measurement and the combination of all three excitation LEDs was used instead of only the 450 nm LED. Four individual sub-samples of *A.maxima* were taken producing four FLCs.

The *A.maxima* samples behaved very similarly to those of *D.maritima* with close approximation of each FLC in the light-limited phase before deviation as light-saturation is reached, as can be seen in Figure 3.10a. The deviation at light-saturation is more pronounced in the *A.maxima* samples as can be seen in the grand mean and grand uncertainties to two standard deviations shown in Figure 3.10b. The saturation parameter was 787±285, where the uncertainty is to 2σ. This E_k is of the same magnitude as those for *D. maritima* in Table 3.2 which makes sense given that both cultures were grown in the same incubator at the same irradiance. The large discrepancy in E_k across the four sub-samples is driving the variation in the light-saturated phase. This may be due to inadequate closing of reaction centres by the excitation protocol. Performing FLCs without accompanying oxygen evolution or ^{14}C-incubation measurements can only provide a rough estimate of the maximum photosynthetic capacity, however, this work shows that in the case of *A. maxima*, the FLCs are more variable than in the case of *D. maritima*. This means that a second measurement is necessary and if there is a significant discrepancy then a third should be run. Each measurement should be made as fast as possible to account for variable algal dynamics. This is useful for FRRf

operators concerned that they only have enough time to run a single FLC measurement per sample whilst doing fieldwork. However, if time allows, it would be advisable to run a second FLC to corroborate the data produced in the first FLC. Even better, the use of two cross-calibrated FRRf would be ideal for running FLC measurements.

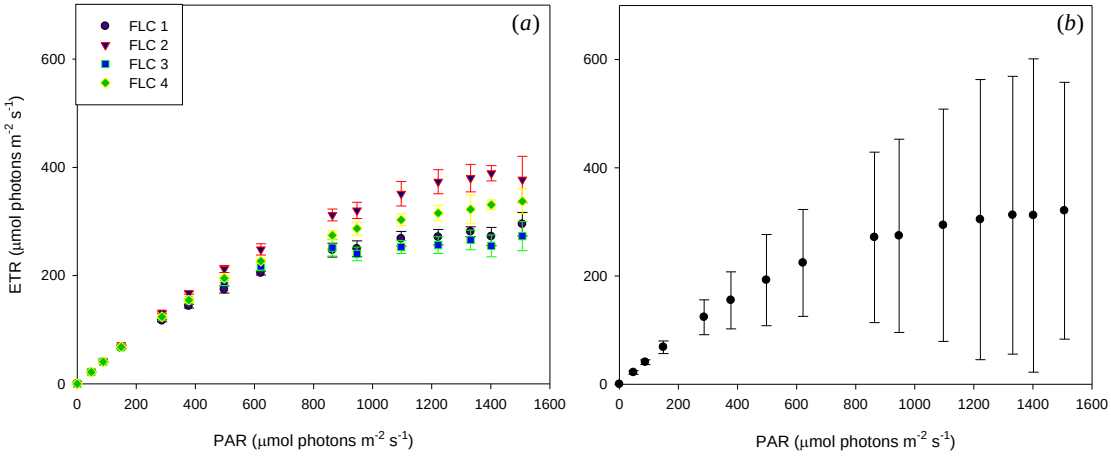

Figure 3.10: (a) FLCs for four sub-samples of A.maxima using the same FLC protocol and measured contiguously (b) The grand mean for the four A.maxima sub-samples with the uncertainty given to two standard deviation.

Steady-state Fluorescence Light Curves

Algal physiology is fluid and constantly responding to environmental cues throughout the day. A major environmental cue affecting phytoplankton is the irradiance level incident upon the water.

The light history of an algal sample refers to the effects of photoinhibition that may have a bearing on the photosynthetic parameters determined by the FRRf (From *et al.*, 2014). The light history is influenced by the solar irradiance the cells have been exposed to, which impacts the photochemical efficiency as the cells will be actively working to dissipate the excess energy incident on their light harvesting antennae. The concept of steady-state illumination in an FRRf measurement is to equilibrate the fast-moving algal dynamics to a particular light history, i.e. removing the previous light history by replacing it with a new one. This idea of a light history was formulated by Steele (1959) to remove some of the variability inherent in algal measurements by attempting to control algal dynamics to a greater extent. This is conducted by illuminating a sample at a particular irradiance for a fixed period of time prior to making measurements. The aim of the following measurements was to

determine whether there was a minimum steady-state illumination period that resulted in a stabilised FRRf signal.

Sub-samples of *D.maritima* were removed from the incubator (during the lit phase of the diel cycle) and exposed to a steady-state illumination of 108 µmol photons m^{-2} s^{-1} for increasing periods of time from 10 seconds to 240 seconds. Fifteen individual repetitions of the 450 nm excitation LED were made proceeding each illumination period and the effect on F_o and F_m tracked. The difference in F_o and F_m between the first and last measurement was used to chart whether steady-state equilibrium had occurred:

$$F_o^1 - F_o^{15} = \Delta F_o \quad (3.5)$$

$$F_m^1 - F_m^{15} = \Delta F_m \quad (3.6)$$

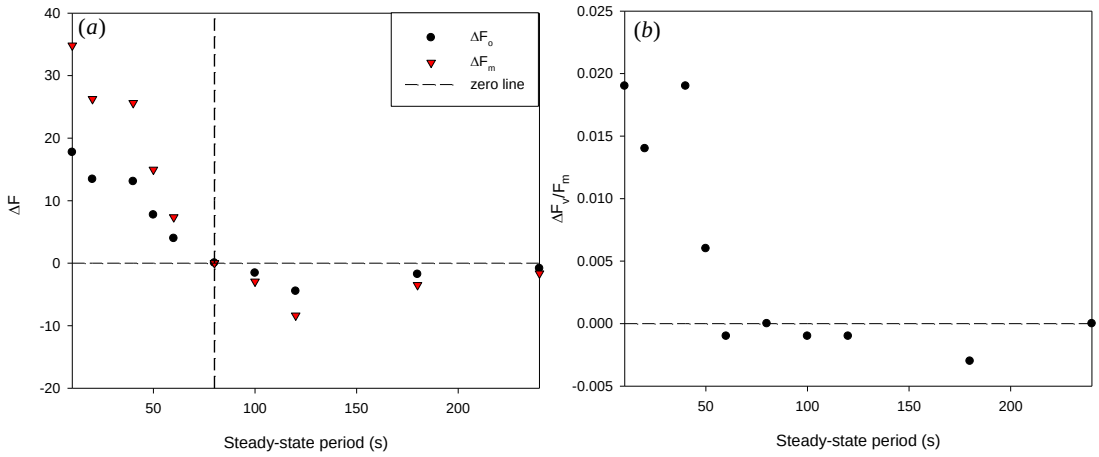

Figure 3:11: Fifteen excitation LED repetitions at 450 nm were made following the period of steady-state illumination with the difference in F_o and F_m charted above (b) The same information for the photochemical efficiency is shown.

With increasing steady-state period, the difference in F_o and F_m progressively reduces to zero at 80 seconds where there is no difference. This reduction in the difference between these parameters may represent a shift in algal dynamics. Table 3.3 shows the comparison of the differences in fluorescence for each steady-state illumination period. The difference is most pronounced for the actual fluorescence parameters with there being less impact on the photosynthetic capacity. The dashed line between 60 and 80 seconds identifies the point at which the fluorescence parameters show little change leading to the conclusion that an 80 second steady-state illumination period is sufficient to affect the light history of the sample.

A study of the effect of the inclusion of different steady-state illumination periods on the fluorescence light curve of a sample of *Dunaliella maritima* was conducted. A control FLC of *D.maritima* with no steady-state period was run followed by a second sub-sample, which was exposed to a 90 second illumination period prior to each light step. Samples were made in triplicate and the mean of these triplicates plotted in Figure 3.12. For a more in-depth discussion of the impact of steady state period and the physiological impacts of steady-state, we refer you to Perkins *et al., (2006).*

Table 3.3: Effect of steady-state illumination is tabulated for varying steady state periods. The dashed line between 60 and 80 seconds represents the point where it is believed steady-state equilibrium has occurred.

Illumination Period	ΔF_o	ΔF_m	$\Delta F_v/F_m$	ΔrP
10 s	17.74	34.83	0.019	2.02
20 s	13.4	26.26	0.014	1.46
30 s	13.07	25.62	0.019	1.99
50 s	7.72	14.96	0.006	0.72
60 s	3.97	7.34	-0.001	-0.03
80 s	0.03	0.01	0	-0.06
100 s	-1.59	-2.95	-0.001	-0.08
120 s	-4.49	-8.38	-0.001	-0.07
180 s	-1.77	-3.5	-0.003	-0.32
240 s	-0.85	-1.64	0	-0.06

Figure 3.12 shows that the photosynthetic capacity was not affected between steady-state illuminated samples. This corroborates previous steady-state experiments conducted in the course of these characterisation experiments (not shown) that found statistically significant variation in the fluorescence parameters with little variation in the electron transport rate.

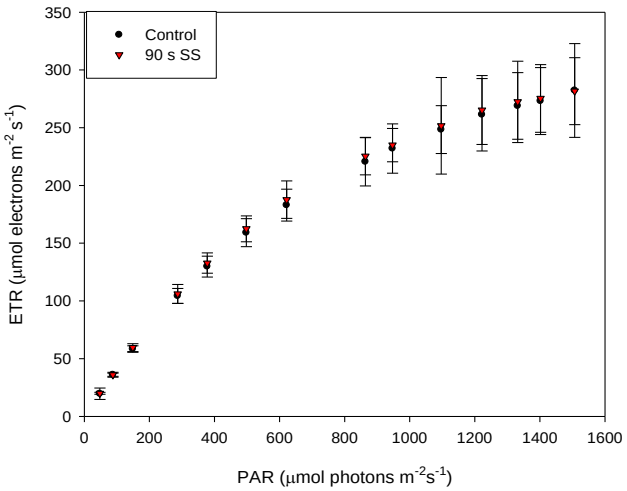

Figure 3.12: Comparison of FLCs for samples of D.maritima with a control that has not been steady-state illuminated and a second sub-sample that was illuminated for 90 seconds per light step.

Table 3.4: The FLC parameters for the control and steady-state D.maritima samples are shown with uncertainties to 2σ.

	Control		Steady-State	
FLC Parameter	Mean	S.D.	Mean	S.D.
α	0.422	0.023	0.441	0.006
E_K	733.9	135.8	754.4	70.6
ETR	327.4	8.3	210.1	16.6

Table 3.4 shows that the initial slope and the saturation parameters are broadly similar between the control and steady-state illuminated sample. The photosynthetic capacity in the steady-state illuminated sample is 36 % smaller than for the control, and is outside the uncertainty range for each sample suggesting that the removal of the light history with steady-state illumination is potentially having a real effect on the algal dynamics. A particular drawback of utilising a steady-state illumination period is that it imposes additional time constraints on the operator. For example, a 20 step FLC using standard settings will take an additional 25 minutes to complete with an 80 second illumination period.

The addition of a steady-state illumination period appears to have a real effect on the algal dynamics when measuring the electron transport rate of a sample, however, this apparent

change in ETR must be balanced with the need for making rapid measurements when conducting experiments at sea. When conducting laboratory measurements, a steady-state illumination period should be used but when at sea, the time constraints imposed may necessitate not including one.

FLC Light Step Repetitions

As the FastOcean system is not currently conFigured for CTD rosette deployment, interrogation of samples *in situ* is not possible. This presents an issue as samples are being removed from their natural environment resulting in changes in irradiance exposure and temperature that will cause changes to the algal physiology. The longer a sample is out of its natural environment, the less useful a marker of that environment it potentially becomes. It is therefore important to perform measurements as quickly as possible as it is not uncommon for a series of measurements including dark-regulated triplicates of photochemical efficiency and a fluorescence light curve to take over an hour to complete by which time the algal dynamics may have shifted.

The aim of these experiments was to find whether the key FLC parameters calculated are significantly affected by the number of repetitions performed at each irradiance with a view to economising the time taken to run a single measurement. When running an FLC, a number of repetitions at each light level are performed depending on the signal to noise levels in the sample. The number of repetitions can vary from 1 to 120 repetitions. In this experiment, four FLCs were run with different numbers of repetitions per light level of 1, 3, 5, and 10 repetitions. The FLC parameters were then compared to see if there was a significant change in the parameters with increasing or decreasing number of repetitions. The results of which are graphed in Figure 3.13.

In Figure 3.13a-d, the light-limited phases of the FLCs are similar with deviation beginning to occur in the light-saturated phase. Analysis of these data suggests that in this particular instance, the number of light step repetitions is less consequential to the outcome of the final FLC shape. A single repetition per light step as in Figure 3.13c is not ideal as there is no statistical analysis of a single data point and it can be seen that the single repetition FLC produces data that outlies in comparison to 10, 5, and 3 repetitions.

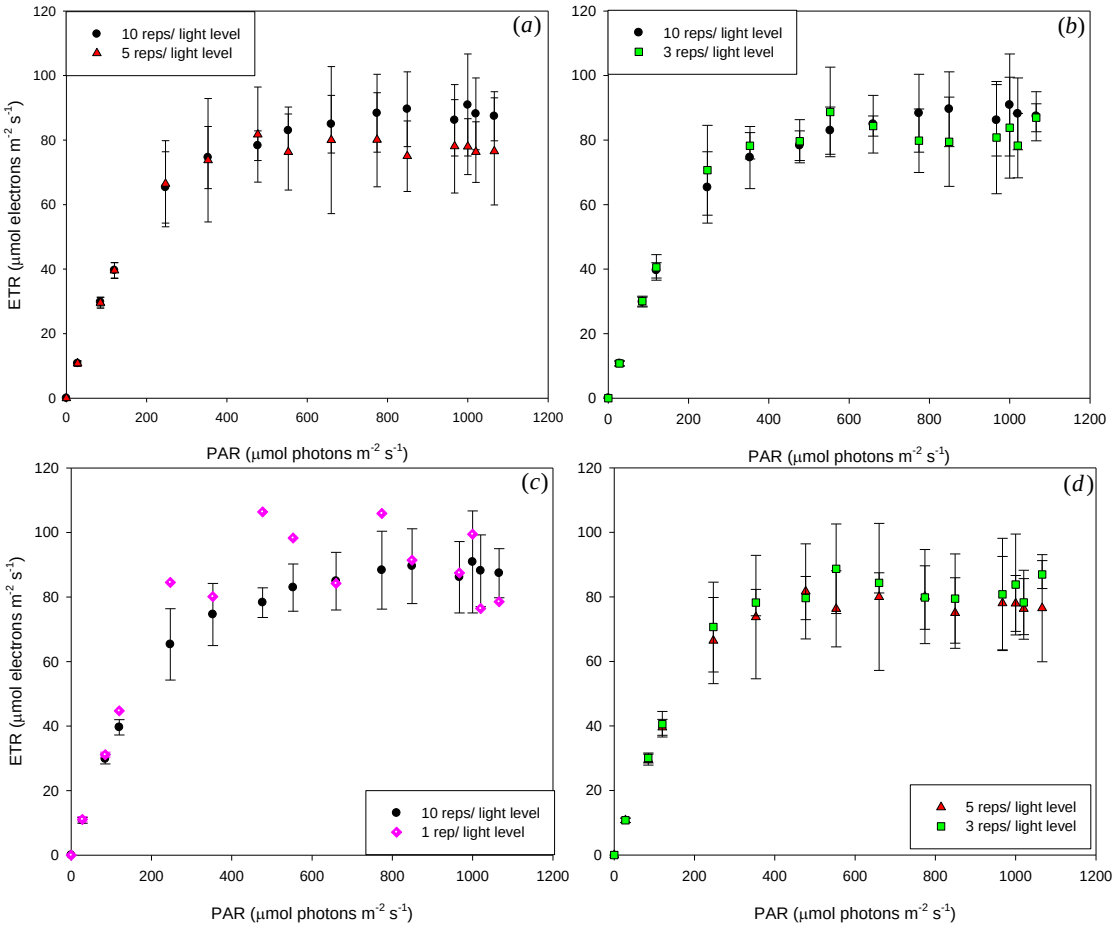

Figure 3.13: (a) Ten repetitions per light step were used as the control against a decreasing number of repetitions (b) Three repetitions is compared to the control of ten repetitions (c) One repetition per light step is compared to the control, as there is only a single repetition, no error bars are possible here (d) Comparing five to three repetitions per light step shows that there is very little difference here when studying a monoculture.

Figure 3.13a shows that there is only a small difference between using 10 or 5 repetitions and Figure 3.13b shows the case to be the same between 10 and 3 repetitions. Figure 3.13d compares using 5 repetitions to using 3 repetitions and indicates that there is not much difference between using either. Using 3 repetitions would be significantly faster than using 10 repetitions per light level. The data presented points towards the use of as few as three repetitions per light level meaning that measurements can be made more quickly and so the algal dynamics have less time to shift meaning samples more closely resemble their natural conditions. A drawback to the experimental setup is that samples used are from axenic

monocultures meaning they are unable to model the nuance and complexity of a natural sample. Additional experiments exploring the effect of the number of repetitions per light step on natural samples of different optical complexity would give a better indication of the use of this approach for field work. For now, these experiments are only able to indicate that FLCs conducted on monocultures produce very broadly similar curves using as few as three repetitions per light step.

Use of Additional Excitation LEDs in an FLC

Previous iterations of the CTG Fast Repetition Rate fluorometer have only contained a single 450 nm excitation waveband. The inclusion of additional wavebands at 530 nm and 624 nm in the current version of the instrument facilitates experiments on a broader range of pigment packages, for example the phycobiliproteins of cyanobacteria. It stands to reason that there would be a species-dependent response to use of these additional wavebands. A possible nuance of the use of additional wavebands is the potential for a holistic categorisation of unknown families or orders based on the differences in response to wavebands. This categorisation would be based on excitation LED protocol and its fine-tuning to identify particular 'functional groups' that are indicative of groups of algae, such as the greater absorption in the green and red areas of the visible spectrum associated with cyanobacteria. This allows for a more complete understanding of the bulk properties of the water column.

The aim of these experiments was to determine to what extent additional wavebands contribute to an FLC for two different species- *Phaeodactylum tricornutum* and *Arthrospira maxima*. FLCs were completed using the standard protocol in section 3.2 and the effect on the FLC parameters using the 450 nm and the 3LED (450, 530, 624 nm) approach was shown for *P.tricornutum*. For *A.maxima*, the 450 nm LED alone is insufficient to promote a variable fluorescence response. As such, the protocol is reversed. Instead of the single 450 nm excitation, the 530 nm and 624 nm LEDs are used to stimulate a response and then the 3LED response is monitored for the additional effect that the 450 nm LED has on the *A.maxima* system.

Table 3.5: The FLC parameters for each of the FLC excitation LED combinations tested for both the P.tricornutum and the A.maxima.

FLC	*P. tricornutum*	*P. tricornutum*	*A. maxima*	*A. maxima*
Parameters	450 nm	450, 530, 624 nm	530,624 nm	450, 530, 624 nm
α	0.519	0.500	0.425	0.428
F_v/F_m	0.519	0.525	0.269	0.266
E_K	81.3	89.3	466.6	480.4
ETR	43.7	44.9	200.3	210.2

From Table 3.5, it is possible to see the impact of the different excitation LEDs. Addition of the 530 and 624 nm LEDs on *P.tricornutum* results in a 3 % increase in the photosynthetic capacity and for *A.maxima*, there is a 5 % increase in the photosynthetic capacity with the inclusion of the 450 nm LED. Table 3.5 illustrates that the two phytoplankton species are in opposition to one another. The 450 nm LED is sufficient to drive photosynthesis in *P.tricornutum* but the 530 and 624 nm LEDs make little contribution and for *A.maxima*, the opposite is true. The 530 and 624 nm LEDs are enough to drive photosynthesis with the 450 nm LED contributing only a small increase.

However, the FRRf when used for natural samples is making a bulk measurement of the physiological state of the total algal population. As such, the additional LEDs give a more accurate representation of the pigment composition in the water column. By not accounting for the signals produced using the additional excitation LEDs, we may potentially misrepresent the true algal physiological state of the water column at that time.

Dark Acclimation and Algal Photophysiology

There is a need for a consistent FastOcean measurement protocol to allow for comparison between measurements. Basic to this need is the question of the dark acclimation period. This is defined as the period between a sample being placed into the darkened sample chamber and a measurement being made. A survey of the literature over the past thirty years suggests that the question of the period of dark acclimation applied has yet to be settled, see Table 3.6, with estimates ranging from no dark acclimation period to 60 minutes of dark acclimation.

Raateoja *et al*. (2004) specifically state that their use of a 10 minute dark acclimation period is to ensure decay of the fast

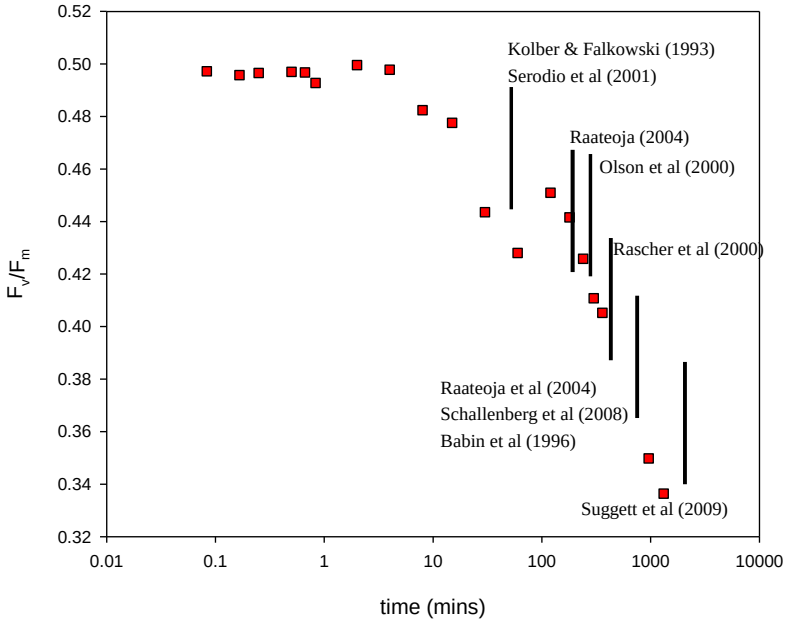

Figure 3.14: The changing dark acclimation period is mapped for the photochemical efficiency with some literature-defined values as collated in Table 3.5

components associated with non-photochemical quenching and oxidation of the electron transport chain. Other studies in the literature are not as transparent in this regard and it may be the case that a particular dark acclimation period is applied because that is the length of time that has always been used with no introspection as to why this is the case. The aim of these measurements is to determine what the impact is of different dark acclimation periods on the maximum photochemical efficiency of algal cells.

Figure 3.14 shows the changing photochemical efficiency with different periods of dark acclimation of a sample of *D.maritima*. Overlaid on Figure 3.14 is a snapshot of different recommendations found in the literature. As can be seen, using different literature-defined dark acclimation periods, a different photochemical efficiency would be found. These rapidly varying algal dynamics make it difficult to compare data measured in different labs and on different research cruises as this aspect of the protocol has the potential to have a major effect on the data.

Table 3.5: The dark acclimation period from thirteen articles in the literature are shown with the particular fluorescence technique used to make the measurements.

Dark Acclimation Period	Active Fluorescence Technique	Source
10 minutes	FastTracka FRR fluorometer	Raateoja, 2004
45-60 minutes	FastTracka FRR fluorometer	Suggett *et al.*, 2009
30 minutes	FastTracka FRR fluorometer	Raateoja *et al.*, 2004
5-10 minutes	Pump and probe fluorometer	Kolber & Falkowski 1993
30 minutes	Turner Designs fluorometer (10-005 R)	Schallenberg *et al.*, 2008
30 minutes	FastTracka FRR fluorometer	Babin *et al.*, 1996
20-30 minutes	Mini-PAM (Waltz)	Rascher *et al.*, 2000
No dark acclimation	Phyto-PAM (Waltz)	Franklin *et al.*, 2009
15 minutes	FastTracka FRR fluorometer	Olson *et al.*, 2000
5 minutes	PAM fluorometer	Serôdio *et al.*, 2001
30 minutes	PAM fluorometer	Belkhodja *et al.*, 1998
30 minutes	Pump and probe fluorometry	Kolber *et al.*, 1990
0-3 minutes	Parallel flow-through fluorometers	Cullen *et al.*, 1979

Our philosophy behind dark acclimating a sample is to allow short-lived quenching mechanisms to relax to their ground states prior to making a measurement. By allowing these mechanisms to relax, the photosystem II reaction centres are being allowed to re-open with a reduction in the role of photoprotective pigments allowing a more accurate assessment of the photochemical efficiency. The aim of these dark acclimation experiments is to identify the effect of long-lived quenching mechanisms on the photochemical efficiency with a view to identifying an optimal dark acclimation period and whether or not a 'steady-state' photochemical efficiency is reached following the requisite dark acclimation period.

Two species were used in the course of these experiments: *Dunaliella maritima* and *Arthrospira maxima*. These two species were used here due to their biological differences allowing a more general statement about dark acclimation to be made. Samples were prepared using the standard protocol and allowed to dark regulate for a specific time before

running a single excitation protocol. Measurements were made in triplicate for each dark acclimation experiment. The dark acclimation periods tested ranged from as few as 5 seconds to over 18,000 seconds (5 hours).

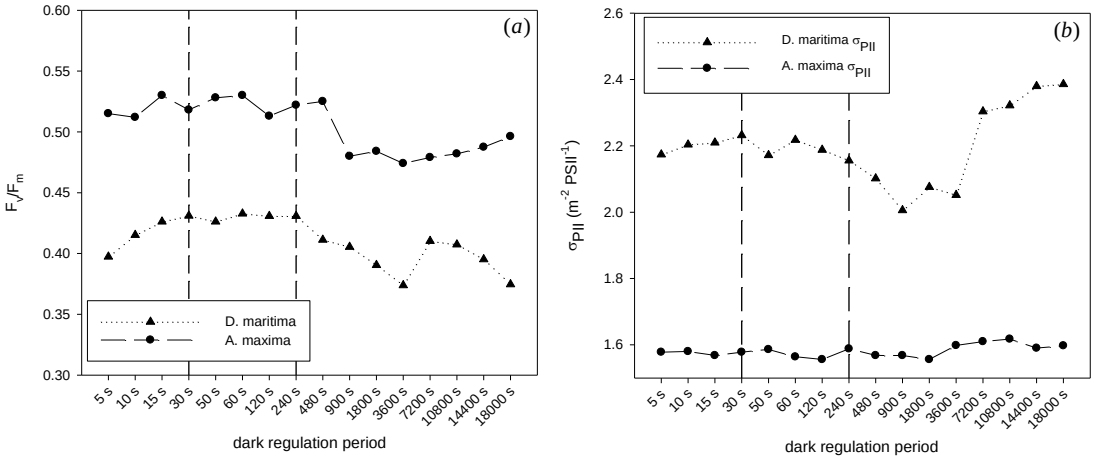

Figure 3.15: (a) The inter-comparison of D.maritima and A.maxima for photochemical efficiency with the dashed lines suggesting minimum and maximum periods of photochemical stability (b) The inter-comparison of the functional absorption cross-sections for both species under the same experimental conditions.

Figure 3.17a-b show that *Dunaliella maritima* and *Arthrospira maxima* have different responses to dark acclimation. However, both species have reached their maximum photochemical efficiencies by 30 seconds of dark acclimation. The dashed lines on Figure 3.17a highlight a period of consistency in the photochemical efficiency for both species that occurs between 30 seconds and 240 seconds (4 minutes). Furthermore, the functional absorption cross-sections in Figure 3.17b are quite different. *A.maxima* remains consistent despite the period of dark acclimation, whereas *D.maritima* shows greater dynamism across the same range. The lack of dynamism in the cyanobacterial cells may be associated with the improved physiological status of these cells, or alternatively, may be an indication of a different response from *D.maritima* to prolonged periods of darkness. The inter-species variability found here beyond 240 seconds of dark acclimation is potentially due to genetic differences in these species.

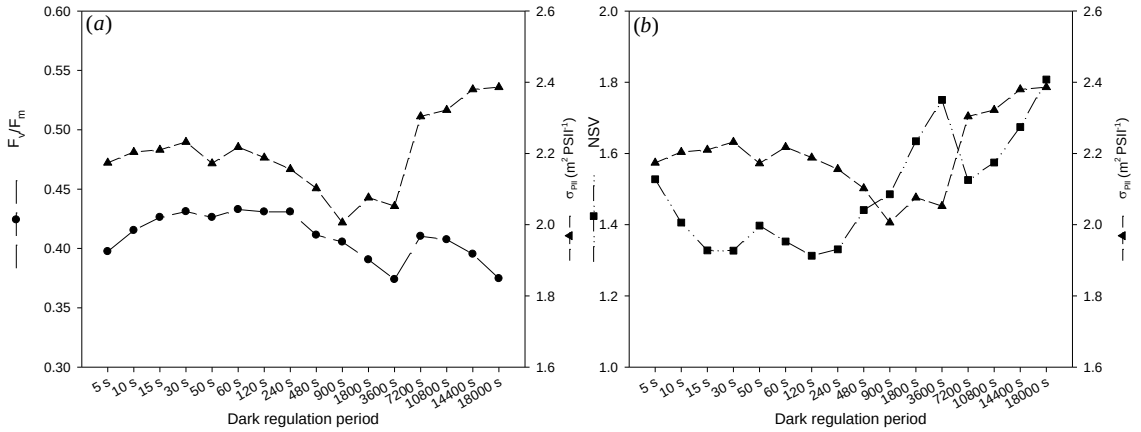

Figure 3.16: (a) The dark acclimation period applied to D.maritima is monitored using the photochemical efficiency and the functional absorption cross-section (b) The functional absorption cross-section is compared to the normalised Stern-Volmer data, which is used as a method of tracking the non-photochemical quenching of a sample.

Figure 3.16 shows the parameters derived for various dark acclimation periods on a sample of *D. maritima*. In Figure 3.16a, there is a rise in F_v/F_m after the first 30 second period. A maximum F_v/F_m is achieved after approximately 120-240 seconds, after which there is a drop to a minimum after 3600 seconds (60 minutes). This initial response in the algal dynamics is explained by the relaxation of quenching mechanisms which are designed to remove excess energy from the photosynthetic pathway to protect it from damage. The relaxation of these mechanisms allows reaction centres to re-open, as if to reset photosystem II. The cell response at longer time periods indicates higher effective rate constants for non-photochemical energy dissipation mechanisms despite the lack of photon input.

There is a fairly clear relationship in the timing of changes in the photochemical efficiency and functional absorption cross-section in Figure 3.15a. The reduction in the functional absorption cross-section, which is the light utilisation efficiency for photochemistry in photosystem II may be a factor in explaining the reduction in the photochemical efficiency. Less photons are being directed to the photosystem II reaction centres meaning a greater proportion of the incoming energy is being dissipated via non-photochemical quenching pathways.

The normalised Stern-Volmer coefficient in Figure 3.15b is taken as the ratio of the total non-photochemical dissipation in the light-adapted state to the rate constant for photochemistry.

This is found to have an inverse relationship with the functional absorption cross-section. In both Figures 3.16a-b, the FRRf parameters measured bisect at 420 seconds (8 minutes) suggesting that the cell's ability to perform photosynthesis is reducing with corollary increases in the energy dissipation via non-photochemical quenching pathways.

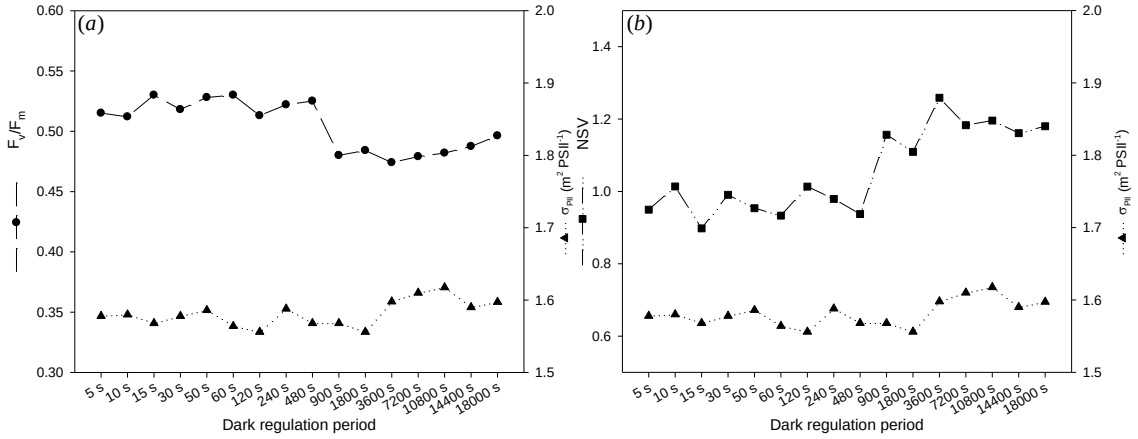

Figure 3.17: (a) The photochemical efficiency and functional absorption cross-section for Arthrospira maxima are compared for increasing dark acclimation periods (b) The functional absorption cross-section is compared with the normalised Stern-Volmer coefficient.

The *Arthrospira maxima* cells used in Figure 3.17 were very healthy at the time of measurement and so there is little increase in F_v/F_m recorded. However, a drop in the photochemical efficiency is noted after 420 seconds (8 minutes) with a small recovery in the efficiency beginning at the one hour dark acclimation point. The functional absorption cross-section of *A.maxima* was not dynamic when compared to that of *D.maritima* in Figure 3.16. This may be a result of the more physiologically robust cyanobacterial cells. Figure 3.17b shows that the normalised Stern-Volmer coefficient still increases with increasing dark acclimation period despite there being relatively little fluctuation in the functional absorption cross-section. The increase in functional absorption cross-section at 1800 seconds (30 minutes) correlates with the minor increases in photochemical efficiency following this point suggesting that these two changes may be linked.

There are similarities between *D.maritima* and *A.maxima* in that following a period of dark acclimation, a reduction in the photochemical efficiency occurs. For *D.maritima*, this occurs

after 4 minutes and for *A.maxima*, the drop occurs after 8 minutes. This difference may be due to the different pigment arrangements and the extent of quenching present in each sample at that time.

From the data above, the main recommendation from these experiments would be to use a dark acclimation period between 30 seconds and 240 seconds over a longer one so as to produce a measure of the maximum photochemical efficiency of the cells without the possibility of beginning to alter the macromolecular structure of the photosynthetic apparatus. These shorter dark acclimation periods appear to represent a minimisation of the fast components of non-photochemical quenching mechanisms resulting in a maximisation of the variable fluorescence capabilities of the cells.

3.2 FastOcean Measurement Protocol

Following on from section 3.1, this section is designed to lead a new user of the FastOcean system through the process of taking the instrument from cold to performing single measurements and fluorescence light curves. The proceeding information is designed to be used in conjunction with the conclusions reached with regards to the optimal performance of the instrument in section 3.1.

Materials Required

- FastOcean Instrument (assembled)
- Laptop Computer
- Laptop charger
- Mains adaptor
- USB adaptor for software-hardware interaction
- LED power lead
- Impulse Lead
- Test tube collar
- Tubing Kit
    - Female connectors for chamber water jacket
    - 2 x narrow bore tubing assemblies

    - 3 mm ID tubing
- Sample test tubes (100 x 16 mm)
- Test tube rack
- Allen keys (various)
- Bath for water bath
- Milli-Q
- Ethanol
- Paper towels
- Pipettes
- Pipette tips (5 ml)

Pre-Sample Setup

The lab-based FastOcean and FastAct systems are operated from the mains supply and connected to the associated computer by a USB connection. A circular power button on the front face of the FastAct system powers the instrument on. The FastPro8 software that controls the instrument can be downloaded for free from the Chelsea Technology Group website. Once the instrument is switched on, the water jacket in which the sample test tube will be placed is filled with purified Milli-Q water.

The water jacket can be operated in one of two ways: non-circulating or circulating water jacket. A non-circulating water jacket is influenced only by the instrument temperature whereas a circulating water bath can be influenced by the ambient temperature of the laboratory. Using either water jacket setup will result in an equilibrium temperature after a given period of time (approximately 5 hours) (see section 3.1, *instrument warm-up time).*

Non-Circulating Water Jacket

A single piece of rubber tubing is used to link the upper and lower connectors on the FastAct head unit. The instrument electronics are then allowed to reach thermal stability. This is found to be after roughly five hours. At this point, the instrument is considered fully temperature stabilised.

Circulating Water Jacket

A circulating water jacket is prepared by connecting a length of tubing from the lower connector of the water jacket to the rear peristaltic pump connector. A second length of tubing is connected from the front peristaltic pump connector to the water bath and is used to bring water up into the pump and via the rear peristaltic pump into the water jacket. A final length of tubing is set up from the upper connector on the water jacket into the water bath and acts as a drain preventing the water jacket from overflowing. Assuming that the water bath is not temperature-regulated, then much in the same way as the non-circulating water jacket, a period of time is required for thermal equilibrium to be achieved. CTG do suggest the use of a temperature-regulated water bath in order to keep the water jacket temperature constant. The use of a temperature-regulated bath has the added benefit of being able to more accurately portray field conditions when working on-board a research cruise.

Pre-Measurement Hardware Setup

Prior to running a measurement, the hardware and software need to be synchronised. At this point, it is then necessary to optimise the hardware to ensure reliable measurements are produced. The hardware setup is described below.

Hardware-Software Synchronisation

Using a 5 ml pipette, a sample of optically thin phytoplankton culture of between 0.5 to 2 ml is added to a 100x16 mm test tube. For consistency, 1 ml of sample is dispensed in all measurements made throughout this thesis. When inserting the test tube into the sample chamber, do not force the test tube down as this can result in the tube shattering within the sample chamber.

With the test tube now securely in place, the FRRf is connected by accessing FastPro8 and clicking **Devices → Attach FRRf3**. The FastAct system is then also connected by clicking **Devices→ Attach FastAct**. The FRRf hardware can now be manipulated.

Optimisation of E_{LED}

The excitation irradiance (E_{LED}) can be varied in the protocol editor, accessed from **Devices→FRRf3 Protocols→ Show Series**. From a physiological standpoint, it is important to get this parameter right. If the excitation irradiance is too high, the population of photosystem II reaction centres will close too quickly resulting in fluorescence quenching during the saturation phase. If the excitation irradiance is too low then it may result in a scenario where some photosystem II reaction centres do not close. The optimal value of E_{LED} is sample-dependent and may even vary across sub-samples from a single culture.

How well the values of E_{LED} fit the current sample can be estimated using a parameter, $R\sigma_{PII}$, which is the probability that a reaction centre is closed by the first flashlet in a single turnover sequence. A value of between 0.035 and 0.055 for $R\sigma_{PII}$ is considered optimal. The values of E_{LED} can be adjusted between 0-1.7; 0-0.5; and 0-1.5 $x10^{22}$ photons m^{-2} s^{-1} for the 450 nm, 530, and 624 nm LEDs respectively.

Optimisation of the PMT Gain

Optimisation of the gain on the photomultiplier tube is necessary to utilise the greatest fraction of the dynamic range of the signal ADC. The working dynamic range of the ADC should be maintained between 20-90 %. Saturation of the ADC results in signal clipping which may produce unreliable data.

The PMT gain setting that is to be used is dependent upon the values of E_{LED} being used, the sample biomass being measured, and the fluorescence excitation spectrum of the sample. For example, dense cultures will require a lower PMT gain to prevent saturation of the ADC or if a cyanobacterial sample is used, the PMT gain may need to be increased to improve detection of the fluorescence signal. Trial and error is required to find the balance between these extremes when measuring the bulk signal from a field sample.

Automation of E_{LED} and PMT Gain

It is possible to allow the software to attempt to optimise E_{LED} and the PMT gain automatically. Automated parameter optimisation works in the same way as doing it manually by attempting to keep $R\sigma_{PII}$ between 0.035 and 0.055 for E_{LED} and maximising the PMT ADC at the same time. This has a time-saving advantage, however, it is recommended that the operator manually controls these parameters as they are very important to producing data of good quality. This could be used to find optimal parameters that are then manually imposed going forward. A continually varying E_{LED} protocol and PMT gain have the additional disadvantage of requiring multiple sample blanks for each protocol setting and individual sample blanking on the software; a step that proves to be much more time consuming than manually setting these parameter values.

Any changes that are made to the E_{LED} and PMT protocols in software will cause the hardware and software to become desynchronised. They can be re-synchronised by right-clicking the FRRf3 sensor window and clicking **Synchronise FRRf3**.

Pre-Measurement Protocol Setup

A single turnover sequence is normally achieved by 100 flashlets on a 2 µs pitch with a relaxation phase of 40 flashlets on a 50 µs pitch. The relaxation phase would normally be included in a lab measurement as there should not be any sample exchange during the 2 ms of that phase. The number of sequence repeats is set at 32 as standard, however, it is possible to vary the number of sequence repeats depending on the optical thickness of the sample, e.g. high concentrations of phytoplankton require fewer repeats (between 8-12) whilst achieving a high signal: noise ratio. Less dense phytoplankton concentrations may require more repetitions (up to 160).

Running a Single Measurement

The FastOcean instrument is not designed for plug and play. It requires patience and knowledge of the parameters being produced. The measuring parameters may require considerable fine-tuning prior to being able to make the actual measurement. Once the operator is confident that the parameters are adequately within range, a protocol can be run

by clicking the black *play* button on the GUI dashboard. Data are returned in the open window within FastPro8.

Sample Blanking a Single Measurement

Sample blanking is used to account for the baseline fluorescence present in a sample that does not contribute to the variable fluorescence. Sample blanks are run following a sample measurement using the exact protocol employed for the sample and are taken as the F_o value produced by the blank.

A sample blank is measured in the same way that a standard sample would be. The black *play* button is pressed and the resulting parameters are displayed in the window. It is recommended that a minimum of three sample blank measurements are made to produce an average for F_o. The sample blank is wavelength-dependent, i.e. it will be different for a 450 nm measurement than for a 624 nm measurement. As such, the sample data must be separated by E_{LED} combination. This can be achieved by clicking on any line of data in the window and right-clicking the screen followed by **Delete Acquisition→All with different LED combinations**. This removes any lines of data with E_{LED} combinations different from the one selected. The sample blank is then applied by right-clicking the data followed by **All acquisitions→ Set sample blank**. A box will appear requesting the value of the sample blank, the averaged F_o value of the blank is entered here. By clicking **OK**, the blank is automatically applied to the data on the screen. To store a measurement, click the *save* icon, an option to choose a filename will then be given. This file is stored as a binary file with an ".fnp" format. This format can only be read by FastPro8. However, it is possible to copy the on-screen information over to a suitable programme from FastPro8 using the Windows clipboard.

Running a Fluorescence Light Curve

Fluorescence light curves (FLC) are commonly used to characterise photoacclimation, providing a convenient means of differentiating between light-limited and light-saturated photosynthesis.

Setting up an FLC

The FastAct system allows manual control of particular aspects of the instrument during an FLC, for example the water jacket pump speed and PAR irradiance output. An FLC is setup by clicking **Devices→FLC→Edit**. A window appears showing 36 individual windows, each representing a step in an FLC, of which there may be a maximum of 36. Each step can be constructed with individual PAR irradiances and repetition settings.

When starting an FLC, dark and low light levels take longer for their fluorescence parameters to settle due to increased photosynthetic rates as a result of activation of the Calvin cycle, therefore more repetitions should be applied at these initial steps. This is an acclimation response to light availability that is controlled by gene expression and so cannot be easily avoided. Under normal conditions, our protocol would apply 10-12 steps for the initial FLC steps before reducing to 6-8 repetitions for additional steps. The additional number of repeats required can depend on the light history of the sample and the phytoplankton that are actually present. For example, physiological differences between species mean that one species may saturate faster than another. If the PAR settings are increased too quickly then this can cause downregulation (photoinhibition) which is a decrease in the photosynthetic rate and may indicate damage to the D1 proteins at photosystem II.

When running an FLC, it is advised to watch the values of F'_m and F'_q/F'_m to ensure they are stabilising by the end of a step. If they do not appear to be stabilising then the number of repetitions used can be adjusted in real time, as well as increasing the number of steps with additional smaller incremental increases in PAR available. An FLC is started by clicking the *Run FLC* option on the GUI dashboard.

Sample Blanking an FLC

Sample blanking of an FLC is carried out in the same way as for a single measurement. Given that the sample blank is based on the dark-regulated initial fluorescence, it is not necessary to account for the irradiated F'_q values.

3.3. Assessing FRRf Performance in Optically Complex Case II Waters

Introduction

Very pure natural water is deep blue in colour. The addition of suspended particles and CDOM into the water alters the optical properties of the water, ultimately affecting the IOPs, remote sensing signal, and fluorescence signal. Morel and Prieur (1977) created a bipartite distinction of the optical complexity of water based on the nature of the suspended particles present. Water masses were subsequently described as being either Case I or Case II waters.

Case I waters are those that are assumed to contain only phytoplankton-related products (including breakdown products such as CDOM) and other microorganisms, the populations of which co-vary with that of phytoplankton. For remote sensing purposes, Case I waters are those that can be modelled as a function of the chlorophyll *a* concentration alone. Case I water classifications tend to be in open ocean regions with some in-land lakes also being classified as Case I. Over 90 % of the World's oceans are considered Case I (Sathyendranath *et al.*, 2000).

Case II waters are those that contain suspended particles and/or CDOM, the concentrations of which do not co-vary with the concentration of phytoplankton, with there being greater complexity in the composition and optical properties of the water. Furthermore, there tends to be greater spatiotemporal variability in the optical properties of Case II waters (Shen *et al.*, 2015). There are taken to be at least three competing variables in Case II waters. The three components that most affect optical properties in coastal waters are the phytoplankton component (with associated organic detritus), suspended inorganic particulates, and coloured dissolved organic material (CDOM). The phytoplankton component takes into account all those organisms that co-vary and co-habit with phytoplankton including zooplankton and flagellates, as well as bacteria and any organic waste products produced by these microorganisms. The species present have an impact on this that may result in variations in the optical properties even within Case I waters. The suspended inorganic particulate component encompasses the remaining suspended particles that the phytoplankton component does not take into consideration; these non-algal particles may come from anthropogenic sources or terrigenous sources (Kondratyev and Filatov, 1999). This component is most affected by muddy rivers with high tidal range and areas of large tidal excursion and is normally confined to coastal areas. The coloured dissolved organic

component takes into account dissolved materials in the water producing a characteristic absorption in the UV/blue region of the electromagnetic spectrum.

Thus far, no attempt has been made, in the course of the characterisation of the FastOcean system, to determine the influence of non-phytoplankton components on the measured fluorescence signal. These experiments are necessary as a lot of subsequent research in this thesis occurs in high sediment areas such as the Bristol Channel and Irish Sea, which may be unwittingly impacting the FRRf signal. The determination of FRRf performance in optically complex waters was split into two sections: the effect of scattering breakthrough and the effect of CDOM. The aim of these experiments was to determine concentrations of CDOM and scattering that influence the quality of FRRf data.

The Effect of Scattering Particles on FRRf Performance

The effect of scattering due to suspended inorganics on FRRf signals was determined in a series of laboratory experiments using Kaolin as a proxy scattering material. An AC9 instrument was used to measure total particulate scattering from the total absorption and attenuation. A sub-sample of the Kaolin suspension was then used for measurement in the FRRf.

Sufficient Kaolin was added to a litre of purified water to produce a milky suspension. Settling effects in the experimental volume were avoided by allowing the Kaolin suspension to settle before drawing a sample from the top of the Duran bottle. Using Kaolin as a scattering agent allows the assumption that there is no absorption as the particles are white so any signal comes solely from scattering. Each sample was measured twice and averaged. Sub-samples from the AC9 measurement were used for FRRf measurements with the sample pulsed twenty times and an average taken. The FRRf protocol applied was 1.77 photons m^{-2} s^{-1} for the 450 nm LED and a PMT gain of 370 V.

Figure 3.18a shows the increasing dilutions of Kaolin in purified Milli-Q water. Starting from the stock solution, each dilution was reduced in concentration by half; this was repeated four times. The AC9 measurements confirm that there was a progressive reduction in the scattering signal for each dilution. Figure 3.1b shows the AC9 sub-sample in the FRRf which were pulsed twenty times each before averaging.

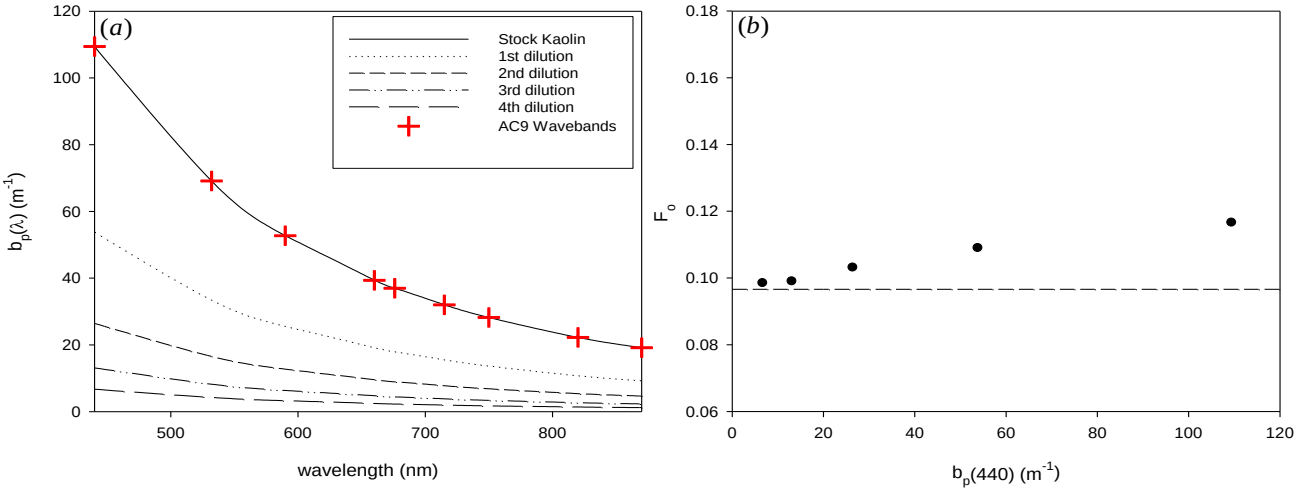

Figure 3.18: (a) Averaged AC9 measurements for each concentration of Kaolin suspended in purified Milli-Q water. The red crosses represent the nine wavebands of the AC9 instrument. Four successive dilutions by half in purified Milli-Q water produced the series above (b) The sub-sampled Kaolin from the AC9 instrument was pulsed twenty times in the FRRf and averaged. The dashed line in (b) is the Milli-Q baseline.

The particulate scattering value for 440 nm was taken in each case. These measurements show that the effects of scattering on F_o are small. There is a change in signal but the effect is minimal. Between the highest level of scattering at approximately 110 m^{-1} and the smallest at 7 m^{-1}, there is a 15 % difference in F_o from 0.117 down to 0.099. Furthermore, the levels of scattering used to conduct these experiments would be considered to be exceptionally high concentrations of suspended solids corresponding to very turbid waters. The 15 % change in F_o would be considered large if operating in oligotrophic waters. However, open ocean oligotrophic waters are normally considered Case I waters and so would not contain high concentrations of particulate scattering material. It can be concluded that the effect of scattering breakthrough is minimal for the vast majority of relevant water conditions.

The effect of CDOM on FRRf Performance

The presence of other absorbing materials (e.g. CDOM and mud) affects the availability of PAR for algal absorption and photosynthesis. With decreasing wavelength, particularly below 450 nm, phytoplankton are typically in competition for photons with coloured dissolved organic matter.

The composition of CDOM is spatiotemporally variable as it encompasses a huge number of molecules with varying chemical properties, however, these molecules are categorised together by their strong absorption in the UV and blue end of the electromagnetic spectrum as shown in Figure 3.19a. The variable nature of CDOM means it is impossible to replicate the exact environmental conditions experienced during field studies; however, it is possible to use humic acid as a proxy for CDOM in the lab (see Figure 3.19b). CDOM occurs in relatively high concentrations in areas of freshwater influence, whilst having less influence in shelf seas (Bowers *et al.*, 2002). There are two possible effects of CDOM on FRRf signals: breakthrough from CDOM fluorescence and competitive absorption. The aim of these experiments is twofold: (a) identification of whether the competitive absorption of photons by CDOM influences the performance of the FRRf instrument and its ability to make reliable and consistent measurements of phytoplankton physiology and (b) the impact of CDOM fluorescence on the FRRf. The hypothesis behind this experiment is that as CDOM increases, F_o will decrease if competitive absorption is an issue and if CDOM fluorescence is a concern, F_o will increase.

A stock solution of humic acid was produced by dissolving humic acid in purified Milli-Q water until the colour of the water became darker. CDOM absorption measurements were made using the Shimadzu UV-2501 PC dual beam spectrophotometer, following the protocol described in chapter 2.

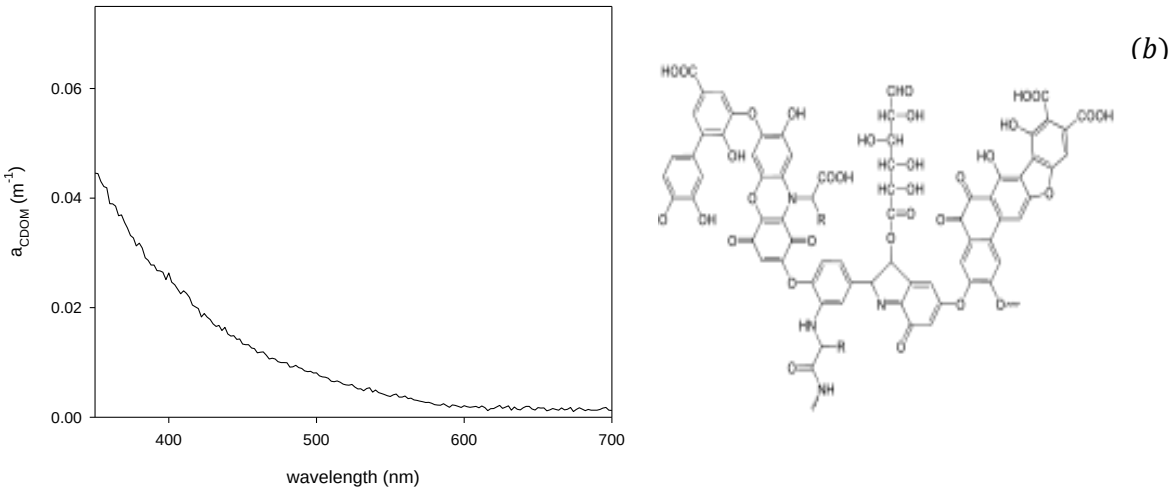

Figure 3.19: (a) Spectral absorption of humic acid measured on a Shimadzu UV-2501 spectrophotometer using the protocol outlined in chapter 2. (b) An example structure of humic acid showing the varied chemistry present on the structure (Wikicommons).

The effect of CDOM on Phytoplankton Physiological Parameters

In the previous section, the impact of CDOM on FRRf performance was only tested for humic acid dissolved in purified Milli-Q water. This is for understanding the physical instrument response to increasing CDOM concentration but does not contribute to our understanding of the effect of increasing CDOM concentrations on the measured algal physiological parameters. To test this, a stock solution of humic acid was prepared as before. A fresh sample of *Dunaliella maritima* was prepared and measured using the FRRf to provide a baseline photochemical efficiency. The baseline phytoplankton sample was filtered through a 0.2 µm filter and the spectral absorption measured on the Shimadzu UV-2501 PC dual beam spectrophotometer.

20 ml of stock humic acid solution was then added to a sub-sample of *D.maritima*. The photochemical efficiency of the sample was measured and a fluorescence light curve taken. The sub-sample was then filtered through a 0.2 µm filter and the spectral absorption determined spectrophotometrically. This was repeated for the addition of 50 ml and 100 ml of stock humic acid solution to successive sub-cultures. Figure 3.20a shows the increasing humic acid absorption measured on the spectrophotometer with increasing concentration of humic acid stock added to sub-cultures of *D.maritima*. Figure 3.20b shows the impact of the increasing CDOM absorption profile of a sample and the concomitant decrease in F_o.

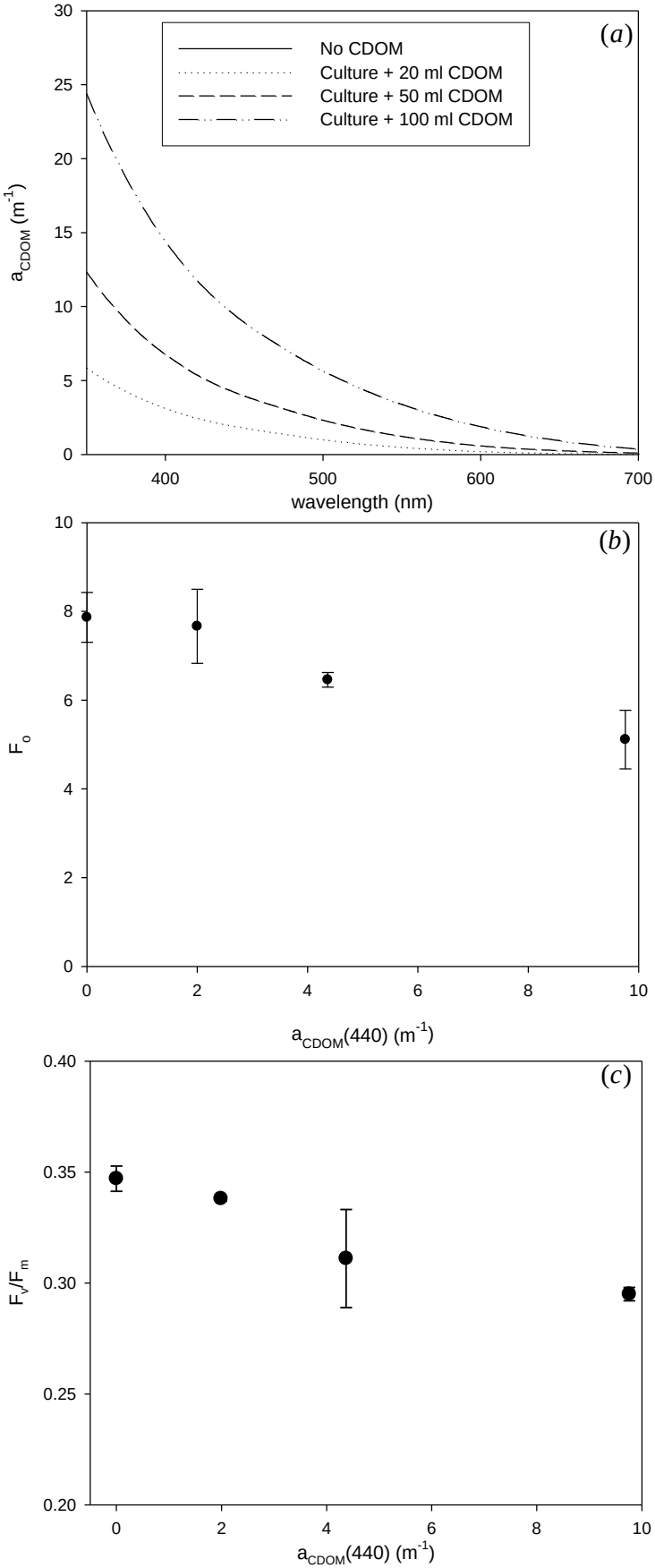

Figure 3.20: (a) The spectral absorption of the four samples with increasing concentrations of stock humic acid solution added to D.maritima measured using the Shimadzu spectrophotometer (b) F_o for each sample of increasing amounts of CDOM is shown with uncertainty given to 2σ (c) The photochemical efficiency of the sub-samples were plotted for increasing concentrations of humic acid with the CDOM absorption at 440 nm used for the Figure.

Lab experiments with humic acid suggest competitive absorption is an issue. Field experiments with natural CDOM suggest CDOM fluorescence is a problem. This is difficult to reconcile. Lefering (personal communication) has found that the processed humic acid from Sigma Aldrich is less fluorescent than equivalent amounts of CDOM from filtered seawater. At the same time, experiments earlier in this chapter suggested the possibility of cell breakage affecting F_o values. There is only very limited spectral overlap between CDOM fluorescence and the emission band of the FRRf. The impact of CDOM on FRRf estimates of F_v/F_m appears to be negligible even though values of F_o, and presumably F_m, are affected.

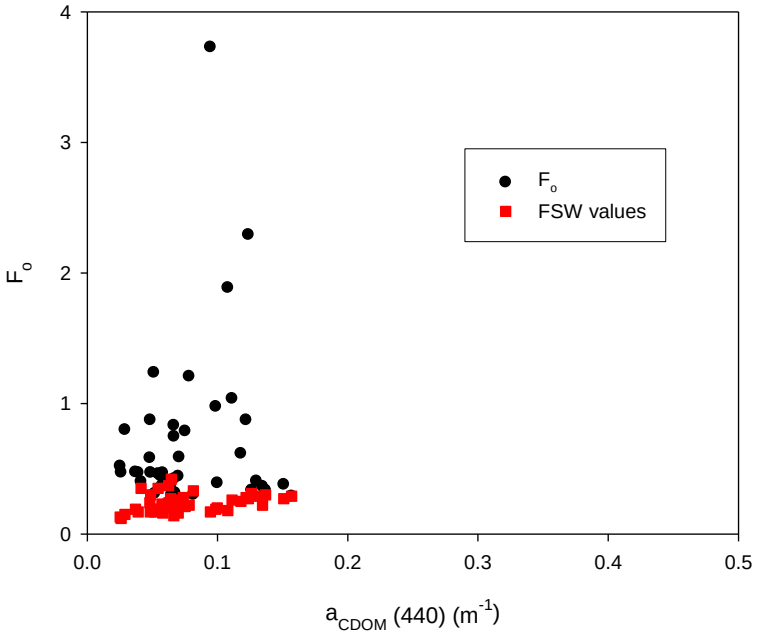

Figure 3.21: F_o and $a_{CDOM}(440)$ were plotted against one another for each station during He442. Alongside these values, the measured filtered seawater values are presented for each station.

In Figure 3.21, the effect of CDOM on the initial fluorescence, F_o, of the He442 natural seawater samples is shown. This shows a highly variable F_o value with CDOM absorption. This variability may be explained, in part, by the work in section 3.1 of this chapter where the possibility of cell breakage at the hands of the operator filtering the sample was observed. The effects of pressure on the filter were carried out after the UK coastal waters cruise and so the necessary precautions in filtering the samples were not followed. Furthermore, the measured CDOM absorption at 440 nm did not exceed 0.2 m^{-1}. A value that is much lower

than levels of absorption expected to cause variation in the signal produced by the FRRf. Overlaid on Figure 3.21 are the filtered seawater blank values produced for each station during He442. From these values, there is no clear indication of large differences in the blank based on the CDOM absorption or location for these particular stations.

3.4 Conclusions on FRRf Characterisation and Performance in Optically Complex Waters

The FRRf is an instrument that requires careful attention in order to achieve optimal performance. There are many aspects of its operation that can be varied, ultimately affecting the quality of the data produced. It is not recommended to switch the instrument on from cold and immediately begin making measurements. Our findings showed that it takes up to five hours for the instrument to achieve thermal stability, where the excitation LED temperature and measured F_o values have stopped varying. Furthermore, there is a range of PMT gain values between 300-600 V where the measured F_o remains stable. However, beyond 600 V there is a drop in F_o for the same Milli-Q purified water sample and so, when operating in highly oligotrophic waters, it may be necessary for a correction to be made to the calculated values in order for them to satisfy the values in the stable range of gain voltages.

The dark acclimation studies showed across multiple studies on two separate algal species that there was an optimal period of dark acclimation where the fast quenching components of non-photochemical quenching were minimised without descending deeper into photoacclimation processes. This period was found to be between 30 seconds and 240 seconds (4 minutes).

The optimisation of FLC measurements showed that it is possible to run fewer repetitions per light step, drastically reducing the time required to run an FLC without necessarily impacting on the quality of the FLC data produced. This, combined with the dark acclimation information, is important as it allows the normally slow process of making FRRf measurements whilst at sea to be carried out much quicker. This means that further replicates may be made improving the precision of the measurements at that station and verifying the quality of the data gathered or more samples may be processed, for example, from different depths.

The presence of scattering inorganic particulate matter and coloured dissolved organic matter can potentially impact upon the performance of the FastOcean system. However, the effects of these variables only becomes significant at concentrations far and above those that one would expect to encounter in the vast majority of natural open ocean or shelf edge waters. The FastOcean system is sensitive to increasing concentrations of CDOM in determination of the physiological state of algal cells even at values of $a_{CDOM}(440)$ that may be encountered in coastal and estuarine regions, however this was not the case during He442. The presence of large concentrations of CDOM and sediment in coastal and estuarine regions may produce inaccuracies in the measured physiological parameters, particularly the electron transport rate, however, due to very small impact, it is unlikely that they would have a major impact on the measured physiological parameters. This issue would be resolved completely with the use of adequate sample blanking, for example an artificial seawater blank or a carefully controlled filtered seawater blank to remove this baseline effect.

4. Multi-Instrument Analysis of UK Coastal Waters: April 2015

4.1 Introduction

In April 2015, the Marine Optics and Remote Sensing group took part in a three week collaborative research cruise on-board the FS Heincke with colleagues from the Helmholtz-Zentrum Geesthacht (HZG), in Germany, and Wet Labs Inc. from the United States. The cruise left from Bremerhaven in Germany and travelled clockwise around the coast of the United Kingdom stopping at 62 stations before returning to Bremerhaven. Optical, physical, and biogeochemical water measurements were made in various water types, such as Case I shelf edge waters to the northwest of the Orkney Islands to highly turbid and optically complex Case II waters such as the Bristol Channel, in support of future ESA Sentinel-3 applications.

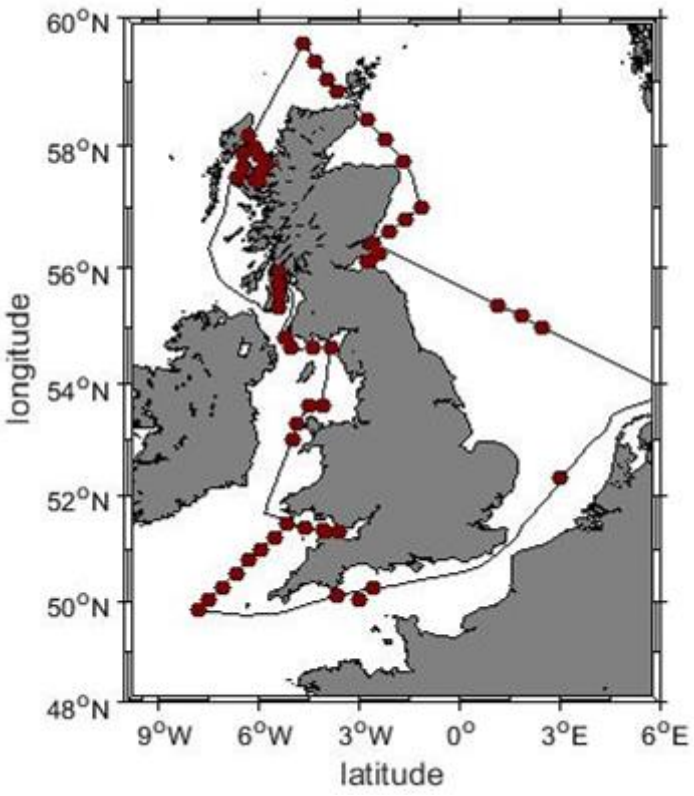

Figure 4.1: Cruise track for He442 showing all station cast locations throughout the cruise.

A full list of parameters measured and analysed in this chapter can be found in Table 4.1. A suite of *in situ* and laboratory measurements were made including *in situ* AC-9, BB-9, and BBFL2 measurements providing profiles of absorption, attenuation, backscattering, and fluorescence. Water samples were collected at discrete depths allowing laboratory

determination of chlorophyll and auxiliary pigment concentrations, physiological status through fast repetition rate fluorometry, absorption measurements for particulate absorption and CDOM using the PSICAM and spectrophotometric methods. Particle size distributions were also collected using a flow cytometer. Data measurement, processing, and inter-comparison of measurements including particle size distributions, total absorption measurements and IOP determination were conducted independently by each research group on board.

Fast repetition rate fluorometry was used to measure the physiological status of phytoplankton in a range of optically complex water types whilst being supported by data produced from other instruments. This information was then used to estimate daily, column-integrated gross primary productivity using FRRf-derived parameters (see chapter 5).

The aim of this chapter is to understand the data that the Fast Repetition Rate fluorometer produces particularly with relation to long term and short term dynamical processes. FRRf data is known to be highly variable and it is important to recognise the extent to which these processes, occurring over multiple timescales, are influencing the FRRf measurements. For example, processes such as photoacclimation and dark acclimation occur very quickly on the milliseconds to minutes timescale with longer term processes, such as water column mixing and stratification occurring on the days to weeks timescale. The proceeding analysis looks at whether there is a pattern between particular optical, physical, and biogeochemical parameters and the FRRf data collected during He442.

Table 4.2: List of parameters that were measured during He442 that are used throughout this chapter.

Parameter	**Units**	**Instrument**	Type
POC	mg m^{-3}	Chemical Methods	lab
DOC	mg m^{-3}	Chemical Methods	lab
TSS	mg m^{-3}	Chemical Methods	lab
Chl a	µg m^{-3}	HPLC	lab
C, T, D		SBE19plus	*in situ*
a,c,b	m^{-1}	ACS/Wetlabs	*in situ*
a,c,b	m^{-1}	AC9/Wetlabs	*in situ*
bb (412 - 715nm)	m^{-1}	BB9/Wetlabs	*in situ*
bb, Chl F, CDOM F	m^{-1}	BBFL2/Wetlabs	*in situ*
a_g, a_{gp}, a_p	m^{-1}	PSICAM	lab
a_p	m^{-1}	Shimadzu	*in situ*
E_d, E_u	mW m^{-2} nm^{-1}	Ramses/TRIOS	*in situ*
Rrs	Sr^{-1}	Ramses/TRIOS	*in situ*
L_u	mW m^{-2} nm^{-1} sr^{-1}	Ramses/TRIOS	lab
F_v/F_m (F_q'/F_m')		FastOcean	lab
σ_{PII}	$Å^2$ $PSII^{-1}$	FastOcean	lab
Electron Transport Rate	µmol e^- m^{-2} s^{-1}	FastOcean	lab

4.2 Analysis of Parameters Measured During He442

Physical Parameters

Phytoplankton physiology does not tend to be dominated by a single factor. However, temperature is often highlighted as a primary factor. Photosynthetic organisms are commonly able to photosynthesise efficiently across a range of temperatures around the optimal temperature (T_{opt}) with an upper limit below 40°C. However, exposure to temperatures outside this bracket can result in photodamage, enzyme denaturation, and cell damage (Mackey *et al.*, 2013; Huner *et al.*, 1996; Falk *et al.*, 1996). Algae require an integrated growth environment, defined by Behrenfeld (2008) as the complex of temperature, light availability, and nutrients necessary to growth.

Temperature

Water temperature varies with season and geographical location. More southerly latitudes tend to be hotter as evidenced in Figure 4.2a. The sea temperatures in the UK have a yearly range of approximately 6-20°C (Joyce *et al.*, 2004).

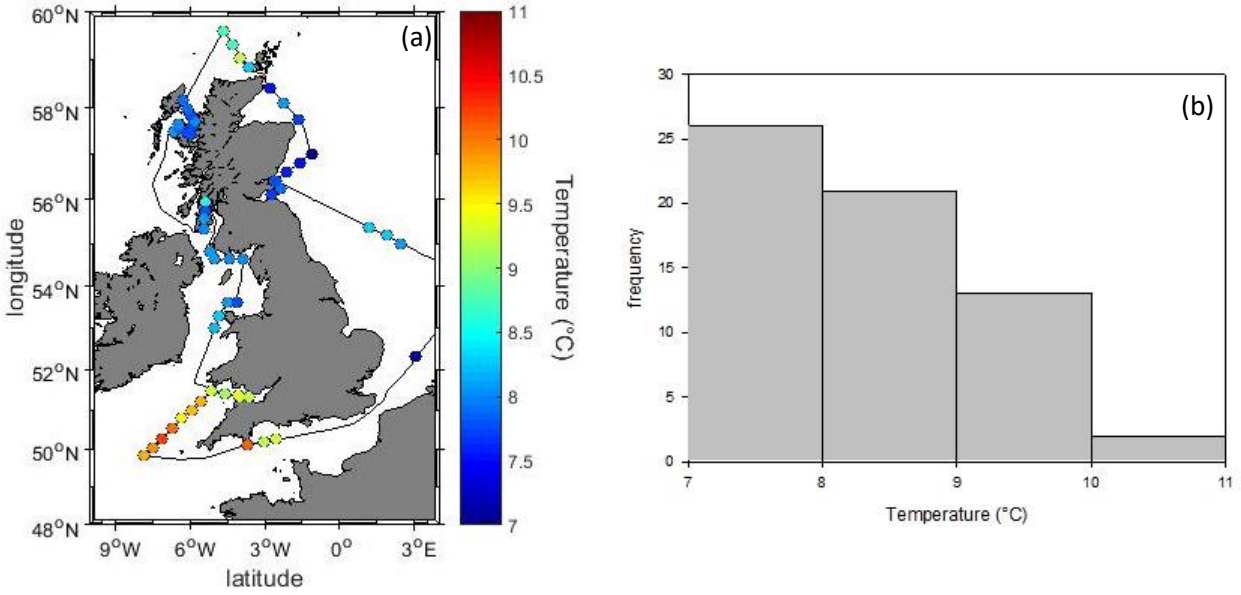

Figure 4.2: (a) The distribution shows the ship sensor temperature measured at each station throughout He442. (b) These distributions are plotted as a histogram.

As the map of the different water temperatures shows, there was only a small range of temperatures experienced during the course of these measurements. The lowest temperature recorded was 7.1 °C with the highest recorded temperature being 10.2 °C. The mean temperature was 8.4 °C with the median at 8.1 °C. The highest water temperatures were measured early in the cruise between stations 2 and 16 taking in the English Channel, Celtic Sea, and Bristol Channel. These higher temperatures may reflect their lower latitudes combined with good weather.

Figure 4.3 shows the impact of changing temperature on P^{B}_{opt}, which is determined from equation 4.1 (Behrenfeld and Falkowski, 1997).

$$P_{opt}^{B} = -3.27x10^{-8}T^{7} + 3.4132x10^{-6}T^{6} - 1.348x10^{-4}T^{5} + 2.462x10^{-3}T^{4} - 0.0205T^{3} + 0.0617T^{2} + 0.2749T + 1.2956 \quad (4.1)$$

Comparing this polynomial relationship with the range of temperatures observed during He442, the temperature may produce a difference in P^B_{opt} of up to 18 % by calculating the difference between the minimum and maximum temperatures measured during He442. This is plotted in Figure 4.3 with the minimum and maximum temperatures plotted as the vertically dashed lines.

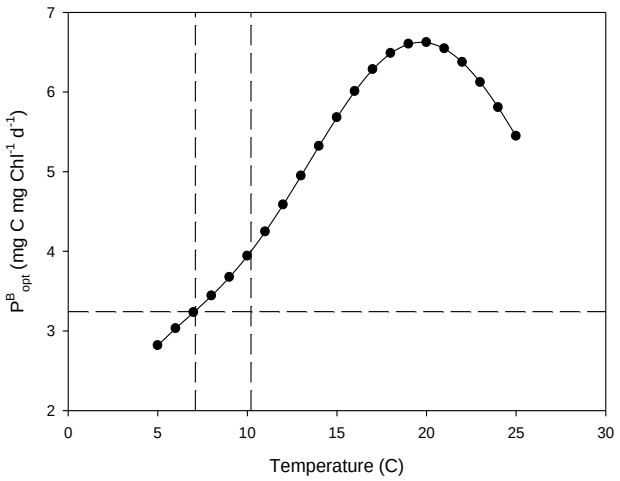

Figure 4.3: The impact of temperature on the chlorophyll specific maximum daily rate of carbon fixation determined using equation 4.1, showing there is a generalised optimal temperature of carbon fixation. The horizontal dashed line shows 50 % of the theoretical maximum P^B_{opt}, where the maximum is taken to be a Summer estimate at 20°C.

Electron Transport Rate and Temperature

Li *et al.,* (1984) concluded that high latitude regions are temperature-sub-optimal for photosynthesis, suggesting that this is likely due to enzyme limitation (e.g. RuBPC or fructose bisphosphate phosphatase) and metabolic repair activity which limits the efficiency of linear electron transport (Jin *et al.,* 2016). This is evidenced by comparison to temperate phytoplankton species at low temperature that produced similar values of P_B^M suggesting that this isn't a genetic adaptation but a low temperature inhibition of enzyme function as shown in Figure 4.4a.

Blanchard *et al.* (1996) mathematically expressed a relationship between P_{max} of motile benthic diatoms and temperature finding a progressive increase in P_{max} to T_{opt} (approximately 25 C) beyond which P_{max} declines rapidly (Figure 4.4b). Claquin *et al.* (1998) builds upon

Blanchard *et al.* (1996) measuring eight species of microalgae and coming to similar conclusions as Blanchard *et al.* (1996).

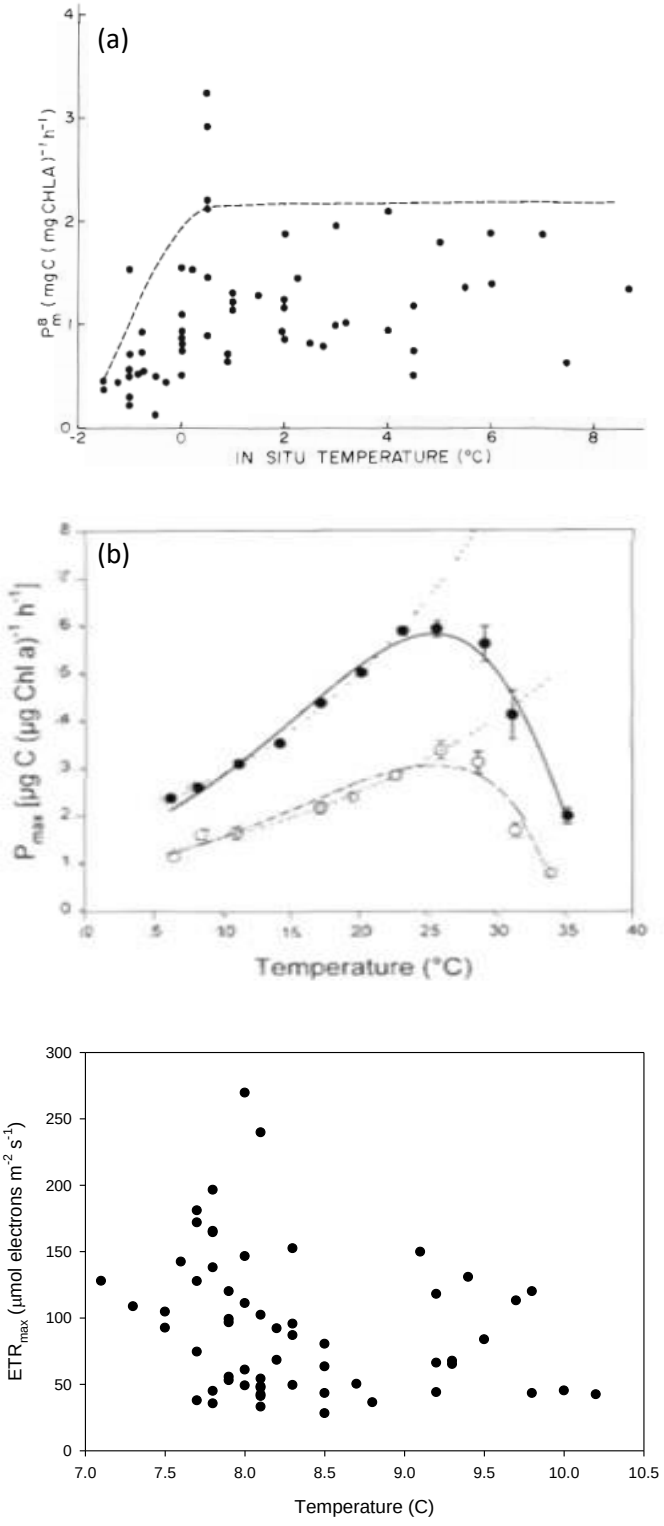

Figure 4.4 (a) Li et al. (1984) showing the small changes in P_{max} with increasing temperature (b) Blanchard et al. (1996) showing increasing P_{max} to an optimal temperature before rapidly declining at two separate times of year. The shaded circles represent experimental data from September 1995 with the open circles being experimental data from December 1995. Fitted curves for each dataset are plotted using Eppley's equation. (c) The electron transport rate measured using the 450 nm excitation LED is contrasted with the temperature at each station taken from ship sensors. The modelled value of ETR_{max} determined by the FastPro8 software was used in each case.

The parameters compared to temperature in Figure 4.4a-c are taken to be broadly equivalent. The exchange factor for converting from electron transport rate to P_{max} used by Li *et al.* (1984) and Blanchard *et al.* (1996) is unknown and so we were unable to convert our ETR data into equivalent units. Figure 4.4c shows the calculated maximum electron transport rate estimate at each station against the recorded ship sensor temperature. It was not possible to draw any particular conclusions from the relationship between temperature and the electron transport rate. Comparing the range of temperatures observed during He442 (~3.5°C) to the range of temperatures in Li *et al.* (1984) and Blanchard *et al.* (1996), ~10°C and 30°C respectively, it is unlikely that we would see any major trends especially given the huge spatiotemporal variability of the stations and the associated algal cells. The variability of the electron transport rate and temperature is very similar to the type of spread that is seen in Li *et al*. (1984).

Salinity

The global average for seawater salinity is 35 PSU with this value ranging between 0 PSU in freshwater to 38 PSU. The salinities measured during He442 range from 31-35 PSU.

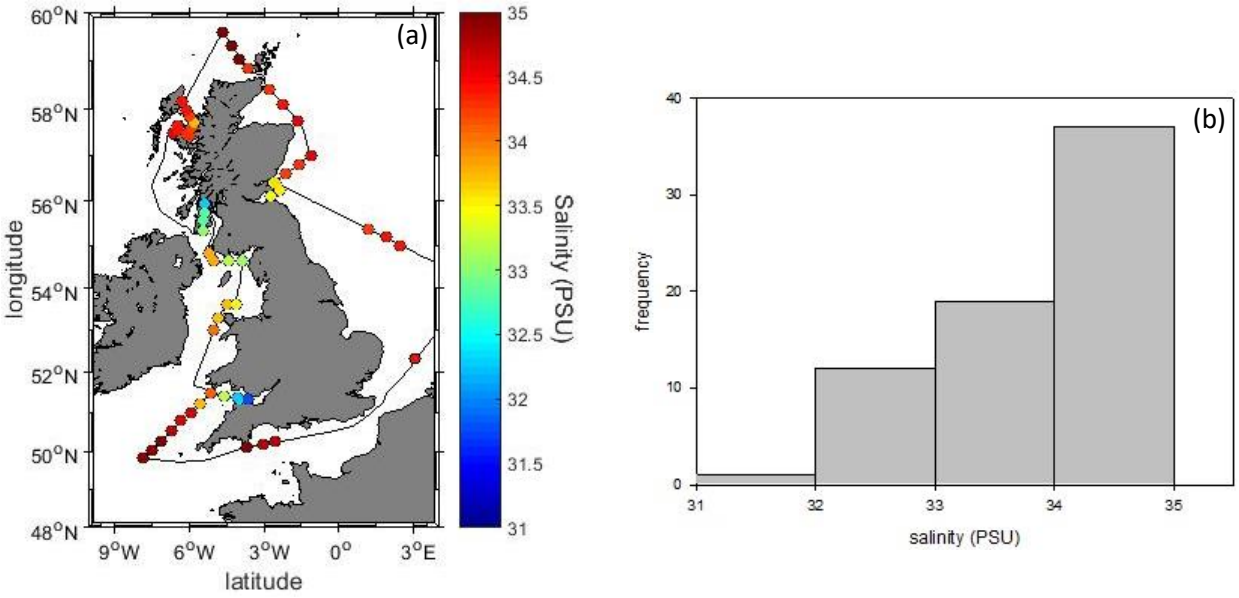

Figure 4.5: (a) Salinity was measured at each station as well as temperature. This data is recorded in the distribution (b) A histogram of these is plotted for salinity.

Much as with the temperature range, the range of salinities measured throughout the cruise were found to fall into a narrow range with the minimum and maximum salinities being 31.8 and 35.0 PSU respectively. The mean and median salinities were 33.8 and 34.2 PSU respectively. From Figure 4.5a, it can be seen that the lower salinities are observed at stations further up the Bristol Channel and Clyde estuary. This reduction in salinity is consistent with the increasing influence of freshwater input to the water system.

Water Column Structure

Seawater density is proportional to the salinity and inversely proportional to the temperature. Changes in the salinity and temperature through the water column can result in the formation of pycnoclines. Stratification of the water column effectively creates a barrier preventing passage of nutrients and particles, e.g. phytoplankton. The degree of stratification determines the surface mixed layer depth which plays a role in determining whether phytoplankton are retained in sunlit surface waters or are regularly cycled into deeper, darker waters with potential implications for photosynthetic rates.

In practice, density is not measured but is calculated from *in situ* measurements of temperature, pressure, and conductivity (salinity). Here, the density anomaly is applied using equation 4.2. The density anomaly is an often used measure of density for simplicity, where the last two digits of the density are shown (Figure 4.7c).

$$\sigma_T = \sigma_{S,T,0} = \rho_{S,T,0} - 1000\,\frac{kg}{m^3} \qquad (4.2)$$

where S,T,0 represent the salinity, temperature, and pressure is a surface equivalent value equal to zero. The subtraction of 1000 kg m^{-3} removes the effect of water pressure.

Figures 4.7a-b show the difference in water column density between the lowest point measured in the water column and the surface water density (equation 4.3).

$$\Delta\sigma_t = \sigma_{bottom} - \sigma_{surface} \qquad (4.3)$$

where $\sigma_{bottom,\ surface}$ are the calculated density values at each position respectively, calculated by Rüdiger Röttgers at HZG.

Figure 4.7b shows that the majority of stations showed very little difference in density with 41 stations having a density difference of less than 0.12 kg m^{-3} between the surface and the bottom of the water column. The remaining stations exhibit a range of $\Delta\sigma_T$ up to a maximum of 2.5 kg m^{-3}, with the greatest value occurring at station 21 in the Irish Sea.

The concept of a mixed layer depth is a well-understood concept but one that is poorly defined with a review of the literature finding at least two separate methods of defining a mixed layer. These are:

- Levitus (1982) defines a mixed layer as any increase in the water column density of greater than 0.125 kg m^{-3}.
- De Boyer Montégut *et al.* (2004) suggests a rather different definition with an increase of only 0.03 kg m^{-3} or reduction in temperature of 0.5 °C to define a mixed layer.

For the purposes of all further discussion of mixed layers, the De Boyer Montégut *et al.*, (2004) method is employed.

Figures 4.6a-b show that mixed layer depths were highly variable depending on the geographical location with water column mixing varying from 3 metres to 95 metres.

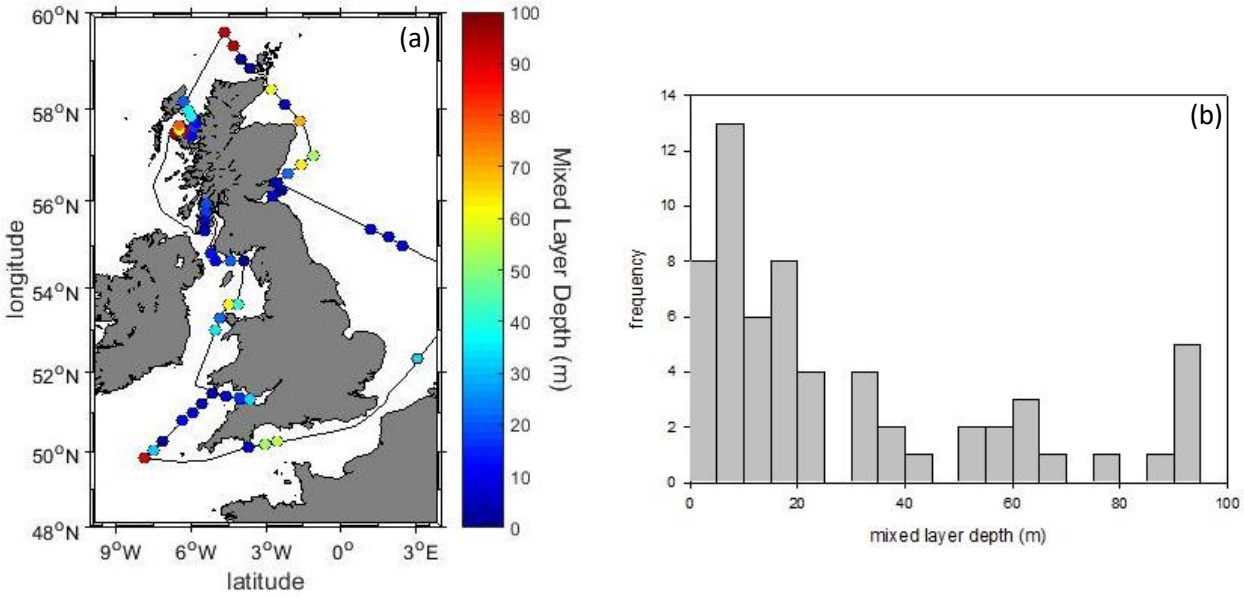

Figure 4.6: (a) De Boyer Montégut et al. (2004) was applied for determining mixed layer depth with mixed layers being described as an increase in density of at least 0.03 kg m^{-3} using the density at a depth of 10 m for reference. This is to account for the strong diurnal cycle in the top few metres of the water column. (b) Histogram of the de Boyer Montégut results is plotted.

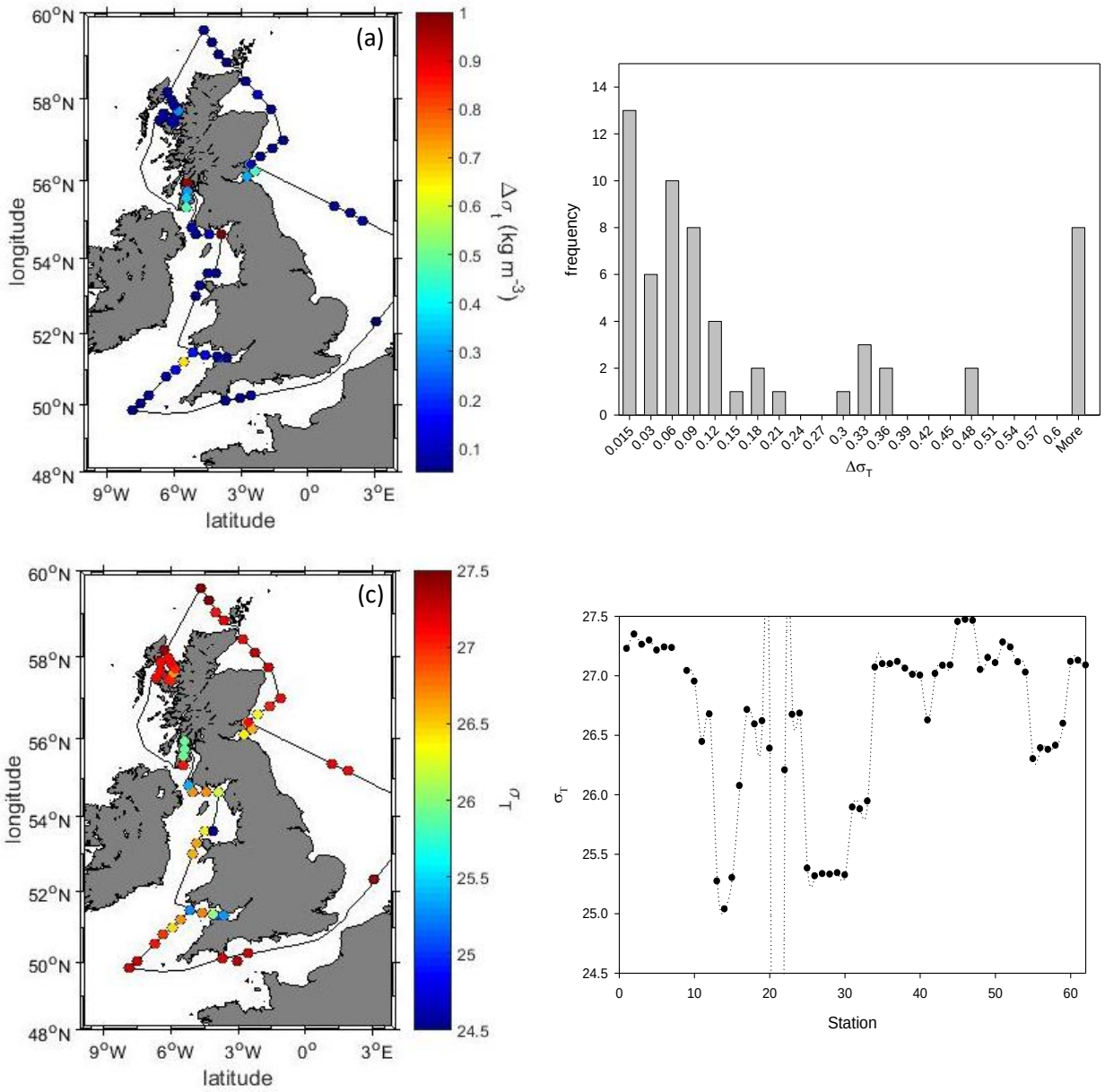

Figure 4.7: (a) The water column density differential ($\Delta\sigma_t$) is plotted across a map of UK coastal waters (b) A histogram of these results are plotted. (c) The density anomaly (equation 4.2) is plotted for each station on He442 (d) The density anomaly for each station is plotted showing the variation in structure through different water masses.

The shallowest mixed layer depth of 3 metres was found at station 21 in the Irish Sea, where the largest density differential was also recorded. These variations could be a result of freshwater input as the station is in the Solway Firth with the rivers Eden and Esk draining into it. The least mixed waters were found at stations 38 and 39, off the coast of the isle of Rona in the inner sound. The inner sound has the deepest section of UK territorial waters. It is therefore difficult to say whether this represents the full water column as in this area, the water column depth is as great as 323 metres and our measurements were limited to a maximum of approximately 100 m depending on the location.

The Bristol Channel provides a useful example of the effect of tidal range on the mixed layer depth. Stations 14, 15, and 16 are situated within the Bristol Channel and have mixed layer depths of 33, 26 and 46 metres respectively, which represent a significant portion of the water column depth which varies between 9 metres to 73 metres.

Surface Irradiance

The surface irradiance is a function of the solar zenith angle, time of year, and overhead environmental conditions, particularly the extent of cloud cover. The surface irradiance can change very rapidly influencing the algal dynamics of *in situ* cells (see chapter 5, Figure 5.1).

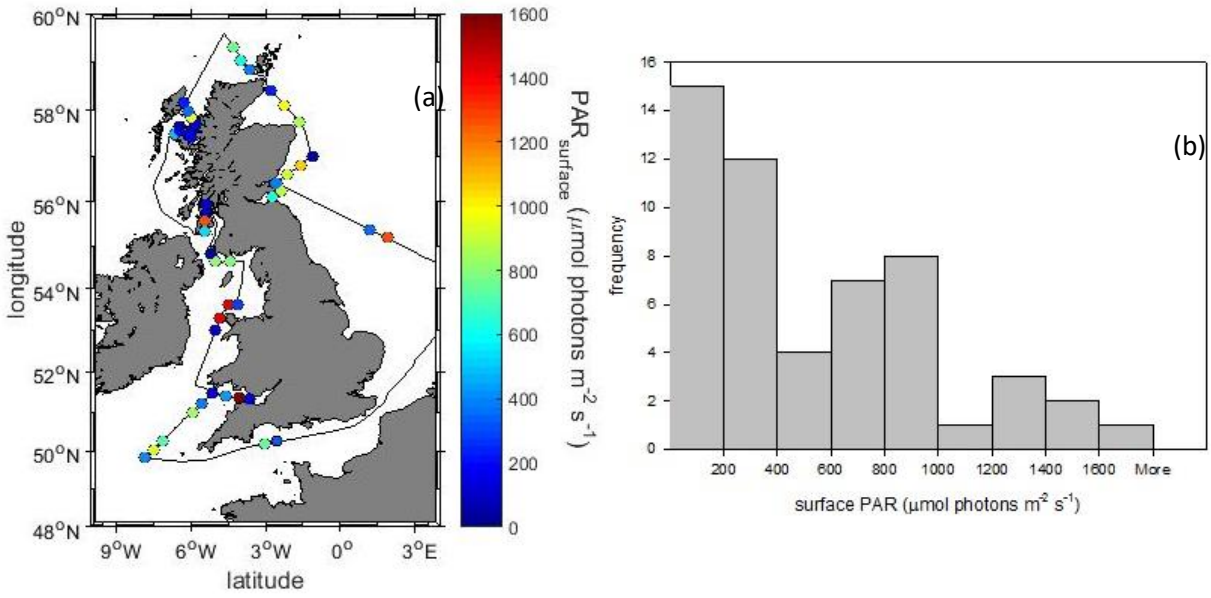

Figure 4.8: Surface PAR was measured using the Trios Ramses irradiance sensors with measurements being made generally twenty to thirty minutes following deployment of the CTD rosette.

The average surface PAR recorded was 585 µmol photons m^{-2} s^{-1} with the median at 399 µmol photons m^{-2} s^{-1}.

Euphotic Depth

The euphotic depth (z_{eu}) is a measure of how deep into the water column the incoming solar irradiance penetrates. It is assumed that 1 % of the surface PAR is the minimum amount of light required to support photosynthesis (Kirk, 1994). The euphotic depth varies with the local environmental and water conditions.

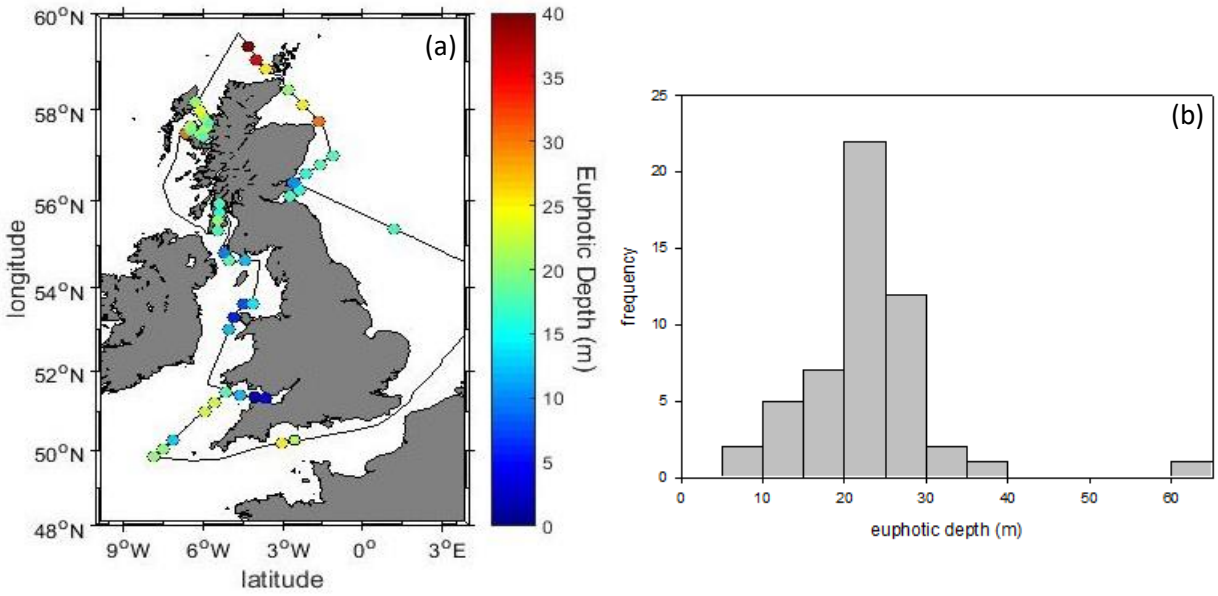

Figure 4.9: The euphotic depth was taken as the depth at which the irradiance is 1 % of its surface value.

During the course of He442, the euphotic depth varied from 2 metres to 55 metres depending upon the location of the station with mean and median values of 18.4 and 18 metres respectively. Below this point, there is very little light available for photosynthesis and so, there would be an expected decrease in the productivity of those waters. To maximise the potential for photosynthesis, the best scenario would be a euphotic zone depth that is deeper than the mixed layer depth as phytoplankton would be fully irradiated assuming there was sufficient mixing of the water column.

Figure 4.10 compares the euphotic depth with the mixed layer depth for all stations. The dashed line is the 1:1 relationship between euphotic depth and mixed layer depth that would need to be satisfied to fully irradiate the water column. The majority of stations measured during He442 were not fully irradiated meaning that for at least part of the day, the phytoplankton in those water columns would have been experiencing less solar irradiance than is assumed to be required to drive photosynthesis.

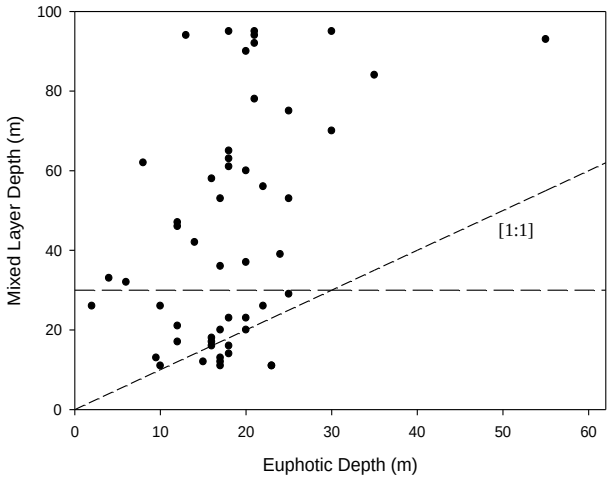

Figure 4.10: Comparison of the euphotic depth and the mixed layer depth for all stations. The dashed line represents the 1:1 relationship between euphotic and mixed layer depth. Values below the dashed line are full irradiated within the mixed layer, all those above are not fully irradiated. The horizontal dashed line represents the mixed layer depth cut-off used in partitioning the data.

The simple grouping in Figure 4.10 of water columns that were approximately fully illuminated and those that were not was used to split the dataset into stations with mixed layer depths of less than 30 m and those with mixed layers of greater than 30m with their corresponding photochemical efficiency. There was not found to be a distinct difference between the two groupings. Water columns with a mixed layer depth of less than 30 m had an average photochemical efficiency of 0.31 with a maximum of 0.45; water columns with a mixed layer depth of greater than 30 m had an average F_q'/F_m' of 0.29 and a maximum value of 0.42.

Biogeochemical Parameters

Verification of HPLC Chlorophyll Concentration Efficacy

Analysis of the He442 dataset raised concerns about the quality of the chlorophyll concentration data produced by colleagues at HZG by HPLC using a monomeric C_8 column and pyridine-containing mobile phase. Quality control was performed by using the HZG HPLC chlorophyll values to derive parameters such as $a^*_{ph}(676)$ amongst others for which there are established distributions in the literature.

Figures 4.11a-d show the relationship between the algal absorption at 450 nm and 676 nm ($a_{ph}(450)$ and $a_{ph}(676)$) and two measures of biomass: the HPLC-measured chlorophyll concentration and the initial fluorescence value from the FRRf. The algal absorption at both wavelengths has a poor relationship with the chlorophyll concentration in comparison to F_o which produces a useful, positive linear relationship with algal absorption at both wavelengths with only a single outlier.

The chlorophyll-specific algal absorption varies on a phytoplankton assemblage level with both the pigment composition and packaging effect having an impact. Bricaud *et al.*, (1995) describes the pigment packaging effect as being a function of the cell size and absorption coefficient of the 'cellular matter'. Bricaud *et al.* observed an empirical covariation between $a^*_{ph}(\lambda)$ and [*Chl*] that was derived by least squares fitting to a power function (equation 4.4).

$$a^*_{ph} = A(\lambda) \times \langle Chl \rangle^{-B(\lambda)} \qquad (4.4)$$

where A and B are positive and wavelength-dependent.

Given the discrepancies observed in Figure 4.11., the relationship between $a_{ph}{}^*{}_{Chl}(450, 676)$ and the HPLC chlorophyll concentration was compared to the relationship between $a_{ph}{}^*{}_{Fo}(450, 676)$ and F_o in Figure 4.12a-d. Using equation 4.4 and the wavelength-dependent constants obtained from Bricaud *et al.*. (1995), it is possible to test the quality of the chlorophyll data by comparing the distribution of field data against the Bricaud *et al*. (1995) predicted values of $a_{ph}{}^*{}_{Chl}(\lambda)$.Figures 4.12a,c show a very poor fit of the chlorophyll-specific algal absorption data for the Bricaud best fit line. Scaled FRRf-derived *Fo* values were used in place of the chlorophyll concentration in Figure 4.10b,d and have a significantly better fit than the HPLC chlorophyll derived data.

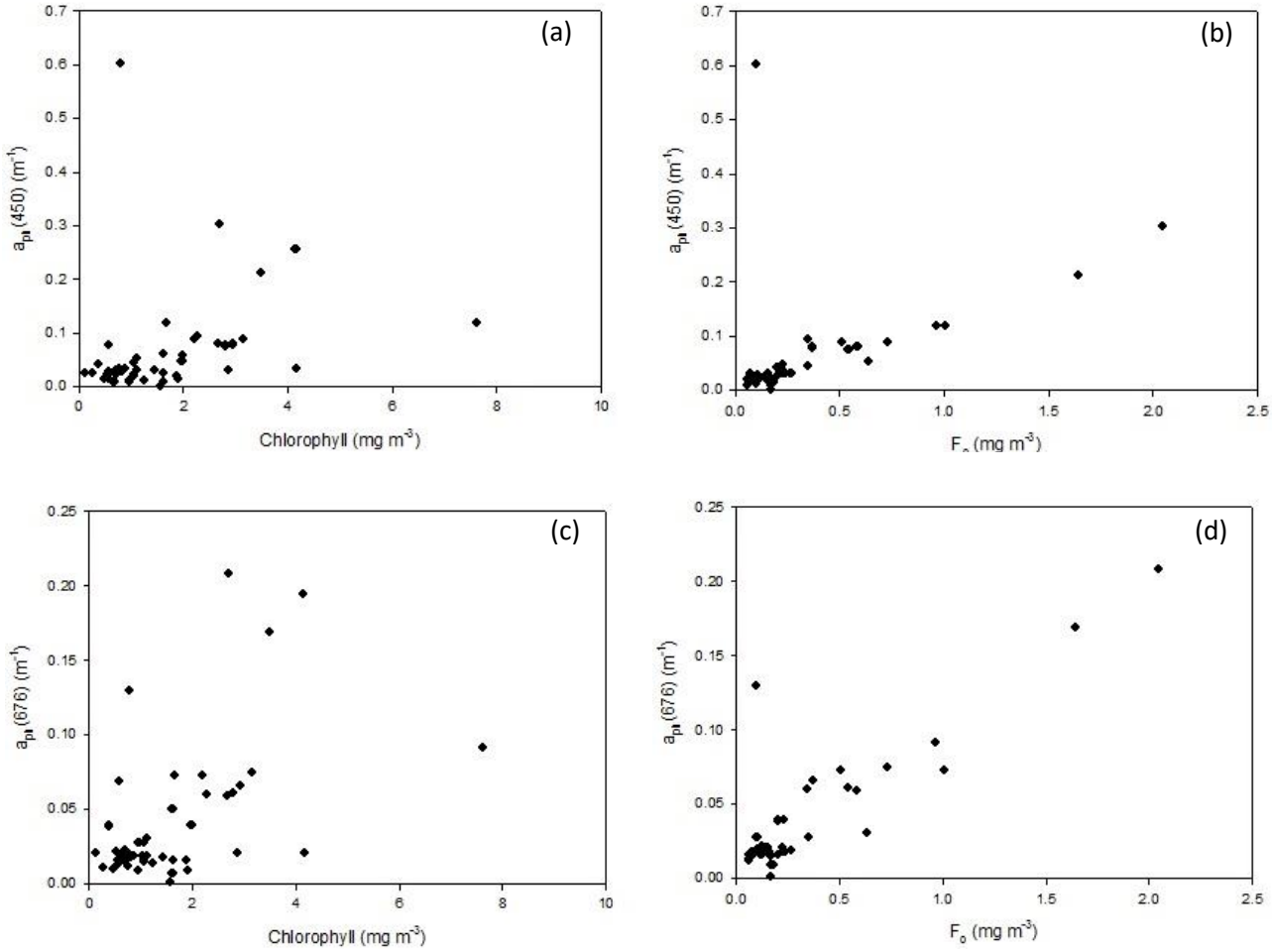

Figure 4.11: (a) Comparison of algal absorption data at 450 nm against HPLC-derived chlorophyll concentration (b) Comparison of FRRf-derived chlorophyll proxy against $a_{ph}(450)$ showing a significantly improved relationship between these two parameters(c) The relationship between HPLC chlorophyll and the algal absorption at 676 nm is shown (d) The FRRf-based chlorophyll concentration shows a good linear relationship with $a_{ph}(676)$. Unlike the HPLC-Chl concentrations, F_o produced a linear relationship at 450 and 676 nm suggesting these data were less noisy and more representative of the biomass present in each of the water samples.

The application of a scaling factor was required to fit the F_o-derived data to the Bricaud expression. This was done by multiplying F_o by 5.5 to give an approximated chlorophyll concentration (henceforth referred to as Chl_F and will be applied to all further analyses requiring a chlorophyll concentration) and the wavelength-dependent algal absorption was normalised to the scaling factor producing Figures 4.12b,d. The HPLC-derived chlorophyll concentration data produced chlorophyll-specific absorption values that were inconsistent with the well-established Bricaud *et al.* (1995) relationships. In comparison, the scaled F_o (Chl_F) values for chlorophyll-specific absorption followed the established relationships well.

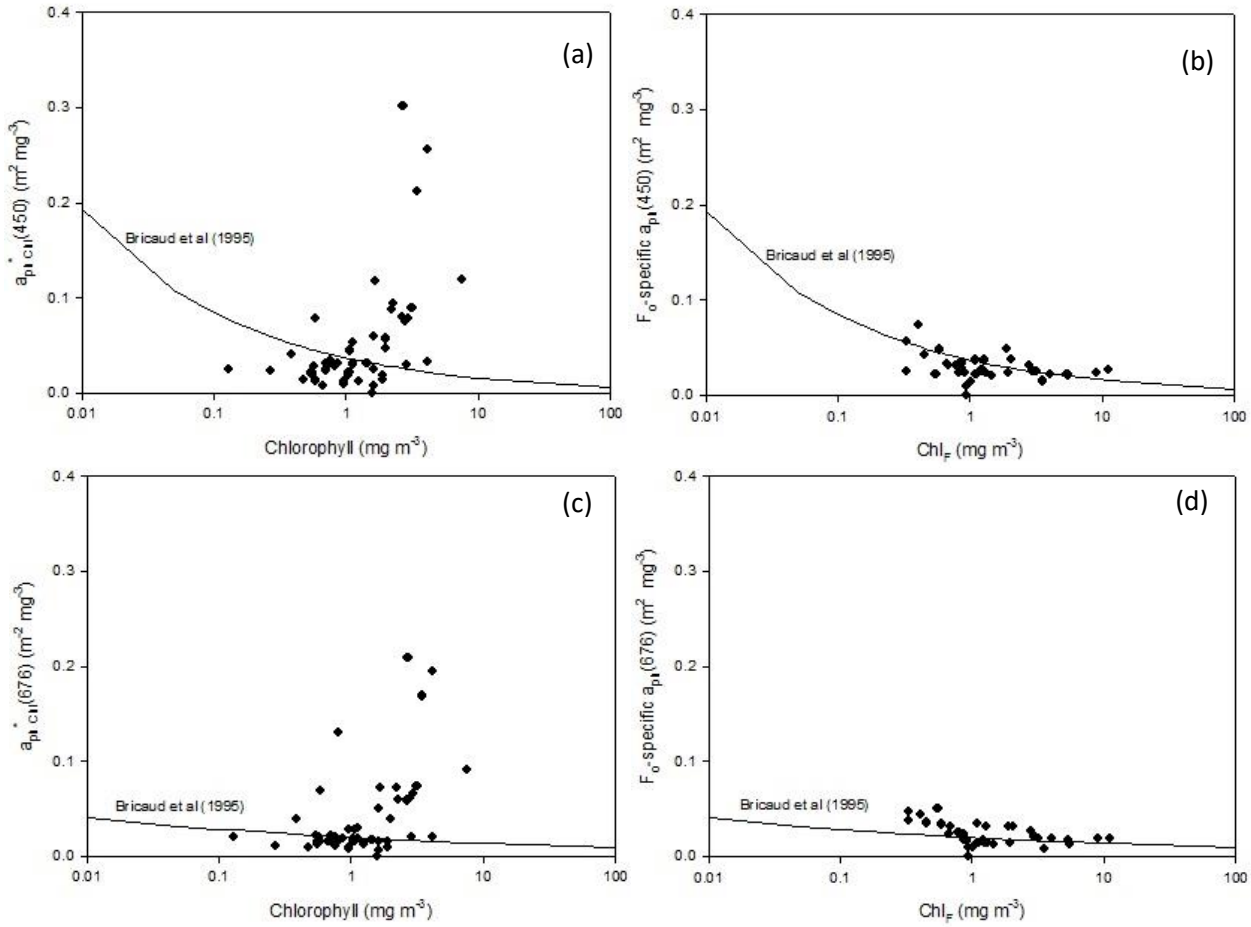

Therefore, the HPLC chlorophyll concentration data were discarded and all further measurements employ the use of Chl_F.

Chlorophyll Concentration

Chlorophyll is the basic molecule of photosynthesis and is used as a proxy for water biomass particularly in remote sensing applications. Chlorophyll concentrations can be estimated by spectrophotometric determination of the absorption or by relative fluorescence emissions. As per the previous chlorophyll validation study, relative fluorescence estimates based on a scaled measure of F_o are employed.

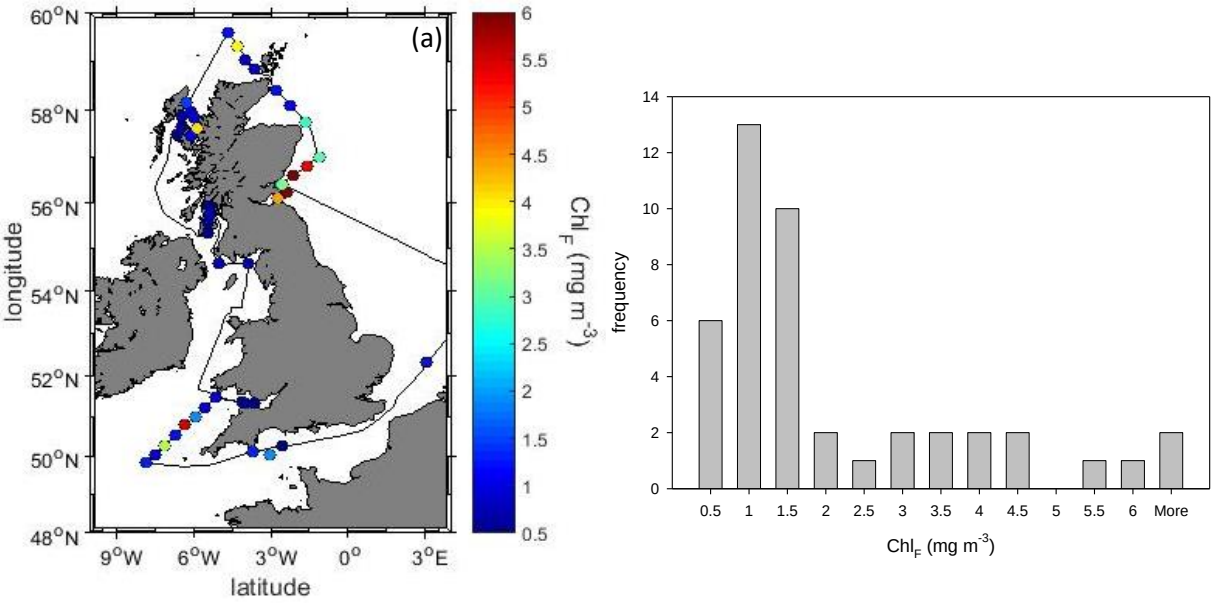

The concentrations measured were highly variable across the different waterbodies with a range of 0.2 to 11.3 mg m^{-3} and the calculated mean and median values being 2.03 and 1.2 mg m^{-3} respectively. Geographically, the majority of high Chl_F values occur in the Forth and Tay estuaries (stations 51-55) on the east coast of Scotland. Elsewhere, Chl_F tends to be less than 1.5 mg m^{-3} suggesting a degree of spatial heterogeneity that is associated with the complex dynamics associated with coastal systems. The electron transport rates at stations 51-55 are on the high end of the spectrum for values measured during He442 (see *FLC-derived Indicators of Physiological Status* later in this chapter). In this particular scenario, the high biomass is found in conjunction with high productivity which may suggest that there may have been a bloom in this area or one is in the process of forming.

CDOM Absorption

Coloured dissolved organic matter is the component of organic decomposition that can be measured optically. CDOM gives water a yellowish hue darkening to a brown colour with increasing concentration. CDOM primarily absorbs light in the blue/ultraviolet region of the electromagnetic spectrum and can compete with chlorophyll for absorption of incoming irradiance, potentially reducing the productivity of the phytoplankton present (Abdelrhman, 2016).

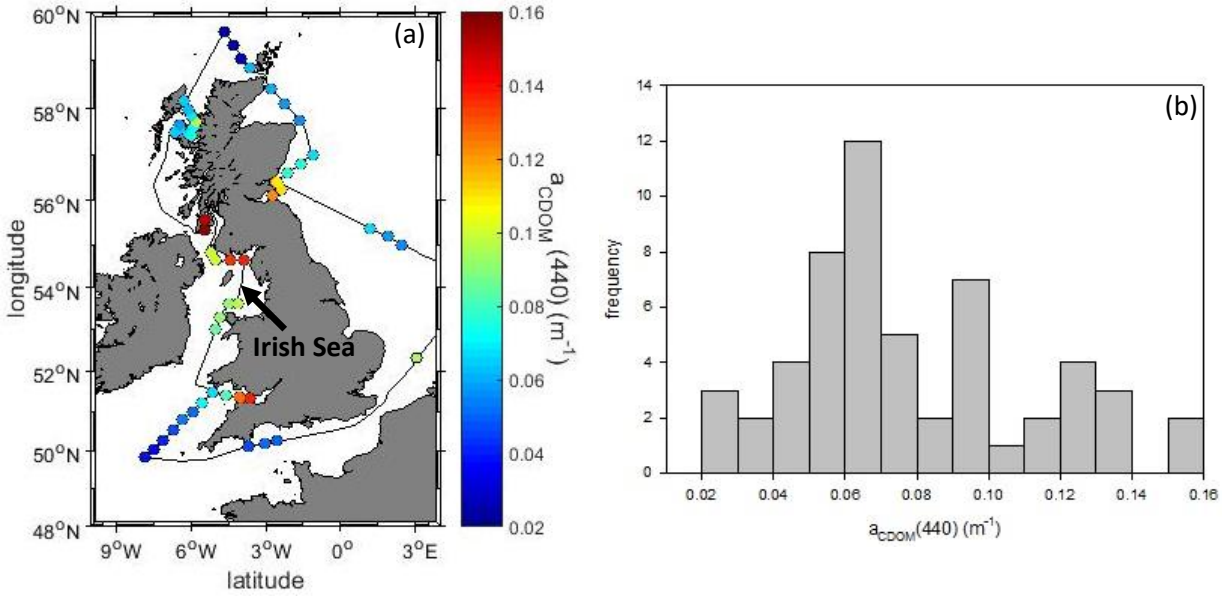

The CDOM absorption coefficient, like the chlorophyll concentration, was variable around the UK coast with regions closer to shore having greater CDOM absorption. This is likely due to the freshwater influence reducing the salinity of the water. This is particularly obvious in the Bristol Channel, Irish Sea and Tay Estuary.

Curiously, the largest CDOM absorption coefficient was not found in the Bristol Channel but rather in the Irish Sea where the maximum value of 0.157 m^{-1} was found. The minimum coefficient of 0.025 m^{-1} was found at station 45, the most northerly station on Figure 4.14a, which is on the North Atlantic shelf edge.

Relationship between CDOM Absorption and Salinity

There is a consistent negative correlation between the absorption coefficient of CDOM at 440 nm ($a_{CDOM}(440)$) and the salinity of the water as shown in Figure 4.15, which has been adapted from Bengil *et al.*, (2016). This negative correlation can be explained by the observation of fresh, high CDOM waters being diluted by mixing with more saline, CDOM poor waters further offshore. The NOMAD global dataset is plotted with the He442 data in Figure 4.15. The $a_{CDOM}(440)$ and salinity data measured on He442 is also negatively correlated with relative increases in CDOM associated with reduction in the salinity, even over small salinity ranges (~2 PSU). The He442 data does not fit the NOMAD relationship very well.

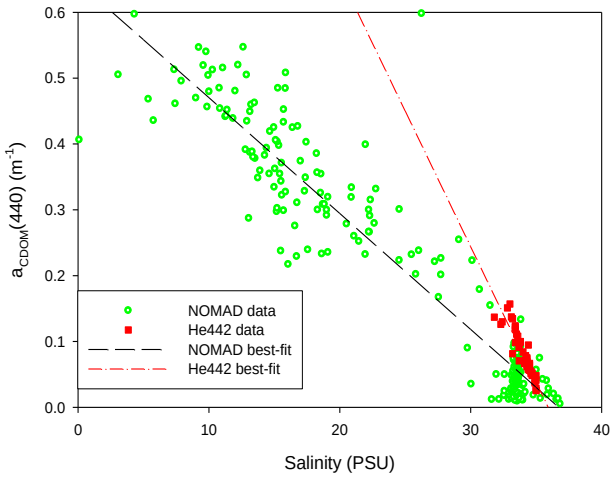

Figure 4.15: The relationship between $a_{CDOM}(440)$ and salinity is shown for the NOMAD global dataset and the corresponding data measured during He442. Lines of best fit are shown for the NOMAD dataset from Bengil et al., (2016) and He442. The data from He442 is within the range of NOMAD, but produces a very different line of best fit.

The best fit for the He442 data was expressed through the relationship in equation 4.5.

$$y = -0.0412x + 1.48 \quad (4.5)$$

This varied from the best fit expression for the NOMAD global dataset, Bengil *et al.* (2016) in equations 4.6.

$$y = -0.0176x + 0.6462 \quad (4.6)$$

At high salinity values, there may be CDOM production associated with phytoplankton (e.g. Case I). The He442 results are broadly consistent with the NOMAD data at equivalent salinities although the simple relationships constructed between CDOM and salinity are likely breaking down at the Case I interface, as can be seen in Figure 4.15.

Organic Carbon Components

The total organic carbon (TOC) present is the sum of the particulate and dissolved organic components (POC and DOC). POC is deemed to be the component that is unable to pass through a 0.22 μm filter with DOC being the component that does pass through the filter. Dissolved organic carbon is formed by the breakdown of organic products into their molecular constituents, for example, DOC encompasses chlorophyll pigments, fat molecules, carbohydrates, and proteins. As they degrade, they begin to form humic substances (Wetzel, 1975; Ogura, 1975).

Generally, POC is associated with allochthonous and autochthonous inputs, e.g. higher plant debris, detritus of terrestrial origin, or biological organisms (Heikkinen, 1994). Heikkinen (1994) suggests that POC concentrations increase with increasing discharge from rivers, indeed this can be seen in Figure 4.16a where there is an increase in POC in the Bristol Channel. However, elsewhere, the POC concentration tends to be an order of magnitude lower.

Maps of the particulate organic carbon (POC) and dissolved organic carbon (DOC) are shown in Figure 4.16a-d. These contribute to the total organic carbon that one is likely to find in the water and when considered together are commonly referred to as detritus, providing a major source of nutrients for the microbial food web (O'Reilly and Dow, 2006).

The dissolved organic content of the water tends to be greater than the particulate organic carbon content. Figure 4.17a shows that the variability in these two parameters can be quite significant with station 15 in the Bristol Channel giving the largest POC:DOC ratio of 0.81. Station 15 has a significantly higher proportion of POC than DOC, a fact that isn't repeated at any other stations during He442. The minimum ratio found in the course of this study was 0.02 at station 43 situated in the middle of the Minch between mainland Scotland and the isle of Harris. This particularly low ratio is a consequence of the POC content of the water being particularly low in this area.

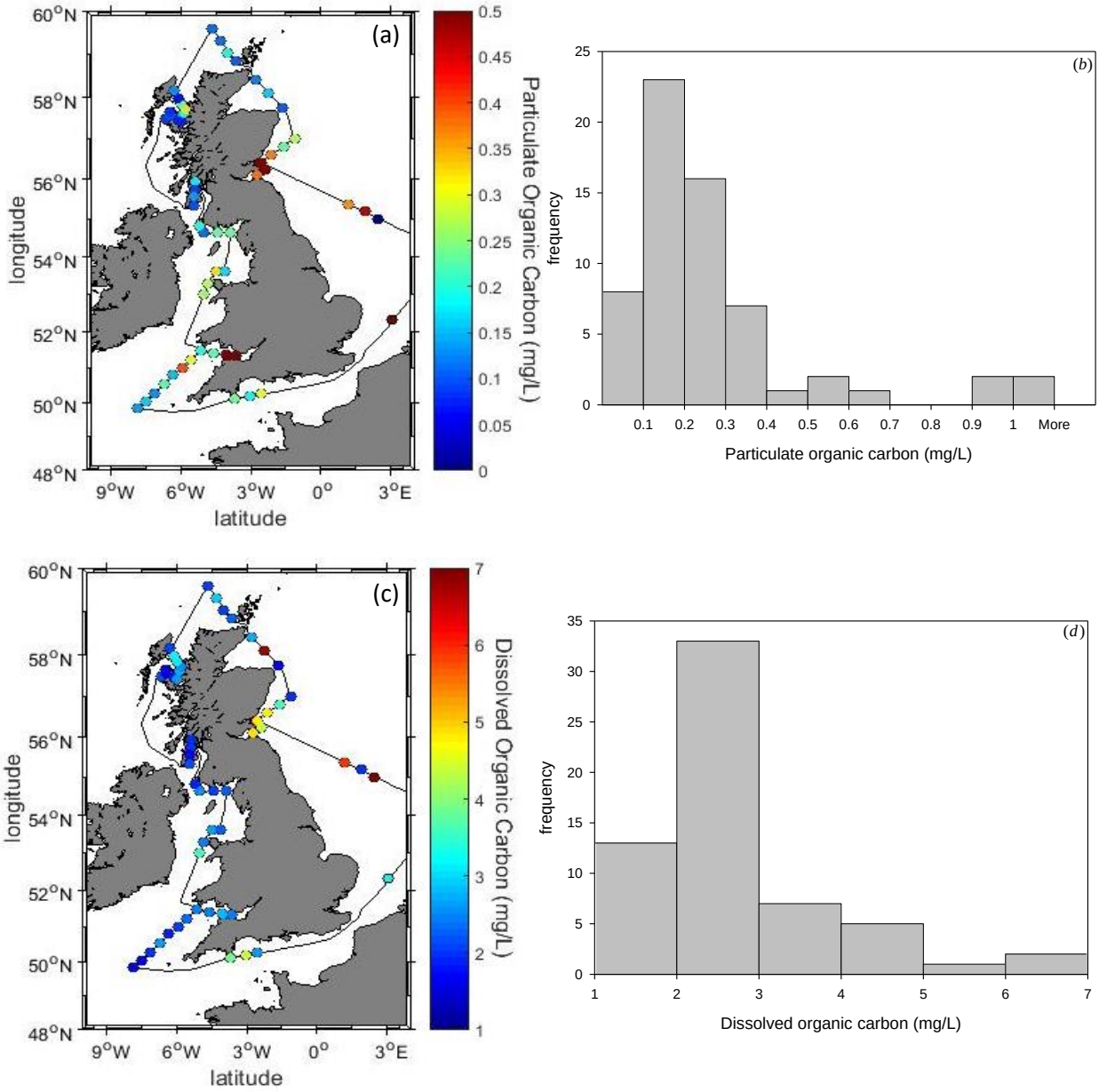

Figure 4.16: (a) Particular organic carbon concentrations (mg/L) at each station on He442 (b) Histogram of POC distributions during He442 (c) Geographical distributions of dissolved organic carbon (mg/L). (d) Histogram distribution for DOC during He442. Both parameters were measured by colleagues working at HZG in Germany.

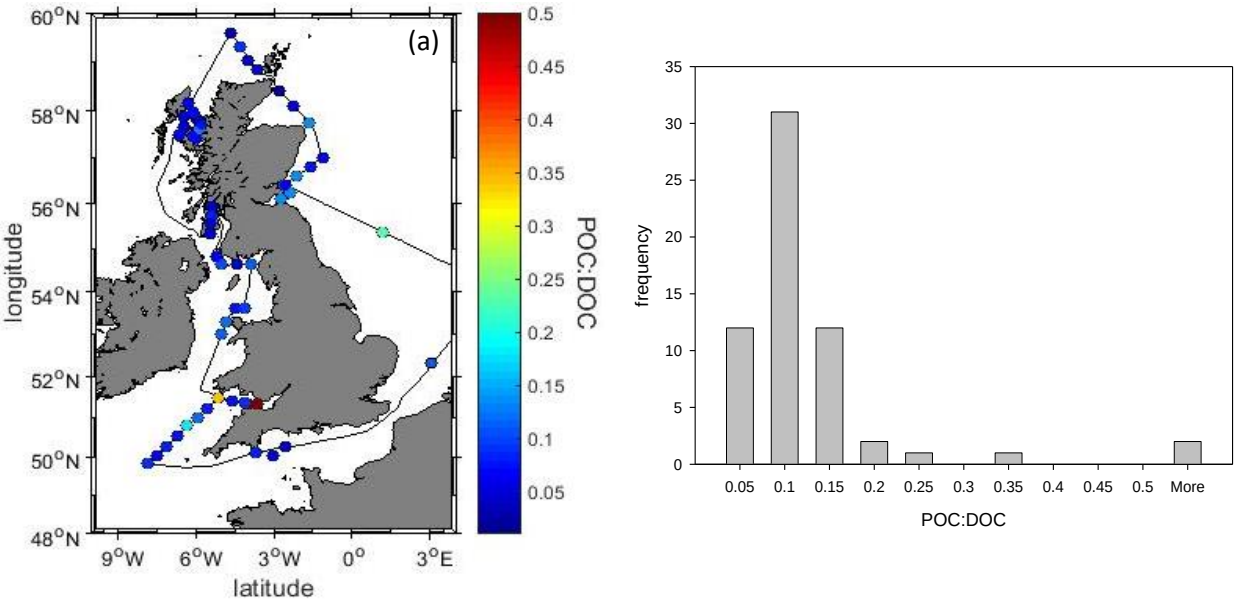

Figure 4.17: (a) The ratio of POC:DOC is shown around UK coastal waters during He442, showing that the ratio between POC and DOC was generally very low except in the highly turbid Bristol Channel (b) The histogram of this distribution is shown.

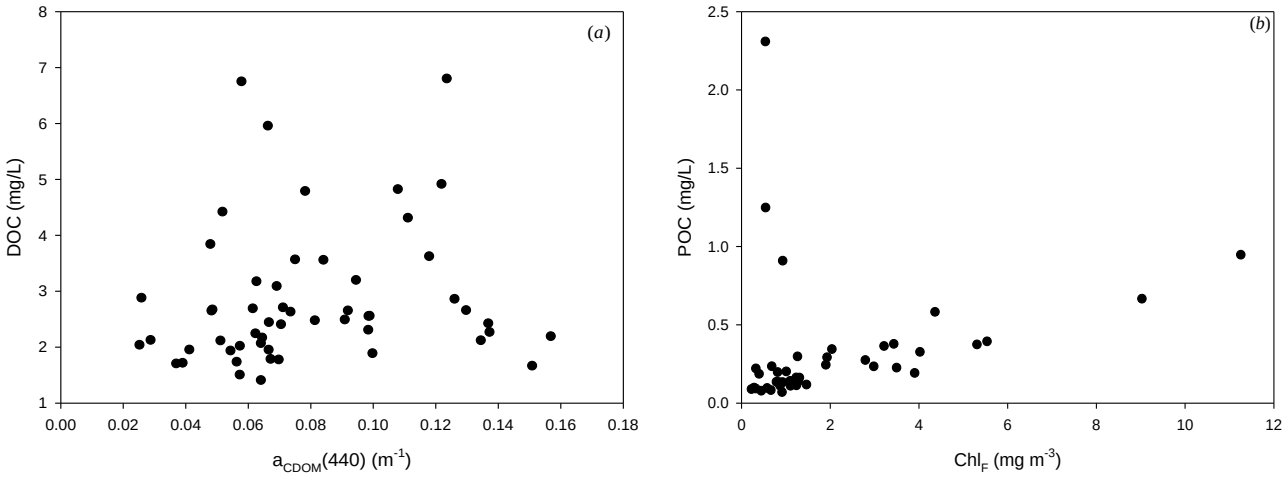

Figure 4.18: (a) The CDOM absorption coefficient at 440 nm was compared to the measured DOC content with no observable relationship found. Estuarine mixing or photodegradation may be responsible for this variability (b) POC and Chl_F were compared for POCs usefulness as a measure of biomass, the three large POC-value stations are from stations 13, 14, and 15 in the Bristol Channel. Figure 4.18b shows a linear correlation between POC and Chl_F

The dissolved and particular organic carbon data were compared to the CDOM absorption (440) and chlorophyll proxy data collected during He442 and shown in Figures 4.18a-b.

Figure 4.18a shows the lack of relationship between the CDOM absorption at 440 nm and the dissolved organic carbon content in the water as determined experimentally by HZG. It is well documented in the literature that there is considerable variability in the fraction of DOC that is coloured (Molot and Dillon, 1997; Benner *et al.*, 1992; Williamson *et al.*, 1999). This is confirmed by Figure 4.18a where even with a relatively restricted geographical range, there is no significant relationship between DOC and CDOM. Reasons for the variability in the relationship between CDOM and DOC include estuarine mixing and photodegradation of coloured molecules, however, it is not possible to determine from this dataset what was driving the variability observed during the UK coastal waters cruise.

Figure 4.18b shows the relationship between the particulate organic carbon and the FRRf-determined chlorophyll concentration (Chl_F). There is a positive linear relationship between these two parameters suggesting that the particulate organic carbon concentration is a useful measure of the *in situ* biomass in all but the most optically complex locations, however, it is difficult to measure POC compared to making easy and rapid FRRf measurements.

Suspended Solid Content

Suspended solids are materials that do not dissolve but rather remain in a particulate form in the water. The presence of suspended solids is often used as an indicator of water quality due to the ease with which measurements can be made (Bilotta and Brazier, 2008; Ferrier *et al.*, 2001). The total suspended matter is composed of two sub-categories: inorganic suspended matter (ISM) and organic suspended matter (OSM). Inorganic suspended matter is generally made up of materials that are not of biological origin such as sands, silt, and clay but siliceous diatom frustules can also contribute to ISM, whereas OSM comes from phytoplankton, phytoplankton breakdown products, and bacteria, as well as matter relating to higher biological species and plant matter.

As can be seen from Figure 4.19a, the total suspended matter (TSS) varies most strongly on the west coast from the Bristol Channel into the Irish and Celtic Seas, whereas all of the other waters sampled showed TSS concentrations about an order of magnitude lower. In Figure 4.19c,d, the ratio of ISM:OSM has been taken to show the relative contributions of each

factor at each station. From the data, the relative contribution of inorganic suspended matter tends to dominate over the organic suspended matter. This may be a result of the fact that measurements tended to be made around coastal waters which are shallower, as well as terrestrial runoff combined with tidal mixing causing increased levels of sediment to be moved around the water column.

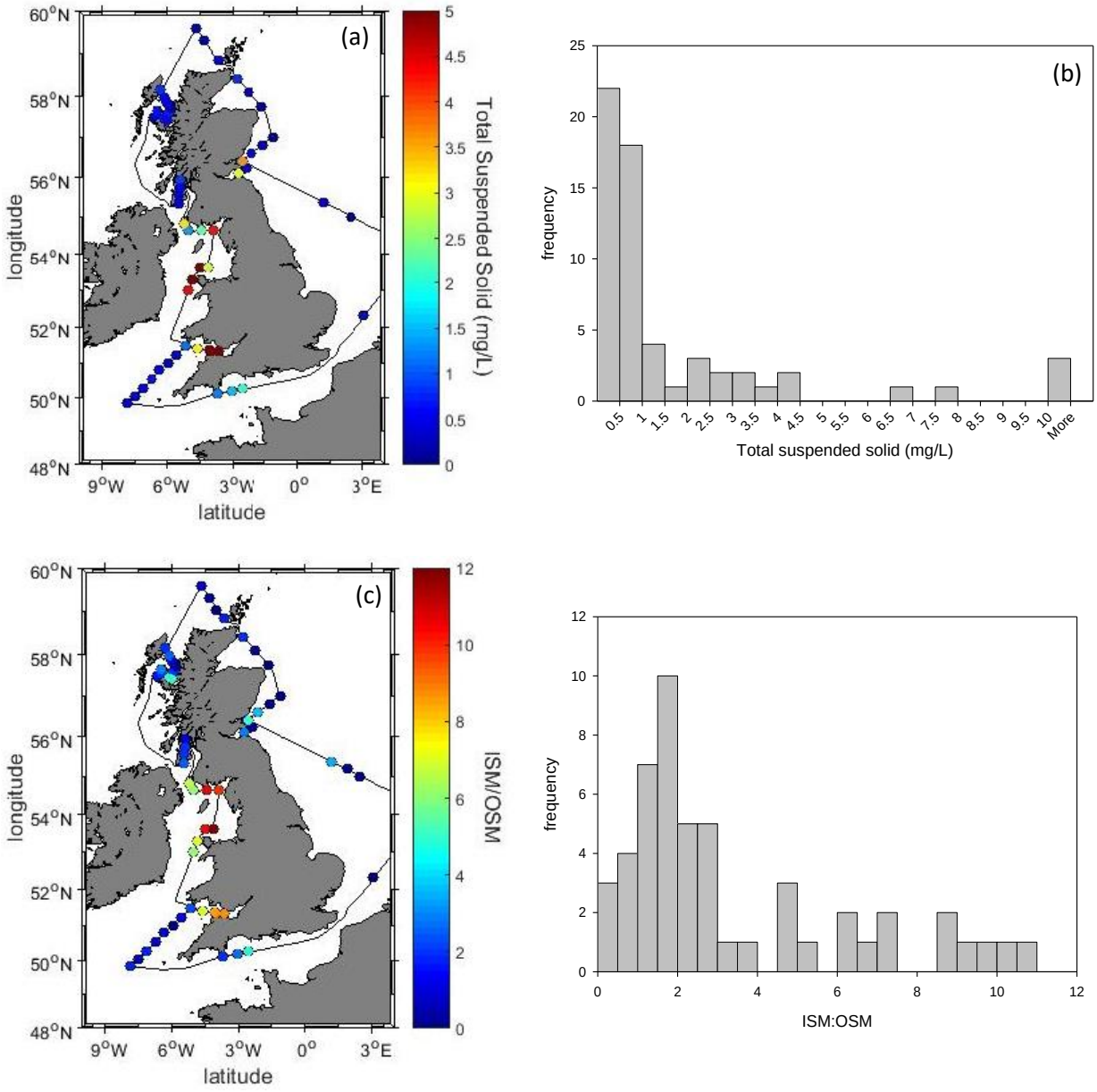

Figure 4.19: (a) Spatial distribution of TSS in UK coastal waters, the highest values (mg/L) are found in the Bristol Channel and Irish Sea, where the concentration of sediment is known to be very high due to the large tidal range and relatively shallow waters (b) Histogram of TSS distributions with the majority of TSS concentrations being less than 1 mg/L, which represent further offshore stations, compared to values greater than 4 mg/L which are closer to the shore such as the Bristol Channel. (c) The ratio of ISM:OSM is shown spatially around the UK coast with the Bristol Channel and Irish Sea containing significant concentrations of inorganic suspended solid (d) The ratio of ISM:OSM is plotted on a histogram showing the variability of this parameter around the UK.

Inherent Optical Properties of Waters

The inherent optical properties (IOPs) define the way in which light interacts with the water and other particles present, i.e. through absorption or scattering. These IOPs are properties of the medium itself, i.e. water and are not affected by the ambient conditions (Mobley, 1994).

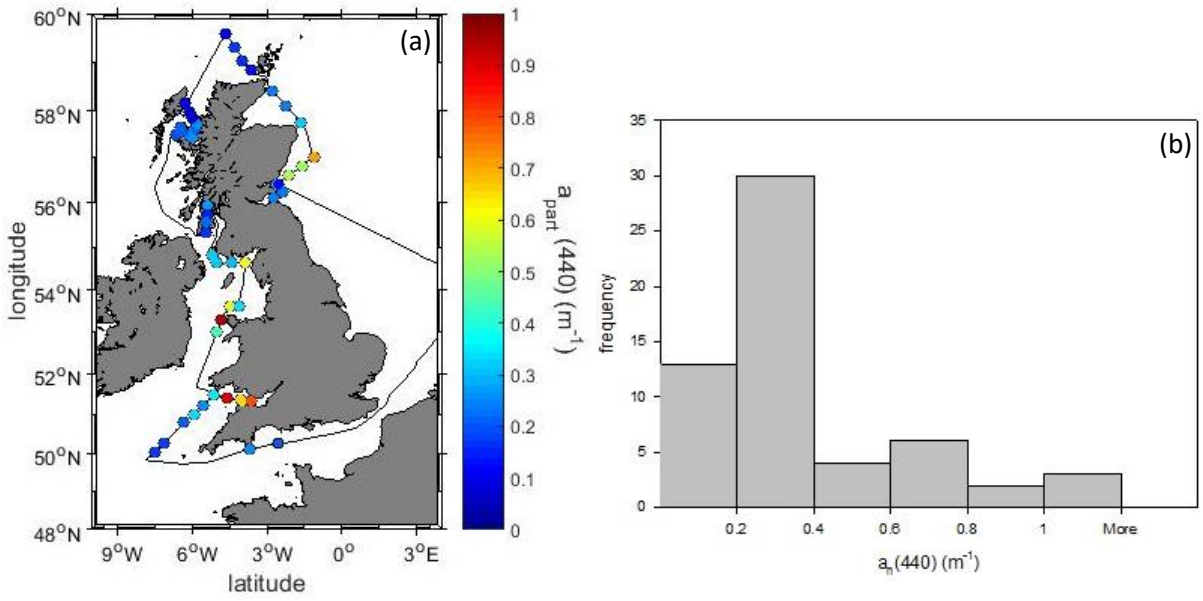

Figure 4.20: (a)Absorption was measured using an AC9, the absorption coefficient at 440 nm was then plotted on the map showing the spatial distribution of $a_{part}(440)$ around the UK coast (b) The histogram of these values are shown

The absorption at 440 nm, measured using the AC-9 is found to vary by over an order of magnitude through the different waterbodies. Excluding the Bristol Channel, the minimum and maximum absorption coefficients measured were 0.07 to 0.95 m^{-1}. However, when the Bristol Channel is taken into consideration, the maximum absorption coefficient was 5.19 m^{-1}, two orders of magnitude larger than the minimum value. These high values in the Bristol Channel are strongly associated with the inorganic suspended sediment found in this area (Figures 4.19a,c)

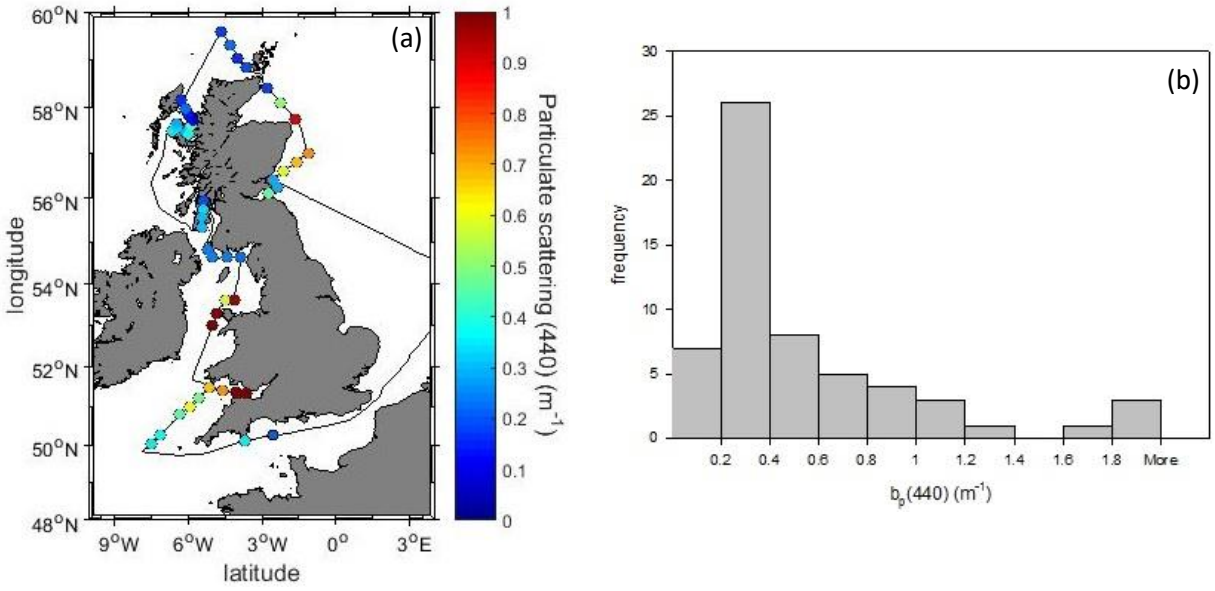

Figure 4.21: (a) Particulate scattering is taken as the difference between the attenuation and the absorption (b=c-a) which is determined by the AC9, the distribution of particulate scattering is shown for the UK (b) A histogram of this distribution is plotted showing that the majority of stations showed scattering of less than 1 m^{-1}.

The turbidity in the Bristol Channel is driven by the tidal mixing associated with the area having the second highest tidal range on the planet. This combined with the shallow waters form an environment with very high absorption and scattering coefficients.

The scattering coefficient was derived by subtraction of the measured absorption from the measured attenuation. This showed a variation of up to two orders of magnitude in the coefficient with the largest coefficients found in the Bristol Channel. The increased presence of particulate matter due to tidal mixing, which keeps a significant proportion of sediment in suspension, results in a very large scattering signal.

Excluding the Bristol Channel, the scattering coefficient at 440 nm varies from 0.10 m^{-1} at station 45 on the North Atlantic shelf edge to 1.63 m^{-1} at station 17 in the Irish sea whereas the maximum value of b_{440} in the Bristol Channel was 8.54 m^{-1}. The median value of the scattering coefficient was 0.35 m^{-1} suggesting there was generally low scattering at the stations measured around the UK coast at this point.

The backscattering coefficient (b_{bp440}) is treated separately from the scattering coefficient. The backscattering coefficient refers specifically to scattering that occurs between 90-180° back from the incident direction of the photon (Kirk, 1994). Backscattering plays a particularly significant role in the formation of remote sensing signals and is measured here using a BB9 instrument (Loisel *et al.*, 2006; Gordon and Clark, 1980; Carder *et al.*, 1989).

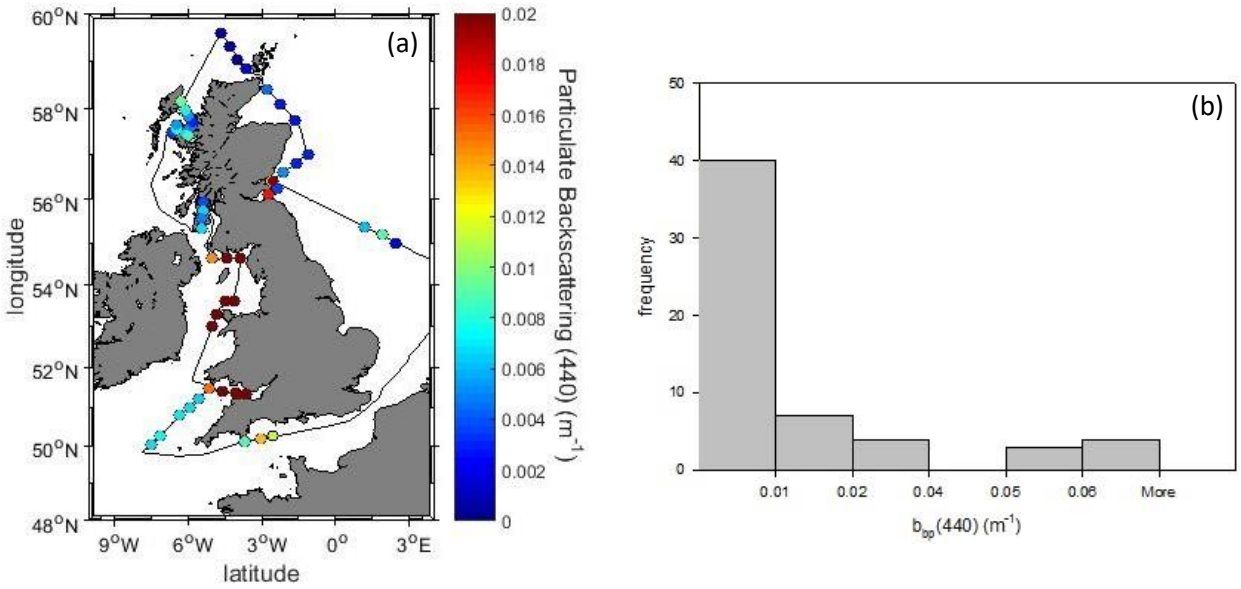

Figure 4.22: (a) The wavelength-dependent particulate backscattering distribution is shown for He442 at 440 nm (b) A histogram of this distribution is shown, this histogram shows that the majority of stations measured a backscattering signal of less than 0.01 m^{-1}.

The range of b_{bp440} was from 0.0007 m^{-1} at station 45 to 0.29 m^{-1}, which was detected at station 15 in the Bristol Channel with mean and median values of 0.023 and 0.007 m^{-1} respectively.

The absorption, scattering, and backscattering at 440 nm in UK waters is variable but looking at the histograms in Figures 4.18b, 4.19b, and 4.20b, these IOPs tended towards lower values. The majority of stations have absorption, scattering and backscattering coefficients in the range of 0.01-0.4 m^{-1}, 0.2-0.6 m^{-1}, and < 0.01 m^{-1} respectively. More extreme values of these IOPs (5.2 m^{-1}, 8.5 m^{-1}, and 0.3 m^{-1} respectively) were observed in the Bristol Channel at station 15. These large values show that in terms of inherent optical properties, the Bristol Channel is an exceptional case.

4.3 Biogeo-optical Discrimination of Water Types

A Simple Bio-optical Partitioning

A basic bio-optical partitioning was used to categorise the water types encountered through the course of He442 via simple relationships between measured parameters. Bengil *et al.*, (2016) and McKee *et al.*, (2007) have shown that natural waters often exhibit biogeochemical and bio-optical properties that can be characterised by bifurcations between specific parameters, such as in Figure 4.23a where TSS and chlorophyll concentration are compared and $a_n(676)$ and $b_{bp}(676)$ in Figure 4.23b.

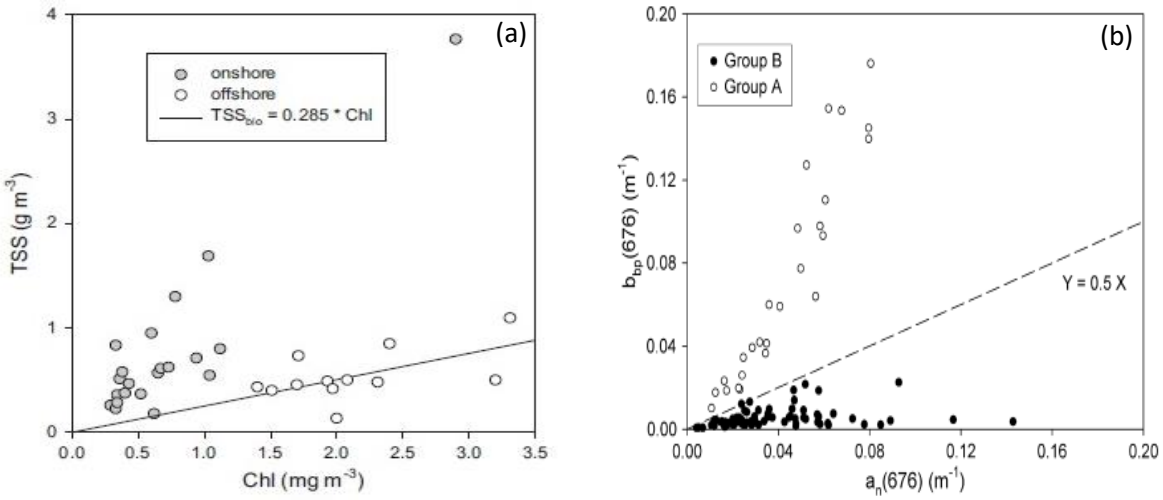

Figure 4.23: (a) Bengil (2016) identified a birfurcation of their dataset using the relationship between TSS and chlorophyll. (b) The McKee (2007) data was collected across 102 stations in the Irish and Celtic Seas showing prominent bifurcation of the dataset using the backscattering coefficient and non-water absorption coefficient at 676 nm.

Here, the dataset has been partitioned into three distinct biogeochemical water types as follows and as shown in Figure 4.24.

Partition 1 *(black circles)*: stations < 1 mgL^{-1} TSS present

Partition 1 is the most Case I-like

Partition 2 *(red squares):* stations > 1 mgL^{-1} TSS & < 1.5 mg m^{-3} chlorophyll

Partition 2 is the most highly scattering/ lowest productivity waters

Partition 3 *(green triangles)*: stations > 1 mgL^{-1} TSS & > 1.5 mg m^{-3} chlorophyll

Partition 3 are the most productive Case II waters

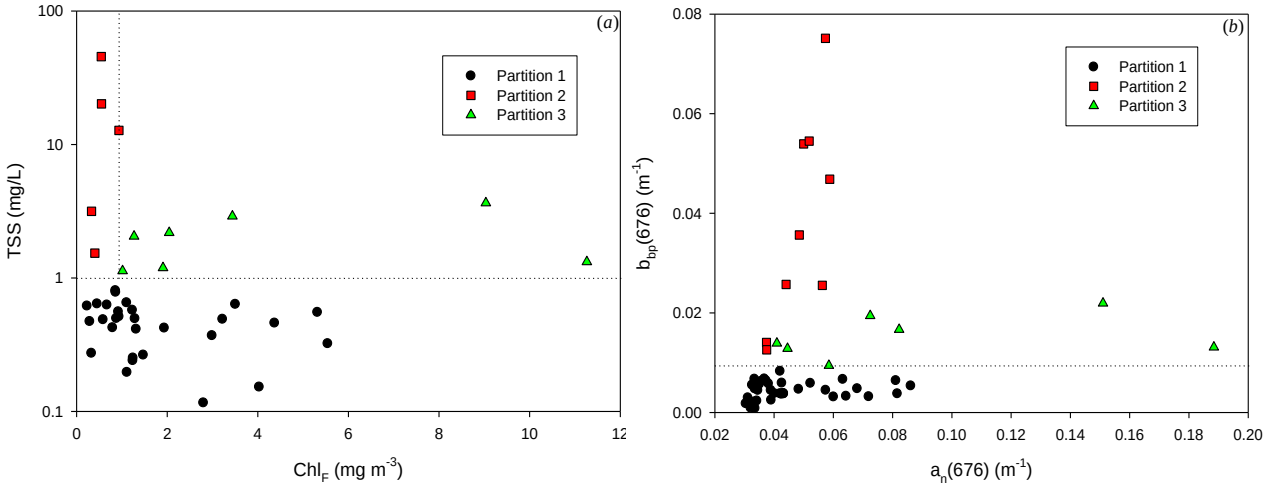

Figure 4.24: (a) Comparison of the total suspended solid (mg/L) against Chl_F (mg m^{-3}) showing a trifurcation of the dataset depending on the optical complexity of the water. (b) The particulate backscattering at 676 nm was plotted against the non-water absorption at 676 nm. The data were separated using the same biogeochemical partitioning that has been applied to the TSS: Chl_F data.

These slightly arbitrary categorisations are not global relationships but rather a useful tool that allows biogeo-optical classification of the water types present around the UK coast during April 2015.The water regions associated with each branch of the trifurcation are shown in Figure 4.25. Figure 4.24a shows the bio-optical trifurcation of TSS and Chl_F data with all partition 1 stations having TSS of less than 1 mg/L. A large increase in TSS with virtually no increase in Chl_F was observed for partition 2 stations. The partition 3 stations had a higher TSS content than partition 1 but larger concentrations of Chl_F were also observed.

Figure 4.24b compares the relationship between the particulate backscattering at 676 nm to non-water absorption as in Figure 4.23b from McKee *et al.* (2007). The partitioning from the He442 data is not as clearly defined as in McKee *et al.* (2007) however it does appear to suggest the presence of three distinct bio-optical water types around the UK coast in April 2015 with increasing non-water absorption and backscattering.

All stations that are designated as partition 1 fall below 0.01 m^{-1} particulate backscattering at 676 nm with the partition 2 stations exhibiting increasing backscattering with only a small

increase in non-water absorption at 676 nm, which is distinct from partition 3 stations where there is an increase in non-water absorption with little increase in particulate backscattering.

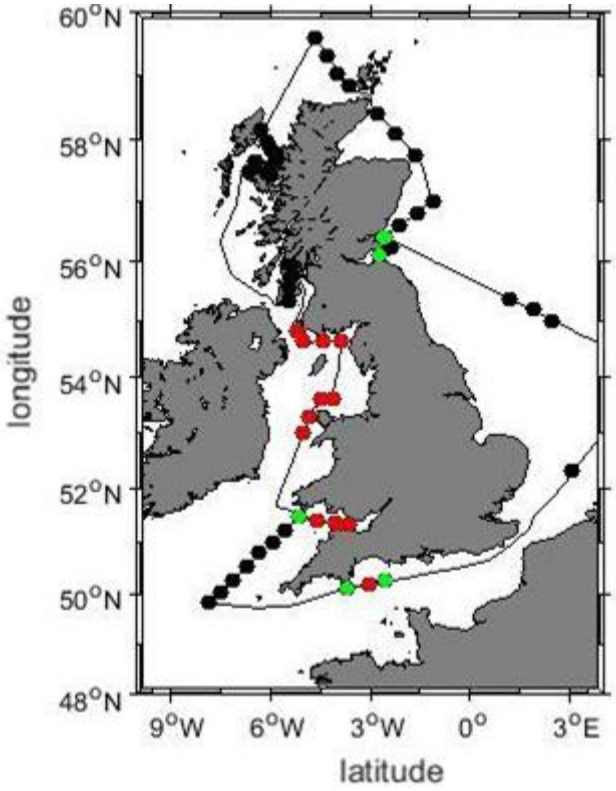

Figure 4.25: Biogeochemical partitioning of each station has been applied for the station's geographical location.

Figure 4.25 shows the geographical distribution of the biogeo-optical partitioning. The majority of stations around the UK coast are identifiable as being Case I-like with low concentrations of total suspended solid. Partition 2 is composed of stations found exclusively around the Bristol Channel and Irish Sea which is a result of this region being particularly turbid with higher concentrations of total suspended solid. Both the Bristol Channel and the area around Anglesey are regions of strong tidal mixing, which consistently presents elevated levels of suspended sediment with associated high levels of backscattering that is easily visible in ocean colour remote sensing imagery (McKee *et* al., 2006). This results in an unfavourable scenario for phytoplankton growth with cells not spending enough time within the photic zone to allow efficient photosynthesis to occur, hence the low chlorophyll concentrations here. Partition 3 stations may represent the intersections of high coastal turbid zones and more productive shelf water which may be evidenced by their geographical locations relative to Case I-like partition 1 stations and Case II-like partition 2 waters.

Ratio of the Euphotic Depth to Mixed Layer Depth and Biogeochemical Drivers

The purpose of this section is to test whether the bio-optical partitioning applied in the previous section helps to explain variations in the ratio of euphotic depth to mixed layer depth.

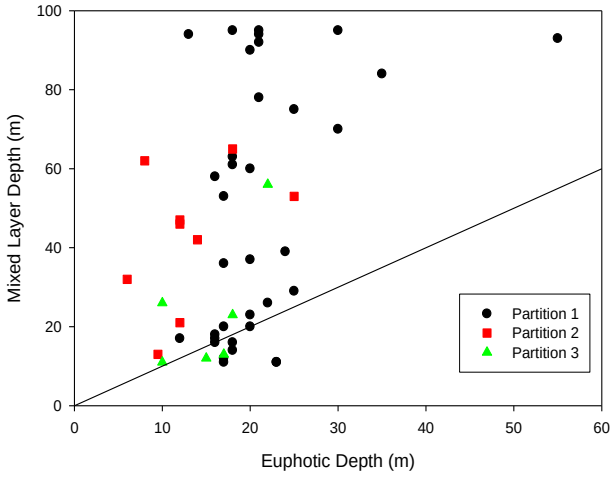

Figure 4.26: A Figure identical to Figure 4.8 is plotted with the stations separated into the bio-optical trifurcation. The solid line shows equality between the euphotic depth and the mixed layer depth. Only very few stations were observed to have a euphotic depth greater than or equal to the mixed layer depth. The bio-optical partitioning is not useful for this relationship.

Figure 4.26 shows the bio-optical partitioning of the mixed depth vs. euphotic depth data. Generally, most surface layers were not fully illuminated, however, 16 stations from He442 cluster around the solid line. Algal cells at these stations are experiencing near to total illumination of the water column. This is particularly apparent for the partition 3 stations around the line (stations 55, 56, 57, 58) which are in the Forth and Tay Estuaries. These stations exhibit high photochemical efficiencies, Chl_F, and electron transport rates which may be indicative of the formation of an algal bloom at these locations.

Filter Pad Absorption Measurements of Contrasting Bio-Optical Waters

Analysis of the absorption spectra measured via filter pad absorption of the contrasting bio-optical waters provides a useful insight into some of the water properties observed using other parameters. Particulate absorption measurements using the Shimadzu

spectrophotometer allow for estimates of the algal absorption and non-particulate absorption to be made.

The total particulate absorption obtained from filter pad determination is composed of two constituents: algal and non-algal particulate absorption. The total particulate absorption measured for the stations in each bio-optical partitioning are shown in Figures 4.27a-c. Figure 4.27b shows the particulate absorption for the most Case II-like waters occurring in the Bristol Channel and Irish Sea with there being a very small chlorophyll signal present with the exponential rise in absorption into the ultraviolet/blue end of the electromagnetic spectrum being characteristic of the presence of high levels of inorganic sediment. Figures 4.27a,c show that the Case I-like waters (partition 1) and productive Case II waters (partition 3) show larger chlorophyll signals which may be indicative of the presence of greater concentrations of phytoplankton.

Figure 4.28a shows the non-algal absorption for all stations during He442and identifies an increase in the non-algal component found in partition 2 stations relative to the other stations. This is compounded by the very low algal absorption component for partition 2 stations found in Figure 4.28b. This strengthens the claim that these optically complex Case II waters are unproductive possibly due to the high sediment content absorbing and reflecting light reducing the number of photons available for photochemistry.

The partition 1 stations are described as being the most Case I-like meaning there is very little to no non-algal particulate influence on the signal. Figure 4.28a shows that the partition 1 stations have the lowest absorption of non-algal constituents meaning these stations are Case I-like in their nature. Figure 4.28c is the normalised algal absorption spectra for partitions 1 and 3 at 440 nm. This panel shows that between partitions 1 and 3, there is not any major variation in the structure of the main photosynthetic molecules, i.e. chlorophyll, however, below 400 nm and between 500-600 nm, there is greater variability that may be indicative of the presence of different pigment systems that are adapted to the requirements of the phytoplankton in these locations. Figure 4.28d shows the same information as Figure 4.28c but for partition 2 showing that there is a very small chlorophyll signal in these waters.

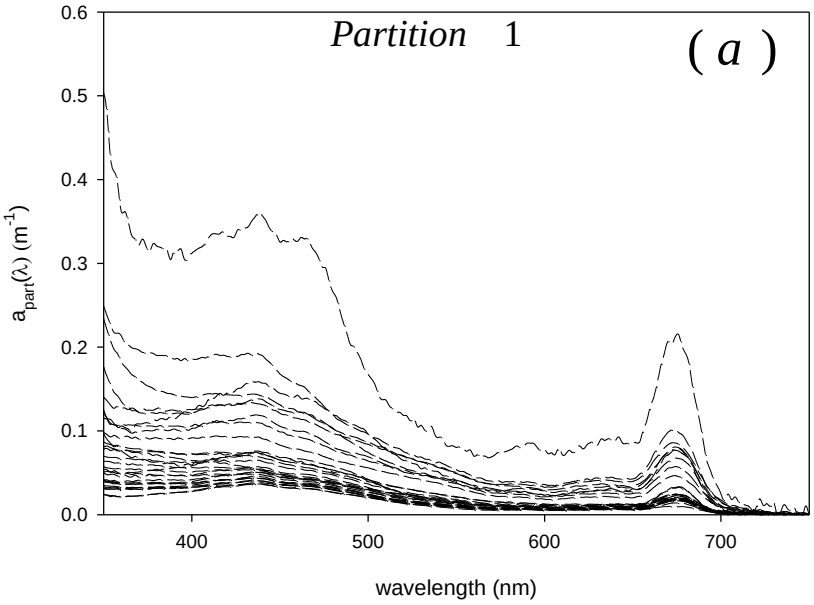

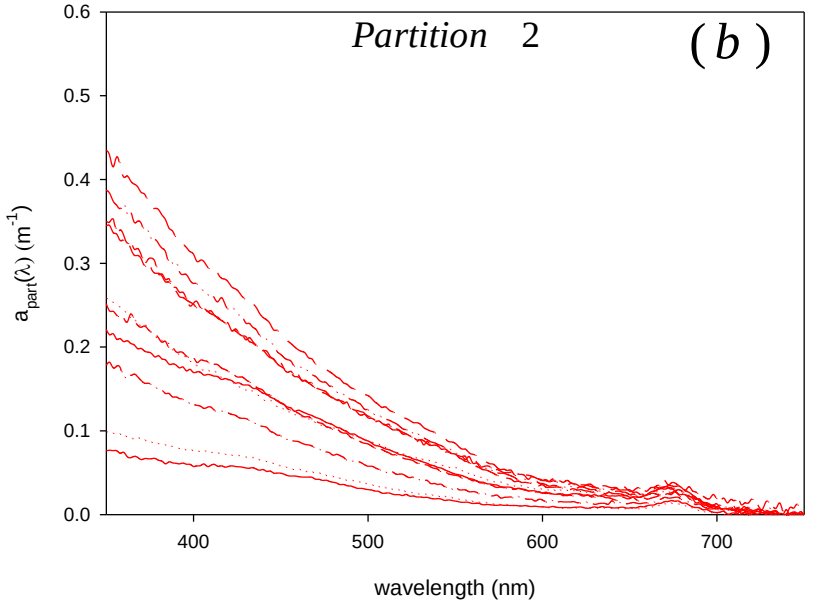

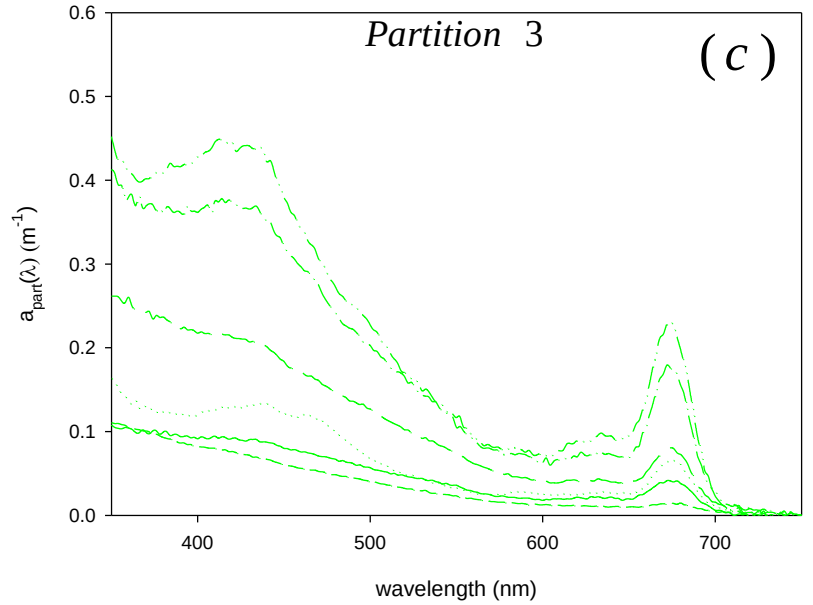

Figure 4.27: Figures 4.27a-c show the particulate absorption at stations around the UK in each biogeochemical partitioning as measured by filter pad absorption. The particulate absorption is the total absorption composed of algal and non-algal components.

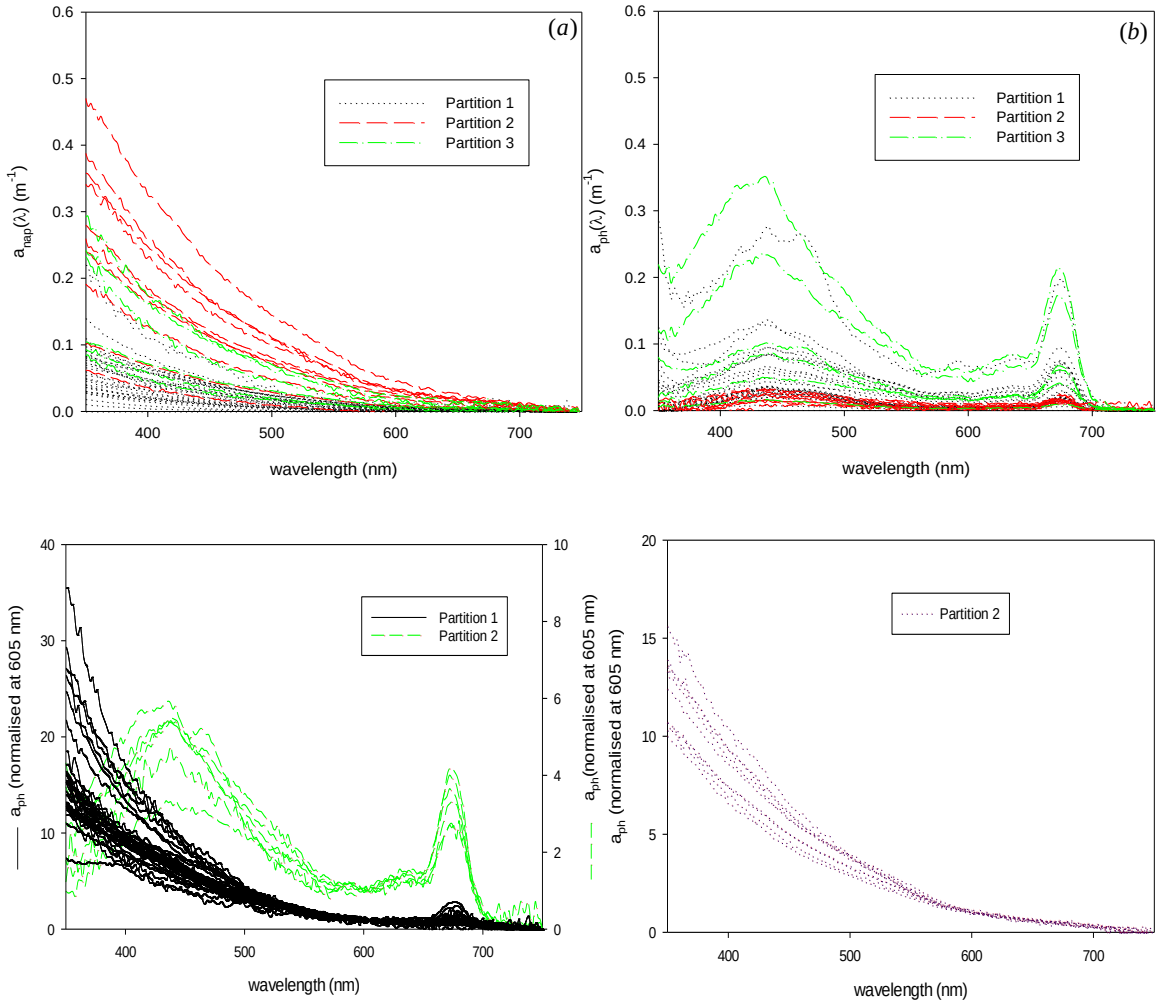

Figure 4.28: (a) Bleaching of the filter pad with sodium hypochlorite removes the influence of the algal component leaving only the non-algal (or particulate detrital constituents) (b) Subtraction of the non-algal component from the total particulate absorption gives the algal particulate absorption. (c) Normalising the algal signal at 605 nm gives a better approximation of the influence of other pigments that may be present in the algal cells. This is most prominently shown in Figure 4.28c, where the partition 3 stations show good chlorophyll structures. Figure 4.28c shows the normalised spectra for the partition 1 and partition 3 stations. (d) The normalised spectra for partition 2 stations are shown. The very low chlorophyll signal at these stations is evident in the noisy data.

4.4. Relating Variability of Photophysiological Parameters to Bio-optical and Physical Drivers

Variable fluorescence measurements with the Fast Repetition Rate fluorometer allow determinations of the bulk physiological state of phytoplankton cells sampled from the water column. The utility of these data are discussed at length in chapter 3. The aim of this section is to determine whether it is possible to correlate observations of phytoplankton physiological state with different biogeochemical and physical parameters measured around UK coastal waters.

Ambient Photochemical Efficiency of Phytoplankton around the UK Coast

The photochemical efficiency estimates how efficiently excitons are passing through the photochemical pathway. The closer the value of photochemical efficiency to 0.6, the better the apparent physiological status of the cells. Due to time constraints, it was not possible to run dark-regulated triplicates of F_v/F_m at each station, however, data exist for the light-adapted F_q'/F_m', where F_q' is the light-adapted equivalent of F_o and F_m' is the light-adapted equivalent of F_m, at most stations in Figure 4.29.

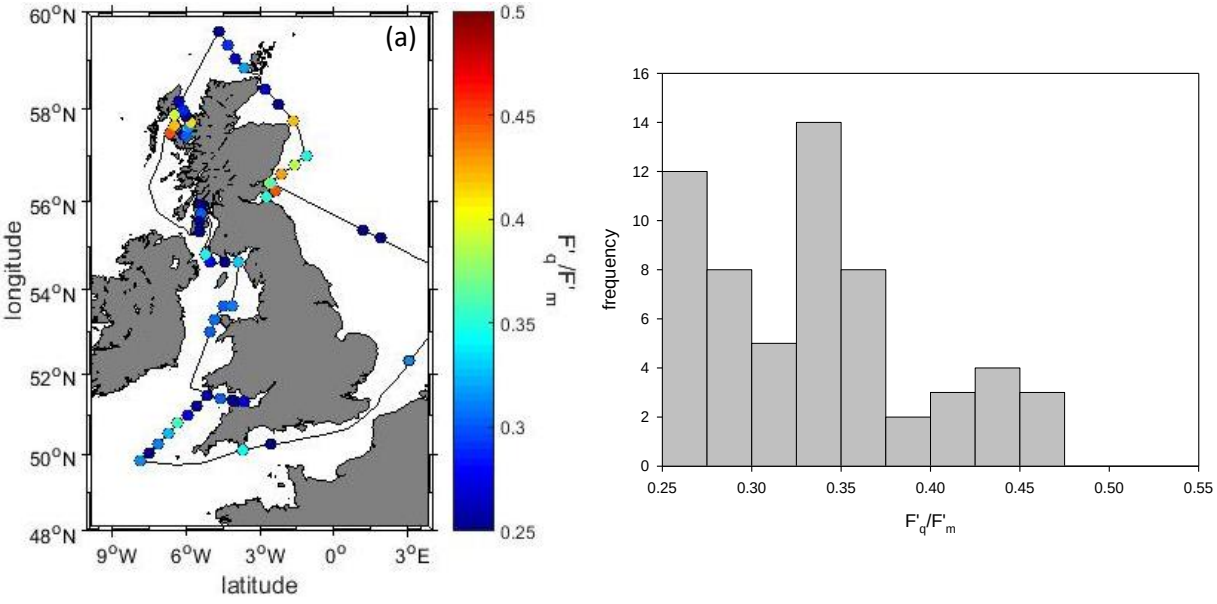

Figure 4.29: (a) Distribution of light-adapted F_q'/F_m' measured with the 450 nm excitation LED (b) The associated histogram for the distribution of light-adapted photochemical efficiency around UK coastal waters.

Light-adapted photochemical efficiencies were determined by immediate measurement (< 5 s) following insertion into the sample chamber. By measuring the physiological state immediately, the aim was to try and account for non-photochemical quenching mechanisms that would ordinarily be quenched following routine dark acclimation.

The light-adapted photochemical efficiency is the most basic physiological parameter produced by the FRRf. Figures 4.29a-b show that there were a range of physiological states around the UK coast in April 2015 but the majority of cells had an F_q'/F_m' of less than 0.4, despite there generally being greater than 1 mg m^{-3} chlorophyll present at the stations measured during He442. This can be due to a variety of factors such as the nutrient status of the water or as a result of the cells being in poorly lit waters as discussed previously.

The most physiologically robust phytoplankton as determined by F_q'/F_m' observed in the course of these measurements were around the Forth and Tay Estuaries as well as in the Raasay Sound. Particularly on the east coast on the approach into the Tay Estuary where the waters were still well-mixed as per Figure 4.7d, the increasing photochemical efficiency may be an indication of a bloom forming in that region.

Functional Absorption Cross-section

The functional absorption cross-section of photosystem II is a measure of how much light is being absorbed and funnelled into photochemical pathways. This variable parameter depends on local physical conditions and the organism's recent environmental history. For example, the functional absorption cross-section of PSII (σ_{PII}) will be different for an organism that is probed in the middle of the night compared to one that is tested when the Sun is at the highest point in the sky (Dubinsky, 1992).

Figure 4.30a shows the distribution of values for the functional absorption cross-section of PSII around UK coastal waters for He442. The stations from the Celtic Sea travelling northeast into the Bristol Channel show a marked reduction in σ_{PII} with increasing proximity to the estuary, which coincides with an increase in optical complexity of the waters (see Figures 4.14a and 4.19a), suggesting that with increasing concentration of non-algal absorption, there is a reduction in the absorption capabilities of the phytoplankton.

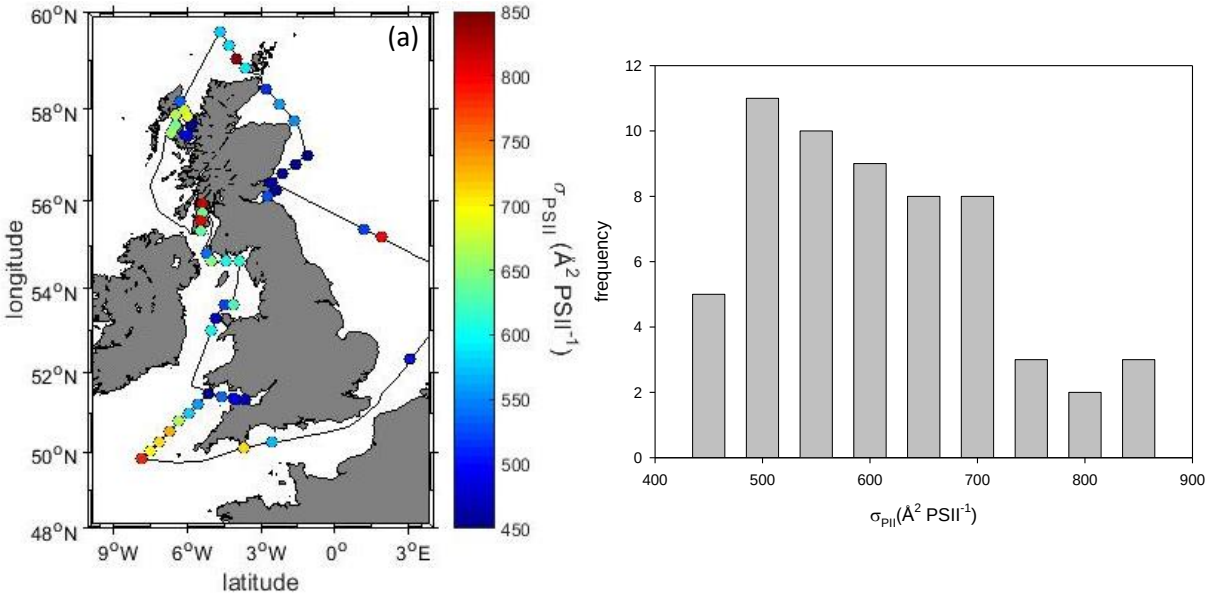

Figure 4.30: (a) Distribution of values of functional absorption cross-section for UK coastal waters during April, 2015. The functional absorption cross-section of photosystem II is determined by an iterative curve fit of the slope of the measured fluorescence transient. (b) Histogram of the distribution of functional absorption cross-sections.

Prieto *et al.* (2008) suggest that some of the variability in the functional absorption cross-section of PSII may be explained by nutrient limitation and the photoacclimation status of cells at the time. Furthermore, σ_{PII} is an environmentally-driven variable. By not measuring the algal physiology *in situ*, it is possible that the values obtained on the lab bench are not entirely representative of the actual sample depth, for example, Ssebiyonga *et al*. (2013) demonstrate a clear depth-dependence for σ_{PII}.

The mean and median values of σ_{PII} were calculated as 581 and 573 $Å^2$ $PSII^{-1}$ respectively with the minimum and maximum values recorded as 417 and 842 $Å^2$ $PSII^{-1}$. The time of day, impact of bio-optical partitioning and spatial position were tested for their effect on the functional absorption cross-section of PSII.

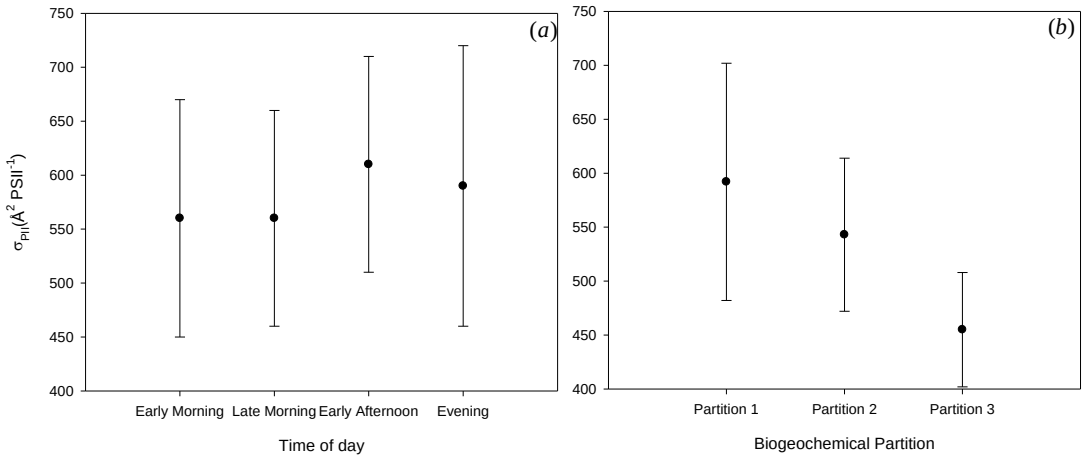

Figure 4.31: (a) The impact of the time of day on functional absorption cross-section was measured with the stations being split into four time periods and averaged: early morning was before 10am and late morning being before midday. Early afternoon was from midday to 3pm and evening was anything beyond this point. Uncertainties are to 1σ (b) The impact of the biogeochemical partitioning was used to separate the values of σ_{PII}. Uncertainties are to 1σ.

Figure 4.31a shows the effect of time of day on the functional absorption cross-section. There is no change in the average for the early morning and late morning stations with σ_{PII} of 560 $Å^2$ $PSII^{-1}$. There is a general increase for the afternoon stations with σ_{PII} reaching an averaged maximum of 610 $Å^2$ $PSII^{-1}$ in the early afternoon and dropping to 590 $Å^2$ $PSII^{-1}$ by evening. These changes over the course of the day may reflect algal dynamical responses to increased solar irradiance to improve the efficiency of photosynthesis.

Figure 4.31b shows the effect of using the biogeochemical partitioning system applied in section 4.3. There is an apparent decrease in σ_{PII} with increasing optical complexity, which appears to be in keeping with findings from the literature (Lesser and Gorbunov, 2001; Raateoja and Kuosa, 2004). Raateoja and Kuosa (2004) suggest this may be due to the need for spectral re-scaling in optically complex case II waters.

Functional Absorption Cross-section and Algal Absorption

The relationship between the FRRf-derived functional absorption cross-section of PSII (σ_{PII}) and the algal absorption ($a_{ph}(\lambda)$) derived from the difference between the total and detrital

absorption calculated from filter pad determination of particulate absorption was compared to identify whether a relationship existed between these two parameters.

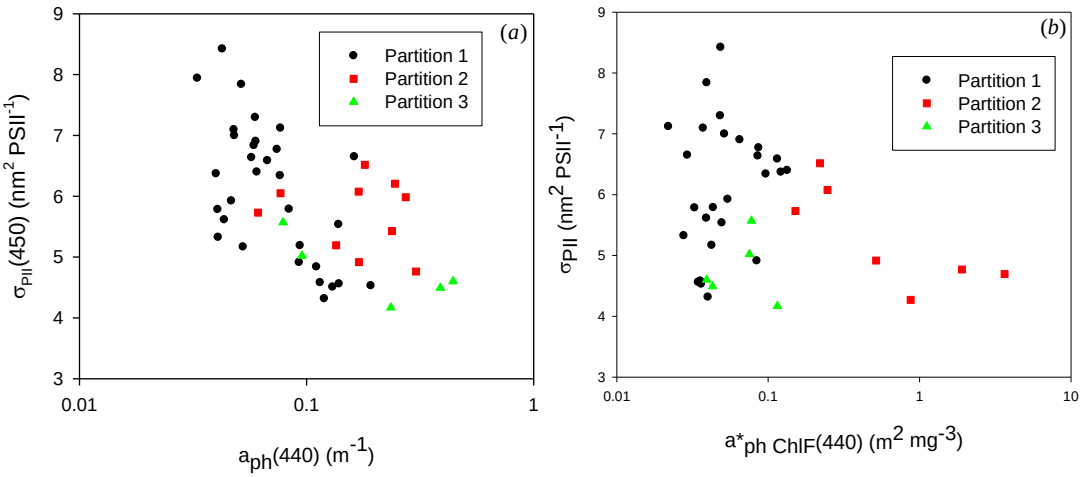

Figure 4.32: (a) algal absorption at 440 nm compared against the functional absorption cross-section of PSII which is derived via iterative fitting of the slope of the fluorescence transient. (b) The Chl$_F$-specific algal absorption is contrasted with the functional absorption cross-section of PSII.

The algal absorption and chlorophyll-specific algal absorption are observed to have similar relationships with the functional absorption cross-section of PSII. Figure 4.32a shows that the value of $a_{ph}(440)$ is generally higher for partition 2 and partition 3 stations than for those in partition 1. Furthermore, for partition 1 stations, there is a general trend of decreasing σ_{PII} with increasing $a_{ph}(440)$. Figure 4.32b is a comparison of Chl$_F$-specific algal absorption and σ_{PII}. Chlorophyll-specific algal absorption for partition 1 and partition 3 stations fall into a narrow band of values ranging between approximately 0.05 and 0.1 m^2 mg^{-3}. Partition 2 stations fall out with this range and have a consistently higher value of chlorophyll-specific algal absorption. From both graphs, it is clear that the functional absorption cross-section is highly variable fitting with the highly dynamic nature of algal photophysiology. The functional absorption cross-section also appears to vary inversely to the Chl-specific absorption which may indicate absorption by additional accessory light-harvesting pigments that are inclusive of the functional absorption cross-section.

Fluorescence Light Curve-derived Indicators of Physiological Status

The Initial Slope and Light Saturation Parameter

The initial slope (α) of an FLC, as discussed previously, is determined by extrapolating the fluorescence transient back to the y-intercept. Different measures of the photochemical efficiency from He442 are shown in Table 4.2 From the data collected on He442, there appears to be good agreement between α_{PAR} and F_v/F_m as determined by averaging all F_v/F_m recorded during an FLC (at 0 PAR). The third measure (F_q'/F_m') shows the statistical data for the information in Figure 4.33.

Table 4.3: The means and range of different physiological measurements made at each station during He442.

	Mean	Minimum	Maximum
α_{PAR}	0.288	0.138	0.471
F_v/F_m	0.291	0.140	0.438
F_q'/F_m'	0.303	0.137	0.449

The apparent similarities in the averaged values of the dark and light-acclimated photochemical efficiencies may be due to the impact of sample handling on deck prior to putting a sample into the FRRf. A more rigorous sample handling protocol including keeping samples at the same irradiance they were experiencing in the water, may help to mitigate this in future.

The saturation parameter is the point in an FLC where the curve moves from the light-limited phase to the light-saturated phase, i.e. at what solar irradiance are the samples reaching their maximum photosynthetic capacity. This parameter varies over the course of a day with E_k ranging from 165 to 395 µmol photons m^{-2} s^{-1} in Loch Fyne. E_k can be affected by nutrient status, environmental conditions, as well as species dependence but is generally considered a good indicator of the state of photoacclimation in a cell (Sakshaug, 1997).

The saturation parameter showed variability around the UK coast with the minimum value of E_K calculated as 116 µmol photons m^{-2} s^{-1} and a maximum of 786 µmol photons m^{-2} s^{-1}, whilst the mean and median were 344 and 324 µmol photons m^{-2} s^{-1} respectively, indicating that the very largest E_K were outliers when compared to the majority of stations made here.

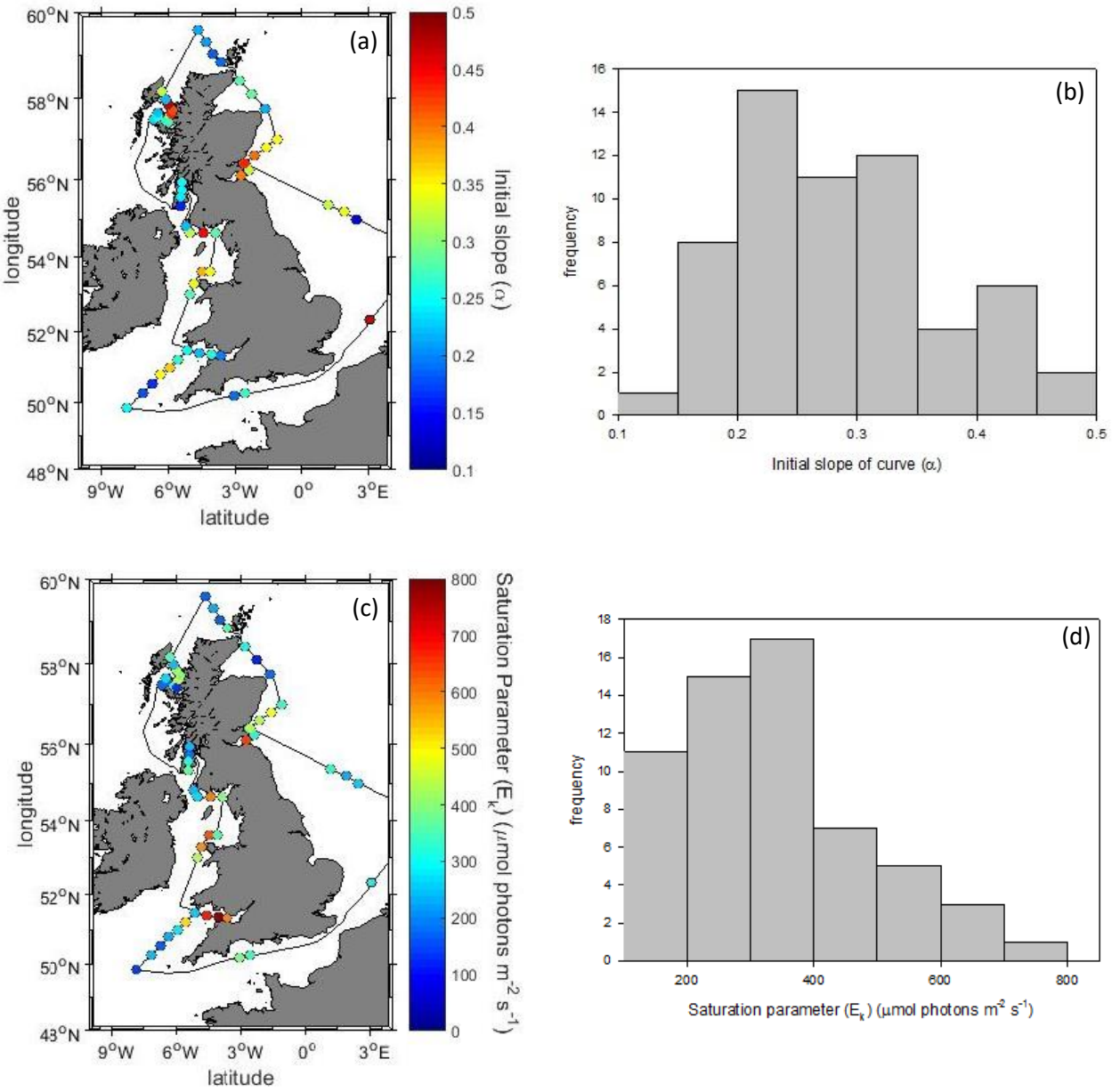

Figure 4.33: (a) Distribution of the initial slope (α) of the curve which can be taken as estimates of the dark-regulated photochemical efficiency (b) Histogram of the initial slope distribution (c) Distribution of the light saturation parameter (E_k) around UK coastal waters (d) Histogram of E_k distribution. The saturation parameter gives an estimate of the irradiance required to saturate photosynthetic capacity, taken as the asymptote of the curve.

Maximum Electron Transport Rate

The maximum electron transport rate is taken as the product of the initial slope and the saturation parameter to give an estimate of how many electrons are being transported through the photosynthesis pathway from PSII.

From the map of calculated ETR, there are regions of high ETR and regions that are not as productive. For example, the F_q'/F_m' values in the Tay Estuary suggest that these waters contain phytoplankton that are physiologically strong. This is reflected in the higher values of ETR found in this region, the same is also true of the phytoplankton in the Raasay Sound.

The minimum ETR was found at station 30, in Loch Fyne, and was calculated as 28.1 µmol e^- m^{-2} s^{-1}, whereas the maximum value was found to be 269.5 µmol e^- m^{-2} s^{-1} at station 22, north of the Isle of Man in the Irish Sea.

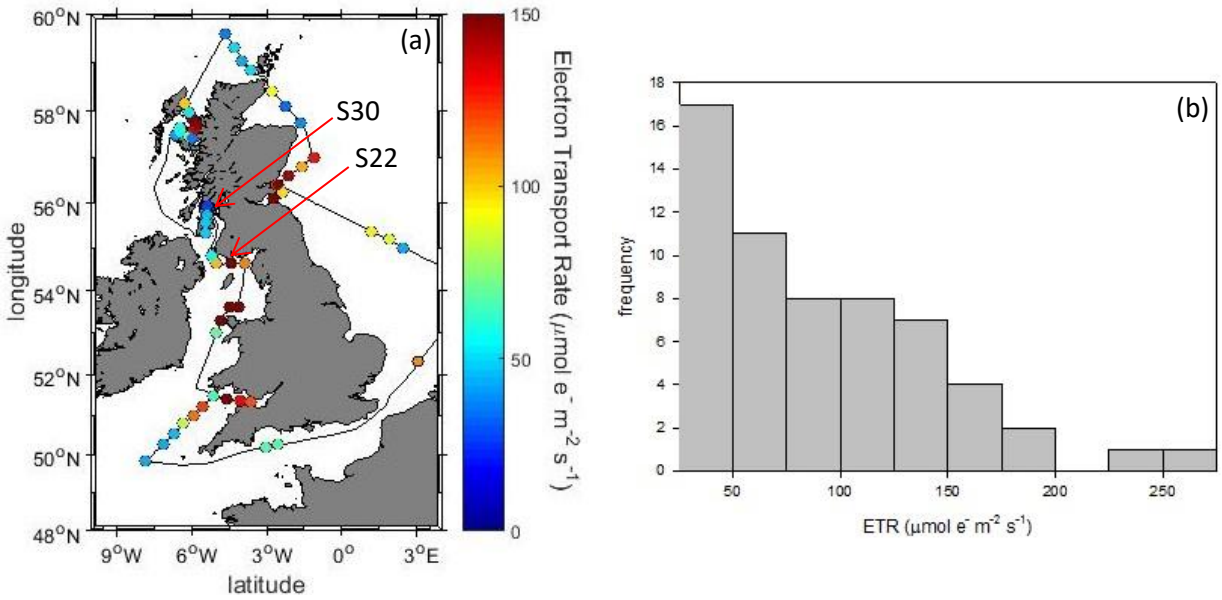

Figure 4.34: (a) The electron transport rate is calculated as the product of the photochemical efficiency measured under ambient light and PAR level at each light step. The distribution of ETR is shown for UK coastal waters during He442 (b) A histogram of this distribution is shown.

Figure 4.34a shows that the electron transport rate appears to increase higher into the Bristol Channel. This is contradictory to the expected physiological state in this region as this falls into partition 2 of the biogeochemical categorisation, which is defined by lower chlorophyll

concentrations and higher sediment content as in Figures 4.11a and 4.12a. Furthermore, Joint *et al.* (1981), in their study of the Bristol Channel observed that lower primary productivity rates were found the deeper into the Bristol Channel, where turbidity was higher. The electron transport rate was compared to F_o, F_v/F_m, and σ_{PII} to determine their effect on ETR and whether there is a pattern in electron transport rates using the biogeochemical partitioning system.

Figure 4.35a shows the relationship between the observed F_o and ETR. The partition 1 stations show a spread of values as one would expect given they cover a large number of different areas with differing environmental conditions. The partition 2 stations all have F_o less than 0.2 but with a large observed ETR (maximum = 269 µmol electrons m^{-2} s^{-1}). The partition 3 stations relating to the Forth and Tay Estuaries had larger F_o and ETR values, which may be indicative of a recent bloom in that area with higher baseline fluorescence in F_o and electron transport rates. This is corroborated by higher Chl_F concentrations in 4.13a. The high ETR in the Bristol Channel with low recorded Chl_F suggests that due to the Bristol Channel being sufficiently shallow, algal cells remain illuminated, which may explain the high ETR values.

Figure 4.35b shows the ETR data with the photochemical efficiency (F_v/F_m). This showed that the partition 2 stations in the Bristol Channel had photochemical efficiencies lower than 0.33. The partition 3 stations had F_v/F_m up to 0.45 but the equivalent ETR were not as high. The most Case I-like waters were observed to be spread across different ETR values and photochemical efficiencies.

In Figure 4.35c, the electron transport rate is plotted against the functional absorption cross-section (σ_{PII}). There is a wide spread of absorption cross-section values and electron transport rates particularly for the most Case I-like partition 1 stations. The partition 3 stations, which are considered to be productive Case II waters have generally lower functional absorption cross-sections with some of the highest electron transport rates. This may be an indication of more efficient photochemical pathways present in these organisms.

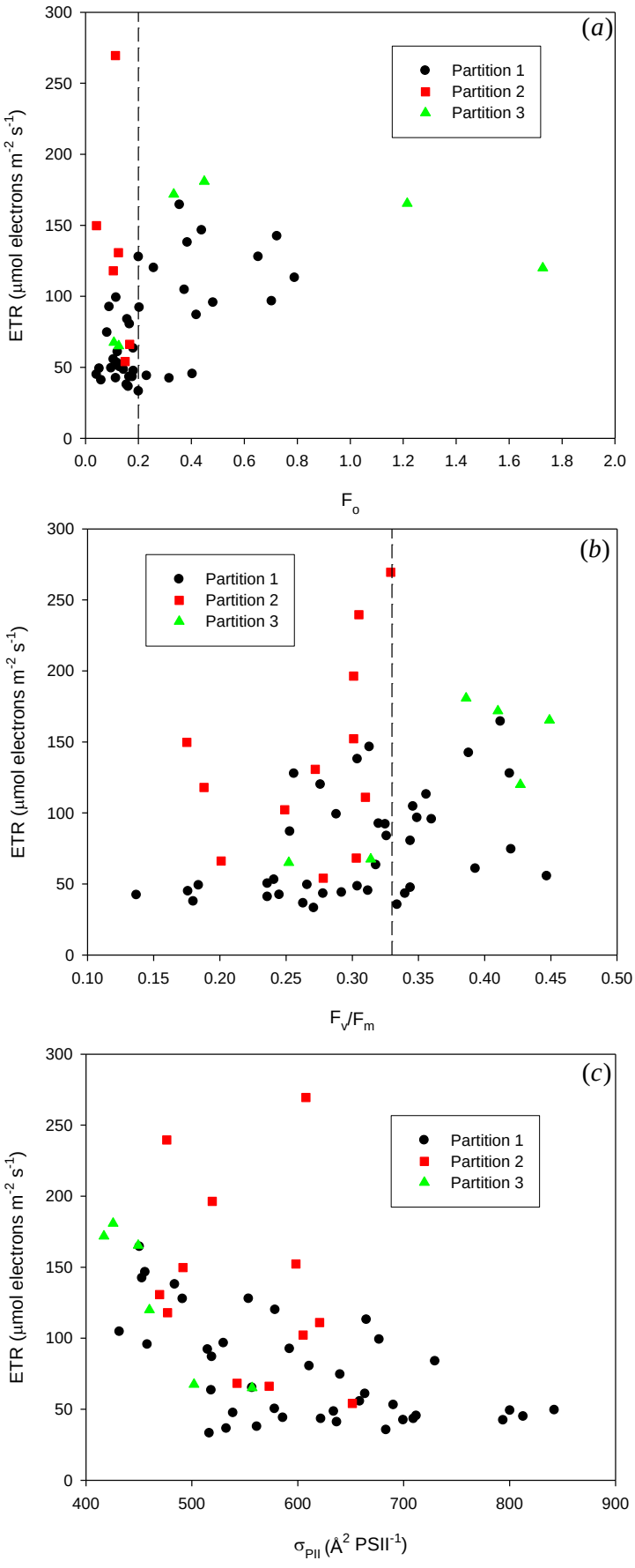

Figure 4.35: (a) ETR compared to F_o observed at each station during He442. The vertically dashed line shows that the partition 2 stations all have F_o lower than 0.2 and most partition 3 stations are above this value. (b) F_v/F_m is compared to the equivalent ETR with all partition 2 stations having an F_v/F_m lower than 0.33. All but two partition 3 stations have relatively high F_v/F_m with associated higher ETR. (c) The impact of the functional absorption cross-section on the electron transport rate is shown for each station. There is a wide spread of absorption cross-section values with no particular pattern discernible for the Case I-like partition 1 stations. The partition 3 stations tended to have lower functional absorption cross-sections.

Spatio-variability as a Potential Biogeo-optical Driver

The 62 stations cast over the course of He442 were made in three distinct biogeochemical water types, each experiencing different mixing regimes, degrees of stratification and turbidity levels raising the question of spatio-specificity of particular biogeo-optical parameters. The relationship between the FRRf-measured physiological parameters and biogeochemical parameters has been discussed at length in the preceding sections in an attempt to draw relationships between the light-adapted, photochemical efficiency (F_q'/F_m') and different short and long term processes that may drive physiology variability.

Figure 4.36a compares the ship sensor temperature data with F_q'/F_m' for all stations. From the biogeochemical partitioning of section 4.3 and photochemical efficiency, there is no particular trend between photochemical efficiency and temperature. The relationship between salinity and photochemical efficiency is compared in Figure 4.36b. During He442, there was a relatively limited spread of seawater salinities observed, which, much like the temperature range, may not be significant in the context of a global relationship between salinity and F_q'/F_m'. Furthermore, there is no evidence of categorisation based on the biogeochemical partitioning used previously. Figure 4.36c compares the photochemical efficiency with the FRRf-based chlorophyll proxy, Chl_F. Partition 1 stations show a wide spread which is indicative of their prevalence around UK waters, whereas with the partition 2 stations, each station has a low Chl_F with a variable value of photochemical efficiency. The majority of F_q'/F_m' fell within the 0.3 to 0.55 range of values, with no clear trend temporally or spatially.

Figure 4.36d compares the photochemical efficiency with the ratio of mixed layer depth to euphotic depth. The majority of stations (as in Figure 4.24) were not fully illuminated, meaning that for a period of time, algal cells would theoretically be receiving insufficient irradiance to power photosynthesis. This would be expected to impact the photochemical efficiencies. The generally low photochemical efficiencies may be an indication of the impact of low light levels and well-mixed water columns. Three partition 3 stations (stations 55, 56, 57) were found to have fully illuminated water columns, a fact that correlates well with the high F_q'/F_m', high *ETR* and high Chl_F at these stations.

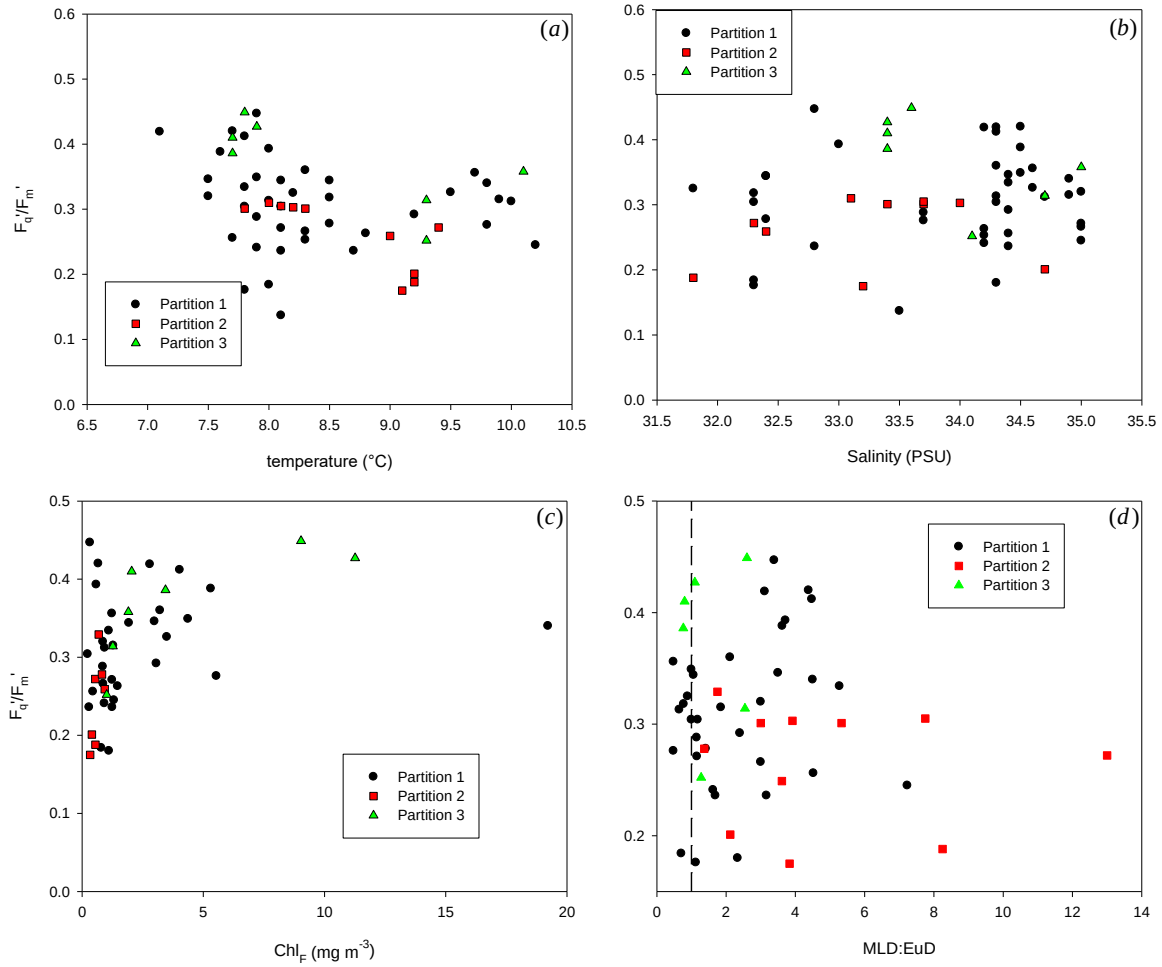

Figure 4.36: (a) Compares the station temperature to the photochemical efficiency (b) Salinity is compared to photochemical efficiency. The salinity was determined from the CTD rosette (c) The chlorophyll proxy, Chl_F, is compared to photochemical efficiency (d) The photochemical efficiency was compared to the ratio of the mixed layer depth to euphotic depth. The dashed line represents the transition from a water column that is not fully illuminated (> 1) to a water column that is (< 1).

Individually, each comparison is unable to make a statement about the underlying physical and biogeochemical processes driving physiology in UK coastal waters during He442. In April, 2015, the water temperatures were low with high salinity as well as well-mixed water columns and low light levels through the water column (MLD:EuD > 1), all of which likely accounts for the generally low photochemical efficiencies and possibly explaining the low average chlorophyll concentrations measured throughout the cruise. It is possible that many of the locations surveyed during He442 were in a pre-bloom phase with the noticeable

exception of the Forth and Tay Estuaries which showed much higher photochemical efficiencies, electron transport rates and Chl_F values than most other locations measured. These data as a whole reinforce the argument that environmental factors are a complex of many parameters making it very difficult to assign responsibility for observed physiological conditions to any one in coastal waters.

Temporal Variability and Phytoplankton Physiology

The given biogeochemical parameters provide limited insight into phytoplankton physiology due to the rapid nature of physiological response. As such, we now take a look at the impact of the diurnal cycle on physiology and examine whether the time of day i.e. changing solar zenith angle and intensity of incoming solar irradiance impacts the physiological response. Figure 5.32 shows the relative change in both the photochemical efficiency and the maximum photosynthetic capacity both determined from individual FLCs in FastPro8.

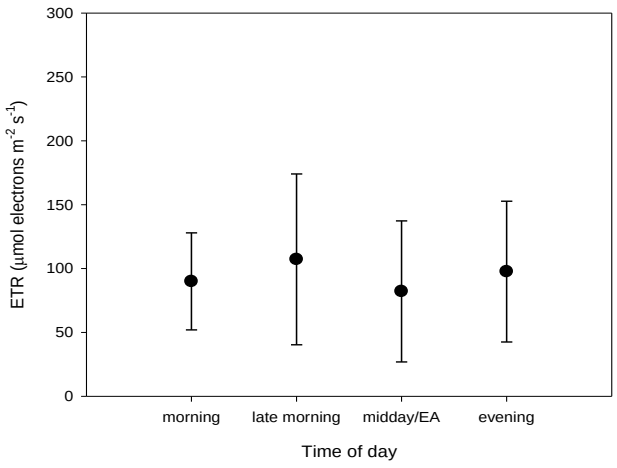

Figure 4.37: Influence of the time of day on the averaged ETR during He442. Stations were separated into four time periods and averaged: early morning was before 10am and late morning being before midday. Early afternoon was from midday to 3pm and evening was anything beyond this point. Uncertainties are to 1σ.

Stations were separated into the time of day that the measurements were made to see if a pattern existed generally across the day. Figure 4.37 shows the impact of time of day on the electron transport rate. On average, there is an increase from the early morning to late morning with a dip in ETR over midday and the early afternoon. As the solar irradiance

decreases as the day progresses, it was observed that there was an increase in ETR, on average.

From the Loch Fyne FLC data shown in Figure 4.38, the averaged dark-regulated photochemical efficiency over the course of the day shows limited variability. However, Figure 4.37b shows the change in the maximum electron transport rate over the course of the day, in Loch Fyne, identifying an apparent drop in ETR at around solar noon which may be the result of photoinhibition effects. The variation in photochemical capacity suggests that the incoming solar irradiance is driving physiological response.

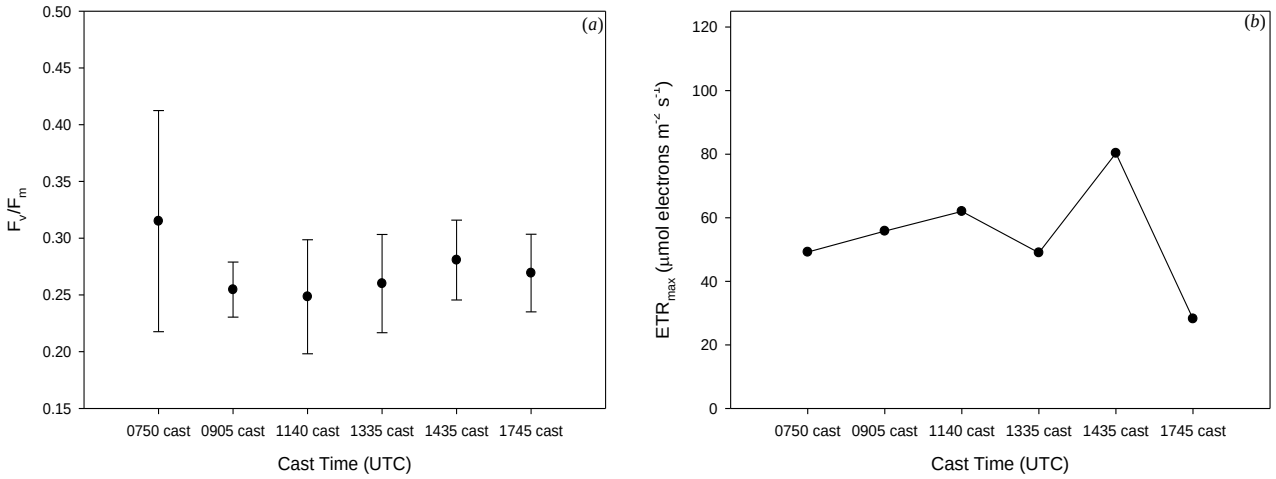

Figure 4.38: (a) The FLC-estimated F_v/F_m is shown, determined from the mean of ten dark measurements(b) The maximum photosynthetic capacity calculated by FastPro8 for the same FLC. All uncertainties are given to 2σ.

4.5. Conclusions

The multi-parametric analysis of UK coastal waters produced a detailed snapshot of the optical, physical, and biogeochemical conditions during April 2015. The parameters observed were highly variable and subject to many individual environmental inputs. Relationships between parameters were made and used to compare the He442 dataset to those in the literature, for example, the relationship between $a_{CDOM}(440)$ and salinity as in Figure 4.15. Further novel relationships in the dataset were identified, such as the bio-optical trifurcation,

with the *in situ* concentrations of total suspended solid and chlorophyll making it possible to separate the different waterbodies by optical complexity.

Using well-established approaches, it is possible to characterise the biogeo-optical and hydrographic properties of this dataset. However, none of those readily identified features are able to satisfactorily explain observed variability in photophysiological responses. It is suggested that these parameters are sufficiently dynamic that fluctuations in local conditions, for example, time of day or cloud cover may be more relevant. This does not diminish the role that the effects of light and nutrient history may have on the physiological response but rather these features are difficult to ascertain from a single hydrological cast.

The responsive nature of algal dynamics to incoming solar irradiance raises several questions, for example, when is the best time to make measurements of algal dynamics and are estimates of photophysiology strongly affected by the choice of time for measurement? Would several measurements over the course of a day be more useful or is a single point measurement sufficient? By addressing these issues, it would be possible to better design a research cruise around more beneficial use of fast repetition rate fluorometry technology, and therefore be able to make better estimates of the productivity of the waters being measured.

In the next chapter, these questions are specifically addressed within the context of the Loch Fyne dataset with the comparison of our own daily, column-integrated GPP model with OCRS models taken from the literature.

5. Impact of Spectral Light Availability on Estimates of Gross Primary Productivity: A case study in Loch Fyne

5.1 Introduction

The spectral light incident on the Earth's surface varies continuously as a function of changing solar zenith angle (θ_s), and environmental conditions such as cloud cover. These above-surface conditions influence the depth of light penetration through the water column and as a result, the productivity of the phytoplankton present in the water column.

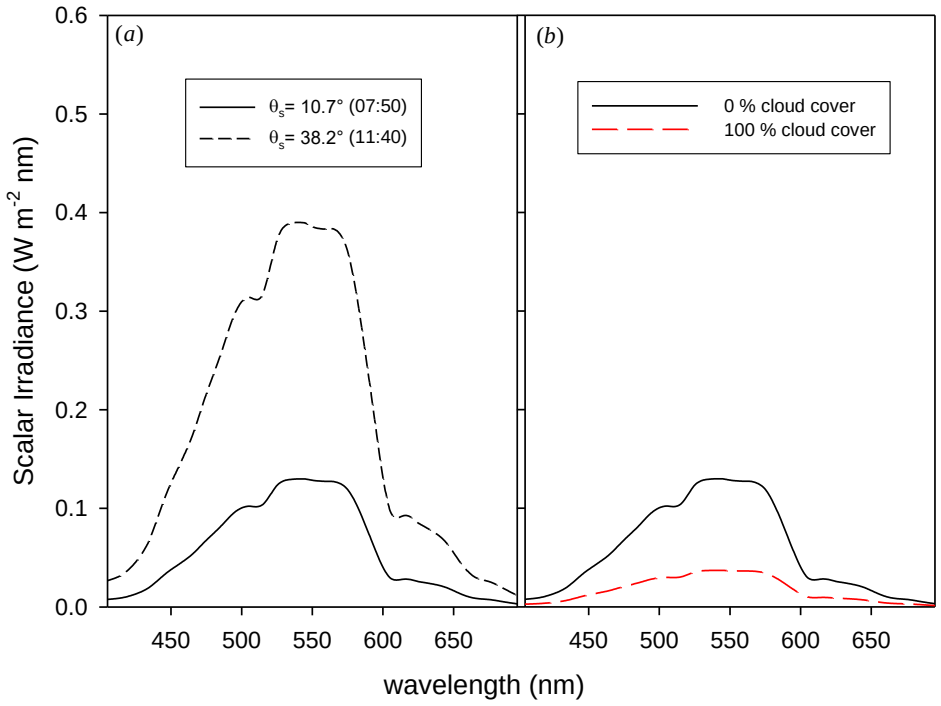

Figure 5.1: The spectral light availability modelled as scalar irradiance at 6 m depth for a time series in Loch Fyne. These data were produced using Hydrolight radiative transfer modelling. (a) Difference in spectral light availability as a function of solar zenith angle with atmospheric cloud cover set to 0 %. (b) The effect of changing cloud cover (0-100 %) at a fixed solar zenith angle of 48.7°.

As can be seen from Figure 5.1, spectral light availability in surface waters can vary over an order of magnitude depending on the time of day and cloud cover. This variability impacts upon the phytoplankton photophysiological apparatus. For example, the photophysiological apparatus under low irradiance, may adapt in such a way that more effort is put into light

harvesting. Alternatively, under high irradiance, phytoplankton cells may struggle to dissipate all the incoming energy effectively and so some light harvesting molecules may undergo non-photochemical quenching to prevent photons being directed through photosystem II into photosystem I (Tilzer *et al.*, 1994; Bracher, 1999; Falkowski, 1984).

Changing spectral light availability through the water column affects the carbon uptake capacity of cells in the water column. The extent to which primary productivity is affected by changing light conditions over the course of a single day was determined during the course of He442 by multiple samples at a single location in Loch Fyne (stations 25 to 30) over the course of a day. Using the measured inherent optical properties of the station and Hydrolight radiative transfer modelling, it was possible to model the underwater light fields at each time of the day through the water column with validation of these models using *in situ* radiometry collected at various times throughout the day. Knowledge of the phytoplankton physiological state from FRRf observations combined with the Hydrolight-derived underwater light fields allowed us to build a daily and column-integrated model of primary productivity for this location.

Further to producing estimates of primary productivity, multiple measurements over the course of a single day allow for discussions centred on the minimum number of measurements required to accurately predict daily GPP as well as the influence of factors affecting spectral light availability on these estimates.

The aim of this work was to ascertain the minimum requirements for primary productivity measurements using fast repetition rate fluorometry, whilst noting the diurnal variability and changing photophysiology. This allowed for an improved understanding of the relationship between the parameters used to make estimates of GPP and their influence on the final calculation. Furthermore, an attempt was made to describe an optimal sampling program, which would facilitate the improved efficiency of these measurements when at sea.

5.2 Depth and Temporal Resolution of Gross Primary Productivity in Loch Fyne: A Case Study (April 11, 2015)

Loch Fyne is a type ‘C’ fjordic sea loch (Milne, 1972) and is the longest and deepest sea loch in Scotland. Situated on the west coast, off the Firth of Clyde forming part of the Cowal

peninsula, the loch itself is approximately 65 km in length, 7.5 km across at its greatest width and 185 m at its deepest (Calvert *et al.*, 1970; Adams *et al.*, 2012). Loch Fyne waters are considered Case II_{CDOM}, as they are surrounded on both sides by farmland composed of soils that waterlog easily affecting streams and rivers in the area that discharge into Loch Fyne (CEFAS, 2008).

Loch Fyne is characterised by steep-sided walls with the position of Loch Fyne on the Firth of Clyde meaning wave action on the loch is minimised. The large size and depth of the loch means that water exchange takes 13 days, the second longest period of any sea loch in Scotland (Edwards and Sharples, 1985).

Table 5.4: Coordinates and cast time of radiometry equipment for each station in Loch Fyne and data recorded on deck with wind speed calculated by ship anemometer.

Cast Time	Station	Longitude (N)	Latitude (W)	Sky Conditions	Wind Speed	Sample Depth
07: 50	25	55°56.84’	5°24.03’	Clear	4.68 ms^{-1}	6.0
09:05	26	55°57.00’	5°23.6’	Partly cloudy	8.08 ms^{-1}	6.0
11:40	27	55°57.27’	5°22.75’	Cloudy	13.79 ms^{-1}	5.0
13:35	28	55°57.33’	5°22.54’	Partly cloudy	13.32 ms^{-1}	7.0
14:35	29	55°57.42’	5°22.55’	Overcast/Rain	13.12 ms^{-1}	7.0
17:45	30	55°57.45’	5°22.55’	Cloudy	10.3 ms^{-1}	5.0

During the UK coastal waters survey, He442 stopped in Loch Fyne for a full day giving an opportunity to study the effects of solar zenith angle on phytoplankton physiology at a single location (Figure 5.2). On 11th April 2015, sunrise and sunset were recorded at 05:28 UTC and 19:19 UTC. Six measurement casts were made across the day (see Table 5.1). *In* situ profiles of absorption, attenuation, and backscattering were made using the AC-9 and BB-9 instruments respectively and Trios Ramses sensors were used to measure *in situ* radiometry profiles including the downwards irradiance (E_d), upward irradiance (E_u), and upwelling radiance (L_u).

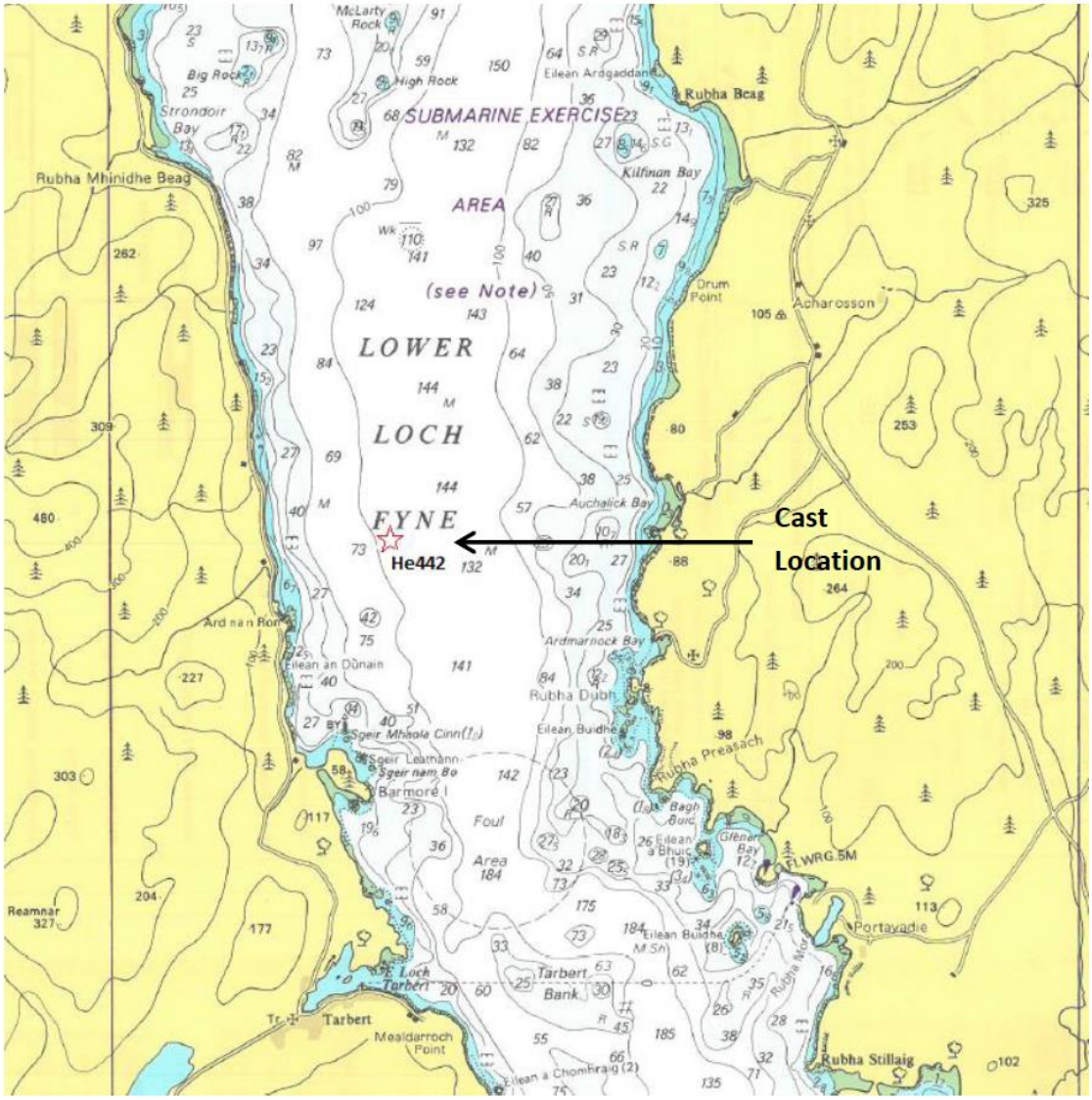

Figure 5.2: Admiralty map of the Firth of Clyde and Loch Fyne area showing the approximate location of the Loch Fyne time series casts.

Admiralty chart 2131 Firth of Clyde and Loch Fyne edition 18/02/2016 © Crown Copyright and/or database rights. Reproduced by permission of the Controller of Her Majesty's Stationary Office and the UK Hydrographic Office (www.GOV.uk/UKHO). Not to be used for Navigation.

Discrete water samples were collected for on-board measurements of phytoplankton physiology (FRRf); total, CDOM, and particulate absorption determination (PSICAM), determination of CDOM absorption using a 1 m pathlength (LWCC), particle size distributions (flow cytometer), and filter pad absorption measurements (spectrophotometer). This sampling effort produced the necessary data required to model underwater light fields using Hydrolight for subsequent use in estimation of gross primary productivity.

Bio-Optical Properties of Loch Fyne

IOP data were collected as per the methodologies in chapter 2 with profiles of particulate absorption at 440 nm, particulate scattering at 440 nm and the fluorescence shown in Figure 5.3. It is likely that the slight variability found in these parameters over the course of the day can be related to the tidal cycle given that Loch Fyne is a sea loch.

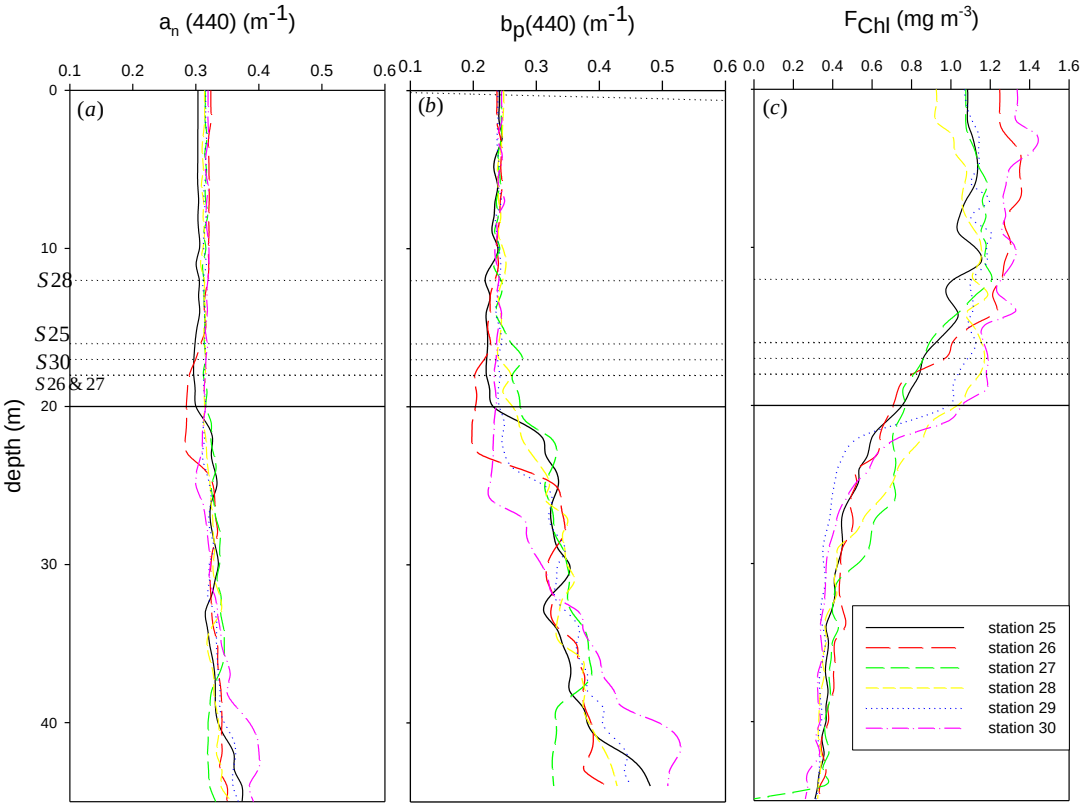

Figure 5.3: (a) Six AC9 absorption profiles at 440 nm for Loch Fyne show limited vertical structure, the euphotic depths at each station are marked for all three plots as the dotted line. The maximum mixed layer depth is noted by the solid black line on all three plots (b) AC9 particulate scattering at 440 nm was uniform through the euphotic zone(see Figure 5.16 for values) for all stations before increasing with increasing depth (c) F_{Chl} shows surface variability, however there are no signs of surface quenching over the day.

Particulate absorption at 440 nm (Figure 5.3b) was essentially unchanged down to 45 m depth in the water column. The particulate scattering was uniform to approximately 20 m depth before beginning to increase, possibly because this is the depth of the sill thereby restricting exchange with the Clyde Sea. The full water column depth measured at this location was between 150 to 200 m, however, the mixed layer depth was measured at a

maximum of 20 metres at stations 29 and 30 (solid black line on Figure 5.3), which may also explain the increase in particulate scattering below this depth. The fluorescence determined with the BBFl2 gives an approximation of chlorophyll. Figure 5.3c shows a drop-off in the fluorescence signal with depth below the euphotic zone.

5.3. Determination of Gross Primary Productivity

The primary productivity of a region is an estimate of the rate at which fixed carbon is being photosynthesised into organic substances. Many attempts have been made at estimating oceanic primary productivity but ultimately, there are two choices: measuring productivity directly or remotely. Given the vastness of the world's oceans, remote sensing techniques are a useful method of gathering globally relevant data in a short period. Remote sensing estimates of primary productivity are made by inference of water parameters from the surface and application of empirical models for primary productivity based on the upwards reflected signal, known as ocean colour remote sensing. *In situ* measurements can determine primary productivity directly but are restricted in terms of temporal and spatial coverage.

Determination of Primary Productivity Using a ^{14}C-based Approach

The first measurements of primary productivity were conducted in 1927 using an oxygen evolution-based approach (Gaarder and Gran, 1927). The original oxygen evolution method was unable to resolve low primary productivity rates and so was of limited use in low productivity areas. Steeman and Nielsen (1952) developed the ^{14}C incubation method for determining primary productivity.

The ^{14}C method measures the uptake of radioactive carbon as a tracer in algal cells. Since its original use in 1952, the technique has been continually criticised for the ambiguity in analysis of its results. Despite this, the technique is a standard in the oceanographic community (Beardall, *et al*., 2009). *In vitro* addition of ^{14}C-labelled bicarbonate to the dissolved organic carbon in a sample is measured for the assimilation rate of the known quantity of radioactive tracer. The rate of assimilation is measured following a period of bottle incubation. The rate of carbon uptake of the radioactive tracer is determined by a scintillation counter.

The ^{14}C method has been used for such a long time thanks to its sensitivity and high reproducibility of results. There are drawbacks to the method though including the requirement of radioactive material, which requires special operating procedures. The type of bottle used for incubation can also have an impact on results. The phytoplankton samples are confined in a bottle that is not representative of their natural environment and may skew the results produced, as well as environmental conditions not being the same as *in situ* (Steele *et al*., 2001; Robinson and Williams, 2005). The most pressing question regarding the ^{14}C method, though, is whether it is measuring gross or net primary productivity. This issue has been covered extensively in the literature (Dring and Jewson, 1982; Peterson, 1980; Caspers, 1970; Regaudie-de-Gioux *et al*., 2014). In reality, ^{14}C-incubation measurements probably lie somewhere between GPP and NPP with the degree to which it approximates either dependent upon the incubation period and photosynthetic rate of the algal cells. It is normally assumed that short incubation periods with low respiration rates are a fair approximation of GPP.

Determination of Primary Productivity By Ocean Colour Remote Sensing

Orbiting the Earth multiple times per day OCRS satellites are able to, in a matter of a few days, provide a spatial and temporally synoptic view of the entire globe, far outpacing the spatial resolution of *in situ* measurements (Babin *et al.,* 2015). However, OCRS is only capable of observing the first optical depth (Smyth *et al.,* 2015), compared to *in situ* measurements which allow for the primary productivity of the entire water column to be estimated. This means that OCRS is incapable of identifying water column structures such as deep chlorophyll maxima.

Ocean colour remote sensing is made possible by the fact that the apparent colour of the ocean changes with the concentration of optical constituents. Pure water i.e. water that contains nothing other than H_2O is a very efficient absorber of red light giving it a slight blueish hue, as illustrated in Figure 5.4a.

In Case I waters, the primary constituent affecting the optical properties of the water are phytoplankton and their associated products. The higher the concentration of phytoplankton

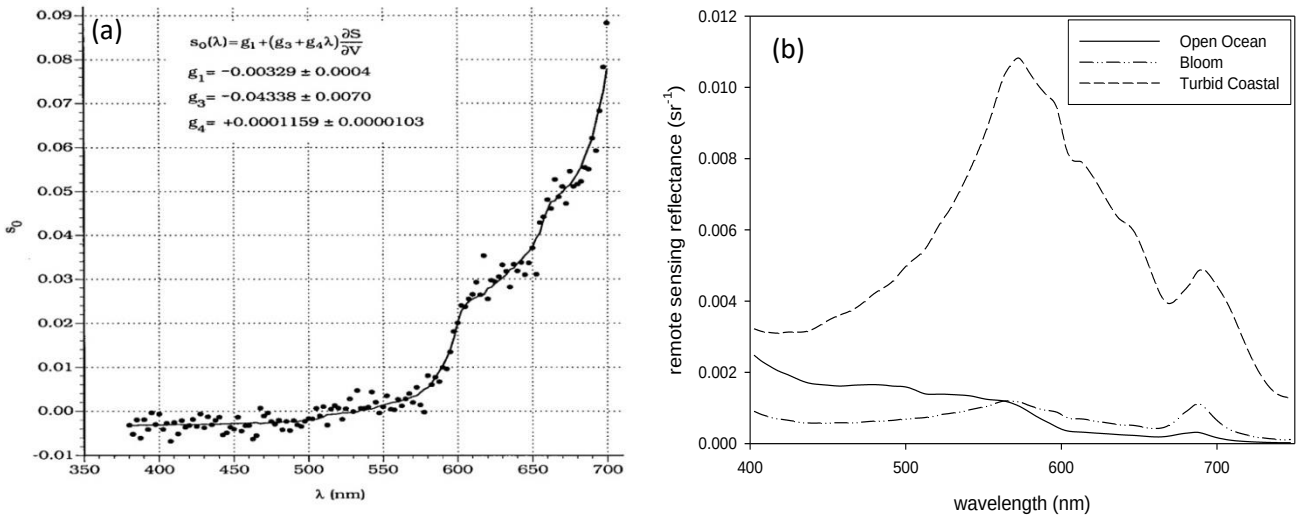

Figure 5.4: (a) The absorption of pure water is shown across the visible spectrum (Figure taken from Pope and Fry, 1997). The Figure shows the larger absorption of red light than for lower wavelengths. (b) The diagram shows the change in the reflectance ratio between three different water bodies where one is clear open ocean water, one represents bloom conditions and the third is highly turbid, as may be encountered in the Bristol Channel. The change in the wavelength-dependent structure is used to estimate chlorophyll a concentration for ocean colour remote sensing (Data obtained in a personal communication with David McKee).

in the water column then the more green the water becomes, as more blue light is absorbed by chlorophyll , with green light being reflected back by the algal particles. More turbid waters such as the Bristol Channel, which are strongly influenced by sediment, or CDOM for other Case II waters, affect the optical properties of the water column differently from phytoplankton. An example of this is shown in Figure 5.4b where the reflectance ratio for the relatively clear waters is smaller in magnitude and structured differently from that in the highly turbid waters.

For the purposes of satellite remote sensing, the chlorophyll concentration can be well-approximated by the ratio of blue: green reflectance on the sea surface.

$$Chl = 10^{(c_0+c_1R+c_2R^2+c_3R^3+c_4R^4)} \quad (5.1)$$

where c_x are empirical coefficients that are determined by iterative minimisation routines and R is the $\log_{10}$ of the maximum reflectance ratio values between the wavelengths (443/555), (490/555), and (510/555) (O'Reilly *et al*., 2000). The change in the blue: green reflectance ratio is compared against calibrated standards for the *in situ* phytoplankton biomass present,

allowing an estimate of the *in situ* chlorophyll concentration to be made (O'Reilly *et al*., 1998). These standard chlorophyll algorithms begin to encounter problems when operating in more optically complex coastal waters. The effect of inorganic sediment loads and increases in CDOM from freshwater inputs result in multiple, independently varying optically active constituents. These all have an impact on the water-leaving radiance and so convolute the resulting spectrum making it more difficult to attribute changes in the reflectance spectra to one particular variable (McKee *et al*., 2007).

Three ocean colour remote sensing models of net primary productivity (NPP) were used to compare against our own daily and column-integrated model of gross primary productivity. These three models represent progressions in the sophistication of estimates of ocean colour-derived primary productivity. These were the Falkowski (1981) depth-integrated model; the vertically generalised productivity model (VGPM) (Behrenfeld and Falkowski, 1997b); and the carbon biomass productivity model (CbPM) (Behrenfeld, 2005). All three were developed to estimate net primary productivity (NPP) using ocean colour remote sensing. Net primary productivity is distinct from gross primary productivity in that NPP accounts for respiration, where algal cells convert oxygen to carbon dioxide to produce energy in the absence of light. NPP is the difference between GPP and the respiration rate (Heinsch *et al.*, 2003). However, in this study, the Loch Fyne *in situ* dataset has been applied to each algorithm in place of remote sensing information. These OCRS models are normally validated using ^{14}C incubation, ^{18}O incubation, chlorophyll concentration data, or coupled physical-biological ocean (CPBO) models (Werner *et al*., 2007; Babin *et al.*, 2015; Behrenfeld *et al*., 2005; Behrenfeld and Falkowski, 1997b).

Falkowski (1981) Productivity Model

Falkowski suggested a simple depth-integrated model to determine the net primary productivity using the relationship below:

$$\Sigma NPP = Chl_{OCRS} \int PAR_0 \psi \tag{5.2}$$

where ΣNPP is the daily depth-integrated NPP (mg C m^{-2} d^{-1}), Chl_{OCRS} is the sea-surface chlorophyll concentration as determined by remote sensing, $\int PAR_0$ is the daily light integral (µmol photons m^{-2} d^{-1}), where the daily light integral (DLI) is taken as the instantaneous surface PAR multiplied by 86,400 s and then divided by $1x10^6$ to convert micromoles into

moles. Ψ is the water column light-utilisation index and is assumed constant at 0.43 mg C m^3 µmol photons^{-1} mg Chl^{-1}.This simple model has the drawback of assuming Ψ to be constant, a parameter which has been shown to be subject to variation through the water column (Antoine and Morel, 1996).

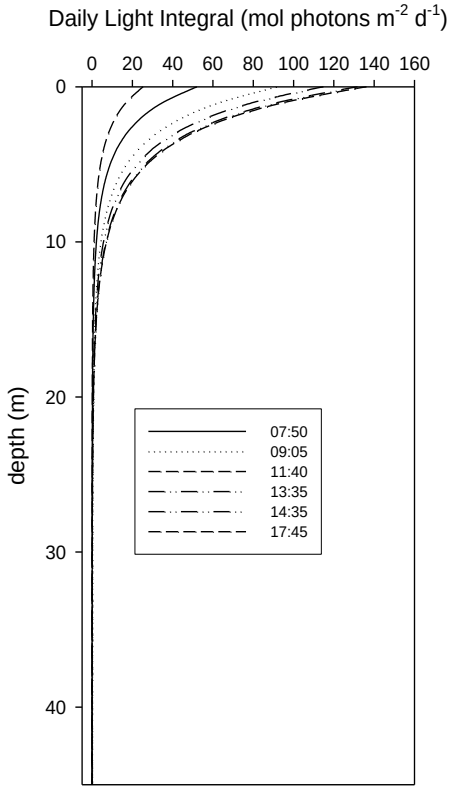

Figure 5.5: The instantaneous PAR is multiplied by 86,400 (number of seconds in a day) then divided by 1x10^6 to turn micromoles into moles.

At first glance, the light utilisation index would appear to be similar to the electron to carbon exchange factor. However, Ψ refers specifically to the algal cell's ability to absorb PAR irradiance, whereas $\varphi_{e,C}$ deals with the efficiency of the linear electron transport chain through the photochemical pathway.

The daily light integral was calculated for each cast at Loch Fyne (Figure 5.5). This was then multiplied by Chl_F and the water column light utilisation index as in equation 5.2. These values were then integrated for depth to produce estimates of NPP over the course of the day (Table 5.4).

Vertically Generalised Productivity Model (VGPM)

The VGPM was suggested by Behrenfeld and Falkowski (1997b) and is a more complex form of the depth-integrated model than the Falkowski (1981) model, as can be seen in equation 5.3.

$$\Sigma NPP = P_{opt}^{B} Z_{eu} Chl_{OCRS} \frac{c_1 \int PAR_0}{c_2 + \int PAR_0} \quad (5.3)$$

Where P_{opt}^{B} is the chlorophyll-specific maximum daily rate of carbon fixation found at depth through a vertical profile (mg C mg Chl^{-1} d^{-1}), Z_{eu} is 1 % of the surface PAR, i.e. the maximum extent of the euphotic zone, and c_1 and c_2 are statistically-derived coefficients produced from a series of large field studies of vertical NPP profiles.

P_{opt}^{B} (equation 5.4) is empirically determined from a seventh-order polynomial based on the sea-surface temperature and has a useful range between -1°C to 29°C (Behrenfeld and Falkowski, 1997a).

$$P_{opt}^{B} = -3.27x10^{-8}T^7 + 3.4132x10^{-6}T^6 - 1.348x10^{-4}T^5 + 2.462x10^{-3}T^4 - 0.0205T^3 + 0.0617T^2 + 0.2749T + 1.2956 \quad (5.4)$$

where T is the sea-surface temperature (°C).

In equation 5.3, the final term:

$$\left[\frac{c_1 \int PAR_0}{c_2 + \int PAR_0}\right]$$

can be expressed as f(I_o):

$$f(I_0) = \frac{0.66125\, I_0}{4.1 + I_0} \quad (5.5)$$

where I_0 is the daily light integral of the surface PAR (Behrenfeld and Falkowski, 1997a).

The VGPM produces a larger estimate (order of magnitude) of NPP than that of the Falkowski (1981) model (Table 5.4). $P_{opt}^{B}$was calculated as in equation 5.4 and z_{eu} was determined as per Figure 5.6.

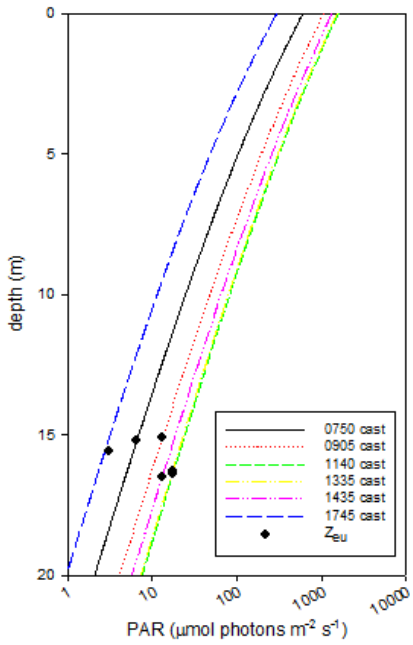

Figure 5.6: Hydrolight-modelled underwater light fields of Loch Fyne showing attenuation with depth. The euphotic depth (Z_{eu}) at each station is marked with a black circle.

Carbon-biomass Primary Productivity Model

Behrenfeld (2005) proposed the use of a carbon-based productivity model (CbPM), an extension of the depth-integrated model that attempts to take into account the variability and complexity of phytoplankton physiology. Here, Behrenfeld *et al.* (2005) assumed it is possible to derive daily, depth-integrated primary productivity (mg C m^{-2} d^{-1}) from knowing the growth rate (μ_g) and the phytoplankton carbon biomass (C_{OCRS}) using equation 5.6.

$$\Sigma NPP = C_{OCRS}\mu_g Z_{eu}\frac{c_1 \int PAR_0}{c_2 + \int PAR_0} \quad (5.6)$$

where C_{OCRS} is derived from knowledge of the surface backscattering in equation 5.7.

$$C_{OCRS} = 13{,}000\left(b_{bp}(440) - 0.00035\right) \quad (5.7)$$

where 0.00035 is an estimate of the particulate backscattering due to non-algal particles, and 13,000 is a scaling factor to directly relate the backscattering to phytoplankton carbon biomass.

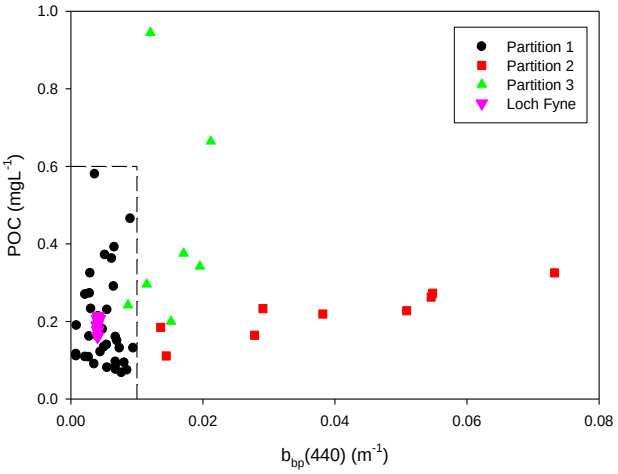

Figure 5.7: The relationship between the particulate backscattering at 440 nm and the particulate organic carbon concentration are shown. For the partition 1 and partition 3 waters, there is no relationship between the two quantities. There is a linear relationship between $b_{bp}(440)$ and POC in partition 2 waters, which are thought to be case II_{CDOM} waters primarily. The Loch Fyne stations are clearly in the partition 1 category.

C_{OCRS} is an estimate of POC, which forms the basis of equation 5.7. Figure 5.7 shows that the ratio of POC: b_{bp} breaks down in coastal waters with an increase in the concentration of variables including sediment load.

The growth rate is estimated using equation 5.8.

$$\mu_g = \mu_{max} \frac{\frac{Chl}{C} - \left[\frac{Chl}{C}\right]_{\mu=0}}{\left[\frac{Chl}{C}\right]_{N-T_{max}} - \left[\frac{Chl}{C}\right]_{\mu=0}} \left[1 - e^{(-3PAR(z))}\right] \qquad (5.8)$$

where μ_{max} is taken from Banse, (1991) and refers to the estimated maximum observed growth rate found in a natural assemblage where $\mu_{max} = 2\ d^{-1}$. $\left[\frac{Chl}{C}\right]_{\mu=0}$ is the estimated ratio when the growth rate is zero. This ratio is assumed to be 0.0003 mg Chl (mg Chl)$^{-1}$. The nutrient-replete Chl: C ratio for optimal growth conditions is calculated from equation 5.9.

$$\left[\frac{Chl}{C}\right]_{N-T_{max}} = \left[0.022 + (0.045 - 0.022)e^{-3PAR(z)}\right] \qquad (5.9)$$

as with the VGPM, the final term is replaced with $f(I_o)$ in equation 5.5.

In all three models, Chl_{OCRS} was replaced with Chl_F, the scaled initial fluorescence determined via FRRf. PAR was determined by underwater light field modelling using Hydrolight down to a depth of 45 m allowing calculation of z_{eu} as in Figure 5.6.

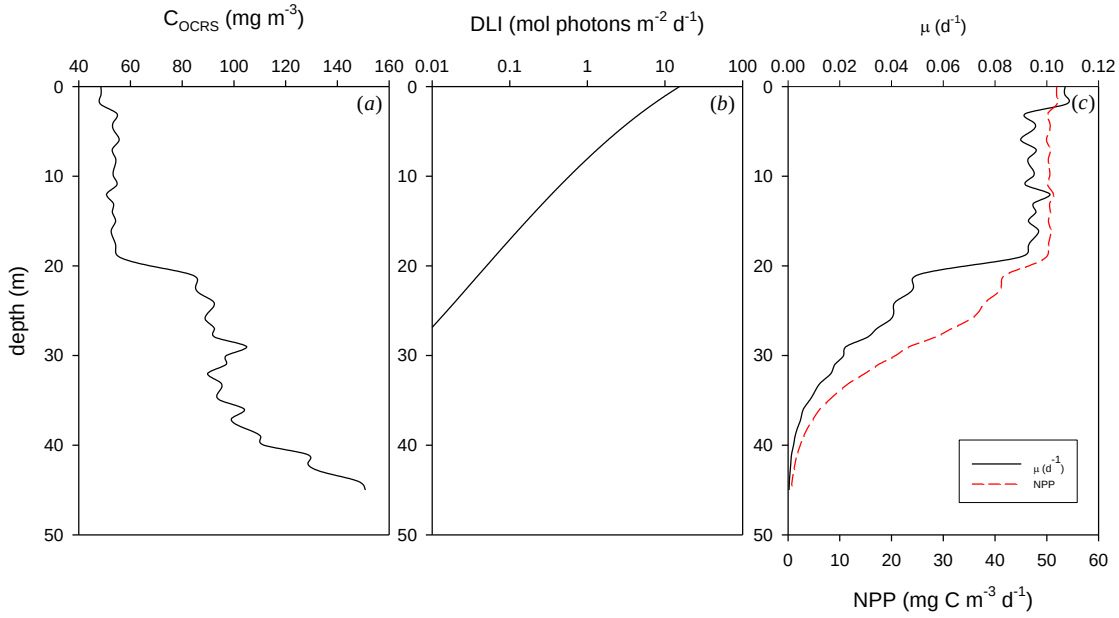

Figure 5.8: The CbPM parameters were calculated for station 25 of He442, the early morning cast that took place in Loch Fyne (07:40). (a) C_{OCRS} as calculated from equation 5.7 is shown against F_{Chl}, a BBFL2-produced chlorophyll proxy. The daily light integral as defined in Figure 5.5 is shown for station 25. (c) The net growth rate from equation 5.8 is plotted against the determined net primary productivity (NPP).

Determination of Primary Productivity by FRRf Observation

Fast repetition rate fluorometry uses the relationship between irradiance and the photochemical efficiency to make an estimate of the number of electrons passing through the photochemical pathway, known as the electron transport rate. In order to make the leap from electron transport rate to carbon fixation rate, an exchange factor is required.

Electron Transport Rate to Gross Primary Productivity: Use of an Exchange Factor

As electrons and oxygen are generated through the same process in the photosynthetic pathway, it is simple to draw correlations between the electron transport rate of photosystem

II (ETR_{PSII}) with oxygen evolution (Haumann *et al.*, 1997; Bard and Fox, 1995; Hoganson and Babcock, 1988). However, taking the next step to determining gross primary productivity from the electron transport rate has proved more challenging. The electron to carbon exchange factor ($\varphi_{e,C}$) shows variability across spatiotemporal regions, phytoplankton taxa, and cell light history (Lawrenz *et al.*, 2013; Brading *et al.*, 2013; Suggett *et al.*, 2009a; Moore *et al.*, 2006). At the single cell level, phytoplankton have developed considerable plasticity to environmental pressures meaning there are many mechanisms used to decouple the electron transport rate from carbon fixation, thereby maximising the photosynthetic rate whilst reducing the likelihood of photosystem damage by excess energy (Schuback *et al.*, 2015).

Lawrenz *et al.* (2013) performed a meta-analysis on the electron requirements for carbon fixation across a broad geographical cross-section of water types from the Baltic Sea to the Southern Atlantic and Pacific Oceans. Fast repetition rate fluorometry measurements were conducted using Mk. I and Mk. II instruments with a mixture of *in situ* and deck-mounted observations. No FastOcean Mk. III instruments were deployed in their study. The carbon fixation rate was measured by one of four methods: *in situ* incubation; simulated *in situ* incubation; PE curves, or ^{13}C-labelled $NaH^{13}CO_3$. Incubation period varied across protocols. Ideally, the carbon fixation rate and FRRf measurement of ETR would be made simultaneously but Lawrenz *et al.* (2013) make it clear that this was not necessarily the case on each field study potentially introducing a source of uncertainty into the measurements. For a complete breakdown of the inter-study discrepancies, refer to Lawrenz *et al.* (2013).

A global mean electron to carbon exchange rate of 10.9 ± 6.9 mol e^- (mol C)$^{-1}$ was identified based on a total global range of exchange factors of 1.2 to 54.2 mol e^- (mol C)$^{-1}$ as can be seen in Figure 5.9. Lawrenz *et al.* found that spatial variability was a more important factor than temporal variability for this parameter. Whilst the global range of exchange factors was large, Figure 5.9 shows that the majority of measurements made actually fell into a much narrower range with values such as 54.2 mol e^- (mol C)$^{-1}$ considered as outlier data. In what follows, the Lawrenz *et al.* (2013) global mean value for the electron to carbon exchange factor of 10.9±6.9 mol e^- (mol C)$^{-1}$ was used for conversion of FRRf-ETR data to estimates of gross primary productivity.

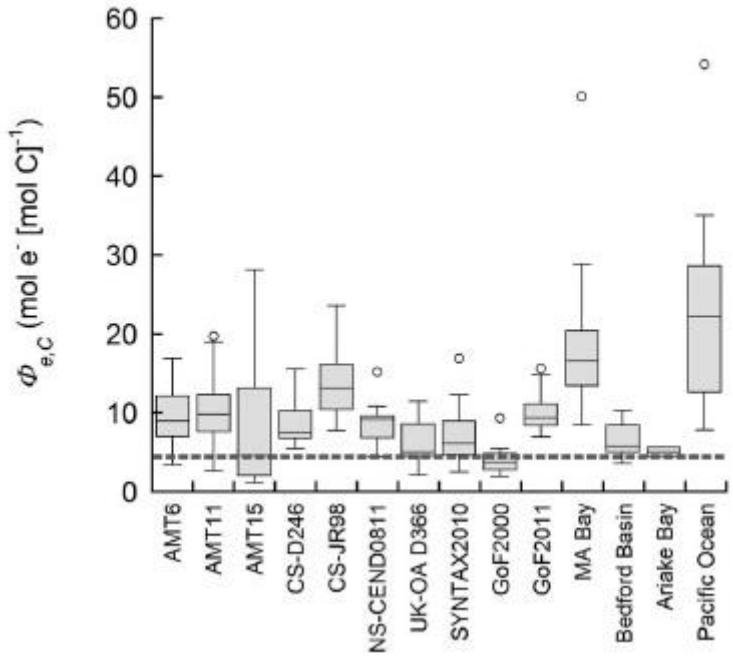

Figure 5.9: Variability in the electron to carbon exchange factor derived from electron transport rate measurements from FRRf and ^{14}C-measurements of primary productivity made on each cruise encompassing the Lawrenz meta-analysis. Boxes are the median, 0.25, 0.75 quartile, whiskers are the 1.5 interquartile range with outliers identified by open circles. 4 mol e^- (mol C)$^{-1}$ is the theoretical minimum number of electrons per carbon fixed and is indicated by the dashed horizontal line. Figure taken from Lawrenz et al., (2013).

Modelling PAR (z,t)

Radiative Transfer Modelling

Underwater light fields were modelled using Hydrolight 5.0, specifically to produce PAR with depth, although a suite of optical outputs are available from each run, e.g. $E_d(\lambda)$, $E_u(\lambda)$, and $R(\lambda)$. Hydrolight calculates radiance distributions and their derived quantities for natural waters (Mobley, 1994). A one-dimensional time-independent radiative transfer equation is used for these calculations with the radiance distribution resolved spectrally and for depth. The Hydrolight model was populated using *in situ* IOP data collected from station profiles in Loch Fyne. The proportional correction (Zaneveld *et al.,* 1994) was applied to the absorption and attenuation data collected by the AC-9. Upper and lower boundaries on the modelled irradiance were set by varying the atmospheric cloud cover between 0 % and 100 % cloud

cover. Pure water absorption values were taken from Pope and Fry (1997) and seawater scattering from Gordon (1973). Raman scattering of water molecules was accounted for in the models. However, due to insufficient data availability, such as the quantum yields, chlorophyll and CDOM fluorescence were not included in the calculations. Wind speed was kept constant at 0 ms^{-1}. Solar zenith angle was determined by the time, date, and spatial coordinates in Table 5.1. Hydrolight further assumes the upper boundary to be the air-water interface, the lower boundary to be either the physical limit of the water column or some determined plane below which the water remains homogeneous with depth, which in this case was 45 m. The model assumes that radiant flux is only incident upon the upper boundary and no radiant flux comes from below the lower boundary.

Optical Closure

It is anticipated that our atmospheric boundary conditions of 0 % and 100 % cloud cover should adequately encompass the variability of surface irradiance, and if the model is accurate, field measurements of sub-surface PAR should fall between the 0 % and 100 % cloud cover estimates. An optical closure study was completed to test this hypothesis. For this study, profiles of PAR from Trios Ramses irradiances measurements were compared to the simulated PAR values through the water column for the two sets of atmospheric conditions. Trios Ramses irradiance profiles were produced for all stations except station 29.

Table 5.1 gives estimates of the sky conditions at the time of each station. Figure 5.10 suggests that all but the 13:35 UTC cast were experiencing almost clear conditions. It is possible that no clouds were obscuring the incoming solar irradiance at the time of measurement for most of these observations, or that the cloud was sufficiently thin to have minimal impact. Furthermore, the weather conditions were described in the lab notes as partly cloudy and overcast at the 13:35 and 14:35 UTC casts respectively. This is reflected in Figure 5.10d. The effect of these changing weather conditions are accounted for later in this chapter.

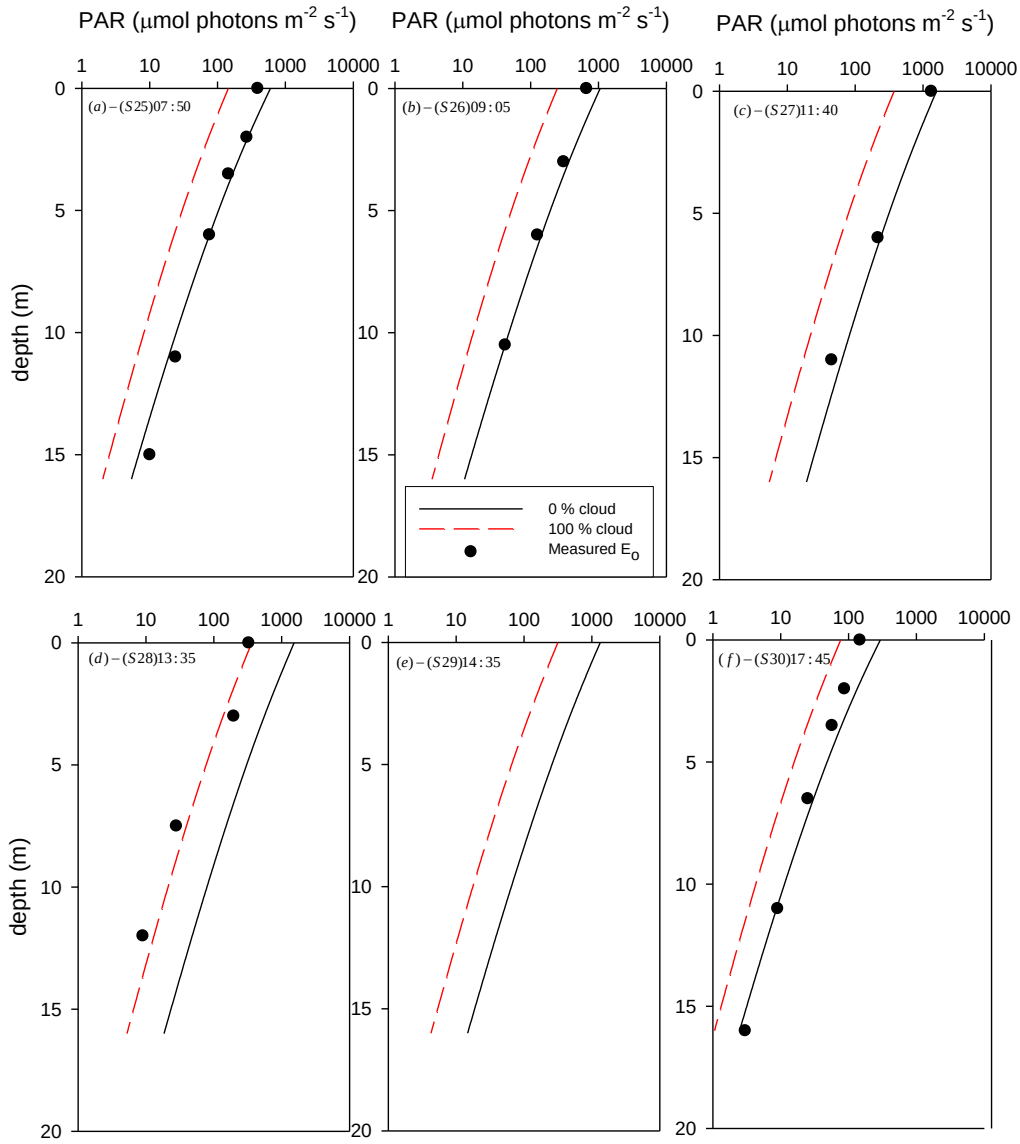

Figure 5.10: Depth profiles of PAR from Trios downwards irradiance measurements (circles) are broadly consistent with the maximum and minimum estimates of PAR (corresponding to 0 % and 100 % cloud cover) from Hydrolight simulations.

Figure 5.10 illustrates the broad similarities in the measured Trios PAR data and calculated Hydrolight underwater PAR profiles.

Based on Figure 5.10, the modelled PAR values are sufficiently reliable to be used for determination of water column gross primary productivity. This allows simulation of underwater light fields across the full period of daylight hours and under controlled cloud cover conditions.

Initial physiological parameters were determined from 450 nm fluorescence light curves and the underwater light fields determined as PAR (µmol photons m^{-2} s^{-1}). Figure 5.12 is a flow diagram of the steps required to calculate daily and column-integrated gross primary productivity (DCIGPP).

For each sample, an estimate of photochemical efficiency is obtained by fitting the Webb *et al*. (1974) model to measured FRRf fluorescence transients. Equations 5.10 and 5.11 show the models fitted to light-limited (PAR < E_K) and light-saturated (PAR > E_K) parts of a fluorescence light curve.

$$F_q'/F_m' = \alpha \cdot E_k \cdot \left(1 - e^{-PAR/E_k}\right) \cdot PAR^{-1} \tag{5.10}$$

$$F_q'/F_m' = \alpha \cdot E_k \cdot \left(1 - e^{-\frac{PAR}{E_k}}\right) - \beta \cdot E_{k\beta} \cdot \left(1 - e^{\frac{-PAR-E_k}{E_{k\beta}}}\right) \cdot PAR^{-1} \tag{5.11}$$

The electron transport rate (ETR) for a sample is obtained by multiplying by the relevant PAR value, as per equation 5.12.

$$ETR = F_q'/F_m' \cdot PAR \tag{5.12}$$

There is an implicit dependence on concentration as the units for ETR are µmol electrons m^{-2} s^{-1}. Therefore, in order to extend analysis to the full water column it is necessary to scale for both changes in PAR and biomass with depth, giving equation 5.13.

$$ETR(z) = F_q'/F_m' \cdot PAR \cdot \frac{Chl(z)}{Chl(z_o)} \tag{5.13}$$

where z_o is the sample depth. As chlorophyll samples are only ever available at discrete depths, and Figure 5.11 shows a reasonable correlation between BBFL2 chlorophyll fluorescence and chlorophyll, equation 5.13 can be re-expressed as equation 5.14.

$$ETR(z,t) = F_q'/F_m'(t) \cdot PAR(z,t) \cdot \frac{F(z,t)}{F(z_o,t)} \tag{5.14}$$

where all parameters are now time-resolved and F(z,t) and $F(z_o,t)$ are theBBFL2 fluorescence normalised to the value obtained at the sample depth.

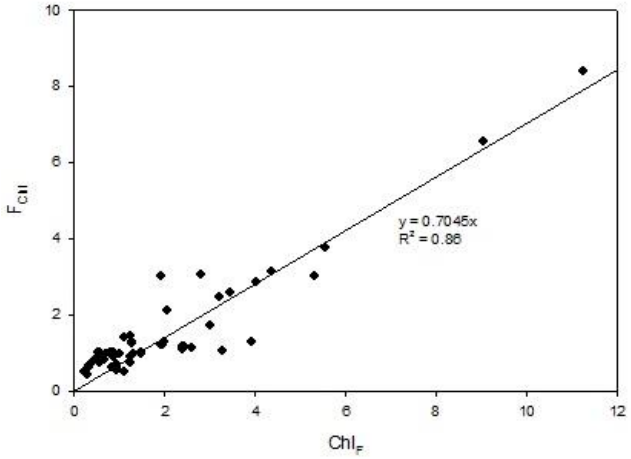

Figure 5.11: Relationship between BBFL2-derived fluorescence and surface values of chlorophyll estimated from F_o measurements on FRRf.

ETR can be converted to an estimate of gross primary productivity (equation 5.15) by applying the global mean value of the electron to carbon exchange factor ($\varphi_{e,C}$), discussed earlier in this section.

$$GPP(z,t) = \frac{ETR(z,t)}{\varphi_{e,C}} \tag{5.15}$$

Finally, daily and column-integrated GPP is obtained by integration as in equation 5.16.

$$GPP_{d,c} = \int_{t_1}^{t_2} \int_{0}^{z_{max}} GPP(z,t)dz\,dt \tag{5.16}$$

where t_1 and t_2 represent sunrise and sunset and z_{max} is the maximum depth recorded by both the BBFL2 and irradiance meter.

This time resolved model of GPP can be compared with the more traditional approach of simply extrapolating a single set of photophysiology observations over the complete day length. This time averaged approach uses equation 5.17 to give a daily integrated estimate of GPP at a given depth.

$$GPP(z,t)_{day} = \frac{GPP(z,t)_{single}}{1000} \cdot 12 \cdot 86400 \tag{5.17}$$

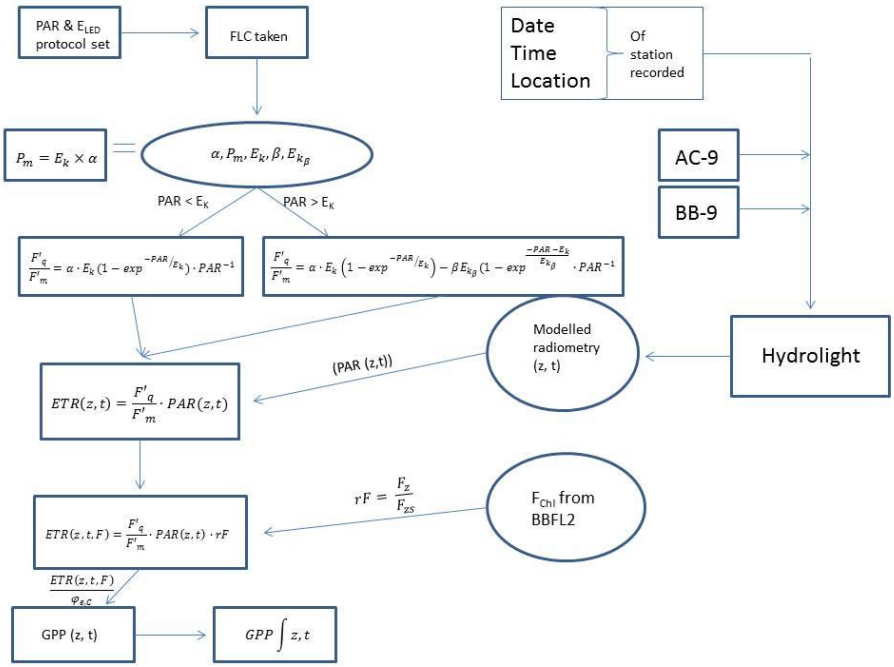

Figure 5.12: An idealised model of the process of calculating daily, column integrated gross primary productivity from FRRf data and IOP inputs with simplified versions of equations 5.10 and 5.11.

Figure 5.12 shows a simplified flow diagram of the processes involved in going from field measurements using the FRRf, AC-9, BB-9, and BBFL2 to estimating daily and column-integrated GPP. This flow diagram is a visual representation of equations 5.10 to 5.17. Knowledge of the inherent optical properties at a sample location is sufficient to build models of the underwater light fields, which can then be fed into the FLC curve equations 5.10 and 5.11 yielding a depth-dependent electron transport rate (ETR(z)). An estimation of the electron to carbon exchange rate allows for conversion of ETR into GPP. As discussed previously, the exchange rate utilised throughout this chapter is 10.9 mol e^{-1}(mol C)$^{-1}$. Blank corrections are made after the FLC is taken but before further downstream calculations.

5.4 Calculating the Daily and Column Integrated Gross Primary Productivity at Loch Fyne Using Fast Repetition Rate Fluorometry: April 11, 2015

Accounting for Diel Variability

Photophysiology varies spatiotemporally as a result of changing environmental conditions. This extrinsic variability has a direct effect on the ability of phytoplankton to effectively

perform photosynthesis. Six fluorescence light curves (FLC) were recorded from discrete water samples taken at a specific sample depth in the water column across the day. Traditionally, casts are made as close to solar noon as possible so as to match up with satellite pass-overs which tend to occur around this time to optimise the signal received from the ground (McCoy, 2005). The aim of these measurements was to identify whether the time of

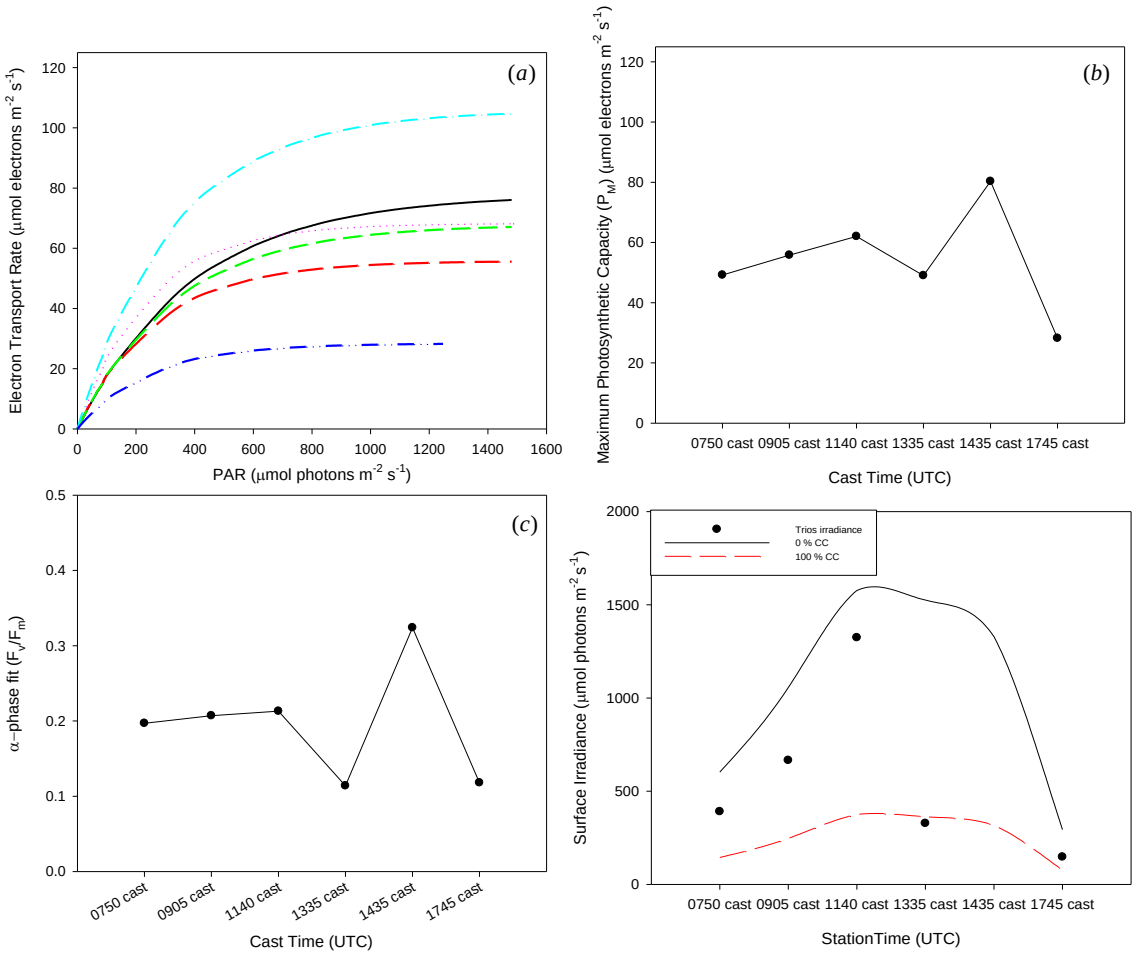

Figure 5.13: (a) FLC curves for each station were plotted with the difference in photosynthetic capacity clearly varying with the time of day. (b) The light-saturated values of P_M from the complete fit for each FLC as calculated by FastPro8 are plotted. (c) The alpha phase 'fit' value of F_v/F_m is shown for each station. The alpha-phase parameter is the initial slope of the curves from Figure 5.13a and is often thought of as a measure of the light utilisation efficiency. The α-phase estimates of F_v/F_m show strong variability in light utilisation efficiency after noon (d) Trios Ramses sensor determined below surface irradiance (0 m) for each cast except 14:35, where no data were recorded.

day that a sample is measured affects the overall primary productivity calculated, and if so

by how much. Figure 5.13b-c shows the effect of changing solar irradiance with solar zenith angle on the FLC parameters P_M and α.

The first cast was taken following sunrise (05:27 UTC) at 07:50 UTC and gave a light-saturated value of P_M of 49.2 ± 0.1 (SE) µmol electrons m^{-2} s^{-1} (Figure 5.13b). P_M progressively increased to 62 ± 0.1 µmol electrons m^{-2} s^{-1} at 11:40 UTC. This increase in the photosynthetic capacity is commensurate with the increase in solar irradiance and increasing availability of photons to drive photosynthesis. Solar noon occurred at 12:22 UTC (42°), however, at the 13:35 cast, a reduction in the maximum photosynthetic capacity of the phytoplankton was observed with an FLC-derived P_M of 49 ± 0.3 µmol electrons m^{-2} s^{-1}. Figure 5.13d shows the surface irradiance determined by the Trios Ramses sensor. This shows the increase in solar irradiance with solar zenith angle and the influence of overhead environmental conditions (11:40 to 13:35). Despite the rapidly changing irradiance conditions through the morning, the estimates of daily GPP remain stable in Figure 5.14b, indicating that whilst solar irradiance is important, it is not the only determinant factor. Station 29 at 14:35 UTC sees a recovery in the photochemical pathway producing the highest value of P_M recorded on the day at 80.3 ± 0.1 µmol electrons m^{-2} s^{-1}, this increase in the photochemical efficiency appears to be concurrent with a reduction in the solar zenith angle, reducing the stress on the energy dissipation pathways of the *in situ* phytoplankton. The final measurements at this station were made at 17:45 UTC with sunset occurring at 19:19 UTC. The solar zenith angle at this point was 21°, half of the calculated angle for the meridian. The reduced number of incident photons resulted in a P_M of 28.2 ± 11.3 µmol electrons m^{-2} s^{-1}. The standard error recorded for this FLC is two orders of magnitude larger than for the preceding FLCs and may indicate an inadequate fitting process. Figure 5.13a shows the Loch Fyne FLC fits for each cast. These show that not all stations reached saturation through the course of the measurement. Figure 5.13c shows the α-phase derived value of the photochemical efficiency. This varies similarly to P_M in Figure 5.13b and is taken as a regression of the light-limited phase of the FLC to zero irradiance, giving an estimate of the dark-regulated photochemical efficiency.

Effect of Model Temporal Resolution on GPP Estimates

Using the standard OCRS setup of a single noontime (13:35) measurement as our starting point, three estimates of GPP were made with increasing levels of complexity. The simplest

model is the time-averaged model, which employs a single FLC and underwater light field and integrates the resulting instantaneous GPP over the full day. This model returns six values of GPP as the effect of taking FLCs at different times of day is tested. The partially resolved model increases in complexity by time resolving the underwater light fields whilst maintaining a single FLC. A single set of IOPs was used for Hydrolight modelling as they were found not to vary over the course of the day (see Figure 5.3a-b). This corresponds to a likely scenario where an IOP profile is available along with a single FLC and radiative transfer modelling can be easily employed to predict underwater light fields over the course of the day. For these estimates of GPP, the effects of cloud cover were not taken into consideration and underwater light fields were modelled for 0 % cloud cover.

The fully time resolved GPP model used individual station FLC parameters with time resolved underwater light fields and requires a great deal more sampling effort as multiple casts must be made to record the change in the FLCs over the course of the day. The fully resolved model is assumed to provide the best estimate of GPP. However, given the extra effort required for this approach, the question is what is the impact of various levels of approximations?

Table 5.2: Increasing levels of complexity for daily and column-integrated gross primary productivity based on equation 5.16 and 5.17.

Approach	PAR	FLC	Sampling Effort
Time averaged	Single profile	Single profile	Single Cast
Partially time resolved	Time resolved	Single profile	Single Cast
Fully time resolved	Time resolved	Time resolved	Multiple Casts

Table 5.3: Estimates of DCIGPP were made with differing levels of complexity, a time-averaged, partially time resolved and fully time resolved model.

		DCIGPP (mg C m^{-2} d^{-1})		
Station	Time	(Time averaged)	(Partially resolved)	(Fully resolved)
25	07:50	175.8	255.9	
26	09:05	273.9	262.2	
27	11:40	318.2	239.6	257.9
28	13:35	290.3	228.5	
29	14:35	425.1	359.6	
30	17:45	65.3	144.3	

Table 5.2 shows the difference in effort required between the three different approaches to daily and column-integrated estimates of gross primary productivity.

Time averaged estimates range from 65.3 to 425.1 mg C m^{-2} d^{-1}, a huge range of uncertainty that straddles the best estimate value of 257.9 mg C m^{-2} d^{-1} by a range of approximately 84 %. This range of uncertainty is dramatically reduced by resolving the temporal variability of the light field, with the partially resolved model varying between 144.3 and 359.6 mg C m^{-2} d^{-1}. This gives an uncertainty of approximately 17 %. It would be possible to further reduce the error in the measurements by restricting FLC data to higher solar zenith angles.

The time-averaged model was consistently less accurate than the partially and fully time resolved models. This appears intuitively correct as multiple data points for the environmental conditions across the day give a more nuanced understanding of the algal dynamical response. From this model, the least accuracy was found at the stations recording the highest and lowest photosynthetic capacities (station 29 (14:35) and station 30 (17:45)).

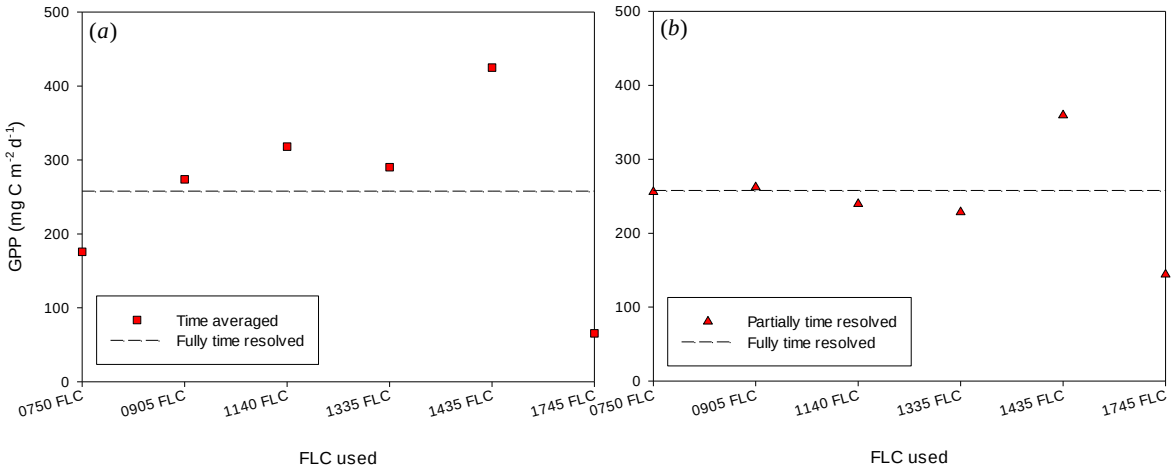

Figure 5.14: (a) The time-averaged and fully time resolved GPP models were compared. The time-averaged model shows greater variability farther away from solar noon. (b) The partially time resolved and fully time resolved models are compared. Calculated GPP up to 13:35 were broadly similar to the fully time resolved model with greater variability at 14:35 and 17:45.

From the limited Loch Fyne dataset, the least accurate method of estimating daily and column-integrated GPP is through the use of a time-averaged model. The alternative to this is to apply a partially time resolved model. Our dataset suggests that for measurements made up to and including 13:35, the partially time resolved model is sufficient to estimate GPP, as in Figure 5.14b, when compared to the fully time resolved model. Furthermore, from the Loch Fyne time series, there was no advantage gained by recording the FLC at lunchtime or before.

However, as mentioned, the highest and lowest photosynthetic capacities were recorded following solar noon resulting in the greatest deviation from 257.9 mg C m^{-2} d^{-1}. In order to identify whether there is a trend present, further time series are required. The conclusion from this work is that using a single FLC with time resolved underwater light fields is sufficient to make a good approximation of the daily, column-integrated gross primary productivity at a location. This potentially negates the requirement to sit at a single location for a full day to estimate the daily GPP and confirms the value of FLC data for predicting photophysiological response to diurnal changes in light climate.

5.5. Sensitivity Analysis of Factors Affecting DCIGPP Estimates

Optical Model Complexity and Spectral Light Availability

The DCIGPP model is essentially the integral product of the FLC-derived parameters measured by the FRRf, the underwater light field modelled using Hydrolight and the experimentally determined *in situ* chlorophyll concentration determined using the BBFl2 (equation 5.16). The aim of this study was to determine how much influence each parameter has on the final estimate.

DCIGPP and the impact of cloud cover

Figure 5.13d shows the changing surface solar irradiance over the course of the day at Loch Fyne. From this Figure, it can be seen that there is a large drop off in the surface irradiance around lunchtime. Given that solar irradiance should, under optimal conditions, be at its greatest at this time, it must be anticipated that this drop in signal was due to the impact of atmospheric cloud cover.

Hydrolight models for the effect of cloud cover using RADTRAN-X, an atmospheric irradiance model developed by Gregg and Carder, (1990). RADTRAN-X is designed to predict the direct and diffuse solar spectral irradiances incident upon the sea surface. Within Hydrolight, this is set as a percentage of the sky covered by cloud given the solar zenith angle and other parameters. Cloud cover was modelled for two conditions here: clear skies, and completely cloudy, where these are 0 % cloud cover and 100 % cloud cover respectively.

GPP estimates were made using only the 100 % cloud cover modelled light fields and were then compared to the 0 % atmospheric cloud cover estimates as shown in Figure 5.15.

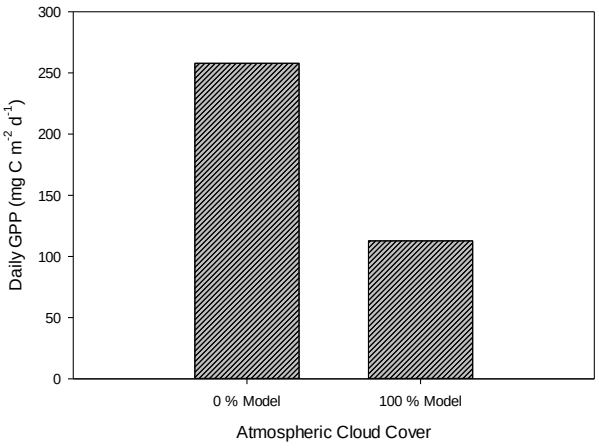

Figure 5.15: Vertical bar chart showing the difference in estimated GPP in the MORSE productivity model depending on the cloud cover percentage input to RADTRAN-X.

100 % atmospheric cloud cover results in a 56 % reduction in the primary productivity as shown in Figure 5.15. This significant reduction highlights the importance of taking into account the local weather conditions when estimating time-resolved GPP. For example, if an FLC and IOP measurement was made at 12:15 in the afternoon when the skies were clear but it had been overcast and raining the entire rest of the day then the propagation of these data for the whole day would result in a very poor representation of the real GPP for that region at that time.

Influence of Relative Fluorescence on Estimates of Gross Primary Productivity

The relative fluorescence from the BBFL2 (rF_{Chl}) is essentially a proxy for chlorophyll concentration (see Figure 5.11). When modelling the electron transport rate across the full day what level of resolution is required to adequately estimate gross primary productivity?

Three levels of complexity were employed in this study: a single, vertically uniform profile; single depth resolved profile; and time and depth resolved profiles with the aim of identifying how much difference this makes to the overall GPP, as shown in Figure 5.16. Each vertical profile is the measured F_{Chl} taken at each time throughout the day at Loch Fyne. The underwater light field for the noon station (station 28- 13:35) was used to calculate ETR through the water column.

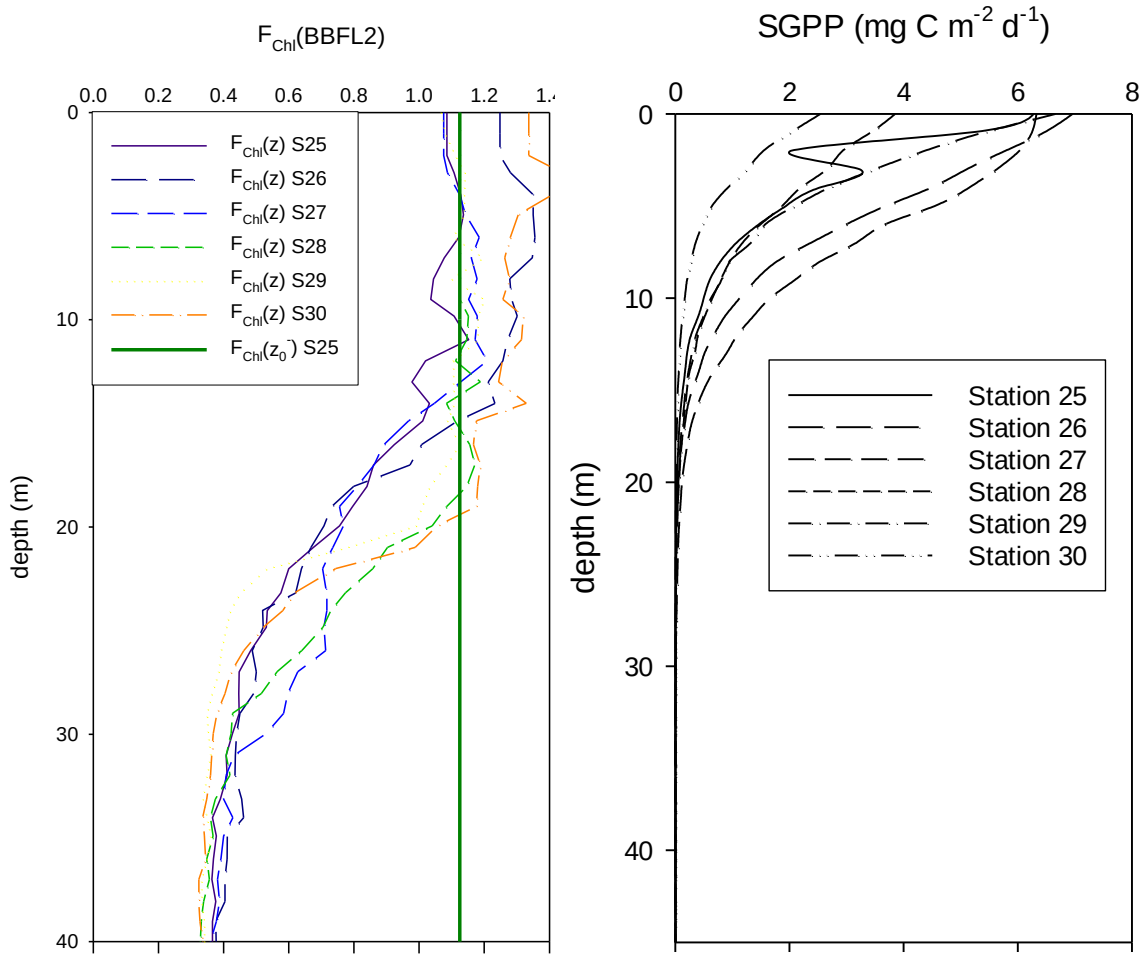

Figure 5.16: (a) Model complexity was tested using three different models of $F_{Chl}(z)$. A single vertically uniform profile of the surface F_{Chl} from the 13:35 cast was produced (dot and dashed line) whilst the solid profile is the time and depth resolved profile for 13:35(b) The depth-resolved profiles of GPP at Loch Fyne are shown. Productivity drops off drastically below 10 m due to the limited light availability generally below this depth.

Figure 5.17 shows the impact of increasing levels of complexity in the fluorescence profiles. From not accounting for the influence of fluorescence to our best estimate of multiple fluorescence profiles throughout the day, there is a 12.5 % increase. However, applying only a surface value or using a uniform surface profile as in Figure 5.16 produces a daily GPP estimate that is a negligibly different 4 % less than our best estimate. This 4 % change in values of GPP is likely a result of the fact that primary productivity is dominated by well-lit surface waters as can be seen in Figure 5.16b where it is clear that the values of GPP drop off rapidly below 10 m due to the limited light availability for photosynthesis.

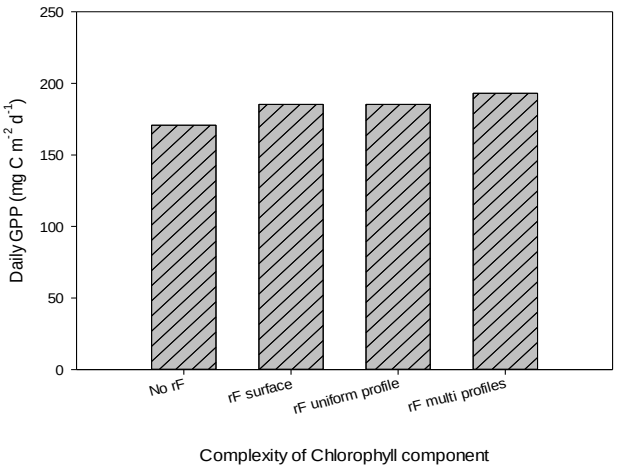

Figure 5.17: Increasing layers of complexity were added to the fluorescence profiles in the calculation of productivity using the DCIGPP model.

Making a Best Estimate of GPP at Loch Fyne Using the DCIGPP Model

Using the information obtained from the Trios Ramses sensors to inform on the overhead sky conditions at Loch Fyne it is possible to incorporate this information into the DCIGPP model to produce a best estimate of GPP through the day.

Using the boundaries set on incoming irradiance by the Hydrolight calculations, it was determined that two stations: 13:35 and 14:35 UTC were measured at times when the incoming irradiance were at minima (Figure 5.13d). For these two stations (stations 28 and 29, respectively), the modelled underwater light field for 100 % cloud cover was applied instead of the 0 % cloud cover models that are used for the four other stations.

Figure 5.18 shows the effect on daily GPP by approximating for the actual weather conditions at Loch Fyne on April 11th, 2015. The best estimate of GPP is 193.1 mg C m^{-2} d^{-1}, which is 25.2 % smaller than the 0 % cloud cover boundary.

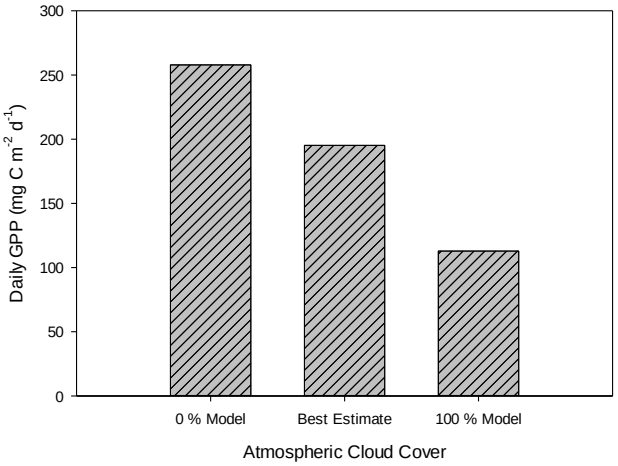

Figure 5.18: The 0 % and 100 % atmospheric cloud conditions create boundaries within which an estimate of GPP can be made. The best estimate of daily productivity more closely resembles the 0 % cloud cover conditions.

The effect of cloud cover has a large effect on the magnitude of the incoming irradiance and thus, impacts on the estimate of daily productivity. When approximating productivity using modelled underwater light fields, it is therefore important to account for the actual light conditions during sampling in an effort to more accurately approximate the actual productivity at the sampling site. Another source of uncertainty in estimating GPP using the FRRf method would be the uncertainty in the electron to carbon exchange factor.

Using the global mean electron to carbon exchange factor ($\varphi_{e,C} = 10.9$), our best estimate of gross primary productivity using the DCIGPP model gives 193.1 mg C $m^{-2}d^{-1}$. However, considering the range of uncertainties in $\varphi_{e,C}$ (10.9± 6.9 mol e^- (mol C)$^{-1}$) and restricting to the theoretical minimum number of electrons required of 4 mol e^- (mol C)$^{-1}$ produces GPP estimates of 118.2 and 526.2 mg C $m^{-2}d^{-1}$. It is clear from these numbers that being better able to approximate the electron conversion to carbon rate would have a large impact on the quality of a GPP estimate.

As a result of the optical model complexity and spectral light availability data, an order of priority for optical complexity can be suggested for estimating daily, column-integrated GPP. These are the impact of cloud cover/ *in situ* weather conditions being of highest priority, followed by the effect of the fluorescence depth profile, and lastly the impact of using multiple light fields over the day. Constraining $\varphi_{e,C}$ is, however, probably more important than each of these, but requires introduction of relatively complex ^{14}C measurements.

Development of an Optimal Sampling Strategy

The aim of this study was to make an estimate of the daily and column-integrated gross primary productivity from *in situ* measurements of the inherent optical properties and ship-board FRRf measurements. This was refined from an initial *best estimate* of 257.9 mg C m^{-2} d^{-1} where all underwater light fields were fully resolved for 0 % cloud cover, as well as individual BBFL2 profiles, and six individual FLC measurements were made. This level of resolution is not feasible on a standard research cruise that would not normally have the time to sit at a single location for a full day.

In the collection of IOP data, several casts were made but it was found that these data were all very similar above the euphotic zone (Figure 5.3a-b) and so a single cast of IOP measurements would be sufficient to model the underwater light fields. F_{Chl} showed greater variability across the day than the IOPs (Figure 5.3c) and may present a source of uncertainty when integrating across the whole day. Table 5.3 showed the effect of accounting for different levels of complexity in the DCIGPP model. Using a single set of measurements across the day (the time-averaged GPP model) showed the greatest variability across the day with a range in daily GPPs of 359±124 mg C m^{-2} d^{-1}. The partially resolved model, which used a single FLC profile but multiple underwater light fields saw a reduction in the range and the uncertainty in each measurement (Δ= 215±69).The median of each partially resolved GPP estimate was 4 % lower than the fully resolved *best estimate* at that time.

The overriding factor that had the greatest impact was accounting for the overhead weather conditions at the time of measurement. The atmospheric cloud cover was accounted for in Hydrolight using two settings: 0 % and 100 % cloud cover. In producing our best estimate of GPP, stations were assigned an underwater light field that best approximated the observed overhead cloud cover when making the field measurement. This resulted in an absolute best estimate of GPP of 193.1 mg C m^{-2} d^{-1}.

An optimal sampling strategy would have several FLC measurements being made across the day with multiple casts for IOPs being made. However, in the absence of this, a single FLC with multiple underwater light fields that are optimised to account for overhead cloud cover is sufficient to make an estimate of the daily, column-integrated gross primary productivity. Validation using ^{14}C-incubation would be useful at this stage, however, this was not available during He442.

5.5 Inter-comparison of Estimates of Net Primary Productivity and Gross Primary Productivity

Applying the OCRS models in section 5.3, estimates of ΣNPP were produced and are shown in Table 5.4. From Table 5.4, it is clear that the different models produce quite separate estimates of NPP using the He442 data. The simpler Falkowski (1981) model produces estimates of NPP that are an order of magnitude smaller than the VGPM and CbPM models. Both the VGPM and CbPM models produced good agreement in their estimates of NPP. The three ocean colour models are conFigured to provide estimates of net primary productivity, which is in contrast to the gross primary productivity estimated by the DCIGPP model.

An approximation of NPP was made for the DCIGPP model using estimates from the literature. These can be seen in Table 5.4 where low and high approximations of respiration contributions are made, although global ocean respiration rates are taken to be high (del Giorgio and Duarte, 2002). A large body of inconclusive research exists in the literature with no estimate of respiration rates being agreed upon, for a variety of factors including geospatial and temporal location, species present, and nutrient status all contributing to these different estimates. Estimates of respiration rate vary from 20 %, 36 %, 50 %, 70 % through

Table 5.4: Instantaneous estimates of NPP for four different productivity models for six temporally-resolved stations in Loch Fyne during He442. Solar noon was recorded as 12:22UTC.

	Model Used (mg C m^{-2} d^{-1})					
Cast Time	F81	VGPM	CbPM	DCIGPP	DCIGPP - R_{low} (20 %)	DCIGPP - R_{high} (97%)
07:50	0.25	1.01	1.39	29.2	23.3	0.9
09:05	0.36	1.00	1.10	45.6	36.5	1.4
11:40	0.52	1.20	1.03	53.0	42.4	1.6
13:35	0.50	1.18	1.07	23.2	18.6	0.7
14:35	0.43	1.01	0.89	31.1	24.9	0.9
17:45	0.07	0.19	0.26	10.9	8.7	0.3

to 100 % of daily carbon uptake making it difficult to assume any particular value (Meera and Barber, 2004; Hashimoto *et al.,* 2005); Balkanski *et al.,* 1999; Church *et al.,* 2009; Langdon,

1993). Low estimates of respiration were taken from Meera and Barber (2004) whom suggested respiration was 20 % of daily carbon uptake, with the high estimates of respiration taken from Siegenthaler and Sarmiento (1993) whom suggest up to 97 % global respiration rate. Without accounting for respiration, the DCIGPP model estimates are much larger than estimates made using the NPP models. However, by taking the NASA estimate of respiration, it is possible to commensurate the DCIGPP values with those of the VGPM and CbPM estimate. A primary motivation in conducting this study was to make estimates of respiration by knowing NPP and GPP. The order of magnitude variation in NPP estimation between the Falkowski (1981) and VGPM and CbPM models makes this difficult. What is clear though is that by assuming a very high respiration rate, the DCIGPP model finds good agreement with the VGPM and CbPM models.

The DCIGPP model identifies a reduction in the photosynthetic rate at around solar noon (station 28 at 13:35). Models based on surface chlorophyll and carbon values, which identify a continued rise in photosynthetic rate to lunchtime, do not account for this. The late morning and early afternoon estimations of GPP are also larger than the equivalent NPP calculations as would be expected.

In the context of using the FRRf and *in situ* IOP measurements to estimate NPP and GPP, the associated uncertainties (1σ) range from 39 to 48 % of the averaged daily GPP. Uncertainties have been minimised as much as possible by maintaining close compliance with the then established sampling protocols and the instruments having been recently calibrated. In recent years, it has become apparent that there is a pressing need to assign uncertainties to ocean colour remote sensing products. This is traditionally done by error propagation or validating the data against field measurements but this has its own problems as the spatiotemporal scale of field measurements is considerably smaller than that achieved by OCRS.

Error propagation involves knowing the uncertainties associated with the input values and model parameters. This method of uncertainty estimation is useful for understanding the impact of varying a model parameter or input on the product (Brewin *et al*., (2017). Ocean colour-derived products aim for a product accuracy goal of ± 35 %, however the OC4V4 algorithm for calculating chlorophyll from the blue: green reflectance ratio finds that in turbid waters the predicted chlorophyll concentration can be between 2-5 times larger than the observed value (McKee *et al*., 2007). At higher chlorophyll concentrations, the predictions can be five times larger than the observed values and is much larger than the product

accuracy goal. These uncertainties would rise even higher in coastal waters (Dierssen, 2010). Furthermore, Sheng *et al*. (2014) applied a Monte Carlo method to the carbon biomass productivity model (CbPM- assessed in our study) to propagate the error through the model. The uncertainties propagated were the chlorophyll estimate, particulate backscattering at 443 nm, and the PAR value. Sheng *et al*. found that in their study, the CbPM coefficient of variation was on average, 110.5 %, with CbPM values giving a bias of 12 %. Sheng *et al*. found that the estimation of chlorophyll had the greatest associated uncertainty in their model.

It is found that when comparing our model of daily, column-integrated gross primary productivity that the associated uncertainties in our measurements are not significantly larger than those estimated using ocean colour remote sensing. Improvements in our sampling strategy with improved understanding of the parameters being measured would also contribute to improving the associated uncertainties in the DCIGPP model.

5.6 Conclusions

The collection of an entire day's worth of IOP and physiological data allowed for the determination of daily, column-integrated gross primary productivity and analysis of the minimum requirements to adequately estimating GPP as well as building an understanding of how each of the key parameters in the DCIGPP productivity model affects the final estimate. The comparison of the DCIGPP productivity model to three distinct models for determining NPP from the literature gave useful insight into determining the quality of the numbers produced by it.

The main conclusion from this work was the identification of a minimum level of complexity required to adequately model the daily, column-integrated gross primary productivity. The best possible estimate, accounting for overhead weather conditions, *in situ* fluorescence profiles and individually modelled underwater light fields gave a GPP estimate of 193.1 mg C m^{-2} d^{-1}. The parameter with the least effect, in isolation, was in accounting for multiple light fields across the day instead of using only a single light field. By only measuring a single set of IOPs at a location, it is possible to return a good estimate of the depth and column-integrated GPP over the day. Figure 5.17 showed that there was an improvement in the estimate of DCIGPP by accounting for rF_{Chl}. This only impacted on the upper 10 m of the

water column as Figure 5.16b shows that GPP falls away rapidly with depth due to the decreasing light availability. Finally, the overhead sky conditions has the most impact on GPP estimates. By accounting for the cloudy weather that occurred in the afternoon of 11th April, 2015, the DCIGPP estimate was reduced from 257.9 mg C m^{-2} d^{-1} to 193.1 mg C m^{-2} d^{-1}, a 34 % reduction showing the impact that the spectral light availability has on the phytoplankton cells's ability to perform effective photosynthesis.

The DCIGPP productivity model when compared to established models from the literature appears to considerably overestimate carbon fixation rates until it is adjusted for respiration. Estimates of respiration rates vary considerably depending on many conditions including spatiotemporal location and the nutrient status and so are difficult to state with certainty. However, Siegenthaler and Sarmiento (1993) suggest respiration rates as high as 97 % of the carbon fixation rate. When this rate is subtracted from the daily, column-integrated GPP, numbers commensurable with those produced by all three NPP model calculations are produced, suggesting that our estimates, whilst unproven, are not completely impossible either.

To conclude, the analysis of the Loch Fyne dataset suggests that it is possible to make a good approximation of the daily, column-integrated gross primary productivity at a location using a single measurement of photophysiology and the IOPs. Our data possibly suggests that it is better to make the measurement at some point prior to solar noon, however, a more prudent approach may be to not make the measurement at minima or maxima of environmental conditions so as to avoid any dramatic variations in the physiological state of the phytoplankton in the water column. Using the *in situ* IOPs, it is possible to calculate upper and lower boundaries for the underwater light fields throughout the day. By mapping this information with the actual weather conditions on site and accounting for the chlorophyll concentration, either using a single vertical profile or extrapolated from the FRRf-estimated chlorophyll concentration, it is possible to make a fair estimate of daily, column-integrated gross primary productivity using a single measurement per day.

6. Summary and Recommendations for Future Work

6.1. Conclusions

Phytoplankton are on the front line of the effects of anthropogenic climate change. The FRRf is a key tool for establishing algal physiological state and it is essential that protocols for making measurements are based on sound understanding of its performance and the underpinning biology. In the course of this thesis, the limits of performance of the FRRf with an optimised measurement protocol were outlined, which to date is the only attempt that has been made at optimising FastOcean FRRf performance in a rigorous manner. In chapter 4, the results of a research cruise around UK coastal waters were shown with the aim of understanding relationships between derived physiological parameters from the FRRf and associated physical, optical, and biogeochemical parameters. Data collected over the course of a day at a single station in Loch Fyne were then used to build a model of the daily, column-integrated gross primary productivity. The calculated DCIGPP was then compared to literature models of net primary productivity from remote sensing algorithms. Accurate measurements of the algal physiological state may prove to be very useful in revealing the impact that a rapidly changing global climate has on our water systems. An ability to measure these changes in algal physiological state accurately and with confidence is a crucial first step in this process.

FastOcean Characterisation: Protocol Optimisation and Understanding Limits of Performance

A series of measurements were undertaken to test the limits of performance for the FastOcean FRRf system with the aim of establishing an optimised measurement protocol that would allow measurements to be made as quickly and efficiently as possible. This optimisation is necessary when conducting field measurements due to the time constraints involved and the potential sources of uncertainty that are introduced by inconsistent and conflicting protocols from the literature. Multiple facets of the FastOcean system are highly tuneable allowing the measurement protocol to be specific to a particular situation. However, the converse of this is that the high tunability of the FRRf protocol leads to unnecessary potential sources of uncertainty in the derived FRRf parameters and difficulty in subsequent comparisons of data from different groups.

Analysis of the hardware response found that a minimum of five hours is required prior to running measurements to allow the instrument to reach full thermal stability. There was a drop in F_o associated with the changing instrument temperature as it reached thermal stability, however, the difference in F_o was small but potentially significant in low chlorophyll waters. With that in mind, immediately switching the instrument on and running a measurement may lead to instability in the derived FRRf parameters and it is recommended that the five hour period is adhered to. The stable gain range of the photomultiplier tube was found to be between 300 V and 600 V with there being poor stability below 300 V. Above 600 V, the Milli-Q purified water signal dropped, however it was determined that it may be possible to apply a correction to measured values made with a PMT gain above 600 V, as may be necessary when operating in oligotrophic waters.

A series of measurement optimisation experiments were run to determine the impact of factors other than the instrument hardware on the derived FRRf parameters. The most important of these results was the identification of potential sources of uncertainty when using a filtered seawater blank. It was found that the pressure applied to the syringe attached to a Spartan filter when producing the filtered seawater blank can produce different blank F_o values. This potential source of uncertainty may overestimate the size of the blank value affecting the resulting measured photochemical efficiency, which may have an impact on calculation of downstream products such as the gross primary productivity. An alternative to this would be to use to the Milli-Q purified water blank or an artificial seawater blank, neither of which are able to capture the complexity or changing nature of natural waters but importantly, remain stable through a series of measurements, something that cannot be guaranteed with the filtered seawater blank.

Prior to the FRRf characterisation and measurement optimisation, a single fluorescence light curve could take upwards of one hour to complete following guidance from the manufacturer. Through a series of measurements, it was possible to show that this is not necessary and that the time taken for a single FLC can be reduced to around 20 minutes for a full FLC cycle. This is useful for conducting field surveys where time is a factor between station casts meaning it is potentially possible to perform more replicates allowing an average to be produced, something that has not been possible in our measurements up till this point. Measurements involving the replicability between sample aliquots and the number of light step repetitions showed that a single FLC would be sufficient whilst using as few as three repetitions per light step. However, experiments did show the possibility that steady-state

measurements make a difference to the quality of an FLC with a minimum steady-state period of 80 seconds for each light level recommended. The effect of using a steady-state illuminated FLC is shown in Table 3.4 on page 66 with there being a general reduction in the associated uncertainties as well as a noticeable change in the maximum electron transport rate. The inclusion of a steady-state illumination period must be balanced with the need for conducting rapid measurements when conducting field surveys. An 80 s illumination prior to every measurement of a 20 step FLC can easily double the length of time required for a measurement and so it is recommended that steady-state illumination is not accounted for in field measurements.

An important aspect of algal physiology when conducting FRRf measurements is the dark acclimation period. The dark acclimation period is often cited as necessary to ensure decay of the fast components of the non-photochemical quenching pathways and to allow all photosystem II reaction centres to re-open. This time, as per Table 3.5, has been cited as anywhere from no dark acclimation to an hour of dark acclimation showing that there is little consensus on the matter. Over the course of several experiments, we showed using two laboratory algal cultures of *D. maritima* and *A. maxima* that there was a stable period of dark acclimation common to both species. Figures 3.15a-b showed that the photochemical efficiencies of both species remained stable between 30 seconds of dark acclimation and 240 seconds (4 minutes) of dark acclimation. Beyond these periods, the photochemical efficiencies of both species dropped and did not recover to their pre-drop levels. These measurements suggest that the fast components of the non-photochemical quenching pathways have relaxed by 30 seconds and that after the 4 minute dark acclimation period, new mechanisms are beginning to impact on the photochemical pathways.

In order to test the impact of optically complex Case II waters on the performance of the FastOcean system, two sets of experiments were set up. The first tested the effects of scattering particles on FRRf performance using increasing concentrations of Kaolin with concurrent AC-9 measurements. Figure 3.18a shows the increasing Kaolin concentration and the impact on the wavelength-dependent particulate scattering coefficient, derived by the difference between attenuation and absorption measured by the AC-9. An AC-9 sub-sample of Kaolin was then measured in the FRRf with the change in F_o monitored. It was found that above approximately 30 m^{-1} of particulate scattering there was noticeable change in the signal response of the FRRf. However, even by increasing the particulate scattering coefficient to over 110 m^{-1}, there was only a 0.02 increase in F_o. This is taken to be insignificant

particularly in the context of optically complex Case II waters where the values of F are likely to be much higher compared to oligotrophic waters.

In a series of laboratory studies, increasing concentrations of coloured dissolved organic matter, where humic acid was used as a proxy for CDOM found that that for $a_{CDOM}(440)$, there was a concentration-dependent decrease in F_o and F_v/F_m with increasing concentration. The results of these laboratory studies produced different results from our field measurements. This suggests there may be two competing modes of action driving these differencess: natural CDOM fluorescence and competitive absorption. It has been found that natural CDOM is more fluorescent, due to its variable chemical make-up, than the humic acid bought from Sigma Aldrich. This lack of fluorescence in laboratory humic acid makes it more likely that competitive absorption is responsible for the concentration-dependent changes in F_o here, whereas in natural samples, it may be more due to CDOM fluorescence. The effect of CDOM on FRRf performance may be more pronounced in optically complex waters as there was a reduction in F_o of approximately 2, however, this translated into a reduction in F_v/F_m of only 0.05.

These characterisation experiments determined that the FastOcean system requires the operator to be monitoring at all times through a series of measurements. The effects of operating in coastal waters are quite small and with careful sample handling it is possible to minimise the impact of these effects on the final FRRf parameters.

We have shown here that it is possible to conduct FRRf measurements efficiently without compromising on the quality and accuracy of the measurements being made. Furthermore, we have identified a stable dark acclimation period that goes some way to advancing the debate on the required dark acclimation period required. Finally, the performance limitations of the FastOcean system in optically complex Case II waters has been found to be limited to very high CDOM absorption coefficients and particulate backscattering coefficients, which are only found in the most optically complex waters.

Multi-Instrument Analysis of UK Coastal Waters

The UK coastal waters research cruise provided an opportunity to test the FRRf alongside multiple other instruments including the AC-9, BB-9, PSICAM, and a host of biogeochemical measurements. This allowed us to determine whether the information being

derived by the FRRf was relatable with the data produced by the other instruments. This was particularly important for the *chlorophyll a* data for the cruise. Using the HPLC-determined *chlorophyll a* values, the anticipated biogeochemical and optical relationships identified in the literature were not present, see Figure 4.11a and c on page 106 and Figure 4.12a and c on page 107. It was later determined that there had been a misregistration of the dataset, however, for the purposes of this thesis, an alternative was required. The FRRf provides a chlorophyll estimate, given as the F_o value for a 450 nm excitation multiplied by a scaling factor. The standard setting on the FastPro8 software is 8 but for the He442 cruise, a scaling factor of 5.5 was found to be more appropriate. This new parameter was referred to throughout as Chl_F. Chl_F was found to correlate very well with the well-established Bricaud *et al*. (1996) relationships (see Figures 4.12b and d on page 107) as well as showing a linear relationship with a_{ph} at 450 and 676 nm. These relationships between Chl_F and independent biogeochemical and optical parameters are useful as they show that the data derived from the FastOcean system are consistent with data produced from other instruments but may require additional tuning beyond the factory set parameters.

A simple biogeo-optical partitioning system based on the concentrations of total suspended solid and Chl_F allowed the dataset to be separated into three distinct types of waterbodies with differing optical complexities. The majority of stations were found to be partition 1 stations, which are defined as being the most Case I-like in nature. The partition 2 and partition 3 stations were Case II-type waters but differed in their productivity with the partition 2 stations being based around the Bristol Channel and Irish Sea. The biogeo-optical partitioning system was unable to satisfactorily explain observed variability in the photophysiological response across geospatial locations. It is thought that changes in the biogeochemical or physical makeup of the water column are only of secondary importance compared to the impact that ambient lighting conditions have on the photophysiological response.

Impact of Spectral Light Availability on Estimates of Gross Primary Productivity: A Case Study in Loch Fyne

The effect of ambient lighting conditions, i.e. cloud cover and changing solar elevation on the algal physiological response. This was tested using data collected on the UK coastal waters cruise. On the 11th April, 2015, six casts were made over the course of a day in Loch Fyne

(see Figure 5.2 on page 144). These six fluorescence light curves were combined with the IOPs collected through the water column. By knowing the time of day and the IOPs for the water column, it was possible to calculate the underwater light fields at that location throughout the day as well as controlling for cloud cover. Two atmospheric cloud cover scenarios were calculated- 0 % cloud cover and 100 % cloud cover. These data were then used to build a daily, column-integrated model for gross primary productivity on April 11th, 2015 at Loch Fyne. Attempts were made to identify which factors contributing to the DCIGPP model have the most influence on the final estimate and what overall complexity and effort would be required to build a useful estimate of DCIGPP at a location. Finally, an attempt was made to reconcile the best estimate of DCIGPP with literature models for determining net primary productivity from ocean colour remote sensing.

When the overhead atmospheric conditions for each cast were accounted for, as well as *in situ* fluorescence profiles derived from the BBFL2 and underwater light fields for each cast were used, an estimate for DCIGPP of 193.1 gC m^{-2} d^{-1} was calculated. When this estimate was compared to the OCRS NPP models, the DCIGPP model naturally overestimated carbon fixation rates as the effects of respiration were not being accounted for. The aim was to establish what level of respiration was needed to align GPP and NPP estimates. By employing Siegenthaler and Sarmiento's (1993) suggestion of a 97 % oceanic respiration rate, it was possible to equate the DCIGPP estimates with those of the vertically generalised productivity model and the carbon biomass productivity model.

Each parameter in the DCIGPP model impacts the final estimate differently. It was found that the parameter that had the least impact on the final estimate was the use of multiple light fields across the day and that a single light field extrapolated across the day was sufficient. The parameter that had the greatest impact on DCIGPP was accounting for the most accurate overhead sky conditions at each cast. It was found that by accounting for the cloudy skies in the afternoon of the day at Loch Fyne, there was a 34 % change in DCIGPP strengthening the argument from the previous chapter that it is, indeed, spectral light availability that is driving photophysiological response in algae.

Finally, it was possible to identify an optimal sampling strategy based on the Loch Fyne measurements. It was found that a single fluorescence light curve, preferably measured at a time that does not represent an extreme in the spectral light availability (for example, early morning or evening) alongwith a single set of IOPs was sufficient to extrapolate over the

course of the day so long as the overhead atmospheric cloud cover was adequately accounted for in the calculation of the underwater light fields. The main conclusion of this work was the identification of a minimum level of complexity required to adequately estimate DCIGPP. It must, however, be noted that the FRRf estimates of GPP were not validated against independent productivity estimates, for example ^{14}C-incubation and the quality of the estimates is still uncertain.

6.2. Concluding Remarks

The FastOcean Fast Repetition Rate fluorometer provides an additional dimension to field surveys where a suite of physical, optical, and biogeochemical measurements are being made simultaneously. This work has shown that it is possible to confidently make rapid and accurate FRRf measurements of natural waters that can then be employed as part of a greater survey effort to estimate the daily, column-integrated gross primary productivity at a location. Furthermore, the DCIGPP model estimate is comparable to the estimates calculated using the VGPM and CbPM ocean colour remote sensing models when respiration is accounted for. If however, the estimates of GPP from the FRRf are taken at face value, then combining with estimates of NPP derived from OCRS algorithms gives estimates of respiration rates. The DCIGPP model is somewhat muted by the lack of independent validation of the results at this time.

This study did however find that in order for high quality FRRf measurements to be made, a great deal of fine tuning had to be performed prior to running a measurement in order to satisfy the proportion of the ADC used and $R\sigma_{PII}$ estimate. Whilst these parameters may be optimised, it is strongly suggested that they are conFigured manually as automation here introduces issues when sample blanking. With the increasing use of FRRf technology, this study provides important groundwork from which future studies are able to build their experimental protocols and gives FRRf operators reason to pause for thought when designing field surveys that aim to make estimates of algal physiological state.

6.3. Future Work

The work carried out in the course of this PhD has shown that there are some potential areas that the work may be continued and are continuing in other places, which would be beneficial to the improvement and wider spread use of the Fast Repetition Rate fluorometer:

1) Much of the work conducted in the course of this study has gone towards characterising the FRRf and optimising experimental protocols to more efficiently conduct field surveys. Further work to better improve these protocols for use in different waterbodies is suggested. For example, the impact of operating in very oligotrophic waters where the PMT gain would have to be greater than the 600 V stability range to produce an adequate signal should be addressed. Further work into elucidating the differing modes of CDOM interaction, e.g. through competitive absorption and natural CDOM fluorescence would be useful for understanding how these different modes of action can impact upon the derived FRRf parameters.
2) Measurements of dark acclimation found that there was a period of stability where the photochemical efficiency remained steady between 30 seconds and 240 seconds for two distinct axenic cultures. These may be taken as useful estimates of dark acclimation periods for laboratory samples, however, further work is required in measuring the effect of dark acclimation period on bulk samples from natural waters.
3) Estimates of gross primary productivity were made at Loch Fyne across the day and through the water column using an FRRf-led approach. ^{14}C-incubation is currently a more common means of estimating gross and net primary productivity and further work in validating the DCIGPP model using ^{14}C-incubation would be useful in helping to refine the model further.
4) Given the rapid nature of measurements using the Fast Repetition Rate fluorometer and our work here showing comparable estimates of net primary productivity to established models, a suggestion for future work is to look at automated FRRf instruments at sea in key locations around the UK coast. This would allow for a much more granular image of the state of algal physiology in UK waters all year round allowing us to better understand the impact of anthropogenic and environmental factors on the state of algal cells. However, any system that would be deployed would need to automatically take filtered samples of the water to ensure adequate blanks are produced.

Bibliography

Abdelrhman, M. (2016). Modeling Water Clarity and Light Quality in Oceans. *Journal of Marine Science and Engineering*, *4*(4), 80. https://doi.org/10.3390/jmse4040080

Adams, T., Black, K., MacIntyre, C., MacIntyre, I., & Dean, R. (2012). Connectivity modelling and network analysis of sea lice infection in Loch Fyne, west coast of Scotland. *Aquaculture Environment Interactions*, *3*(1), 51–63. https://doi.org/10.3354/aei00052

Allen, J. F., & Pfannschmidt, T. (2000). Balancing the two photosystems: photosynthetic electron transfer governs transcription of reaction centre genes in chloroplasts. *Philosophical Transactions of the Royal Society of London. Series B, Biological Sciences*, *355*(1402), 1351–1359. https://doi.org/10.1098/rstb.2000.0697

Antoine, D., André, J.-M., & Morel, A. (1996). Oceanic primary production: 2. Estimation at global scale from satellite (Coastal Zone Color Scanner) chlorophyll. *Global Biogeochemical Cycles*, *10*(1), 57–69. https://doi.org/10.1029/95GB02832

Ask, J., Karlsson, J., Persson, L., Ask, P., Byström, P., & Jansson, M. (2009). Terrestrial organic matter and light penetration: Effects on bacterial and primary production in lakes. *Limnology and Oceanography*, *54*(6), 2034–2040. https://doi.org/10.4319/lo.2009.54.6.2034

Atkinson, A., Siegel, V., Pakhomov, E., & Rothery, P. (2004). Long-term decline in krill stock and increase in salps within the Southern Ocean. *Nature*, *432*(November), 100–103. https://doi.org/10.1038/nature02950.1.

Babin, M., Belanger, S., Ellingsen, I., Forest, A., Le Fouest, V., Lacour, T., … Slagstad, D. (2015). Estimation of primary production in the Arctic Ocean using ocean colour remote sensing and coupled physical-biological models: Strengths, limitations and how they compare. *Progress in Oceanography*, *139*, 197–220. https://doi.org/10.1016/j.pocean.2015.08.008

Babin, M., Morel, A., Claustre, H., Bricaud, A., Kolber, Z., & Falkowski, P. G. (1996). Nitrogen- and irradiance-dependent variations of the maximum quantum yield of carbon fixation in eutrophic, mesotrophic and oligotrophic marine systems. *Deep-Sea Research Part I: Oceanographic Research Papers*, *43*(8), 1241–1272. https://doi.org/10.1016/0967-0637(96)00058-1

Balkanski, Y., Monfary, P., Battle, M., & Heimann, M. (1999). Ocean primary production derived from satellite data: An evaluation with atmospheric oxygen measurements. *Global Biogeochem. Cycles*, *13*(2), 257–271.

Bard, A., & Fox, M. A. (2013). Artificial Photosynthesis: Solar Splitting of Water to Hydrogen and Oxygen. *Journal of Chemical Information and Modeling*, *53*(9), 1689–1699. https://doi.org/10.1017/CBO9781107415324.004

Bannister, W. H. (1992), *The biological chemistry of the elements: The inorganic chemistry of life*: By J J R Fraústo da Silva and R J P Williams. pp 561. Clarendon Press, Oxford. 1991. ISBN 0-19-855598-9. Biochem. Educ., 20: 62–63. doi:10.1016/0307-4412(92)90039-O

Beardall, J., Ihnken, S., & Quigg, A. (2009). Gross and net primary production: Closing the gap between concepts and measurements. *Aquatic Microbial Ecology*, *56*(2–3), 113–122. https://doi.org/10.3354/ame01305

Behrenfeld, M. J., Boss, E. S., Siegel, D. A., & Shea, D. M. (2005). Carbon-Based Ocean Productivity and Phytoplankton Physiology From Space. *Global Biogeochemical Cycles*, *19*(GB1006), 1–14. Retrieved from: http://www.science.oregonstate.edu/ocean.productivity/references/GBC paper.pdf

Behrenfeld, M. J., & Kolber, Z. S. (1999). Widespread iron limitation of phytoplankton in the south Pacific Ocean. *Sceince*, *283*(February), 840–843.

Behrenfeld, M. J., & Falkowski, P. G. (1997). Photosynthetic rates derived from satellite-based chlorophyll concentration. *Limnology and Oceanography*, *42*(1), 1–20. https://doi.org/10.4319/lo.1997.42.1.0001

Behrenfeld, M. J., Halsey, K. H., & Milligan, A. J. (2008). Evolved physiological responses of phytoplankton to their integrated growth environment. *Philosophical Transactions of the Royal Society B*, *363*(1504), 2687–2703. https://doi.org/10.1098/rstb.2008.0019

Behrenfeld, M. J., O'Malley, R. T., Siegel, D. a, McClain, C. R., Sarmiento, J. L., Feldman, G. C., Boss, E. S. (2006). Climate-driven trends in contemporary ocean productivity. *Nature*, *444*(7120), 752–755. https://doi.org/10.1038/nature05317

Behrenfeld, M., & Falkowski, P. G. (1997). A consumer's guide to phytoplankton primary productivity models. *Limnology and Oceanography*, *42*(7), 1479–1491. https://doi.org/10.4319/lo.1997.42.7.1479

Belkhodja, R., Morales, F., Quílez, R., López-Millán, A. F., Abadía, A., & Abadía, J. (1998). Iron deficiency causes changes in chlorophyll fluorescence due to the reduction in the dark of the Photosystem II acceptor side. *Photosynthesis Research*, *56*(3), 265–276. https://doi.org/10.1023/A:1006039917599

Bengil, F., McKee, D., Beşiktepe, S. T., Sanjuan Calzado, V., & Trees, C. (2016). A bio-optical model for integration into ecosystem models for the Ligurian Sea. *Progress in Oceanography*, *149*, 1–15. https://doi.org/10.1016/j.pocean.2016.10.007

Benner, R., Pakulski, J. D., McCarthy, M., Hedges, J. I., & Hatcher, P. G. (1992). Bulk Chemical Characteristics of Dissolved Organic Matter in the Ocean. *Science*, *255*(5051), 1561–1564. Retrieved from http://www.jstor.org/stable/2876778

Berteotti, S., Ballottari, M., & Bassi, R. (2016). Increased biomass productivity in green algae by tuning non-photochemical quenching. *Scientific Reports*, *6*(1), 21339. https://doi.org/10.1038/srep21339

Bilotta, G. S., & Brazier, R. E. (2008). Understanding the influence of suspended solids on water quality and aquatic biota. *Water Research*, *42*(12), 2849–2861. https://doi.org/10.1016/j.watres.2008.03.018

Bishop, J. K. B. (2009). Autonomous observations of the ocean biological carbon pump. *Oceanography*, *24*(3), 162–173. https://doi.org/10.5670/oceanog.2011.65

Blanchard, G., Guarini, J., Richard, P., Gros, P., & Mornet, F. (1996). Quantifying the short-term temperature effect on light-saturated photosynthesis of intertidal microphytobenthos. *Marine Ecology Progress Series*, 134(1/3), 309-313.

Bowers, D. G., Harker, G. E. L., Smith, P. S. D., & Tett, P. (2000). Optical properties of a region of freshwater influence (the Clyde Sea). *Estuarine, Coastal and Shelf Science*, *50*, 717–726. https://doi.org/10.1006/ecss.1999.0600

Boyce, Daniel & Lewis, Marlon & Worm, Boris. (2010). Global phytoplankton decline over the past century. *Nature.* 466. 591-6. 10.1038/nature09268.

Bracher, A. (1999). Photoacclimation of phytoplankton in different biogeochemical provinces of the Southern Ocean and its significance for estimating primary production. *Berichte Zur Polarforschung*, *34(1)*, 1999) 90. Retrieved from http://epic.awi.de/26520/1/BerPolarforsch1999341.pdf

Brading, P., Warner, M. E., Smith, D. J., & Suggett, D. J. (2013). Contrasting modes of inorganic carbon acquisition amongst *Symbiodinium* (Dinophyceae) phylotypes. *New Phytologist*, *200*(2), 432–442. https://doi.org/10.1111/nph.12379

Brennan, T. M. (2008, March 25). Basic Photosynthesis. Retrieved November 06, 2017, from http://photobiology.info/Brennan.htm

Bricaud, A., Babin, M., Morel, A., & Claustre, H. (1995). Variability in the Chlorophyll-specific Absorption Coefficients of Natural Phytoplankton: Analysis and Parameterization. *Journal of Geophysical Research*, *100*(C7), 13321–13332.

Bricaud, A., & Stramski, D. (1990). Spectral absorption coefficients of living phytoplankton and nonalgal biogenous matter: A comparison between the Peru upwelling areaand the Sargasso Sea. *Limnology and Oceanography*, *35*(3), 562–582. https://doi.org/10.4319/lo.1990.35.3.0562

Calvert, S. E., & Price, N. B. (1970). Composition of manganese nodules and manganese carbonates from Loch Fyne, Scotland. *Contributions to Mineralogy and Petrology*, *29*(3), 215–233. https://doi.org/10.1007/BF00373306

Calzado, V. S., McKee, D., Trees, C., & Zibordi, G. (2011). Multi and single cast radiometric processing and merging in the Ligurian Sea.

Canuti, E., & Van der Linde, D. W. (2006). Measuring the absorption coefficient of aquatic particles retained on filter using a photo-oxidation bleaching technique. *European Commission Joint Research Centre*, *EUR 22142*, 1–13.

Capuzzo, E. , Stephens, D. , Silva, T. , Barry, J. and Forster, R. M. (2015), Decrease in water clarity of the southern and central North Sea during the 20th century. *Glob Change Biol*, 21: 2206-2214. doi:10.1111/gcb.12854

Carder, K. L., Steward, R. G., Harvey, G. R., & Ortner, P. B. (1989). Marine humic and fulvic acids: Their effects on remote sensing of ocean chlorophyll. *Limnology and Oceanography*, *34*(l), 68–81. https://doi.org/10.4319/lo.1989.34.1.0068

Caspers, H. (1970). Richard A. Vollenweider: A Manual on Methods for Measuring Primary Production in Aquatic Environments. IBP Handbook No. 12. – Oxford and Edinburgh: Published for the International Biological Programme by Blackwell Scientific Publications 1969. 213 pp. 45 . *Internationale Revue Der Gesamten Hydrobiologie Und Hydrographie*, *55*(4), 685–686. https://doi.org/10.1002/iroh.19700550415

Chisholm, S. W. (1995). The iron hypothesis: basic research meets environmental policy. Cambridge, MA: Center for Global Change Science, Massachusetts Institute of Technology. Retrieved from file://catalog.hathitrust.org/Record/012260194

Claquin, P., Probert, I., Lefebvre, S., & Veron, B. (2008). Effects of temperature on photosynthetic parameters and TEP production in eight species of marine microalgae. *Aquatic Microbial Ecology*, *51*(1), 1–11. https://doi.org/10.3354/ame01187

Cournac, L., Redding, K., Ravenel, J., Rumeau, D., Josse, E. M., Kuntz, M., & Peltier, G. (2000). Electron flow between photosystem II and oxygen in chloroplasts of photosystem I-deficient algae is mediated by a quinol oxidase involved in chlororespiration. *Journal of Biological Chemistry*, *275*(23), 17256–17262. https://doi.org/10.1074/jbc.M908732199

Cullen, J. J., & Renger, E. H. (1979). Continuous Measurement of the DCMU-lnduced Fluorescence Response of Natural Phytoplankton Populations. *Marine Biology*, *20*, 13–20.

Cullen, John & F. Davis, R. (2003). The blank can make a big difference in oceanographic measurements. *Limnology and Oceanography Bulletin*. 12. 29-35. 10.1002/lob.200413229.

de Boyer Montégut, C., Madec, G., Fischer, A. S., Lazar, A., & Iudicone, D. (2004). Mixed layer depth over the global ocean: An examination of profile data and a profile-based climatology. *Journal of Geophysical Research C: Oceans*, *109*(12), 1–20. https://doi.org/10.1029/2004JC002378

De Deckker, P., & Gingele, F. X. (2002). On the occurrence of the giant diatom Ethmodiscus rex in an 80-ka record from a deep-sea core, southeast of Sumatra, Indonesia: Implications for tropical palaeoceanography. *Marine Geology*, *183*(1–4), 31–43. https://doi.org/10.1016/S0025-3227(01)00252-3

del Giorgio, P. A., & Duarte, C. M. (2002). Respiration in the open ocean. *Nature*, *420*(6914), 379–384. https://doi.org/10.1038/nature01165

Denman, K. L., & Brasseur, G. (2007). Couplings Between Changes in the Climate System and Biogeochemistry. *Climate Change 2007: The Physical Science Basis*, *21*(7), 499–587. https://doi.org/Cited By (since 1996) 525\rExport Date 12 August 2012

Dierssen, H. M. (2010). Perspectives on empirical approaches for ocean color remote sensing of chlorophyll in a changing climate. *Proceedings of the National Academy of Sciences*, *107*(40), 17073–17078. https://doi.org/10.1073/pnas.0913800107

Dore, J. E., Lukas, R., Sadler, D. W., Church, M. J., & Karl, D. M. (2009). Physical and biogeochemical modulation of ocean acidification in the central North Pacific. *Proceedings of the National Academy of Sciences*, *106*(30), 12235–12240. https://doi.org/10.1073/pnas.0906044106

Dring, M. J., & Jewson, D. H. (1982). What Does ^{14}C Uptake by Phytoplankton Really Measure? A Theoretical Modelling Approach. *Proceedings of the Royal Society of*

London. Series B, Biological Sciences, *214*(1196), 351–368. Retrieved from http://www.jstor.org/stable/35642

Dubinsky Z. (1992) The Functional and Optical Absorption Cross-Sections of Phytoplankton Photosynthesis. In: Falkowski P.G., Woodhead A.D., Vivirito K. (eds) Primary Productivity and Biogeochemical Cycles in the Sea. *Environmental Science Research,* vol 43. Springer, Boston, MA

Durrant, J.R., Giorgi, L.B., Barber, J., Klug, D.R., Porter, G., Characterisation of triplet states in isolated Photosystem II reaction centres: Oxygen quenching as a mechanism for photodamage*, Biochimica et Biophysica Acta (BBA) - Bioenergetics*, Volume 1017, Issue 2, 1990, Pages 167-175, ISSN 0005-2728, http://dx.doi.org/10.1016/0005-2728(90)90148-W.

Edwards, A., Sharples, F., 1985. Scottish sea lochs: a catalogue. SMBA Internal Report 134, 110. Food Standards Agency, 2006. Classification of Shellfish Harvesting Areas 2006. Available from: http://www.foodstandards.gov.uk/multimedia/pdfs/classshellscot0806.pdf [Accessed: 18th March 2018]

Falk S., Maxwell D.P., Laudenbach D.E., Huner N.P.A. (1996) Photosynthetic Adjustment to Temperature. In: Baker N.R. (eds) *Photosynthesis and the Environment. Advances in Photosynthesis and Respiration*, vol 5. Springer, Dordrecht

Falkowski, P. (2000). Minireview: Rationalizing elemental rations in unicellular algae. *Journal of Phycology*, *36*, 3–6.

Falkowski, P. G. (1984). Physiological responses of phytoplankton to natural light regimes. *Journal of Plankton Resarch*, *6*(2), 295–307. https://doi.org/10.1093/plankt/6.2.295

Falkowski, P. G., & Kolber, Z. (1993). Estimation of phytoplankton photosynthesis by active fluorescence. *ICES Marine Science Symposium*, *197*(1978), 92–103.

Falkowski P.G., Kolber Z. (1990) Phytoplankton Photosynthesis in the Atlantic Ocean as Measured from a Submersible Pump and Probe Fluorometer in Situ. In: Baltscheffsky M. (eds) *Current Research in Photosynthesis*. Springer, Dordrecht

Falkowski, P. G., & Wirick, C. D. (1981). A simulation model of the effects of vertical mixing on primary productivity. *Marine Biology*, *65*(1), 69–75. https://doi.org/10.1007/BF00397069

Falkowski, P. G., & Raven, J. A. (2007). An Introduction to Photosynthesis in Aquatic Systems. *Aquatic Photosynthesis*, 1–44. https://doi.org/10.1017/CBO9781107415324.004

Falkowski, P. G., Katz, M. E., Knoll, A. H., Quigg, A., Raven, J. a, Schofield, O., & Taylor, F. J. R. (2004). The Evolution of Modern Eukaryotic. *Science*, *305*(July), 354–360. https://doi.org/10.1126/science.1095964

Ferrier, R. C., Edwards, A. C., Hirst, D., Littlewood, I. G., Watts, C. D., & Morris, R. (2001). Water quality of Scottish rivers: spatial and temporal trends. *Science of the Total Environment*, *265*(1–3), 327–342. https://doi.org/10.1016/S0048-9697(00)00674-4

Field, C. B., Behrenfeld, M. J., Randerson, J. T., & Falkowski, P. (1998). Primary Production of the Biosphere: Integrating Terrestrial and Oceanic Components. *Science*, *281*(5374), 237–240. https://doi.org/10.1126/science.281.5374.237

Fleming, G. R., Martin, J. L., & Breton, J. (1988). Rates of primary electron transfer in photosynthetic reaction centres and their mechanistic implications. *Nature*, *333*(6169), 190–192. https://doi.org/10.1038/333190a0

Franklin, D. J., Choi, C. J., Hughes, C., Malin, G., & Berges, J. A. (2009). Effect of dead phytoplankton cells on the apparent efficiency of photosystem II. *Marine Ecology Progress Series*, *382*, 35–40. https://doi.org/10.3354/meps07967

From, N., Richardson, K., Mousing, E. A., & Jensen, P. E. (2014). Removing the light history signal from normalized variable fluorescence (F_v/F_m) measurements on marine phytoplankton. *Limnology and Oceanography: Methods*, *12*(11), 776–783. https://doi.org/10.4319/lom.2014.12.776

Fry, E. S., Kattawar, G. W., & Pope, R. M. (1992). Integrating cavity absorption meter. *Applied Optics*, *31*(12), 2055–2065. https://doi.org/10.1364/AO.31.002055

Gaarder, T., & Gran, H. H. (1927). Investigations of the production of plankton in the Oslo Fjord. Copenhague: *Høst en comm*.

Galbraith, L., Gillespie, E., & Macleod, A. (2008). Scottish Sanitary Survey Project Sanitary Survey Report Loch Fyne : Ardkinglas AB 147, (July).

Geider, R. J., & La Roche, J. (1994). The role of iron in phytoplankton photosynthesis, and the potential for iron-limitation of primary productivity in the sea. *Photosynthesis Research*, *39*(3), 275–301. https://doi.org/10.1007/BF00014588

Genty, B., Harbinson, J., Briantais, J. M., & Baker, N. R. (1990). The relationship between non-photochemical quenching of chlorophyll fluorescence and the rate of photosystem 2 photochemistry in leaves. *Photosynthesis Research*, *25*(3), 249–257. https://doi.org/10.1007/BF00033166

Giordano, M., Beardall, J., & Raven, J. A. (2005). CO_2 Concentrating Mechanisms in Algae: Mechanisms, Environmental Modulation, and Evolution. *Annual Review of Plant Biology*, *56*(1), 99–131. https://doi.org/10.1146/annurev.arplant.56.032604.144052

Goericke, R., & Repeta, D. (1993). Chlorophylls a and b and divinyl chlorophylls a and b in the open subtropical North Atlantic Ocean. *Marine Ecology Progress Series*, *101*, 307–313. https://doi.org/10.3354/meps101307

Gordon, H. R. (1973). Simple Calculation of the Diffuse Reflectance of the Ocean. *Applied Optics*, *12*(12), 2803–2804.

Gordon, H. R., & Clark, D. K. (1980). Remote sensing optical properties of a stratified ocean: an improved interpretation. *Applied Optics*, *19*(20), 3428. https://doi.org/10.1364/AO.19.003428

Govindjee, Amesz, J., & Fork, D. C. (1986). *Light Emission by Plants and Bacteria*. (Govindjee, J. Amesz, & D. C. Fork, Eds.). London: Academic Press.

Govindjee (1995) Sixty-Three Years Since Kautsky: Chlorophyll *a* Fluorescence. *Functional Plant Biology* **22**, 131-160.

Hallegraeff, G. M. (2010). Ocean climate change, phytoplankton community responses, and harmful algal blooms: A formidable predictive challenge. *Journal of Phycology*, *46*(2), 220–235. https://doi.org/10.1111/j.1529-8817.2010.00815.x

Harvey, E. T., Kratzer, S., & Andersson, A. (2015). Relationships between colored dissolved organic matter and dissolved organic carbon in different coastal gradients of the Baltic Sea. *Ambio*, *44*(3), 392–401. https://doi.org/10.1007/s13280-015-0658-4

Hashimoto, S., Horimoto, N., Yamaguchi, Y., Ishimaru, T., & Saino, T. (2005). Relationship between net and gross primary production in the Sagami Bay, Japan. *Limnology and Oceanography: Methods*, *50*(6), 1830–1835.

Haumann, M., Bögershausen, O., Cherepanov, D., Ahlbrink, R., & Junge, W. (1997). Photosynthetic oxygen evolution: H/D isotope effects and the coupling between electron and proton transfer during the redox reactions at the oxidizing side of photosystem II. *Photosynthesis Research*, *51*(3), 193–208. https://doi.org/10.1023/A:1005861917596

Heikkinen, K. (1994). Organic matter, iron and nutrient transport and nature of dissolved organic matter in the drainage basin of a boreal humic river in northern Finland. *Science of the Total Environment, The*, *152*(1), 81–89. https://doi.org/10.1016/0048-9697(94)90553-3

Heinsch, F. A., Reeves, M., Votava, P., Kang, S., Milesi, C., Zhao, M., … Running, S. W. (2003). GPP and NPP (MOD17A2/A3) Products NASA MODIS Land Algorithm. *MOD17 User's Guide*, 1–57. https://doi.org/10.1111/j.1600-0447.2011.01711.x

Hemsley, V. S., Smyth, T. J., Martin, A. P., Frajka-Williams, E., Thompson, A. F., Damerell, G., & Painter, S. C. (2015). Estimating Oceanic Primary Production Using Vertical Irradiance and Chlorophyll Profiles from Ocean Gliders in the North Atlantic. *Environmental Science and Technology*, *49*(19), 11612–11621. https://doi.org/10.1021/acs.est.5b00608

Herlory, O., Richard, P., & Blanchard, G. F. (2007). Methodology of light response curves: Application of chlorophyll fluorescence to microphytobenthic biofilms. *Marine Biology*, *153*(1), 91–101. https://doi.org/10.1007/s00227-007-0787-9

Herold, A. (1980). Regulation of Photosynthesis By Sink Activity–the Missing Link. *New Phytologist*. https://doi.org/10.1111/j.1469-8137.1980.tb03184.x

Hobbs, D. M., & McCormick, N. J. (1999). Design of an integrating cavity absorption meter. *Applied Optics*, *38*(3), 456–461. https://doi.org/10.1364/AO.38.000456

Hoganson, C. W., & Babcock, G. T. (1988). Electron-transfer events near the reaction center in oxygen-evolving photosystem II preparations. *Biochemistry*, *27*(16), 5848–5855. https://doi.org/10.1021/bi00416a005

Huner, N. P. A., Maxwell, D. P., Gray, G. R., Savitch, L. V., Krol, M., Ivanov, A. G., & Falk, S. (1996). Sensing Environmental Temperature Change through Imbalances between Energy Supply and Energy Consumptiom: Redox State of Photosystem II. *Physiologia Plantarum*, *98*, 358–364.

IOCCG (2000). Remote Sensing of Ocean Colour in Coastal, and Other Optically-Complex Waters. Sathyendranath, S. (ed.), *Reports of the International Ocean-Colour Coordinating Group*, No. 3, IOCCG, Dartmouth, Canada

Jeffrey, S. W., Mantoura, R. F. C., & Wright, S. W. (1997). Phytoplankton pigments in oceanography: guidelines to modern oceanographyNo Title. *UNESCO Publishing*. https://doi.org/10.1023/A:1007168802525

Jin, P., Gao, G., Liu, X., Li, F., Tong, S., Ding, J., … Gao, K. (2016). Contrasting photophysiological characteristics of phytoplankton assemblages in the northern South China Sea. *PLoS ONE*, *11*(5), 1–16. https://doi.org/10.1371/journal.pone.0153555

Joint, I.R., Pomroy, A.J., Primary production in a turbid estuary, In Estuarine, Coastal and Shelf Science, Volume 13, Issue 3, 1981, Pages 303-316, ISSN 0272-7714, https://doi.org/10.1016/S0302-3524(81)80028-X.

Joliot P and Joliot A (1972) Different types of quenching involved in Photosystem II centers. Biochim Biophys Acta 305: 302–316 Lavergne J and Trissl HW (1995) Theory of fluorescence induction in Photosystem II: derivation of analytical expressions in a model including Exciton-Radical-pair equilibrium and restricted energy transfer between photosynthetic units. *Biophys J* 68: 2474–2492

Joliot, P., & Joliot, A. (2003). Excitation transfer between photosynthetic units: The 1964 experiment. *Photosynthesis Research*, *76*(1–3), 241–245. https://doi.org/10.1023/A:1024908829819

Joyce, A. E. (2006). The coastal temperature network and ferry route programme: long-term temperature and salinity observations. *Science Series Data Report Cefas Lowestoft*, (43), 129pp.

Kaczor, A., Baranska, M. and Czamara, K. (2016) *Carotenoids, in Carotenoids: Nutrition, Analysis and Technology* (eds A. Kaczor and M. Baranska), John Wiley & Sons, Ltd, Chichester, UK. doi: 10.1002/9781118622223.ch1

Karl, T. R., & Trenberth, K. E. (2003). Modern Global Climate Change. *Science*, *302*(December), 1719–1724.

Kautsky, H., & Hirsch, A. (1931). Neue Versuche zur Kohlensäureassimilation. *Die Naturwissenschaften*, *19*(48), 964. https://doi.org/10.1007/BF01516164

Kiefer, D. A., Chamberlin, W. S., & Booth, C. R. (1989). Natural fluorescence of chlorophyll a: Relationship to photosynthesis and chlorophyll concentration in the western South Pacific gyre. *Limnology and Oceanography*, *34*(5), 868–881. https://doi.org/10.4319/lo.1989.34.5.0868

Kirk, J. T. (1997). Point-source integrating-cavity absorption meter: theoretical principles and numerical modelling. *Applied Optics*, *36*(24), 6123–6128. https://doi.org/10.1364/AO.36.006123

Kirk, J. T. (1995). Modeling the performance of an integrating-cavity absorption meter: theory and calculations for a spherical cavity. *Applied Optics*, *34*(21), 4397–4408. https://doi.org/10.1364/AO.34.004397

Klausmeier, C. A., Litchman, E., Daufresne, T., & Levin, S. A. (2008). Phytoplankton stoichiometry. *Ecological Research*, *23*(3), 479–485. https://doi.org/10.1007/s11284-008-0470-8

Kolber, Z. S., & Falkowski, P. G. (1992). Fast Repetition Rate (FRR) Fluorometer For Making In Situ Measurements Of Primary Productivity. *OCEANS '92. Mastering the Oceans Through Technology. Proceedings.*, *2*, 637–641. https://doi.org/10.1109/OCEANS.1992.607657

Kolber, Z., & Falkowski, P. G. (1993). Use of Active Fluorescence to Estimate Phytoplankton Photosynthesis In Situ. *Limnol. Oceanogr.*, *38*(8), 1646–1665. Retrieved from http://www.aslo.org/lo/toc/vol_38/issue_8/1646.pdf

Kolber, Z. S., Prášil, O., & Falkowski, P. G. (1998). Measurements of variable chlorophyll fluorescence using fast repetition rate techniques: defining methodology and experimental protocols. *Biochimica et Biophysica Acta (BBA) - Bioenergetics*, *1367*(1), 88–106.

Kondratyev, K.Y., Filatov, N.N. (Eds.), *Limnology and Remote Sensing. A Contemporary Approach*. Springer–Praxis Series in Remote Sensing, Springer, Berlin (1999)

Krause, G. H., & Weis, E. (1991). Chlorophyll Fluorescence and Photosynthesis: The Basics. *Annu. Rev. Plant Physiol. Plant Mol. Bioi*, *42*, 313–49. https://doi.org/10.1146/annurev.pp.42.060191.001525

Kreilgard, B., Higuchi, T., & Repta, A. J. (1975). Complexation in formulation of parenteral solutions: Solubilization of the cytotoxic agent hexamethylmelamine by complexation with gentisic acid species. *Journal of Pharmaceutical Sciences*. https://doi.org/10.1002/jps.2600641122

Kromkamp, J. C., & Forster, R. M. (2003). The use of variable fluorescence measurements in aquatic ecosystems: differences between multiple and single turnover measuring protocols and suggested terminology. *European Journal of Phycology*, *38*(2), 103–112. https://doi.org/10.1080/0967026031000094094

Kuhn, H., Försterling, H. and Waldeck, D. (n.d.). *Principles of physical chemistry*. 2nd ed. Wiley.

Langdon, C. (1993). The significance of respiration in photsynthetic measurements based on oxygen. *Marine Sciences Symposium*, *197*, 69–78.

Laurion, I., Blouin, F., & Roy, S. (2011). The quantitative filter technique for measuring phytoplankton absorption: Interference by MAAs in the UV waveband. *Limnology and Oceanography: Methods*, *1*(1996), 1–9. https://doi.org/10.4319/lom.2011.1.1

Lavaud, J., Rousseau, B., & Etienne, A.-L. (2004). General Features of Photoprotection by Energy Dissipation in Planktonic Diatoms (Bacillariophyceae). *Journal of Phycology*, *137*(1), 130–137. https://doi.org/10.1046/j.1529-8817.2004.03026.x

Lavorel, J., & Joliot, P. (1972). A connected model of the photosynthetic unit. *Biophysical Journal*, *12*(7), 815–31. https://doi.org/10.1016/S0006-3495(72)86125-3

Lawrenz, E., Silsbe, G., Capuzzo, E., Ylöstalo, P., Forster, R. M., Simis, S. G. H., … Suggett, D. J. (2013). Predicting the Electron Requirement for Carbon Fixation in Seas and Oceans. *PLoS ONE*, *8*(3). https://doi.org/10.1371/journal.pone.0058137

Leathers, R. A., Downes, T. V., & Davis, C. O. (2000). Analysis of a Point-Source Integrating-Cavity Absorption Meter. *Applied Optics*, *39*(33), 6118–6127.

Lefering, I., Röttgers, R., Weeks, R., Connor, D., Utschig, C., Heymann, K., & McKee, D. (2016). Improved determination of particulate absorption from combined filter pad and PSICAM measurements. *Optics Express*, *24*(22), 24805. https://doi.org/10.1364/OE.24.024805

Lefering, K. (2016). Characterisation of a Point-Source Integrating Cavity Absorption Meter for applications in optical oceanography. University of Strathclyde

Lerebourg, C. J. Y., Pilgrim, D. a, Ludbrook, G. D., & Neal, R. (2002). Development of a point source integrating cavity absorption meter. *Journal of Optics a-Pure and Applied Optics*, *4*(4), S56–S65. https://doi.org/10.1088/1464-4258/4/4/364

Lerebourg, C. J.-Y. J. (2003). *Development and Modelling of a Point Source Integrating Cavity Absorption Meter (PSICAM)*. University of Plymouth.

Lesser, M. P., & Gorbunov, M. Y. (2001). Diurnal and bathymetric changes in chlorophyll fluorescence yields of reef corals measured in situ with a fast repetition rate fluorometer.

Marine Ecology Progress Series, *212*(Vincent 1980), 69–77. https://doi.org/10.3354/meps212069

Levitus, S., Climatological Atlas of the World Ocean, NOAA/ERL GFDL Professional Paper 13, Princeton, N.J., 173 pp. (NTIS PB83-184093) 1982.

Li, W. K., Rao, D. V, Harrison, W. G., Smith, J. C., Cullen, J. J., Irwin, B., & Platt, T. (1983). Autotrophic picoplankton in the tropical ocean. *Science*. https://doi.org/10.1126/science.219.4582.292

Li, W., Smith, J., & Platt, T. (1984). Temperature response of photosynthetic capacity and carboxylase activity in Arctic marine phytoplankton. *Ecology*, *17*, 237–243. https://doi.org/10.3354/meps017237

Lindsey, R., & Scott, M. (2010, July 28). *What are Phytoplankton?* Retrieved from https://palebluedotreview.wordpress.com/a-closer%C2%A0look/what-are-phytoplankton/

Lock, M. A., & Williams, D. D. (1981). *Perspectives in running water ecology*. New York, NY: Plenum.

Lohrenz, S. E. (2000). A novel theoretical approach to correct for pathlength amplification and variable sampling loading in measurements of particulate spectral absorption by the quantitative filter technique. *Journal of Plankton Research*, *22*(4), 639–657. https://doi.org/10.1093/plankt/22.4.639

Loisel, H., Nicolas, J. M., Sciandra, A., Stramski, D., & Poteau, A. (2006). Spectral dependency of optical backscattering by marine particles from satellite remote sensing of the global ocean. *Journal of Geophysical Research: Oceans*, *111*(9), 1–14. https://doi.org/10.1029/2005JC003367

Longhurst, A., Sathyendranath, S., Platt, T., & Caverhill, C. (1995). An estimate of global primary production in the ocean from satelite radiometer data. *Journal of Plankton Research*, *17*(6), 1245–1271.

Mackey, K. R. M., Paytan, A., Caldeira, K., Grossman, A. R., Moran, D., McIlvin, M., & Saito, M. A. (2013). Effect of Temperature on Photosynthesis and Growth in Marine

Synechococcus spp. *Plant Physiology*, *163*(2), 815–829. https://doi.org/10.1104/pp.113.221937

Marra, J., & Barber, R. T. (2004). Phytoplankton and heterotrophic respiration in the surface layer of the ocean. *Geophysical Research Letters*, *31*(9), 12–15. https://doi.org/10.1029/2004GL019664

Martiny, A. C., Pham, C. T. A., Primeau, F. W., Vrugt, J. A., Moore, J. K., Levin, S. A., & Lomas, M. W. (2013). Strong latitudinal patterns in the elemental ratios of marine plankton and organic matter. *Nature Geosci*, *6*(4), 279–283. Retrieved from http://dx.doi.org/10.1038/ngeo1757

McClelland, H. L. O., Barbarin, N., Beaufort, L., Hermoso, M., Ferretti, P., Greaves, M., & Rickaby, R. E. M. (2016). Calcification response of a key phytoplankton family to millennial-scale environmental change. *Scientific Reports*, *6*(August), 34263. https://doi.org/10.1038/srep34263

McCoy, R. M. (2005). *Field Methods in Remote Sensing*. New York: The Guilford Press.

McGowan, J. A., Chelton, D. B., & Conversi, A. (1996). Plankton patterns, climate, and change in the California Current. *California Cooperative Oceanic Fisheries Investigations Reports*, *37*, 45–68.

McKee, D., & Cunningham, A. (2006). Identification and characterisation of two optical water types in the Irish Sea from in situ inherent optical properties and seawater constituents. *Estuarine, Coastal and Shelf Science*, *68*(1), 305–316. https://doi.org/10.1016/j.ecss.2006.02.010

McKee, D., Cunningham, A., & Dudek, A. (2007). Optical water type discrimination and tuning remote sensing band-ratio algorithms: Application to retrieval of chlorophyll and Kd(490) in the Irish and Celtic Seas. *Estuarine, Coastal and Shelf Science*, *73*(3–4), 827–834. https://doi.org/10.1016/j.ecss.2007.03.028

McKee, D., Piskozub, J., & Brown, I. (2008). Scattering error corrections for in situ absorption and attenuation measurements. *Optics Express*, *16*(24), 19480–19492. https://doi.org/10.1364/OE.16.019480

McManus, M. A., & Woodson, C. B. (2012). Plankton distribution and ocean dispersal. *J. Exp. Biol.*, *215*(6), 1008–1016. https://doi.org/10.1242/jeb.059014

Melis, A., & Brown, J. S. (1980). Stoichiometry of system I and system II reaction centers and of plastoquinone in different photosynthetic membranes. *Proceedings of the National Academy of Sciences*, *77*(8), 4712–4716. https://doi.org/10.1073/pnas.77.8.4712

Menzel, D. W., & Vaccaro, R. F. (1964). The Measurement of Dissolved Organic and Particulate Carbon in Seawater. *Woods Hole Oceanographic Institution*, 138–142.

Mitchell B.G., Kiefer D.A. (1984) Determination of Absorption and Fluorescence Excitation Spectra for Phytoplankton. In: Holm-Hansen O., Bolis L., Gilles R. (eds) *Marine Phytoplankton and Productivity. Lecture Notes on Coastal and Estuarine Studies,* vol 8. Springer, Berlin, Heidelberg

Mitchell, B. G., & Kiefer, D. (1988). Chlorophyll a specific absorption and fluorescence excitation spectra for light-limited phytoplankton. *Deep Sea Research Part A. Oceanographic …*, *35*(5), 639–663. https://doi.org/10.1016/0198-0149(88)90024-6

Mobley, C. D. (1994). Light and water: Radiative transfer in natural waters. *Academic Press*, (January 1994).

Moeini-Meybodi, H. (2009). UN-DESA Policy Brief No . 15 The significance of forests. *United Nations Department of Economic and Social Affairs*, (15).

Molot, L. A., & Dillon, P. J. (1997). Colour – mass balances and colour – dissolved organic carbon relationships in lakes and streams in central Ontario. *Canadian Journal of Fisheries and Aquatic Sciences*, *2795*, 2789–2795. https://doi.org/10.1139/cjfas-54-12-2789

Moore, C. M., Suggett, D. J., Hickman, a. E., Kim, Y.-N., Tweddle, J. F., Sharples, J., … Holligan, P. M. (2006). Phytoplankton photoacclimation and photoadaptation in response to environmental gradients in a shelf sea. *Limnol. Oceanogr*, *51*(2), 936–949. https://doi.org/10.4319/lo.2006.51.2.0936

Mora, C., Wei, C. L., Rollo, A., Amaro, T., Baco, A. R., Billett, D., … Yasuhara, M. (2013). Biotic and Human Vulnerability to Projected Changes in Ocean Biogeochemistry over the 21st Century. *PLoS Biology*, *11*(10). https://doi.org/10.1371/journal.pbio.1001682

Morel, A., & Prieur, L. (1977). Analysis of variations in ocean color. *Limnology and Oceanography*, *22*(4), 709–722. https://doi.org/10.4319/lo.1977.22.4.0709

Müller, P., Li, X. P., & Niyogi, K. K. (2001). Non-photochemical quenching. A response to excess light energy. *Plant Physiology*, *125*(4), 1558–1566. https://doi.org/10.1104/pp.125.4.1558

Nedbal, L., Trtflek, M., & Kaftan, D. (1999). Photochemistry Flash fluorescence induction : a novel method to study regulation of Photosystem II. *Energy*, *4*, 3–6. https://doi.org/10.1016/S1011-1344(99)00032-9

Ogura, N. (1975). Further studies on decomposition of dissolved organic matter in coastal seawater. *Marine Biology*, *31*(2), 101–111. https://doi.org/10.1007/BF00391622

Ohnishi, N., Allakhverdiev, S., Takahashi, S., Higashi, S., Watanabe, M., Nishiyama, Y., & Murata, N. (2005). Two-step mechanism of photodamage to photosystem II: step 1 occurs at the oxygen-evolving complex and step 2 occurs at the photochemical reaction center., (July), 8494–8499. https://doi.org/10.1021/bi047518q

Olson, R. J., Sosik, H. M., Chekalyuk, A. M., & Shalapyonok, A. (2000). Effects of iron enrichment on phytoplankton in the Southern Ocean during late summer: Active fluorescence and flow cystometric analyses. *Deep-Sea Research Part II: Topical Studies in Oceanography*, *47*(15–16), 3181–3200. https://doi.org/10.1016/S0967-0645(00)00064-3

O'Reilly, J., & Maritorena, S. (2000). Ocean color chlorophyll a algorithms for SeaWiFS, OC2, and OC4: Version 4. *SeaWiFS Postlaunch …*, 8–22. https://doi.org/10.1111/j.1600-0404.1995.tb01704.x

O'Reilly, J. E., & Dow, D. (2004). 19. Detritis - Particulate Organic Carbon (POC) and Dissolved Organic Carbon (DOC). *US Department of Commerce*, 107–112.

O'Reilly, J. E., Maritorena, S., Mitchell, B. G., Siegel, D. A., Carder, K. L., Garver, S. A., … McClain, C. R. (1998). Ocean color chlorophyll algorighms for SeaWiFS. *Journal of Geophysical Research*, *103*(C11), 24937–24953. https://doi.org/10.1029/98JC02160

Oreskes, N. (2005). The Scientific Consensus on Climate Change. *Science*, *306*(January), 2004–2005. https://doi.org/10.1126/science.1103618

Pascal, A. A., Liu, Z., Broess, K., van Oort, B., van Amerongen, H., Wang, C., Ruban, A. (2005). Molecular basis of photoprotection and control of photosynthetic light-harvesting. *Nature*, *436*(7047), 134–137. https://doi.org/10.1038/nature03795

Paulsen, H., Finkenzeller, B., & Kuehlein, N. (1993). Pigments induce folding of light-harvesting chlorophyll a/b-binding protein. *European Journal of Biochemistry*, *215*(3), 809–816. https://doi.org/10.1111/j.1432-1033.1993.tb18096.x

Paytan, A., & Street, J. (2005). Iron, Phytoplankton Growth, and the Carbon Cycle. In *Metal Ions in Biological Systems, Volume 43 - Biogeochemical Cycles of Elements* (pp. 153–193). CRC Press. https://doi.org/doi:10.1201/9780824751999.ch7

Pegau, W. S., Gray, D., & Zaneveld, J. R. V. (1997). Absorption and attenuation of visible and near-infrared light in water: dependence on temperature and salinity. *Appl. Opt.*, *36*(24), 6035–6046. https://doi.org/10.1364/AO.36.006035

Perkins R.G., Mouget J.L., Lefebvre S., Lavaud J, (2006). Light response curve methodology and possible implications in the application of chlorophyll fluorescence to benthic diatoms. *Mar Biol.* 149: 703-712

Peterson, B. J. (1980). Aquatic Primary Productivity and the 14C-CO2 Method: A History of the Productivity Problem. *Annual Review Ecologic Systems*, *11*, 359–385.

Pope, R. M., & Fry, E. S. (1997). Absorption spectrum (380-700nm) of pure water. II . Integrating cavity measurements. *Applied Optics*, *36*(33), 8710–8723.

Post, W. M., Peng, T.-H., Emanuel, W. R., King, A. W., Dale, V. H., & DeAngelis, D. L. (1990). The Global Carbon Cycle. *Science*.

Preisendorfer, R. W., “Application of radiative transfer theory to light measurement in the sea,” *Union Geod. Geophys. Inst. Monogr*. 10, 11–30 (1961).

Prieto, L., Vaillancourt, R. D., Hales, B., & Marra, J. (2008). On the relationship between carbon fixation efficiency and bio-optical characteristics of phytoplankton. *Journal of Plankton Research*, *30*(1), 43–56. https://doi.org/10.1093/plankt/fbm093

Raateoja, M., Seppälä, J., & Kuosa, H. (2004). Bio-optical modelling of primary production in the SW Finnish coastal zone, Baltic Sea: Fast repetition rate fluorometry in Case 2 waters. *Marine Ecology Progress Series*, *267*, 9–26. https://doi.org/10.3354/meps267009

Raateoja, M. P. (2004). Fast repetition rate fluorometry (FRRF) measuring phytoplankton productivity : A case study at the entrance to the Gulf of Finland , Baltic Sea, (June), 263–276.

Rabinowitch, E., & Govindjee. (1969). The photosynthetic pigments. *Photosynthesis*. Retrieved from http://www.life.illinois.edu/govindjee/Electronic Publications/Books/Photosynthesis.pdf

Rascher, U., Liebig, M., & Lüttge, U. (2000). Evaluation of instant light-response curves of chlorophyll fluorescence parameters obtained with a portable chlorophyll fluorometer on site in the field. *Plant, Cell and Environment*, *23*(12), 1397–1405. https://doi.org/10.1046/j.1365-3040.2000.00650.x

Raven J.A, Beardall J. 2003. CO_2 acquisition mechanisms in algae: Carbon dioxide diffusion and carbon dioxide concentrating mechanisms. In: Larkum A, Raven JA, Douglas S, eds. Photosynthesis in the Algae. *Advances in Photosynthesis* (Series Editor, Govindjee). Kluwer, 225–244.

Redfield, A. C. (1934). On the Proportions of Organic Derivatives in Sea Water and Their Relation to the Composition of Plankton. *University Press of Liverpool, James Johnstone Memorial Volume*. https://doi.org/citeulike-article-id:11236440

Regaudie-de-Gioux, A., Lasternas, S., Agustí, S., & Duarte, C. M. (2014). Comparing marine primary production estimates through different methods and development of

conversion equations. *Frontiers in Marine Science*, *1*(July), 1–14. https://doi.org/10.3389/fmars.2014.00019

Reimers, J. R., Cai, Z.-L., Kobayashi, R., Rätsep, M., Freiberg, A., & Krausz, E. (2013). Assignment of the Q-bands of the chlorophylls: coherence loss via Qx - Qy mixing. *Scientific Reports*, *3*, 2761. https://doi.org/10.1038/srep02761

Robinson, C., & Peter, P. J. (2007). Respiration and its measurement in surface marine waters. *Respiration in Aquatic Ecosystems*, (i). https://doi.org/10.1093/acprof:oso/9780198527084.003.0009

Röttgers, R., Schönfeld, W., Kipp, P.-R., & Doerffer, R. (2005). Practical test of a point-source integrating cavity absorption meter: the performance of different collector assemblies. *Applied Optics*, *44*(26), 5549–5560. https://doi.org/10.1364/AO.44.005549

Röttgers, R., Häse, C., & Doerffer, R. (2007). Determination of the particulate absorption of microalgae using a point-source integrating-cavity absorption meter : verification with a photometric technique , improvements for pigment bleaching, and correction for chlorophyll flu. *Limnology & Oceanography: Methods*, *5*, 1–12.

Röttgers, R., & Doerffer, R. (2007). Measurements of optical absorption by CDOM using a point-source integrating cavity absorption meter. *Limnology & Oceanography: Methods*, *5*, 126–135.

Röttgers, R., Heymann, K., & Krasemann, H. (2014). Suspended matter concentrations in coastal waters: Methodological improvements to quantify individual measurement uncertainty. *Estuarine, Coastal and Shelf Science*, *151*, 148–155. https://doi.org/10.1016/j.ecss.2014.10.010

Sakshaug. (1997). Parameters of photosynthesis definitions theory and interpretation. *Journal of Plankton Research*. https://doi.org/10.1093/plankt/19.11.1637

Sathyajith, M., & Geeta, S. P. (2011). *Environmental Science and Engineering Environmental Engineering*. *Advances in Wind Energy Conversion Technology* (Vol. 3). https://doi.org/10.1007/978-3-540-88258-9

Schallenberg, C., Lewis, M. R., Kelley, D. E., & Cullen, J. J. (2008). Inferred influence of nutrient availability on the relationship between Sun-induced chlorophyll fluorescence and incident irradiance in the Bering Sea. *Journal of Geophysical Research: Oceans*, *113*(7), 1–21. https://doi.org/10.1029/2007JC004355

Schmidt, T. M., Delong, E. F., & Pace, N. R. (1991). by 16S rRNA gene cloning and sequencing . Analysis of a Marine Picoplankton Community by 16S rRNA Gene Cloning and Sequencing, *173*(14), 4371–4378.

Schreiber, U., Schliwa, U., & Bilger, W. (1986). Continuous recording of photochemical and non-photochemical chlorophyll fluorescence quenching with a new type of modulation fluorometer. *Photosynthesis Research*, *10*, 51–62. Retrieved from http://download.springer.com/static/pdf/298/art%253A10.1007%252FBF00024185.pdf?auth66=1383302205_db17564b62f2d1d4023205baac545c93&ext=.pdf

Schuback, N., Schallenberg, C., Duckham, C., Maldonado, M. T., & Tortell, P. D. (2015). Interacting Effects of Light and Iron Availability on the Coupling of Photosynthetic Electron Transport and CO2-Assimilation in Marine Phytoplankton. *PloS One*, *10*(7), e0133235. https://doi.org/10.1371/journal.pone.0133235

Schuurmans, R. M., Schuurmans, J. M., Bekker, M., Kromkamp, J. C., Matthijs, H. C. P., & Hellingwerf, K. J. (2014). The Redox Potential of the Plastoquinone Pool of the Cyanobacterium Synechocystis Species Strain PCC 6803 Is under Strict Homeostatic Control. *Plant Physiology*, *165*(1), 463–475. https://doi.org/10.1104/pp.114.237313

Serôdio, J., Da Silva, J. M., & Catarino, F. (2001). Use of in vivo chlorophyll a fluorescence to quantify short-term variations in the productive biomass of intertidal microphytobenthos. *Marine Ecology Progress Series*, *218*, 45–61. https://doi.org/10.3354/meps218045

Serôdio J., Ezequiel J., Frommlet J., Laviale M., Lavaud J., (2013) A method for the rapid generation of non-sequential light response curves of chlorophyll fluorescence. *Plant Physiol.* 163: 1089-102

Shen, Q., Li, J., Zhang, F., Sun, X., Li, J., Li, W., & Zhang, B. (2015). Classification of several optically complex waters in China using in situ remote sensing reflectance. *Remote Sensing*, *7*(11), 14731–14756. https://doi.org/10.3390/rs71114731

Sheng, M. a, Xiaofeng, Y., Zui, T., Ziwei, L., & Xuan, Z. (2014). Assessment of uncertainties of ocean color parameters for the ocean Carbon-based Productivity Model. *IOP Conference Series: Earth and Environmental Science*, *17*, 1–8. https://doi.org/10.1088/1755-1315/17/1/012102

Siegenthaler, U., & Sarmiento, J. L. (1993). Atmospheric carbon dioxide and the ocean. *Nature*, *365*(6442), 119–125. https://doi.org/10.1038/365119a0

Singh, B. P. (2013). *Biofuel Crop Sustainability (Google eBook)*. (B. P. Singh, Ed.). Ames: John Wiley & Sons, Inc. Retrieved from http://books.google.com/books?hl=en&lr=&id=fCCVmkLIKisC&pgis=1

Singhal, G.S., Renger, G., Sopory, S.K., Irrgang, K-D, Govindjee (eds) *Concepts in Photobiology: Photosynthesis and Photomorphogenesis*, Narosa Publishers/New Delhi; and Kluwer Academic/Dordrecht, pp. 11-51

Smith, S. V. (1984). Phosphorus Versus Nitrogen Limitation in the Marine-Environment. *Limnology and Oceanography*, *29*(6), 1149–1160. https://doi.org/10.4319/lo.1984.29.6.1149

Sosik, H. (2008). Characterizing seawater constituents from optical properties. *Op. cit., UNESCO*,281–329. Retrieved from: flora.geog.ucsb.edu/public/opl/tommy/optics_class/HABWatch/Sosik/Chapter12_Sosik3.doc

Sournia, A., & Ricard, M. (1991). Marine phytoplankton : how many species in the world ocean ? *Journal of Plankton Research*, *13*(5), 1093–1099.

Ssebiyonga, N., Erga, S. R., Hamre, B., Stamnes, J. J., & Frette, Ø. (2013). Light conditions and photosynthetic efficiency of phytoplankton in Murchison Bay, Lake Victoria, Uganda. *Limnologica*, *43*(3), 185–193. https://doi.org/10.1016/j.limno.2012.09.005

Stavn, R. H., Rick, H. J., & Falster, A. V. (2009). Correcting the errors from variable sea salt retention and water of hydration in loss on ignition analysis: Implications for studies of estuarine and coastal waters. *Estuarine, Coastal and Shelf Science*, *81*(4), 575–582. https://doi.org/10.1016/j.ecss.2008.12.017

Steele, J. H. (1959). The Quantitative Ecology of Marine Phytoplankton. *Biological Reviews*, *34*(2), 129–158. https://doi.org/10.1111/j.1469-185X.1959.tb01287.x

Steele, J. H., Thorpe, S. A, Turekian, K. K. (2001). *Encyclopedia of ocean sciences*(2nd ed.). Amsterdam, MA: Elsevier.

Steeman-Nielsen, 1952. The use of radioactive carbon (C14) for measuring organic production in the sea. *J. Cons. Int. Explor. Mer*., 18, 117-140.

Steinberg-Yfrach, G., Rigaud, J. L., Durantini, E. N., Moore, A. L., Gust, D., & Moore, T. A. (1998). Light-driven production of ATP catalysed by F0F1-ATP synthase in an artificial photosynthetic membrane. *Nature*, *392*(6675), 479–482. https://doi.org/10.1038/33116

Stirbet, A. (2013). Excitonic connectivity between photosystem II units: What is it, and how to measure it? *Photosynthesis Research*, *116*(2–3), 189–214. https://doi.org/10.1007/s11120-013-9863-9

Stockett, M. H., Musbat, L., Kjær, C., Houmøller, J., Toker, Y., Rubio, A., … Nielsen, S. B. (2015). The Soret absorption band of isolated chlorophyll a and b tagged with quaternary ammonium ions. *Phys. Chem. Chem. Phys.*, *17*, 25793–25798. https://doi.org/10.1039/C5CP01513H

Stramski, D., Reynolds, R., Kaczmarek, S., UItz, J., & Zheng, G. (2015). Correction of pathlength amplification in the filter-pad technique for measurements of particulate absorption coefficient in the visible spectral region. *Appl. Opt.*, *54*(22), 6763–6782. https://doi.org/10.1364/AO.54.006763

Strasser, R. J., Srivastava, A., & Tsimilli-Michael, M. (2000). The fluorescence transient as a tool to characterize and screen photosynthetic samples. *Probing Photosynthesis: Mechanism, Regulation & Adaptation*, (January), 443–480. Retrieved from http://ww.hansatech-instruments.com/docs/the fluorescence transient.pdf

Strasser, R. J., & Stirbet, A. D. (2001). Estimation of the energetic connectivity of PS II centres in plants using the fluorescence rise O-J-I-P - Fitting of experimental data to three different PS II models. *Mathematics and Computers in Simulation*, *56*(4–5), 451–461. https://doi.org/10.1016/S0378-4754(01)00314-7

Strickland, J. D. H., & Parsons, T. R. (1972). *A Practical Handbook of Seawater Analysis*. (J. D. H. Strickland & T. R. Parsons, Eds.) (2nd ed.). Ottawa: Canadian Government Publishing Centre.

Suggett, D. J., Moore, C. M., Hickman, A. E., & Geider, R. J. (2009). Interpretation of Fast Repetition Rate (FRR) Fluorescence: Signatures of Phytoplankton Community Structure Versus Physiological State. *Marine Ecology Progress Series*, *376*, 1–19. Retrieved from http://www.int-res.com/articles/feature/m376p001.pdf

Tassan, S., Ferrari, G. M., Bricaud, A., & Babin, M. (2000). Variability of the amplification factor of light absorption by filter-retained aquatic particles in the coastal environment. *Journal of Plankton Research*, *22*(4), 659–668. https://doi.org/10.1093/plankt/22.4.659

Telfer, De Las Rivas, J., Barber, J., β-Carotene within the isolated Photosystem II reaction centre: photooxidation and irreversible bleaching of this chromophore by oxidised P680, *Biochimica et Biophysica Acta (BBA) - Bioenergetics*, 1060(1), 1991, 106-114, ISSN 0005-2728, http://dx.doi.org/10.1016/S0005-2728(05)80125-2.Metal Ions in Biological Systems, 153-193. doi:10.1201/9780824751999.ch7

Tilman, D., Kilham, S. S., & Kilham, P. (1982). Phytoplankton Community Ecology: The Role of Limiting Nutrients. *Annual Review of Ecology and Systematics*, *13*(1), 349–372. https://doi.org/10.1146/annurev.es.13.110182.002025

Tilzer, M. M., Gieskes, W. W., Heusel, R., & Fenton, N. (1994). The impact of phytoplankton on spectral water transparency in the Southern Ocean: implications for primary productivity. *Polar Biology*, *14*(2), 127–136. https://doi.org/10.1007/BF00234975

Twining, B. S., Baines, S. B., & Fisher, N. S. (2004). Element stoichiometries of individual plankton cells collected during the Southern Ocean Iron Experiment (SOFeX). *Limnology and Oceanography*, *49*(6), 2115–2128. https://doi.org/10.4319/lo.2004.49.6.2115

Valeur, B. (2001). *Molecular Fluorescence: Principles and Applications*. (B. Valeur, Ed.), *Methods* (Vol. 8). Weinheim: Wiley-VCH Verlag GmbH. https://doi.org/10.1002/3527600248

Vredenberg, W. J., and Duysens, L. N. (1963). Transfer of Energy from Bacteriochlorophyll to a Reaction Centre During Bacterial Photosynthesis. *Nature*, 197(4865), 355-357. doi:10.1038/197355a0

Webb, W. L., Newton, M., & Starr, D. (1974). Carbon dioxide exchange of Alnus rubra - A mathematical model. *Oecologia*, *17*(4), 281–291. https://doi.org/10.1007/BF00345747

Werner, F. E., Cowen, R. K., & Paris, C. B. (2007). Coupled Biological and Physical Models. *Oceanography*, *20*(3), 54–69. https://doi.org/10.1016/S0967-0645(00)00079-5

Wetzel R G. *Limnology*. Philadelphia: Saunders, (1975) 1983. 860 p. [Freshwater Ecology Program, Dept. Biological Sciences. Univ. Alabama, Tuscaloosa, AL]

Williamson, C. E., Morris, D. P., Pace, M. L., & Olson, O. G. (1999). Dissolved organic carbon and nutrients as regulators of lake ecosystems: Resurrection of a more integrated paradigm. *Limnology and Oceanography*, *44*(3_part_2), 795–803. https://doi.org/10.4319/lo.1999.44.3_part_2.0795

Zapata, M., Rodríguez, F., & Garrido, J. L. (2000). Separation of chlorophylls and carotenoids from marine phytoplankton: A new HPLC method using a reversed phase C8 column and pyridine-containing mobile phases. *Marine Ecology Progress Series*, *195*, 29–45. https://doi.org/10.3354/meps195029

Zaneveld, J. Ronald V., Kitchen, J.C., Moore, C.C.,; Scattering error correction of reflecting-tube absorption meters. *Proc. SPIE 2258, Ocean Optics XII*, 44 (October 26, 1994); doi:10.1117/12.190095.